2005

AFM and C-AFM Studies of GaN Films

Katherine Cooper
Virginia Commonwealth University

AFM and C-AFM Studies of GaN Films

A thesis submitted in partial fulfillment of the requirements for the degree of Master of Science in Physics/Applied Physics at Virginia Commonwealth University.

By

Katherine A. Cooper

B.S. in Mechanical Engineering

Virginia Polytechnic and State University, 2002

M.S. in Physics/Applied Physics

Virginia Commonwealth University, 2005

Director: Alison. A. Baski, Associate Professor, Department of Physics

Virginia Commonwealth University,

Richmond, Virginia, 23284

August 9, 2005

Acknowledgments

This thesis would not have come to fruition were it not for the help and assistance of my friends, and my lab- and work-mates here in the Physics Department. I particularly want to thank the following people for their special brands of support: Matt, for his brilliant instruction on the AFM; Lindsay, Penee, Laura and Jenn, for their kind ear when things were hectic and for their support, and Dr. Munoz, for his patience with my questions and his advice. To the entire Physics Department: thank you for your warm welcome and acceptance and for your unceasing support.

I now want and need to thank Dr. Alison Baski for her faith in my abilities and for her correction when I was not living up to my potential. Dr. Baski has encouraged me silently and has been an active advocate for my future graduate career. She has enabled me to pursue the path I want to take and I hope she knows how much I appreciate her efforts on my behalf.

Finally, I have to thank my family. Firstly, let me thank my parents who have allowed me to live at home and be a bum so that I could afford to pay off my debts and go to school to advance my education. Secondly, I want to thank my sisters who, though they are probably not aware, have been a monumental support to me just by listening to my complaints when I've had a bad day. This thesis is dedicated to all the afore-mentioned people, but especially to my parents who have always encouraged me to strive for what I want with no limitations. Mom and Dad this is for you.

Table of Contents

List of Figures

Abstract

AFM and C-AFM Studies of GaN Films

By Katherine A. Cooper, M.S.

A thesis submitted in partial fulfillment of the requirements for the degree of Master of Science at Virginia Commonwealth University. Virginia Commonwealth University, 2005.

Major Director: Alison A. Baski, Associate Professor, Department of Physics

This thesis uses the techniques of atomic force microscope (AFM) and conductive AFM (C-AFM) to study the conduction properties of n-type GaN films. A total of 16 samples were examined and grouped according to their surface morphologies and conduction behaviors. The most common type of surface morphology was that of Ga-rich samples having undulating "hillocks" with interspersed holes. Although most of the samples had this common morphology, their local conduction behaviors were not all similar. Local I-V spectra of the tip-sample Schottky contact could be grouped according to three major types: low leakage, high leakage, and "p-type". The highest quality samples with low leakage were usually grown at moderate temperatures (~650 °C). For such samples, localized leakage only occurred at screw dislocations located at small pits terminating surface hillocks. I-V spectra taken on and off such hillocks were fit in forward bias to determine whether field emission or Frenkel-Poole conduction were dominant . Although field emission is a good fit compared to Frenkel-Poole, yielding reasonable values for the barrier height, the results are not yet conclusive without variable temperature studies.

Chapter 1. Atomic Force Microscopy (AFM) and Conductive AFM

1.1 Atomic Force Microscopy (AFM)

The atomic force microscope (AFM) was invented in 1986, when researchers at IBM (Binnig and Gerber) and Stanford University (Quate) recognized the need for a microscopy technique that could examine insulating surfaces using a force mechanism. The original prototype AFM scanned a gold foil lever across the surface and measured the accompanying deflections caused by changes in force. Now, with the capability to micromachine such levers, commercial instruments are available which use lasers to detect deflection. The AFM is heavily relied on as a tool for researchers and can be used to image conducting, insulating, and biological specimens. This makes the AFM a highly versatile instrument with many possible modifications.

The fundamental AFM design consists of a micromachined cantilever that is brought into contact with a sample surface while the tip-sample force is monitored during scanning. The force is measured by reflecting a laser beam off the backside of the cantilever and monitoring the beam's reflected position with a photodetector. As the cantilever bends due to the induced tip-sample forces, the laser moves on the detector. There are two basic methods used to scan the sample surface: contact mode and TappingMode™. In contact mode, the tip is always in contact with the sample, similar to the needle on a record player. A feedback circuit maintains a constant tip-sample force as the sample is scanned. In this manner, the reflected laser beam is in a fixed position on the photodetector. In TappingMode™ the cantilever is vibrated at its resonance frequency while scanning. When the tip approaches the sample, it touches only during the downward cycle of its oscillation. A feedback loop is used to control the tip-sample force by maintaining a constant oscillation amplitude as the surface is scanned.

TappingMode™ is often preferred for topographic imaging of a sample, as it reduces the lateral forces that can damage the tip and sample.

Typically, the cantilevers used in AFM are micromachined from Si or Si_3N_4 because low force constants (~1 N/m) and high resonant frequencies (50 – 500 kHz) are desirable. All cantilevers have an integrated tip with a diameter of 40 – 120 nm for Si_3N_4 and 10 – 20 nm for Si cantilevers. TappingMode™ cantilevers usually have a larger force constant (20 – 100 N/m) and higher resonant frequencies (200 – 400 kHz) than those used for contact mode. The two most common cantilever designs are the so-called diving-board constructed from Si, or a triangle-shaped Si_3N_4 tip. For the applications discussed here, the diving-board tip was used.

A photograph of our Dimension 3100 AFM is shown in Fig 1.1a. A sample is placed on the chuck plate and can be moved on a translational stage using computer controls. The AFM head above the sample contains the laser, cantilever, piezoelectric tube scanner, and photodetector in one unit. An optical microscope is mounted to the side of the head, and is used to locate the tip and sample with respect to one another. Once a sample is mounted on the chuck, the laser beam is aligned on the cantilever by means of adjusting two knobs on the top of the AFM head, and then aligned on the photodetector by knob adjustments on the left side of the AFM head. The cantilever must then be tuned to its resonance frequency in order to obtain a TappingMode™ image. Tuning is performed by means of an automated computer routine activated by clicking the tuning icon indicated in Fig. 1.2. Please note that occasionally the tip will not tune properly and an error message window will appear notifying the user that the tip may be broken or misaligned. After a successful tuning, the tip and sample must be properly located so that the automatic computer approach may commence. A trackball control is used to adjust the relative position of tip and sample and to focus on each of these using the optical microscope. This is accomplished by clicking the Focus Tip and Focus Sample icons on the operating screen (see Fig. 1.2). Finally, the tip can approach the surface to begin scanning, a step completed by clicking the Engage icon.

When the tip is engaged and an image is being obtained, several user adjustments are necessary to optimize imaging. Firstly, the scope trace should be inspected to ensure that the cantilever is "tracking" the sample topography (click the Scope Trace icon indicated in Fig. 1.2). The trace (left to right, indicated by a white line) and retrace (right to left, indicated by a yellow line) should follow a nearly identical path. Generally, if this path is not similar, the tip is not properly tracking the sample and the tip-sample force must be increased. The best method to gradually increase the force (i.e., Amplitude Setpoint value in the Feedback Controls menu) is to manually adjust the force by means of the left/right arrow keys on the keyboard. In TappingMode™, the minimum Amplitude Setpoint for a "softer" tip (one with a lower oscillation frequency) should be in the range of 0.9 V. For a stiffer tip (higher oscillation frequency), the minimum voltage setting is usually in the range of 1 to 1.3 V. Note that a *lower* amplitude setpoint corresponds to a *higher* tip-sample force in TappingMode™, due to the fact that the setpoint indicates the amplitude range of the vibrating cantilever. The amplitude is largest when the cantilever is free to oscillate above the sample, and decreases as the tip is brought closer to the surface and experiences a greater force. When an optimal force has been achieved (i.e., the trace/retrace lines are nearly the same), the Integral and Proportional Gains should next be adjusted. The Integral Gain should be in the range of 0.2 – 0.5 and the Proportional Gain in the range of 0.4 – 1.0. After the Amplitude Setpoint and Gains are adjusted, the image can be displayed again (click the Image Mode icon).

1.2 Conductive Atomic Force Microscopy (C-AFM)

Frequently, local conductivity data is useful to correlate electrical activity of a sample to its topography. This data can be acquired using a modification of AFM known as conductive AFM (C-AFM). In this application, the AFM is operated in *contact* mode using an electrically conductive cantilever connected to a voltage source. In this study of GaN films, we have used Pt-coated Si cantilevers, and have made an Ohmic contact between the film and sample holder using silver paint on a Ti/Al/Ti/Au contact. During

C-AFM imaging, a DC bias voltage in the range of –12 V to 12 V is applied to the sample and a low-noise amplifier detects the localized *current* between the tip and sample. A schematic of this setup can be seen in Fig. 1.3. Here, the tip acts as a microscopic Schottky contact with the sample surface (i.e., conduction under only one voltage bias). A special cantilever holder is used for C-AFM (see Fig. 1.4c), which includes a wire with a small plug that is inserted into one of two conductive-AFM modules: the C-AFM module and the TUNA module. The modules work in a similar manner, but have different current sensitivities and ranges. The C-AFM module has a current range of ±10 nA, while the TUNA module has a current range of ±100 pA (1 pA sensitivity).

For the applications discussed here, the same tip holder was used to obtain both TappingMode™ topography images and C-AFM or TUNA data. (Henceforth, reference to C-AFM will include both types of modules.) The common method for C-AFM imaging is to first take a TappingMode™ image, which typically has higher resolution than a contact mode image. Once the scan is completed, it is necessary to *retract* the tip before switching to C-AFM mode. This is accomplished by clicking the retract tip icon. A window appears giving the option of Tapping, C-AFM, or contact mode. Click C-AFM and the settings will change automatically. After the settings change, the user must readjust the laser beam on the detector so that the RMS voltage is –2.0 V before approaching the surface to perform C-AFM imaging. In order to correlate topographic features from the Tapping-mode image with enhanced current conduction in the C-AFM images, it is necessary to check the alignment of the imaging area. When changing from Tapping mode to contact mode for C-AFM imaging, the cantilever position may change on the surface. It is useful to export the TappingMode™ image to a file and display it in another window so that adjustments to the contact mode image position can be made until the desired area is located.

During C-AFM imaging, the tip-sample forces are optimized by adjusting the Deflection Setpoint (similar to the Amplitude Setpoint on the TappingMode™ screen) and the Integral and Proportional Gains. Note that in contact mode, a *higher* Deflection

Setpoint corresponds to a *greater* tip-sample force, which is opposite to the relationship in TappingMode™. The Integral and Proportional Gains have typical values of 1.0 – 2.0 for the Integral Gain and 2.0 – 4.0 for the Proportional Gain. The gain relationship is optimized when the Proportional Gain is approximately twice that of the Integral Gain. Figures 1.5 and 1.6 show representative input screens for the TUNA and C-AFM modules, respectively, and indicate important values. Once the contact mode topography image is optimized, the voltage can be set in order to detect current conduction. In these studies on n-type GaN, forward bias to the sample corresponds to a negative voltage and reverse bias to a positive voltage.

1.3 Localized I-V Spectra

One of the aspects which make C-AFM and TUNA so advantageous is the ability to take microscopic current-voltage (I-V) spectra on a sample. There are two methods for taking spectra: 1) Point-Scan method, where the user can take point spectra at a specific location, and 2) Matrix method, where the user can take a matrix of spectra across an area of the sample. Both of these methods have advantages. Spectra at a point location can give excellent data relevant to specific features. Spectra taken as a matrix, however, can provide more comprehensive data as to how these features conduct with respect to other topographic features. In this study, matrix spectra have been primarily used to differentiate the behavior of I-V spectra on and off features such as "hillocks". Such features have been found to be associated with leakage current on the GaN samples under study.

The Point-Scan Method involves first taking a preliminary scan of an area to locate a feature of interest. These scans are usually taken at an 8:1 aspect ratio (yielding a rectangular image) so that the feature dominates the scan area. To acquire a spectrum, the Advanced Force Mode option is used (View → Force Mode → Advanced or click the button indicated in Fig. 1.5). The screen will change and the user will need to set the Ramp Channel to DC Sample Bias and the Data Type to Tuna Current (same for TUNA

or C-AFM module). In this study, the remainder of the settings were typically chosen as follows:

a. Ramp Begin: -12.0V (Maximum negative voltage)
b. Ramp End: 12.0V (Maximum positive voltage)
c. Scan Rate: 0.3 Hz
d. Number of Samples: 512 (Number of data points in each I-V spectrum)
e. Average Count: 10 (Number of I-V spectra to be averaged)
f. Ramp Delay: 500μs
g. Reverse Delay: 500μs

Once these parameters are adjusted, the spectra must be saved, or captured, previous to the spectra being taken (click the capture button). The capture status at the bottom of the screen will change to "Next". The computer routine will take the I-V spectrum at the center of the previous image, and the curve will appear on the screen. The capture status will then change to "Done". A screen capture indicating the important values can be seen in Fig. 1.7.

The Matrix Method is somewhat more complicated. Again, the first step is to take an image with the 8:1 aspect ratio, so that the feature of interest is dominating the scan area. In this study, the majority of the scans were 1.0 – 2.0 μm in size, which typically results in one feature appearing in the scan window. This image should then be captured before taking spectra. Again, enter the Advance Force Mode in the manner described above. When the screen changes, check that the Ramp Channel and Data Type are set to "DC Sample Bias" and "TUNA Current", respectively. In this study, the remainder of the settings were typically chosen as follows:

a. Ramp begin: –12.0 V
b. Ramp end: 12.0 V
c. Scan rate: 0.3 Hz
d. Number of samples: 512
e. Average count: 10
f. Ramp Delay: 500 μs
g. Reverse Delay: 500 μs

h. Columns: 11 (Number of positions along a row at which spectra are taken; set to an odd number so that spectra are taken at each end of the scan area and one at the center of the area.)
i. Rows: 1 (Number of rows along which spectra are taken – only one row was used in this study.)
j. Column Step: (Distance between spectra as calculated for the number of columns and the image width.)
k. Capture: Enabled

The number of columns is the most important setting. The value used in this study is 11, which ensures that a sufficient number of spectra are taken so that changes can be detected with respect to topographic features. The column setting is incomplete without the column step value. This value is designated by the number of columns and the size of the image. For example, a 1.0-μm image with 11 columns results in a column step of 100 nm. Once all of these parameters are properly set, press the **matrix scan button** (indicated in Fig. 1.7) to begin the matrix scan. The computerized routine will then store an averaged I-V spectrum for each point in the matrix defined by the Column, Column Step, and Row.

Chapter 1 Figures

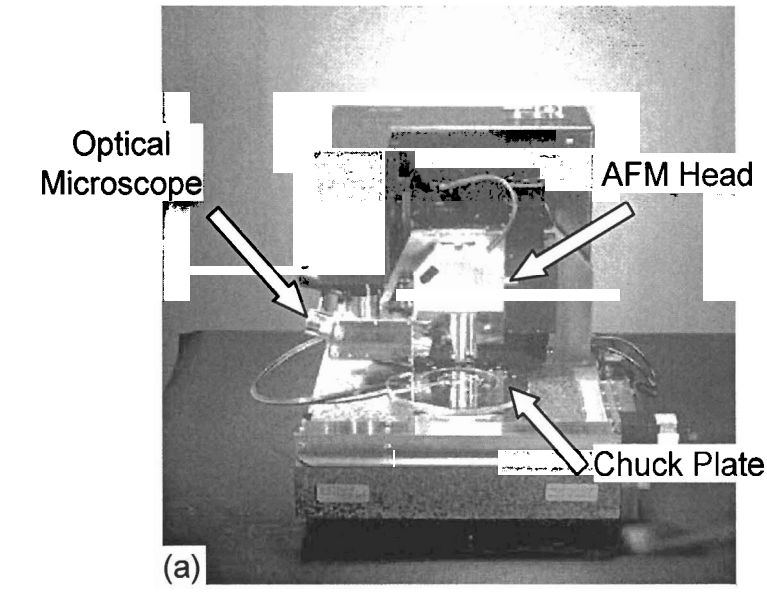

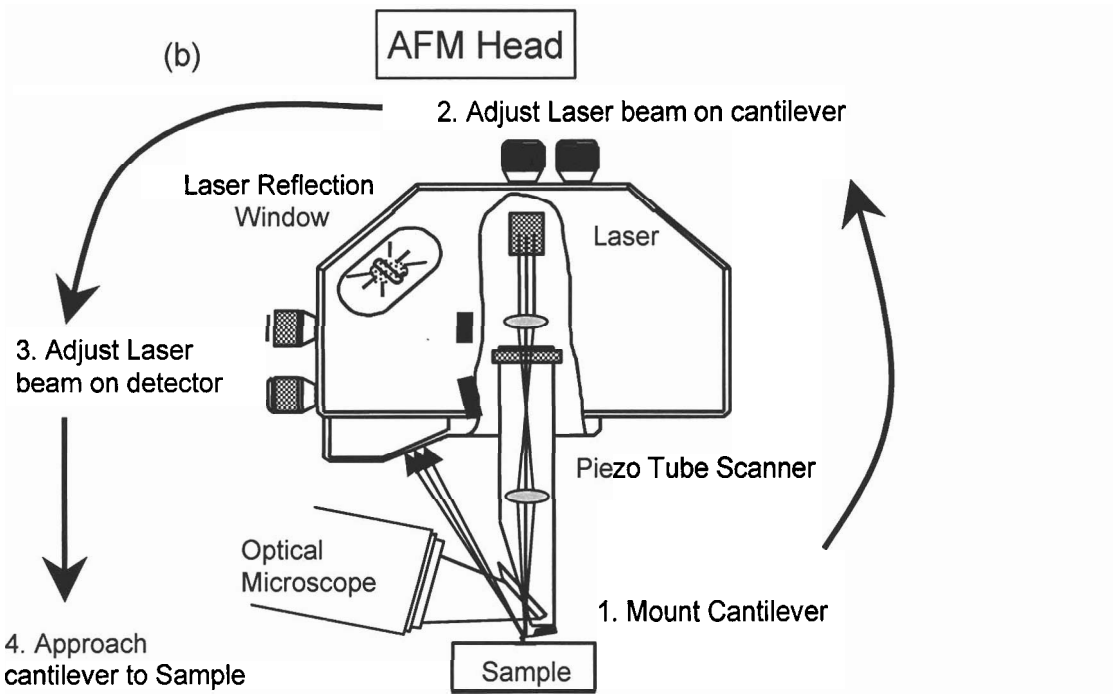

Fig. 1.1: (a) Dimension 3100 AFM unit and (b) schematic of AFM head.[1]

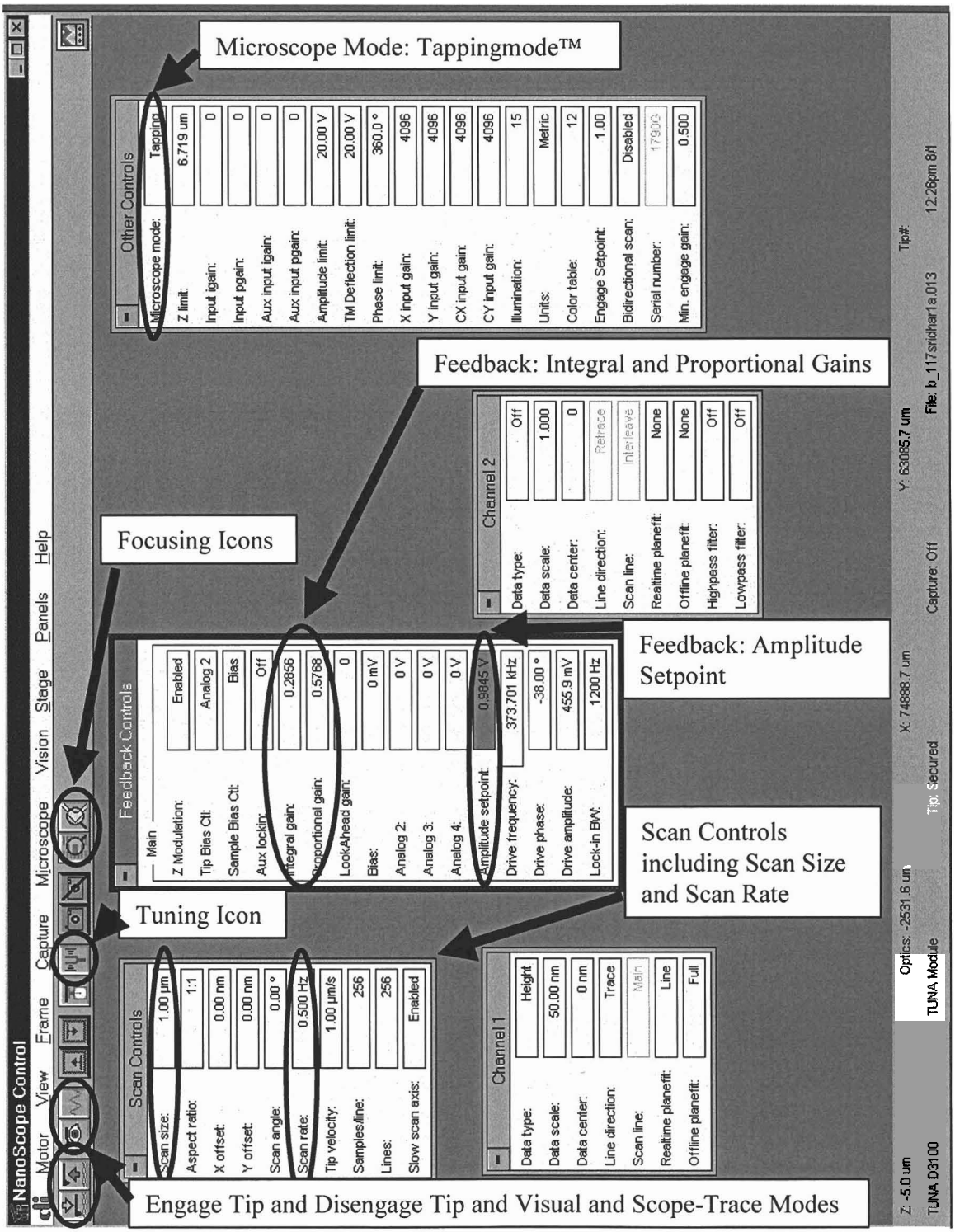

Fig. 1.2: Screen capture of AFM TappingMode Data Screen.

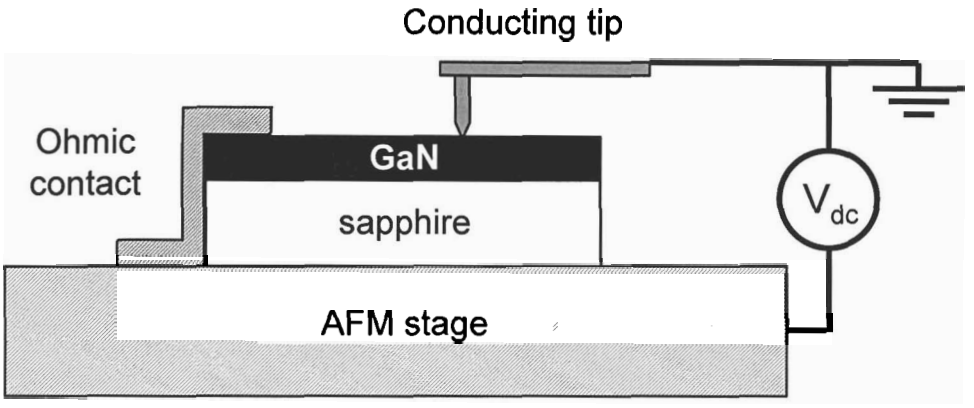

Fig. 1.3: Schematic of the Conductive AFM (C-AFM) and Tunneling AFM (TUNA) techniques.[1]

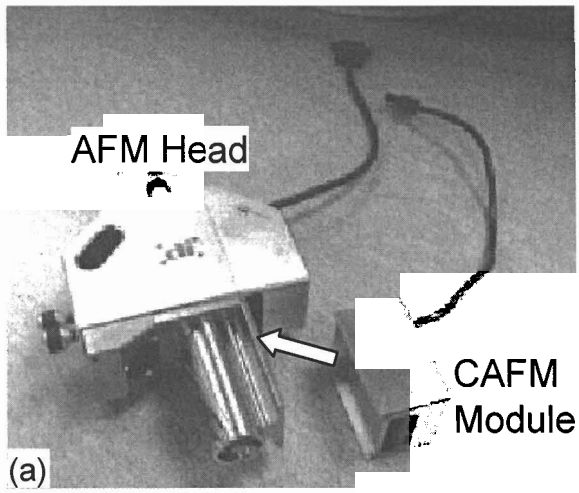

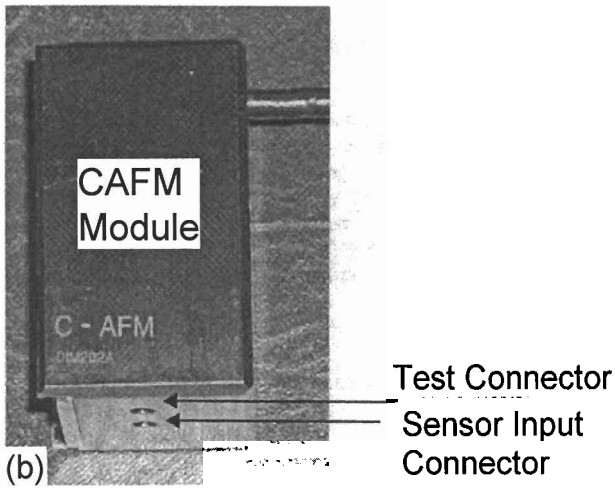

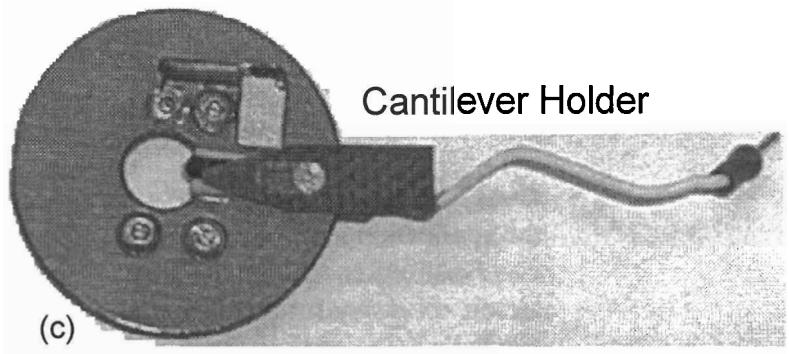

Fig. 1.4: (a) AFM head and C-AFM module attachment, (b) close-up of module, and (c) C-AFM cantilever holder.

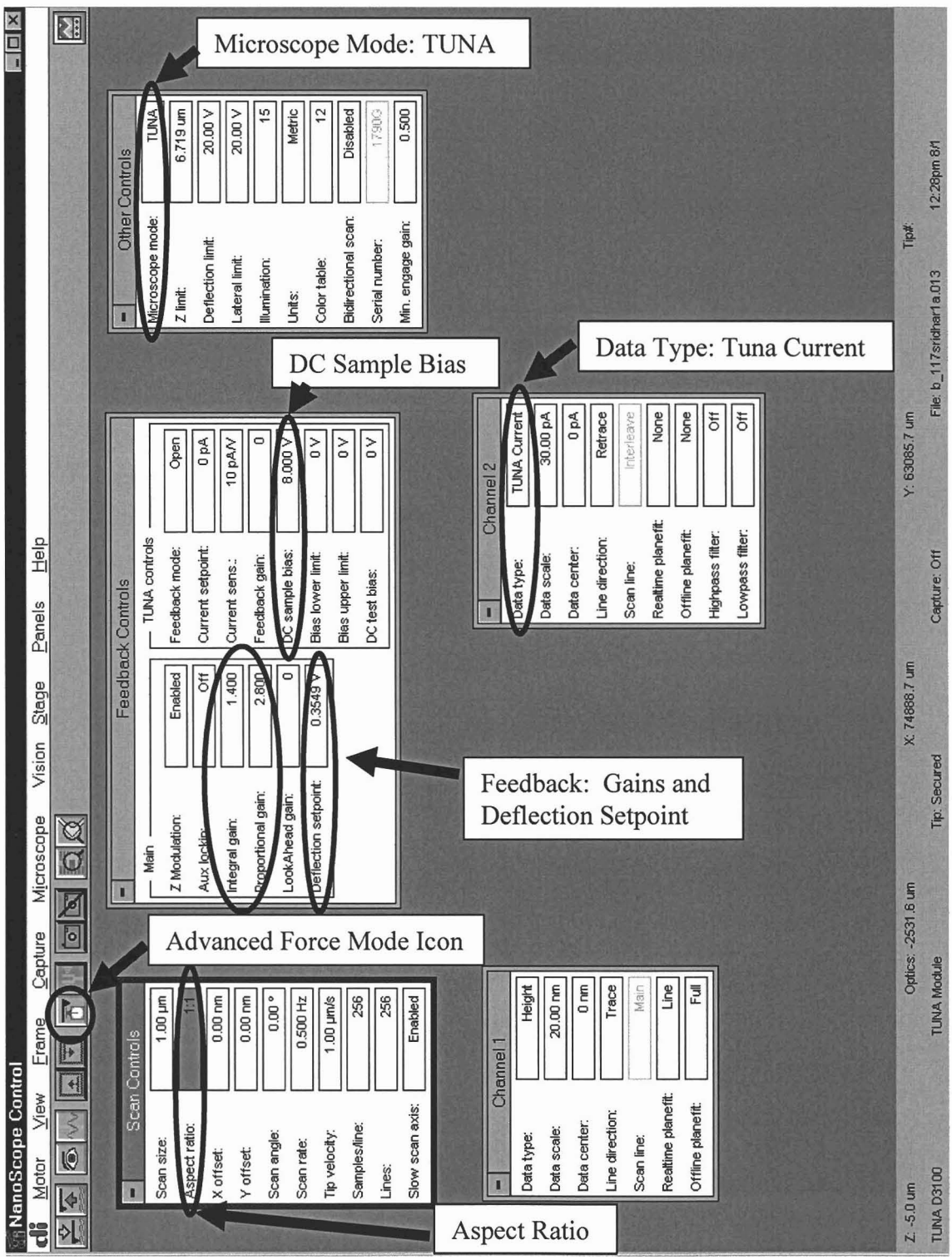

Fig. 1.5: Screen capture of the TUNA input screen indicating important values with typical settings.

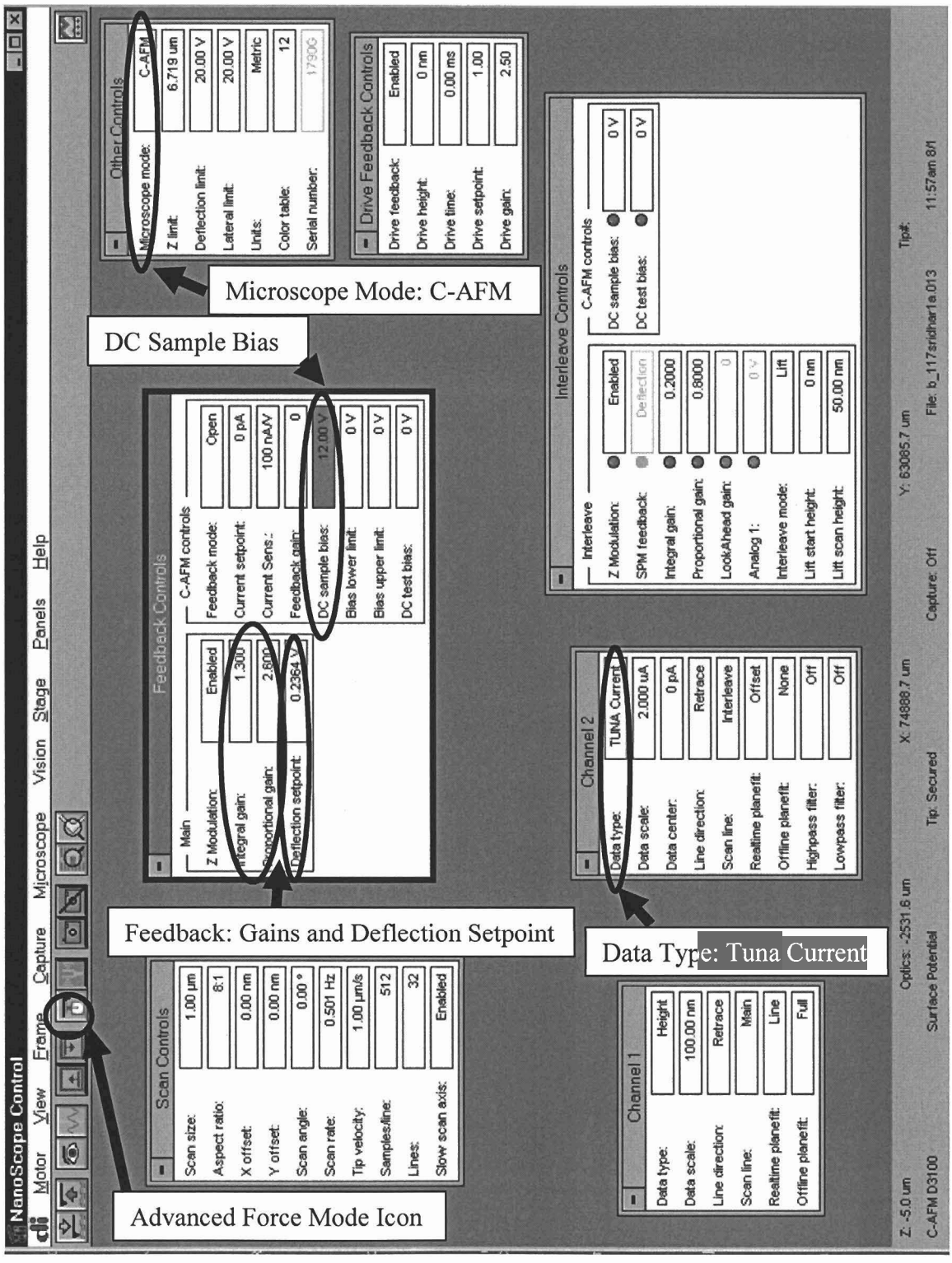

Fig. 1.6: Screen capture of the C-AFM input screen indicating important values with typical settings.

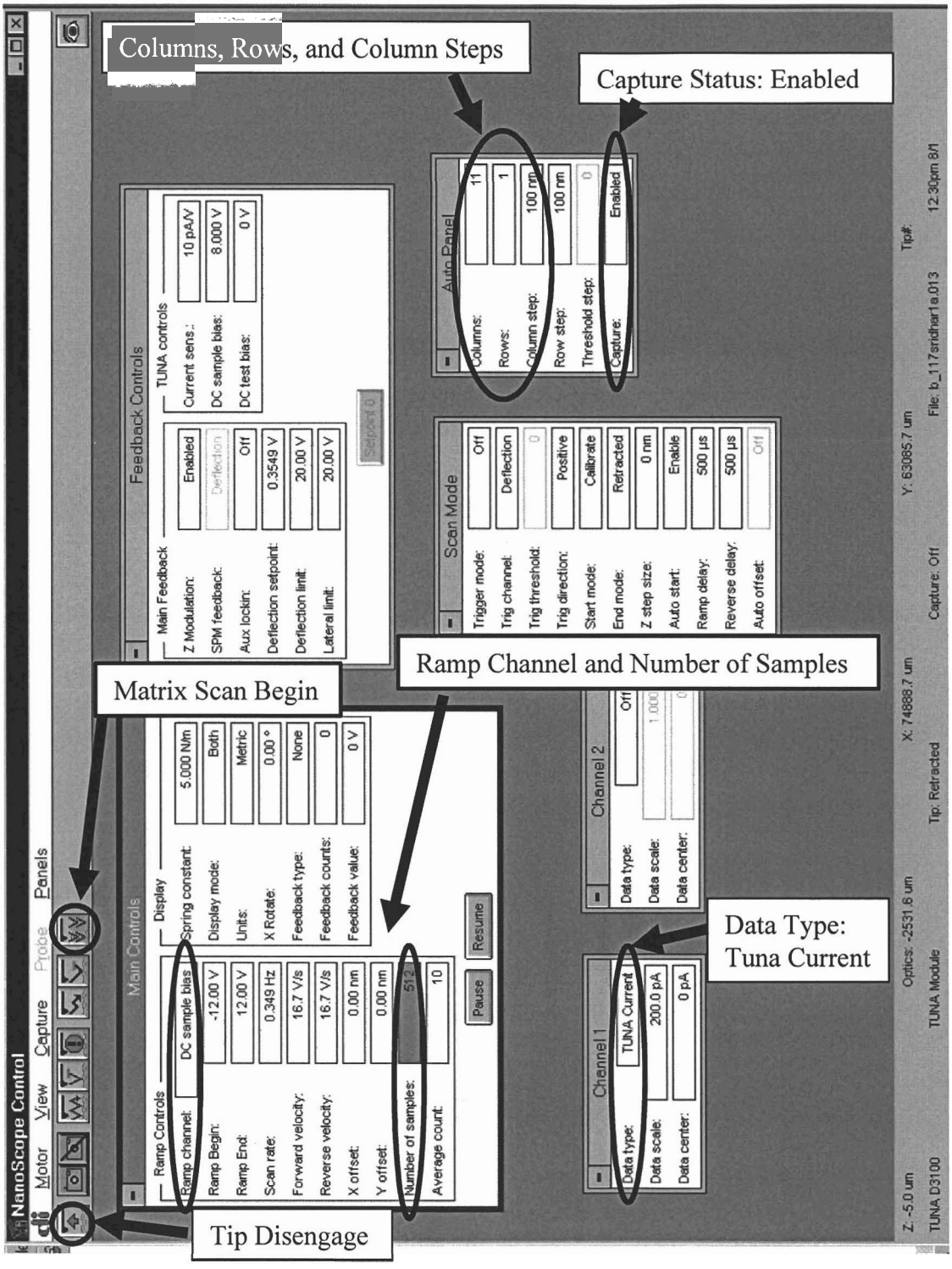

Fig. 1.7: Screen capture of the Advanced Force Mode input screen indicating important values with typical settings.

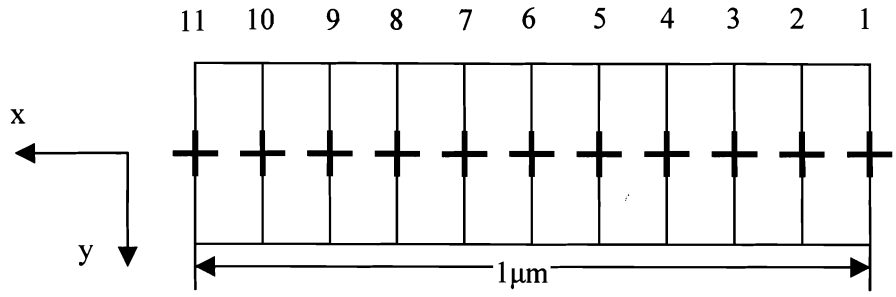

Fig. 1.8: Schematic of I-V spectra locations, where crosses represent spectra taken as the scan progresses from *right to left*.

Chapter 2. GaN Morphology

2.1 Introduction

GaN is a difficult material to grow because of the lack of high-quality, lattice-matched substrates and the kinetics involved. Unfortunately, GaN films have a high defect density when grown on substrates with a poor lattice match. Typical substrates used for epitaxial growth include sapphire, SiC, and ZnO. Sapphire is the most frequently used substrate for III-nitride growth because of its low cost, availability of large, high-quality crystals, and transparency.[2] All samples in this study were grown by the Morkoç Group of the Electrical Engineering Department at VCU. GaN films were grown by molecular beam epitaxy (MBE) on 1-2 μm thick GaN templates prepared by metal organic chemical vapor deposition (MOCVD) on sapphire substrates. The Ga sources were two double-zone Ga cells, and nitrogen was supplied by an RF plasma source. Before loading into the MBE chamber, the MOCVD templates were cleaned by HNO_3:HCl (1:3) acid (100 °C, 20 min). To produce Ga-rich conditions, both Ga cell filaments were set to 1140 °C with a 900 °C base temperature. After opening the Ga cell shutters for 10 s, the nitrogen RF source was opened with a power setting of 300 W. Typical growth rates were 200-300 nm/hr, where a 2×2 RHEED pattern was observed for Ga-rich growth conditions.

The MOCVD templates had atomically flat surfaces characterized by undulations and interspersed pits. Subsequent MBE growth can yield surface morphologies that are either Ga-rich or N-rich.[3] Figure 2.1 shows a growth diagram as a function of III-V ratio and substrate growth temperature produced by L. He from the Morkoç group.[4] Ga-rich surfaces are relatively flat with hillocks and interspersed holes, whereas N-rich surfaces are rough with a high density of holes and pits. The samples used in this research were primarily grown in the Ga-rich regime. The growth parameters for each sample are listed in Table 2.1, and AFM images of all samples are included in Appendix A.

2.2 Sample Grouping by AFM Topography

Sample set #1 shown in Fig. 2.2 consists of four samples (1903, 1906, 1912, 1916) grown at 645 °C under similar conditions. The hillocks are terminated by small pits (15–30 nm wide, 50–85 nm deep) that have been linked to screw or mixed dislocations.[5] The large holes (~130 nm wide and ~350 nm deep) are not associated with individual dislocations.[6] The densities of the hillocks, holes, and pits are all ~10^6 cm^{-2}.

Sample set #2 in Fig. 2.3 consists of three samples (2004, 2009, 2024) grown at 700 °C on superlattice templates with two Ga cells. The superlattice templates were composed of 20 periods of alternating AlN and GaN, where each layer was 2 nm thick. The purpose of the superlattice template was to reduce the threading dislocation density. Sample 2004 has the best surface morphology, but it has cracks due to strain. Therefore, a GaN interlayer was inserted between the superlattice periods to avoid cracking (2009 and 2024). This sample set has a Ga-rich morphology with a slightly higher density of pits on the surface. The hole density is moderate (~10^7 cm^{-3}), where sample 2009 has roughly twice the hole density as 2004 and 2024. The hillocks (most evident on 2024) appear to wrap around in a screw-like fashion and terminate in pits, consistent with the presence of screw dislocations that terminate in open cores.

Sample set #3 in Fig. 2.4 consists of four samples (1966, 2042, 2043, 2161) grown at higher temperatures (695 °C – 705 °C). These samples all appear to reside close to the Ga-droplet regime which is characterized by monatomic terraces on an undulating surface with no visible holes. These samples have wavy-terraced, hillock features with a high pit density (~10^6 to 10^7 cm^{-2}) and low hole density (~10^4 to 10^6 cm^{-2}). The two samples grown at 705 °C (2042 and 2043) show very similar morphology, even though only 2042 was Si-doped. Si-doping has been shown to reduce the dislocation density of GaN films.[7] An interesting sample in this set is 2161, which incorporates features that appear to be pits that align in a "moat-like" manner around flat mesas. The typical width of these "moats" is ~18 nm and depth is ~55 nm.

Sample set #4 in Fig. 2.5 consists of three samples that have less Ga-rich morphologies with a high density of large holes (~10^7 to 10^8 cm^{-2}). This set consists of two samples grown at 660 °C with one Ga cell (1840, 1921) and one sample grown at 720 °C with two Ga cells (2034).

Sample set #5 in Fig. 2.6 only contains one sample (1899) that is characterized by large, irregular holes which are indicative of the transition regime shown in Fig. 2.1. Such a rough surface morphology is evidence of a reduced Ga-adlayer coverage. The holes are ~700 nm wide and 700-800 nm deep, with a density of 10^6 to 10^7 cm^{-2}.

Finally, sample set #6 in Fig. 2.7 also contains only one sample (2037) and demonstrates the only terrace-plus-step morphology in this study. This sample is characterized by flat terraces and straight, bunched step edges with heights of 300 to 1000 nm. This distinctive, non-hillock morphology is most likely related to the fact that this sample is grown at the highest substrate temperature (735 °C) in this study. The higher temperatures induce significant step bunching that dramatically changes the surface morphology.

Chapter 2 Figures

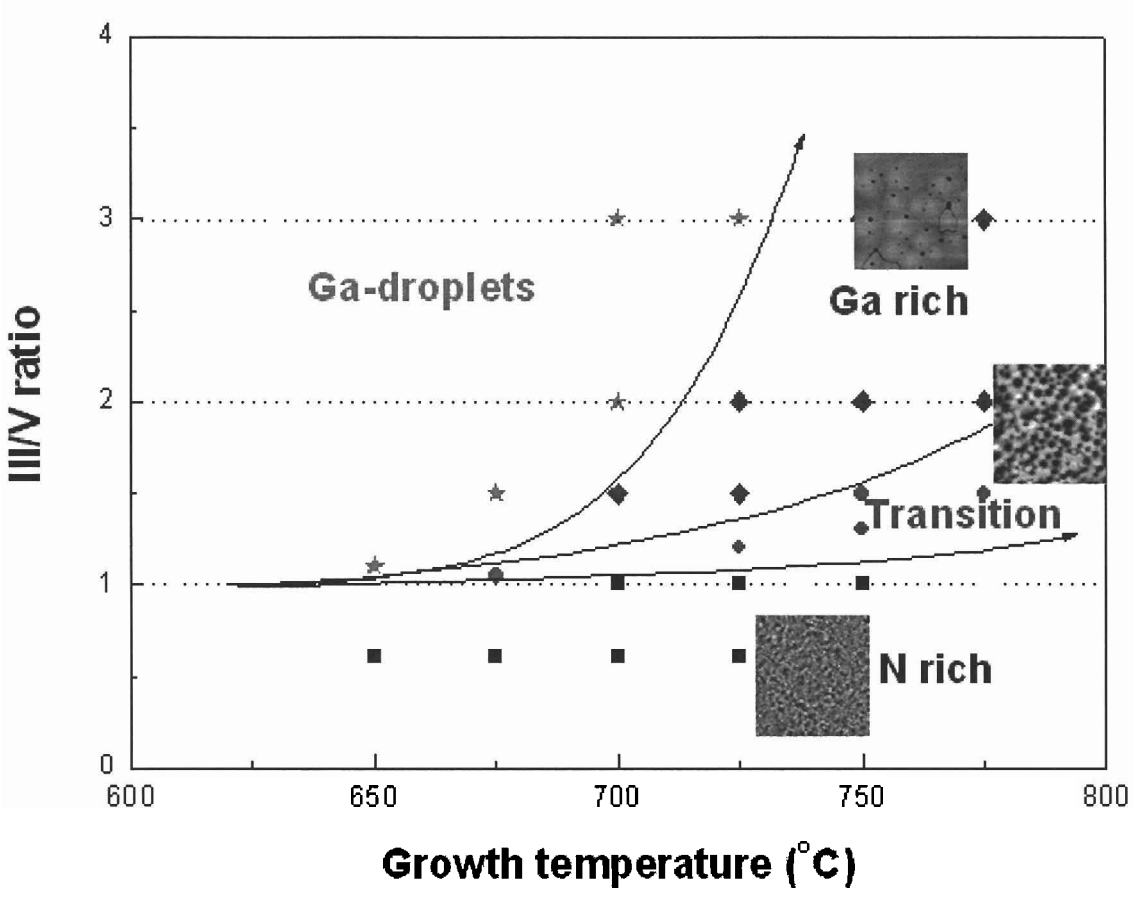

Fig. 2.1: Growth diagram of III-V ratio versus growth temperature, where the AFM images indicate Ga-rich, transition, and N-rich regimes.[4]

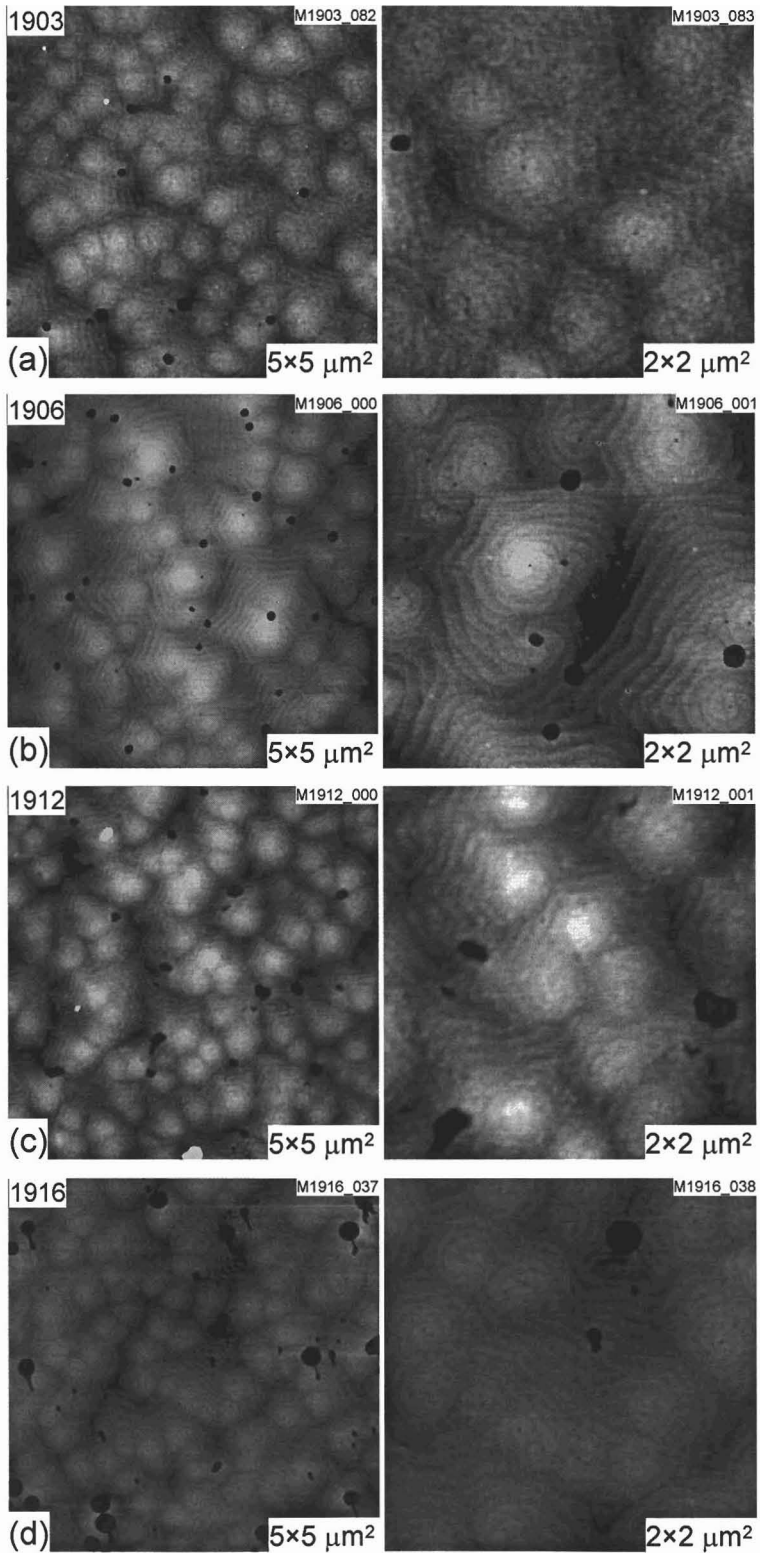

Fig. 2.2: Ga-rich sample set #1 grown at 645 °C with one Ga cell (1903, 1906, 1912, 1916).

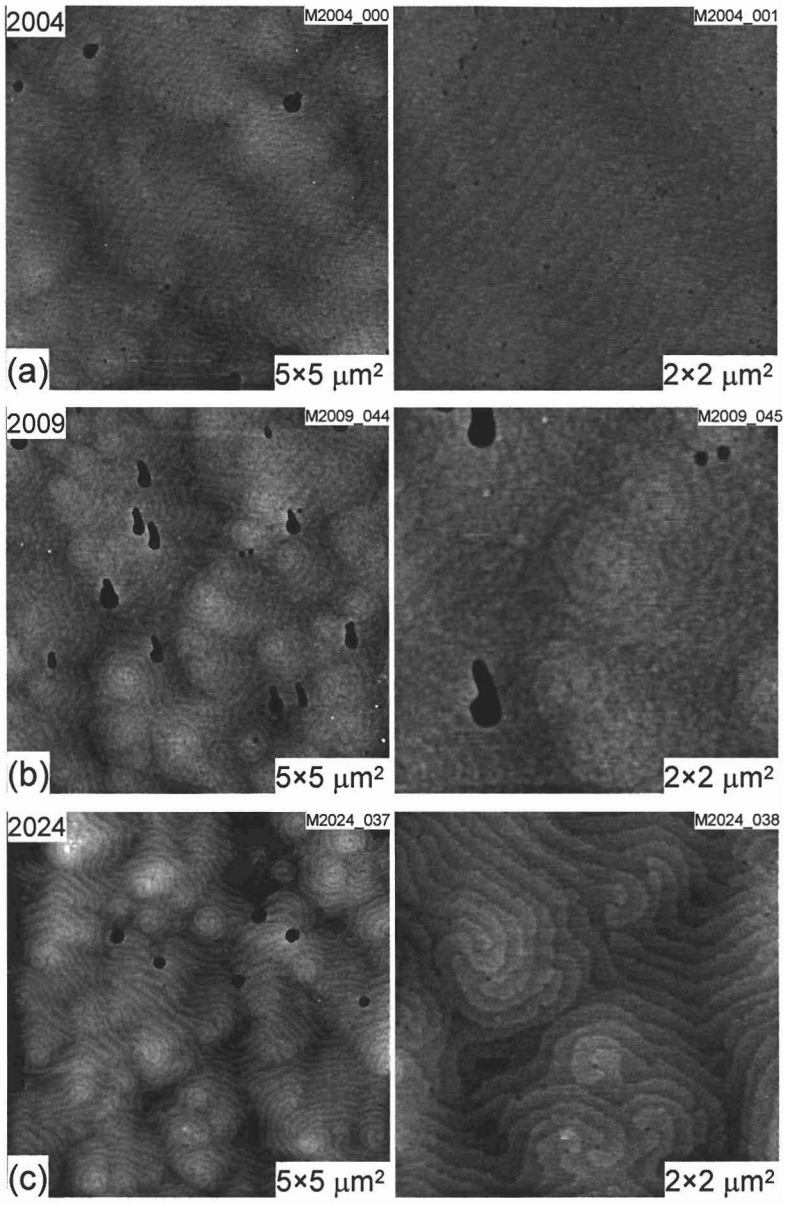

Fig. 2.3: Ga-rich sample set #2 grown at 700 °C on superlattice templates with two Ga cells (2004, 2009, 2024).

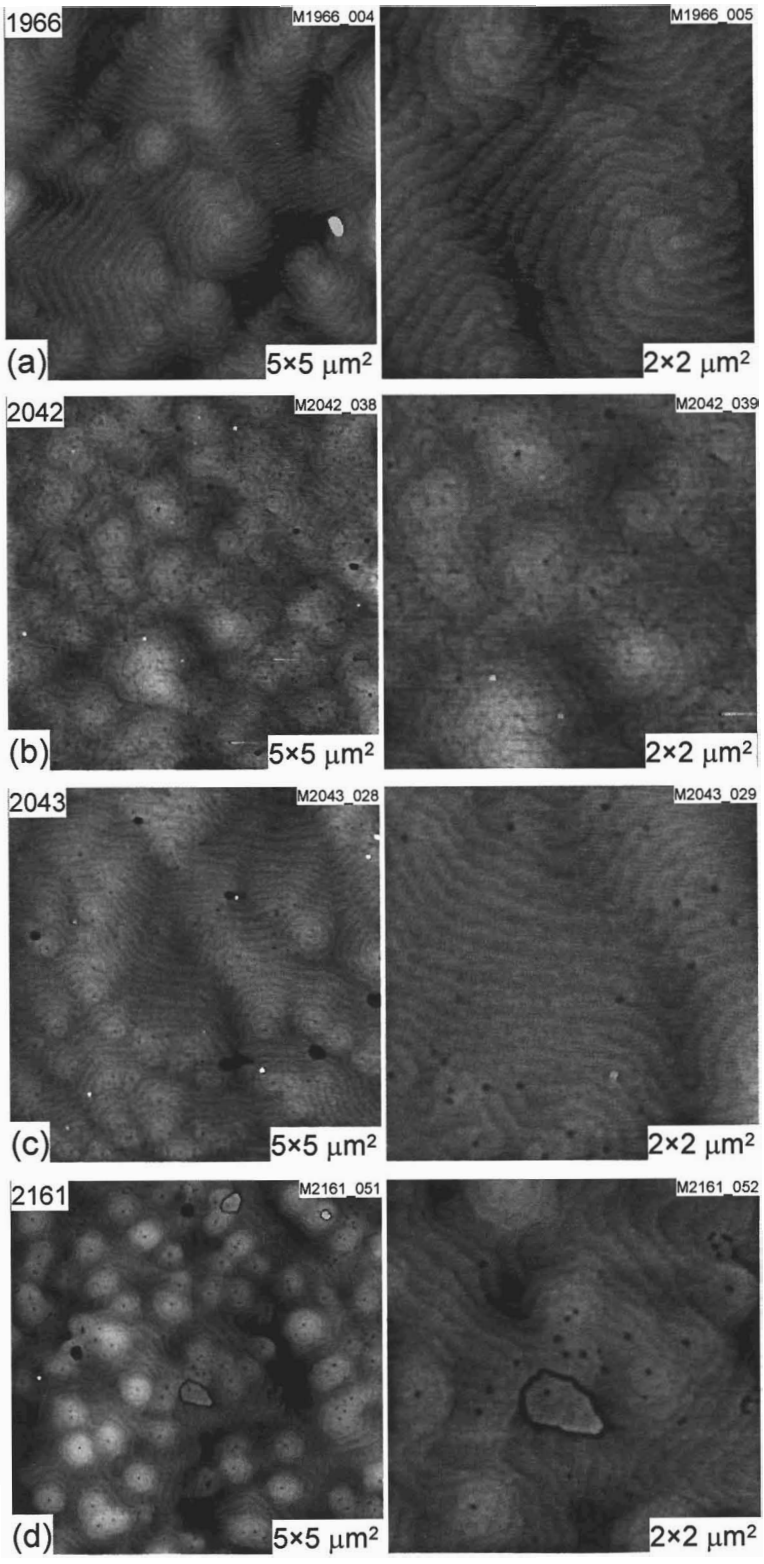

Fig. 2.4: Ga-rich sample set #3 grown at 695 °C (1966), 705 °C (2042, 2043), and 700 °C (2161) with two Ga cells.

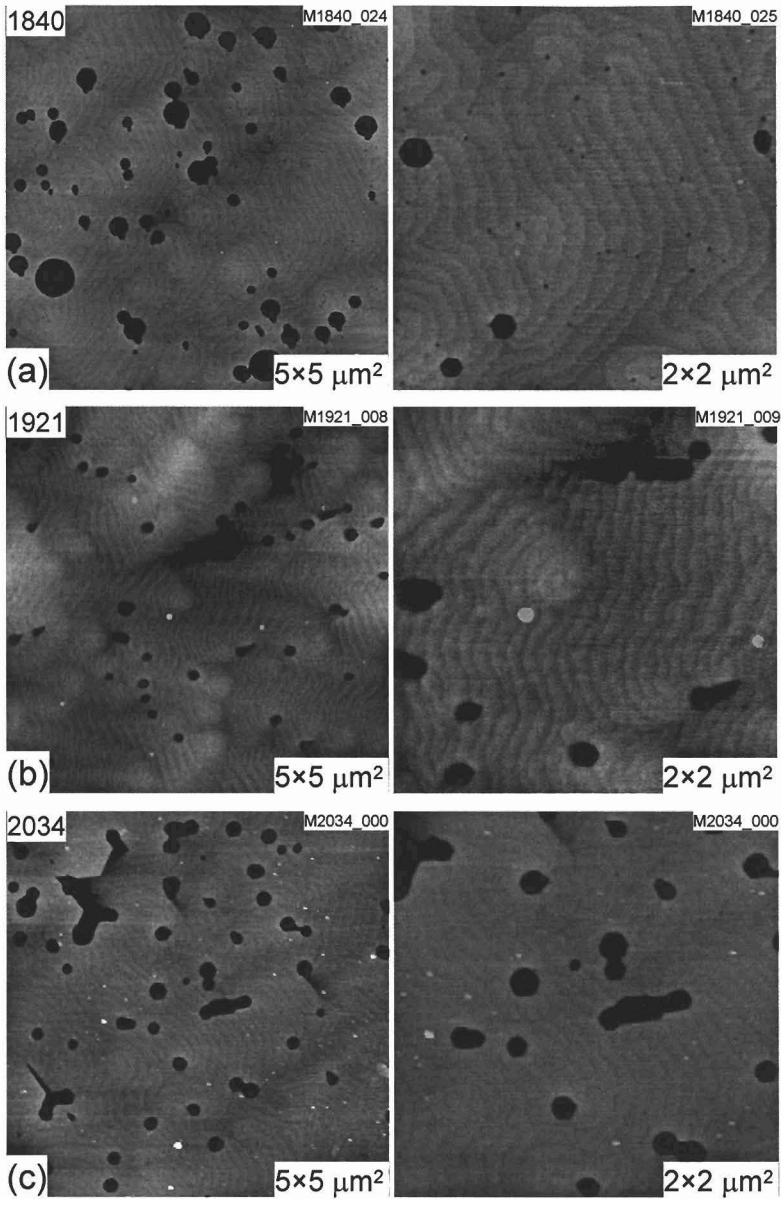

Fig. 2.5: Less Ga-rich sample set #4 grown at 660 °C with one Ga cell (1840, 1921) or at 720 °C with two Ga cells (2034).

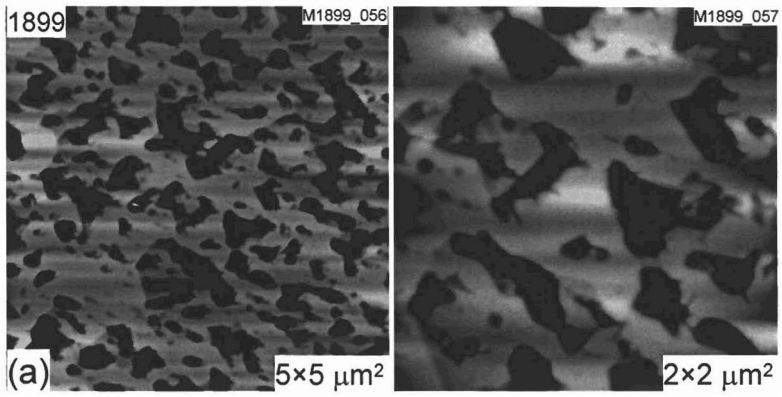

Fig. 2.6: Ga-lean sample set #5 grown at 655 °C with one Ga cell (1899).

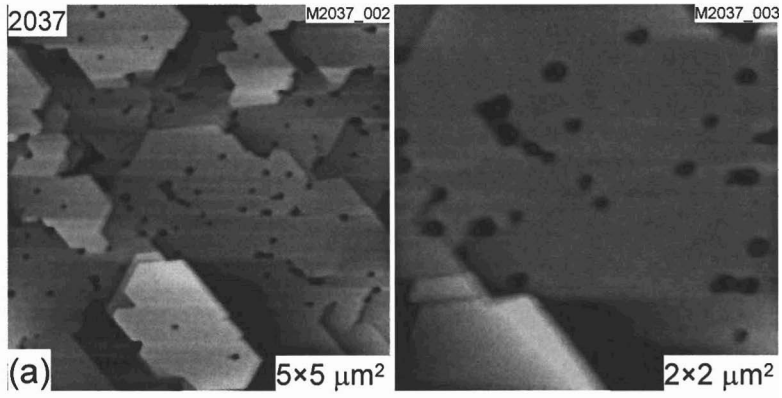

Fig. 2.7: Terrace-plus-step sample set #6 grown at 735 °C with two Ga cells (2037).

Table 2.1: Growth data for each sample and their sample set numbers. The morphologies of the sample sets are: 1-3 = Ga-rich with undulating hillocks, 4 = less Ga-rich with holes, 5 = Ga-lean, and 6 = terrace-plus-step. The corresponding I-V types are given by: A = low leakage, B = high leakage, C = "p-type"

Sample No.	Sample Set No.	I-V Type	Hillock Density (cm^{-2})	Pit Density (cm^{-2})	Hole Density (cm^{-2})	Pressure (Torr)	Substrate Temp. (°C)	Ga I (°C)	Ga II (°C)	Si (°C)
1840	4	A	–	1.0×10^{7}	1.7×10^{6}	8.0×10^{-6}	660	1140		
1899	5	B	–	–	5.3×10^{6}	8.6×10^{-6}	655	1140		
1903	1	A	1.6×10^{6}	3.7×10^{6}	5.5×10^{5}	1.2×10^{-5}	645	1140		
1906	1	A	1.5×10^{6}	5.0×10^{6}	1.4×10^{6}	1.5×10^{-5}	645	1140		
1912	1	A	2.2×10^{6}	1.8×10^{6}	1.0×10^{6}	1.8×10^{-5}	645	1140		
1916	1	B	1.5×10^{6}	2.6×10^{6}	2.3×10^{6}	1.8×10^{-5}	645	1140		
1921	4	A	1.0×10^{6}	7.5×10^{5}	1.7×10^{6}	1.5×10^{-5}	660	1140		
1966	3	B/C	6.0×10^{5}	3.0×10^{6}	7.0×10^{4}	1.2×10^{-5}	695	1140	1140	
2004	2	B	4.2×10^{5}	8.7×10^{6}	2.5×10^{5}	1.2×10^{-5}	700	1130	1130	1220
2009	2	B	1.7×10^{6}	3.6×10^{6}	1.0×10^{6}	1.4×10^{-5}	700	1140	1140	1250
2024	2	C	1.6×10^{6}	5.1×10^{6}	1.6×10^{5}	1.2×10^{-5}	700	1135	1135	
2034	4	C	–	4.1×10^{6}	2.3×10^{6}	8.0×10^{-6}	720	1140	1140	
2037	6	C	–	–	3.7×10^{6}	8.0×10^{-6}	735	1140	1140	
2042	3	A/B	1.2×10^{6}	1.6×10^{7}	4.6×10^{5}	1.2×10^{-5}	705	1140	1140	
2043	3	B	8.0×10^{5}	7.9×10^{6}	3.1×10^{5}	1.2×10^{-5}	705	1140	1140	1220
2161	3	A	1.7×10^{6}	6.6×10^{6}	3.9×10^{5}	1.0×10^{-5}	700	1140	1130	

Chapter 3. Conductive AFM and I-V Spectra

3.1 Introduction

A local probe of surface current such as conductive AFM (C-AFM) is critical to the identification of anomalous current behavior. GaN films have inherent problems with leakage current, which has been linked to surface terminations of threading dislocations with a screw or mixed component.[8,9,10] On MBE films, hillocks tend to be the leakiest features in reverse bias because of their intrinsic screw component, and several groups have attempted to link specific behavior in I-V curves to the enhanced conduction that often occurs on dislocations.[11,12,13] It has also been proposed that specific conduction mechanisms are responsible for this leakage behavior.[11,14]

It has been hypothesized[15] and experimentally verified[10] that threading dislocations have an intrinsic associated negative charge. This negatively charged dislocation type has been imaged by techniques such as scanning Kelvin probe microscopy (SKPM) and scanning capacitance microscopy (SCM).[10,16,17,18,19] There have been a few attempts to link these negatively charged dislocations with reverse bias leakage centers. However, no strong correlation exists between the negatively charged dislocations and the localized reverse bias leakage paths, implying that these phenomena have different origins. It has been found that dislocations with an edge component tend to be negatively charged, whereas dislocations with a screw component tend to be leaky.[17]

It has also been found in C-AFM studies of Ga-rich samples that *only* pure screw dislocations leak in reverse bias.[17,18] Fig. 3.1 shows a typical TappingMode™ image with a corresponding contact mode image and TUNA current map. It appears that the only hillocks that leak are ones with a pit at the top. It should also be noted that occasionally a hole may show leakage behavior. It is unclear whether this leakage is an artifact dependent on scan direction, or whether it is due to the presence of off-axis planes. According to TEM studies of GaN films, the majority of dislocations are mixed or edge

type (~90%), while the remaining 10% are pure screw type.[18] This is consistent with results indicating that only 10 to 30% of hillocks show reverse-bias leakage.[11,18] The exact mechanism responsible for such leakage is still debated, and has been attributed to both excess Ga incorporation and oxygen-related impurities[20] near the opening of these screw dislocation cores.

Several groups have attempted to correlate I-V behavior to leakage on and off dislocations. Two groups have found no change in I-V spectra taken on and off dislocations,[12,13] whereas Spradlin et al. have observed discernible changes in both forward and reverse bias.[11] They also noted that a marked decrease in current occurred after three to five scans in the same location. This agrees with others who have noticed the formation of insulating bumps on the surface of leaky hillocks after several repeated scans.[21] A few groups have fit I-V spectra with a variety of conduction mechanisms. Miller *et al.* attributed leakage to two mechanisms: field-emission tunneling and exponential temperature dependence consistent with trap-assisted tunneling or 1D hopping associated with threading dislocations.[14] Spradlin *et al.* attributed forward bias conduction to field-emission and Frenkel-Poole conduction in regions off and on leakage sites, respectively.[11]

3.2 Sample Grouping by I-V Characteristics

The n-type samples examined here can be grouped according to their I-V spectra into three types: Type A with low reverse-bias leakage; Type B with high leakage; and Type C with unexpected, "p-type" behavior. Representative I-V curves for each type of behavior are shown in Figs. 3.2 to 3.6.

Type A samples demonstrate low leakage and can be divided into two subgroups: no leakage (Fig 3.2: 1840, 1921, 2161) and localized leakage at 10-30% of hillocks (Fig. 3.3: 1903, 1906, 1912). Fig. 3.4 shows superimposed I-V spectra for locations both off and on a hillock, where the I-V curve on the hillock clearly shows leakage above 10 V. A large percentage of the hillocks that leaked had visible pits at the top, indicating the presence of open-core screw dislocations. The on-hillock behavior has also been verified

when I-V spectra were taken with no preliminary scan to determine if a conductive hillock was present.

Type B samples shown in Fig. 3.5 exhibits moderate to heavy leakage. This group contains the largest number of samples: 1899, 1916, 1966b, 2004, 2009, 2042, and 2043. The leakage on these samples does not appear to have any correlation to morphology. Instead, most of these samples show "sheetlike" leakage in current images and reach the current limit of the TUNA module above 4 to 5 V. Sample 1916 shows some enhanced leakage at hillocks, but perhaps this large amount of leakage is masking a baseline leakage that is evident in the I-V spectra. Several samples (1966b, 2042, and 2043) appear to be nearly Ohmic.

Type C samples shown in Fig. 3.6 is the most difficult group to explain, as the I-V spectra appear to demonstrate "p-type" behavior. The samples in this group include 1966, 2024, 2034, and 2037 and do not belong to the same topographical group. It has been suggested that these samples may incorporate trace levels of Mg from the growth chamber. It should be noted that the spectra taken from sample 2024 exhibit extreme hysteresis, which was only minimally controlled by reducing the scan speed to 0.1 Hz.

It would be desirable to correlate surface morphology with I-V behavior, but that does not seem to be the case here. Instead, we can attempt to correlate conduction characteristics to the preparation conditions occurring during growth. As described in Chapter 2, there are six sample sets as follows: Ga-rich set #1 (645 °C), Ga-rich set #2 (700 °C on superlattice templates), Ga-rich set #3 (695–705 °C), less Ga-rich set #4, Ga-lean set #5, and terrace-plus-step set #6. These sample sets are shown in Figs. 3.7 to 3.11 with typical I-V spectra. Appendices B and C show additional I-V data.

Sample set #1 (Fig. 3.7) is grown at moderate temperature (645 °C) and in general shows desirable I-V behavior. The first three samples (1903, 1906, 1912) show overall low leakage with localized leakage at ~30% of hillocks. The third sample, however, does have isolated spectra with high leakage, indicating some change in the growth conditions. This poor I-V behavior then persists for the fourth sample (1916) in the sample set.

These results indicate that although the surface morphology remains consistent in this sample set, there are other critical factors that strongly influence the I-V behavior of the films.

Sample set #2 (Fig. 3.8) consists of samples grown at higher temperature (700 °C) on superlattice templates and yields very poor quality I-V spectra. Samples 2004 and 2009 both show very high leakage, while sample 2024 exhibits "p-type" conduction. It should be noted that samples 2004 and 2009 were both doped with Si, while sample 2024 was not. It does not appear that superlattice templates or Si doping improve the I-V characteristics of the samples.

Sample set #3 (Fig. 3.9) is a collection of various samples grown at higher temperatures (695 °C – 705 °C) with two Ga cells in operation. Sample 1966 (695 °C) was the first sample to be grown using two Ga cells and sample 2161 (695 °C) was the last sample used in this study. Pieces A and B from 1966 exhibit "p-type" behavior and high leakage, respectively. Such different behaviors on the same sample may be attributed to a temperature differential across the wafer during growth. Samples 2042 and 2043 were grown at 705 °C and primarily show high leakage, with the exception of piece 2042A. This is another example of a sample that has a variation of I-V behavior between pieces. Finally, sample 2161 was grown at 700 °C and shows no leakage, possibly because the chamber conditions had changed significantly by the time this sample was prepared. Overall, there is no obvious trend between the growth conditions and I-V behaviors of this sample set. However, it does seem that high temperatures do not, in general, produce high quality films.

The less Ga-rich samples in set #4 (Fig. 3.10) were each prepared at different times, but show very similar surface morphologies. The two samples grown at a lower temperature (1840 and 1921 @ 660 °C) demonstrate minimal leakage, whereas the sample grown at a higher temperature (2034 @ 720 °) exhibits "p-type" behavior. This result again indicates that higher temperatures are not favorable for high quality device growth.

Sample set #5 (Fig. 3.11) is the only Ga-lean sample (1899) and overall shows high leakage. It should be noted, however, that some isolated spectra did show reasonable I-V characteristics. Finally, sample set #6 (Fig. 3.12) is the only very high temperature sample (2037 @ 735 °C) and demonstrates undesirable "p-type" behavior. These two sample sets indicate that less common morphologies do not improve I-V characteristics.

Note that it is primarily the samples grown at higher temperatures (>695 °C) that show p-type behavior. The sample grower, Andy Xie, has suggested that low-level Mg doping may be occurring in these samples. When GaN is grown at high temperatures, the crystal quality improves and p-type doping may be possible with lower metal concentrations. Although no Mg cell was in operation during growth, there is the possibility of Mg contamination in the chamber that becomes noticeable at higher growth temperatures.

3.3 Conduction Mechanisms

It has been suggested by several groups that the two main conduction mechanisms in forward bias for GaN films are: 1) Field emission [11,14] and 2) Frenkel-Poole.[11] Field emission conduction is given by:[22]

$$J = J_0 \exp(V/E_{00})[1 - \exp(-qV/kT)] \qquad (1)$$

$$\text{where} \quad J_0 = A^*T^2\exp(-q\phi/kT) \qquad (2)$$

$$\text{and} \quad E_{00} = \hbar/2[N_A/m^*\varepsilon]^{1/2} \qquad (3)$$

with J = current density, q = charge of electron, kT = thermal Boltzmann energy, A* = effective Richardson's constant [A* = m*A/m with A = 120 A/cm^2K^2], ϕ = effective barrier height, $\hbar$ = Planck's constant, N_A = doping density, m* = effective mass ($0.2m_e$ for GaN), and ε = dielectric constant ($9\varepsilon_0$ for GaN). Field emission conduction primarily involves tunneling through the barrier between the metal contact and GaN. A schematic of this process is shown with respect to the band diagram in Fig. 3.13. The above expression for the current density assumes that $qE_{00} >> kT$.

Frenkel-Poole conduction is given by:[23]

$$J = q\mu n_0 E \exp[-(\phi_{PF} - \Delta\phi_{PF})/kT] \qquad (4)$$

where μ = electron mobility, E = applied electric field, n_0 = carrier concentration ($\sim 10^{17}$) given by:

$$n = n_0 \exp(-\phi/kT) \qquad (5)$$

The change in the barrier height $\Delta\phi_{PF}$ is defined as follows:

$$\Delta\phi_{PF} = (e^3 E/\pi\varepsilon\varepsilon_0)^{1/2} = \beta_{PF} E^{1/2} \qquad (6)$$

Frenkel-Poole conduction is dominated by the movement of carriers in the GaN film between traps of depth ϕ_{PF}, as shown in Fig. 3.14. An applied electric field changes the shape of the trap barrier and lowers the effective trap depth by an amount $\Delta\phi_{PF}$.

3.4 Curve-fitting of Forward-Bias Data

In order to test the viability of these conduction mechanisms in our samples, we have curve-fit the forward bias portion of select I-V spectra. In the following section, the original I-V data have been "reversed" so that positive bias now corresponds to forward conduction. The curve fitting was performed using Microcal Origin™. The equation entered for field emission conduction was given by:

$$y = y0 + A1*\exp((x-x0)/t1)*(1-(\exp(-(x-x0)/t2))) \quad \text{where}$$

y0	y-offset value (y-crossing value)
x0	x-offset value (user adjusted)
A1	represents J_0 (varied by Origin)
t1	represents E_{00} (varied by Origin)
t2	represents kT = 0.0252 eV at RT

The expression used for Frenkel-Poole curve fitting was given by:

$$y = y0 + A1*((x-x0)/B1)*\exp(-(C1-(D1*\text{sqrt}((x-x0)/B1)))/t1) \quad \text{where}$$

y0	y-offset value (y-crossing value)
x0	x-offset value (user adjusted)
A1	represents $e\mu n_0 = 480$ A^2s/Jm

B1 represents distance $x = 5\times10^{-8}$ m for electric field E

C1 represents barrier height ϕ (varied by Origin)

D1 represents constant β in the $\Delta\phi_{PF}$ term = 4.07×10^{-24} $C^{1/2}N^{1/2}m$

t1 represents $kT = 4.03\times10^{-21}$ J

The variables in the Frenkel-Poole expression were originally input in SI units. A1 was calculated using $\mu = 300$ cm^2/Vs and $n_0 \sim 10^{17}$. The only unknown value of interest was the barrier height, which was a fitting parameter in Origin.

Field emission and Frenkel-Poole conduction were fit to the forward bias portion of select spectra of two samples, 1906 and 1912, both of which showed leakage on hillocks. Fig. 3.15 shows the original I-V data for sample 1906 on and off a hillock, and Fig. 3.16 shows similar data for sample 1912. Note the shifts in the forward bias curves and the leakage in reverse bias.

The field emission fitting for sample 1906 is shown in Fig. 3.17 for locations off and on a hillock. The variables representing J_0 and E_{00} were allowed to vary in Origin as the curve-fitting parameters were calculated. The resulting E_{00} values were 0.09 eV (off hillock) and 0.12 eV (on hillock), which is consistent with $qE_{00} >> kT$. The barrier heights were found to be 0.72 eV (off hillock) and 0.61 eV (on hillock). These values are consistent with the value of 0.78 eV found by Miller *et al.*[14] The barrier heights were calculated from J_0 using a Richardson's constant of 24 $Acm^{-2}K^{-2}$ ($m^* = 0.2m_e$). For comparison, the same fitting routine was performed for sample 1912 in locations off and on a hillock and is shown in Fig. 3.18. The resulting E_{00} values were 0.28 eV (off hillock) and 0.14 eV (on hillock), and the barrier heights were 0.51 eV (off hillock) and 0.67 eV (on hillock). In this case, the E_{00} values appear to be high, but the barrier heights are comparable. Unfortunately, there does not seem to be a trend of higher barrier heights for on or off the hillocks.

Finally, Fig. 3.19 shows a Frenkel-Poole fit for sample 1906. As can clearly be seen, the fit is very poor using the reasonable values discussed previously. Barrier heights of

0.61 eV (off hillock) and 0.64 eV (on hillock) are found, but these values are not reliable since the fits are so poor.

3.5 Conclusion

It is evident in this study that Ga-rich morphologies can be produced for a variety of growth temperatures and Ga fluxes. As the substrate temperature is increased, the Ga flux must be increased as well (two vs. one Ga cell) to maintain Ga-rich growth conditions. It would also seem that moderate temperatures are advantageous for producing low-leakage films, as seen for sample set #1 grown at 645 °C and sample set #4 at 660 °C. These sample sets show some enhanced leakage at 10 – 30% of hillocks or show no leakage, respectively. In contrast, high temperatures yield poor I-V characteristics. The four samples which show "p-type" behavior were all grown at or above 695 °C. This unexpected behavior may result from background Mg doping. When GaN is grown at higher temperatures, it creates a higher quality crystal which is more susceptible to p-type doping. The curve-fitting results for high-quality samples are best modeled with a field emission mechanism under forward bias conditions. For a better comparison of field emission vs. Frenkel-Poole mechanisms, however, it appears that variable temperature I-V data is necessary.

Chapter 3 Figures

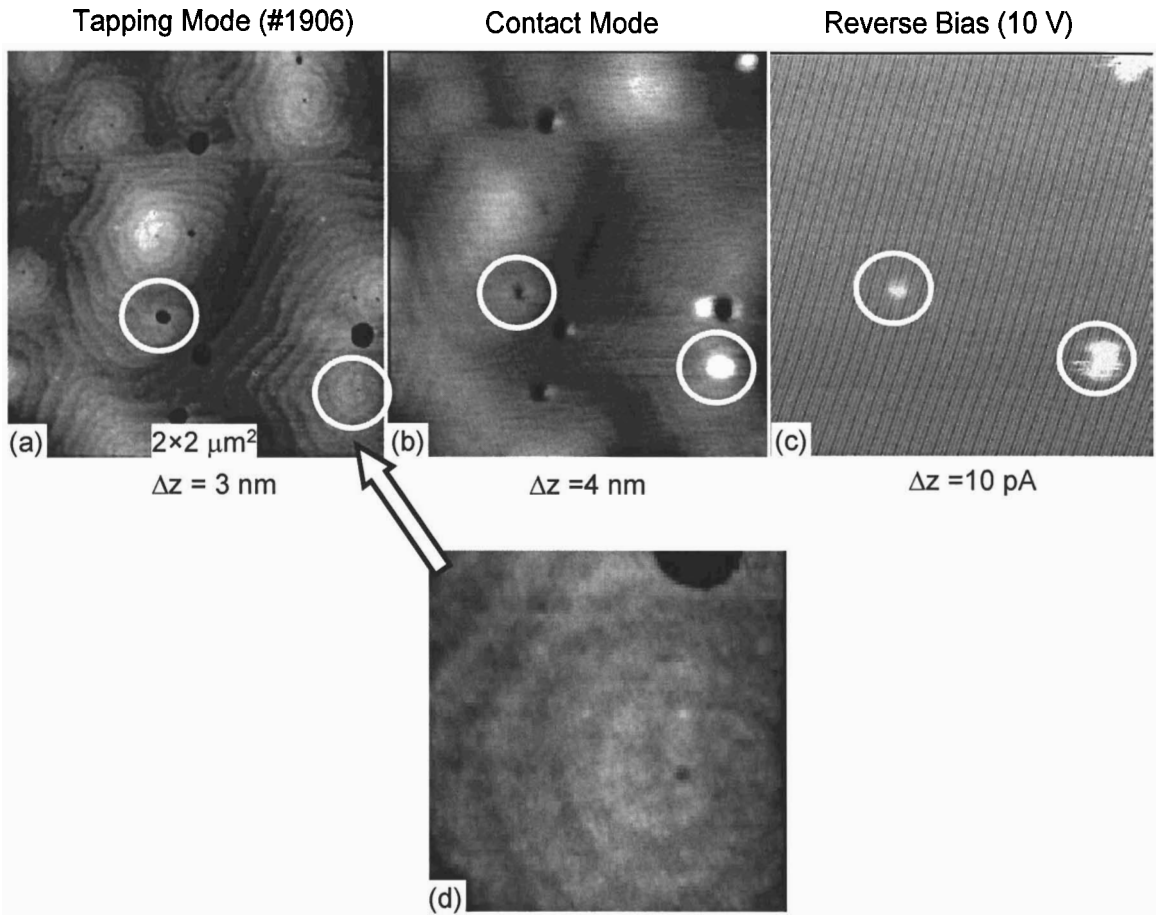

Fig. 3.1: (a) Tapping mode topography, (b) Contact mode topography, and (c) current map showing high leakage on a hillock terminated by a pit.

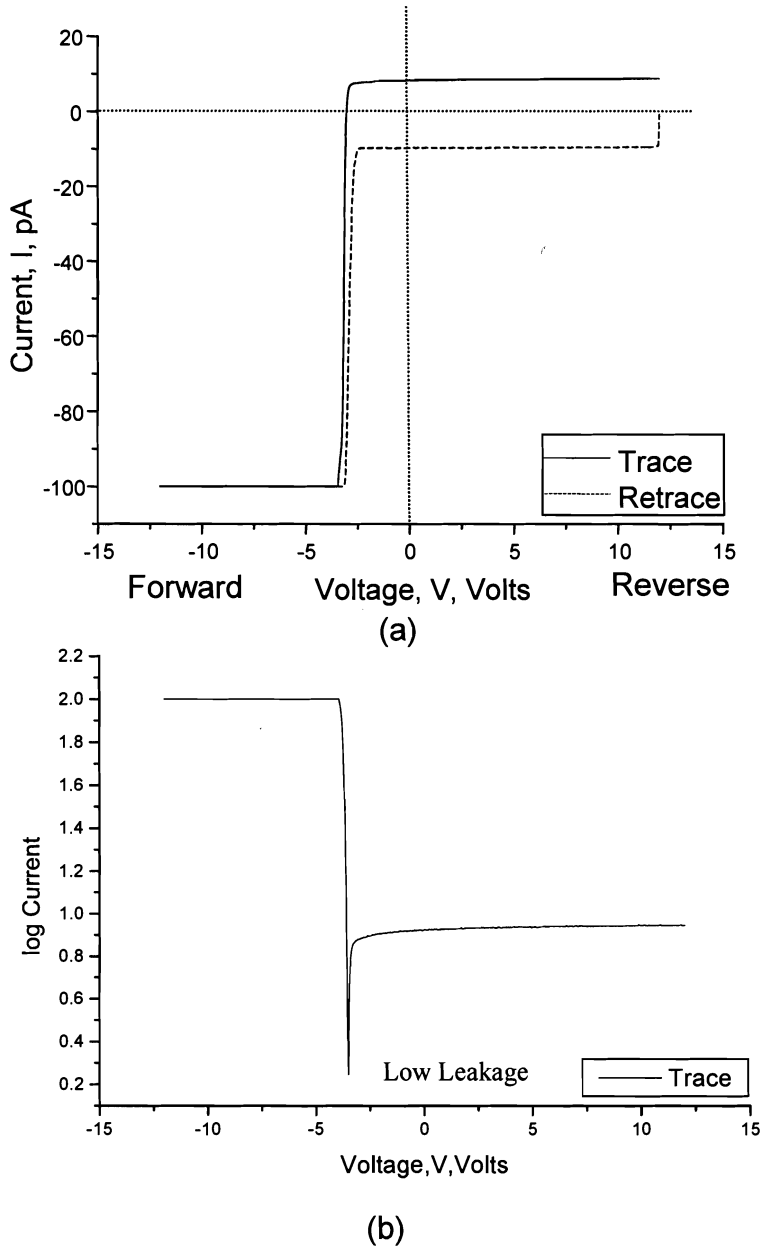

Fig. 3.2: (a) Linear and (b) semi-log I-V spectra for Type A samples with low reverse-bias leakage (1840).

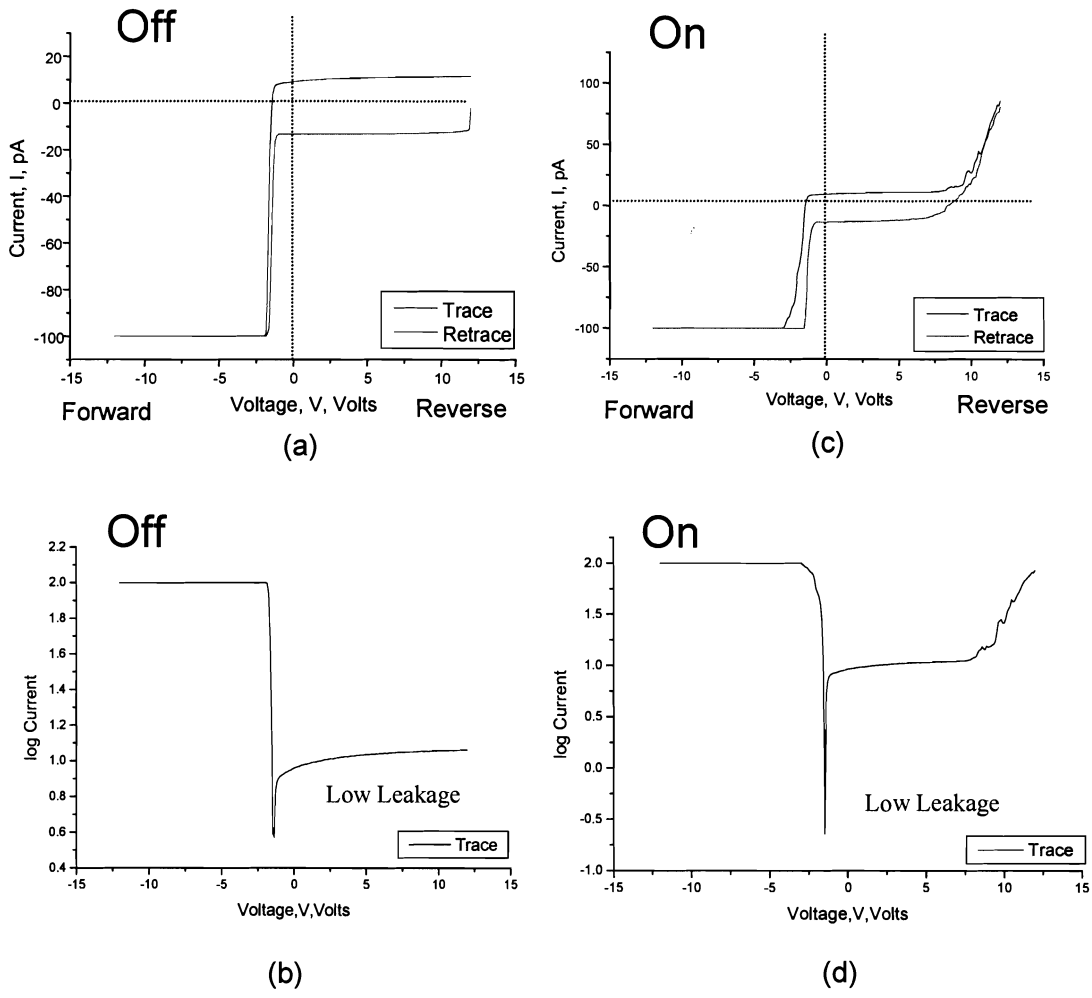

Fig. 3.3: Type A samples with I-V spectra taken at locations (a,b) off hillocks and (c,d) on hillocks (1903).

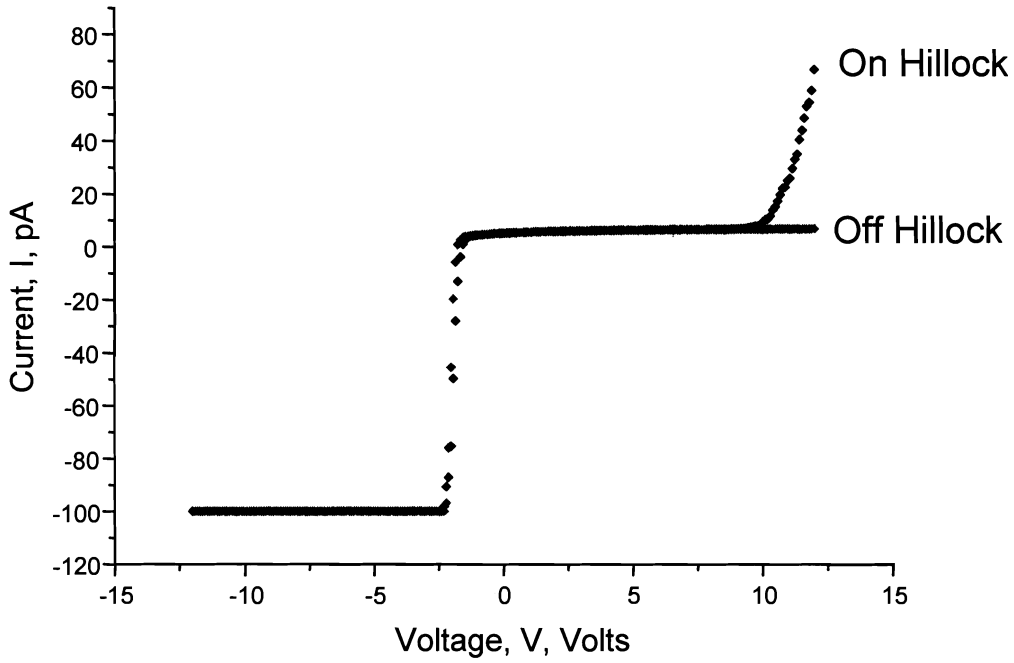

Fig. 3.4: Superimposed I-V spectra taken on and off a hillock (1906).

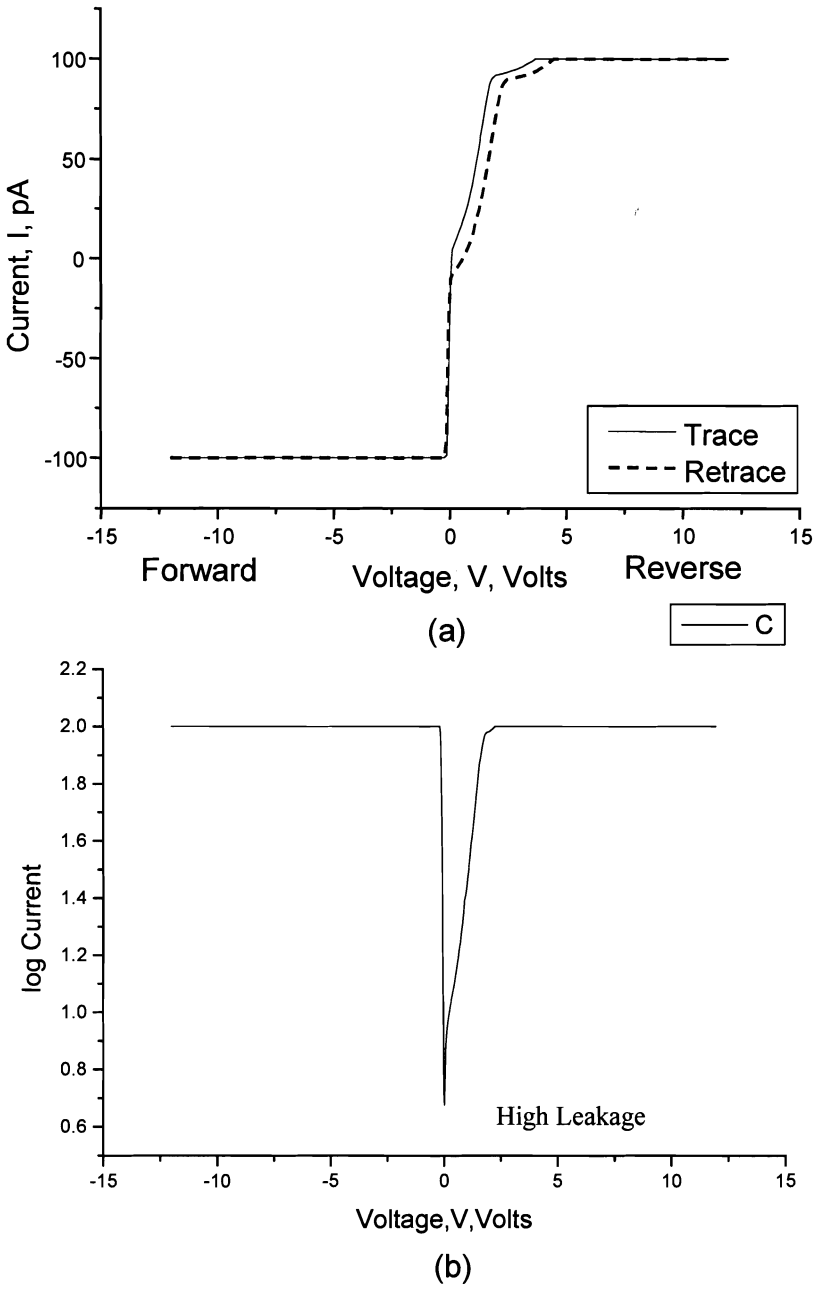

Fig. 3.5: Type B samples showing high reverse-bias leakage (2004).

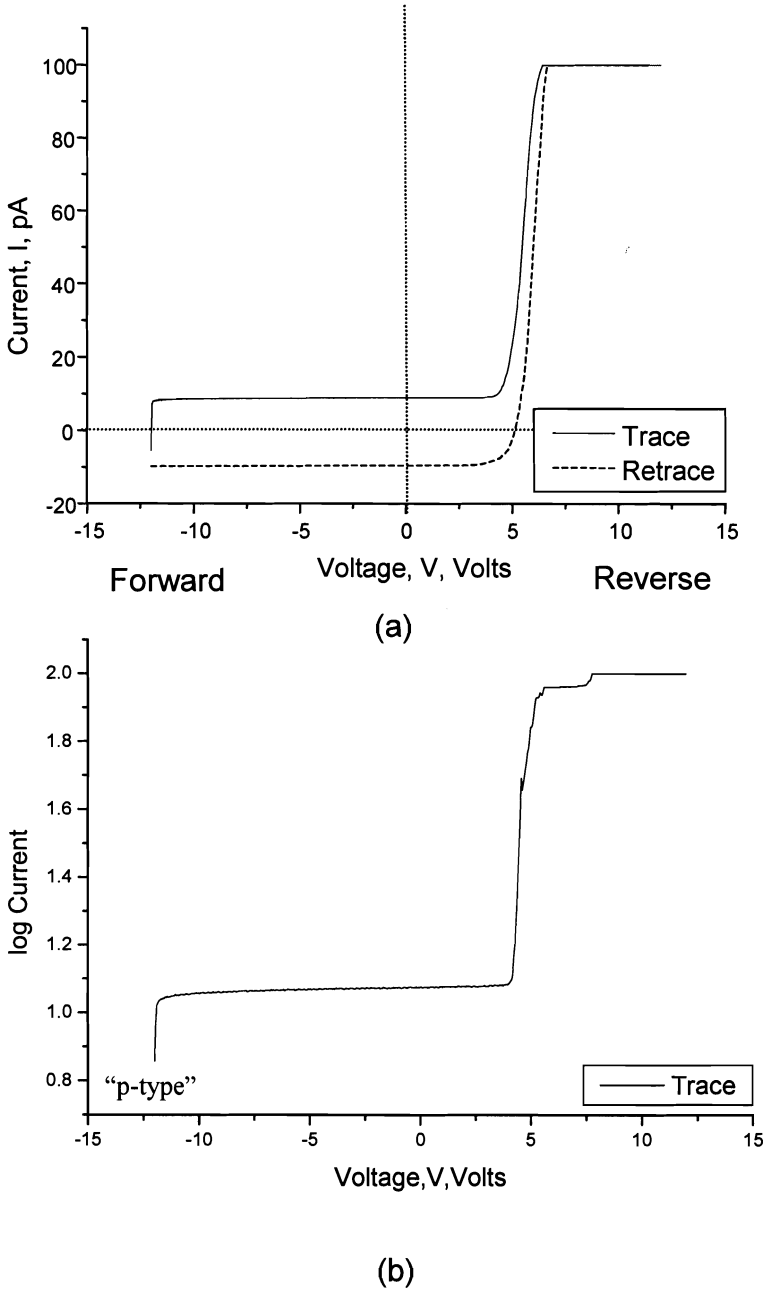

Fig. 3.6: Type C samples showing "p-type" conduction (2037).

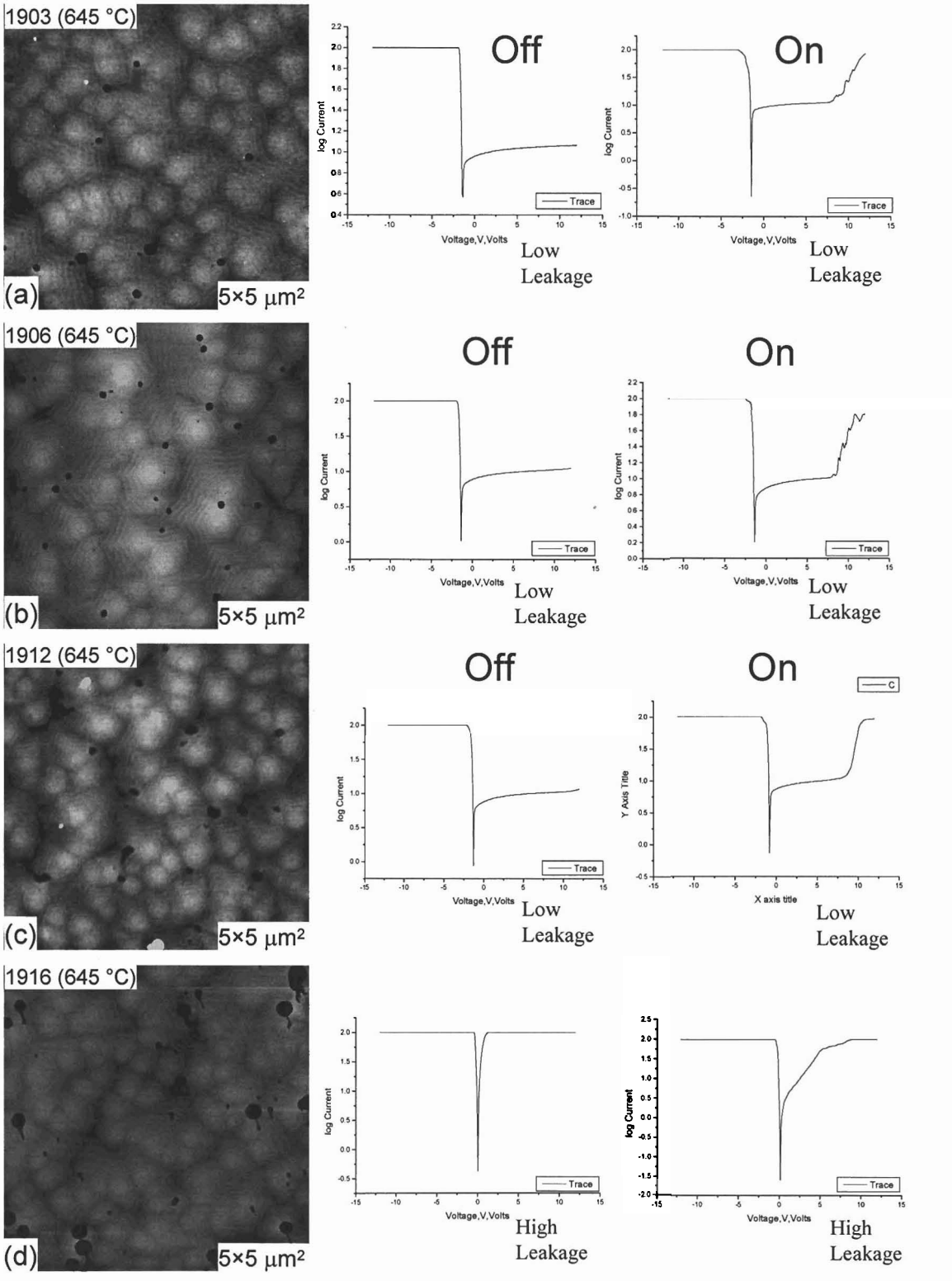

Fig. 3.7: I-V spectra for Ga-rich sample set #1 grown at 645 °C with one Ga cell (1903, 1906, 1912, 1916).

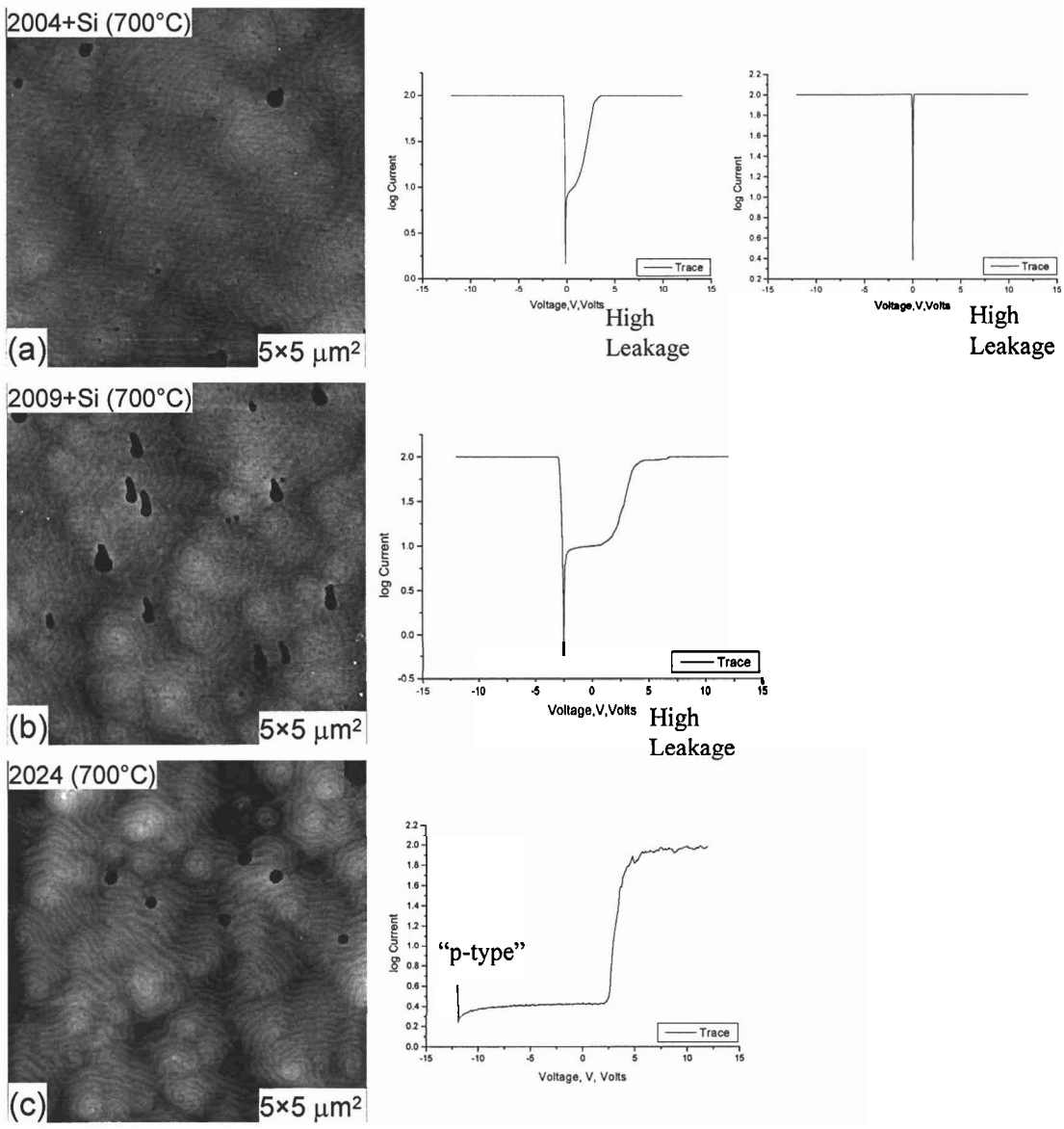

Fig. 3.8: I-V spectra for Ga-rich sample set #2 grown at 700 °C on superlattice templates with two Ga cells (2004, 2009, 2024).

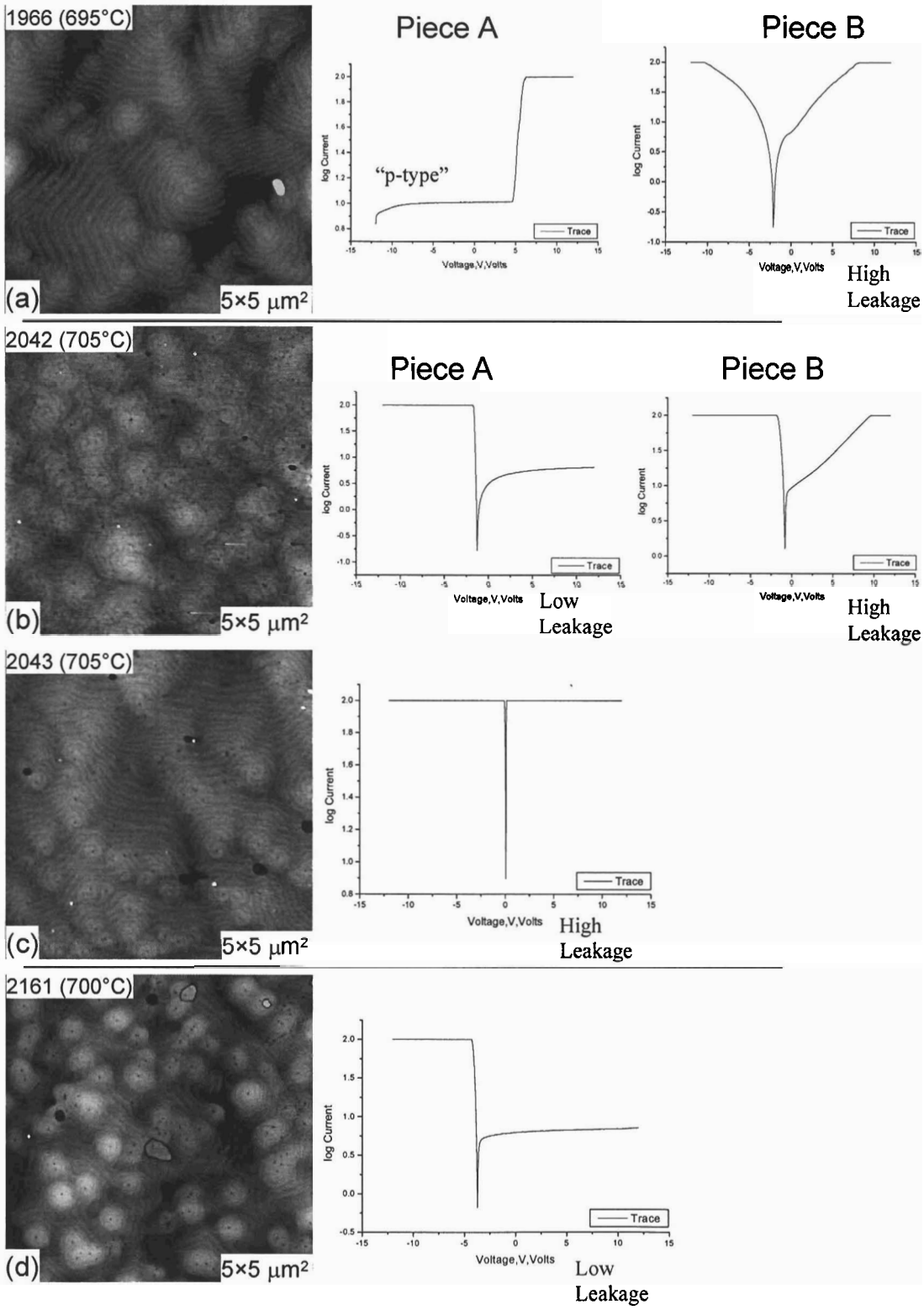

Fig. 3.9: I-V spectra for Ga-rich sample set #3 grown at 695 °C (1966), 705 °C (2042, 2043), and 700 °C (2161) with two Ga cells.

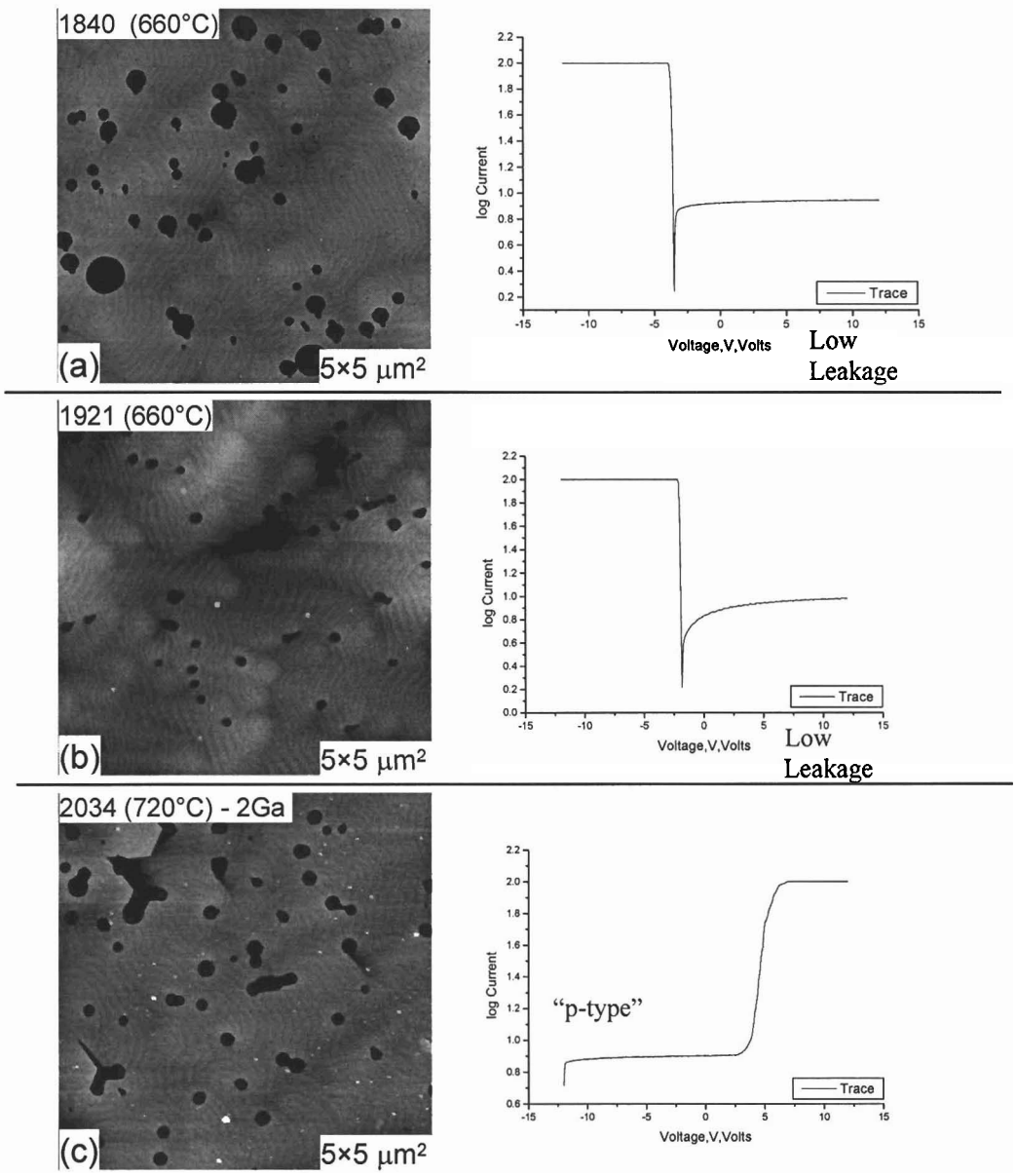

Fig. 3.10: I-V spectra for Less Ga-rich sample set #4 grown at 660 °C with one Ga cell (#1840, 1921) or at 720 °C with two Ga cells (#2034).

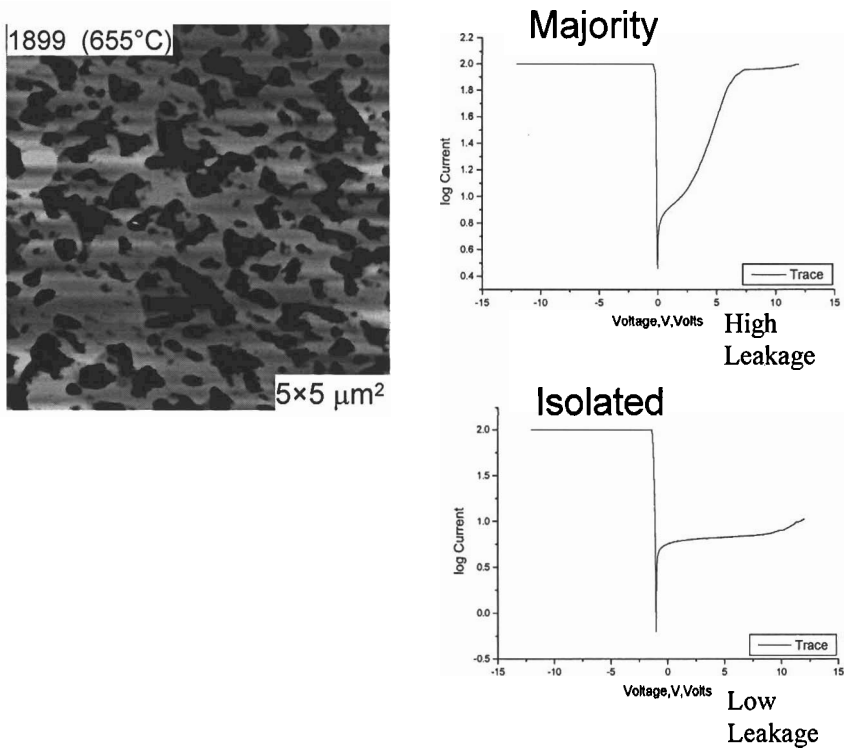

Fig. 3.11: I-V spectra for Ga-lean sample set #5 grown at 655 °C with one Ga cell (1899).

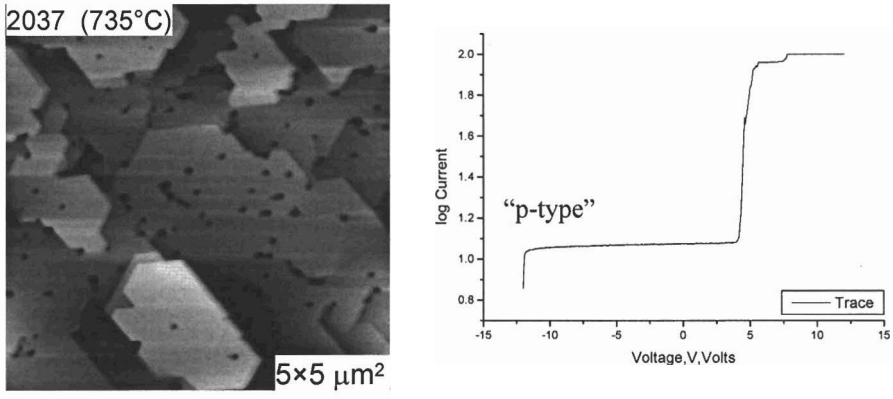

Fig. 3.12: I-V spectra for terrace-plus-step sample set #6 grown at 735 °C with two Ga cells (2037).

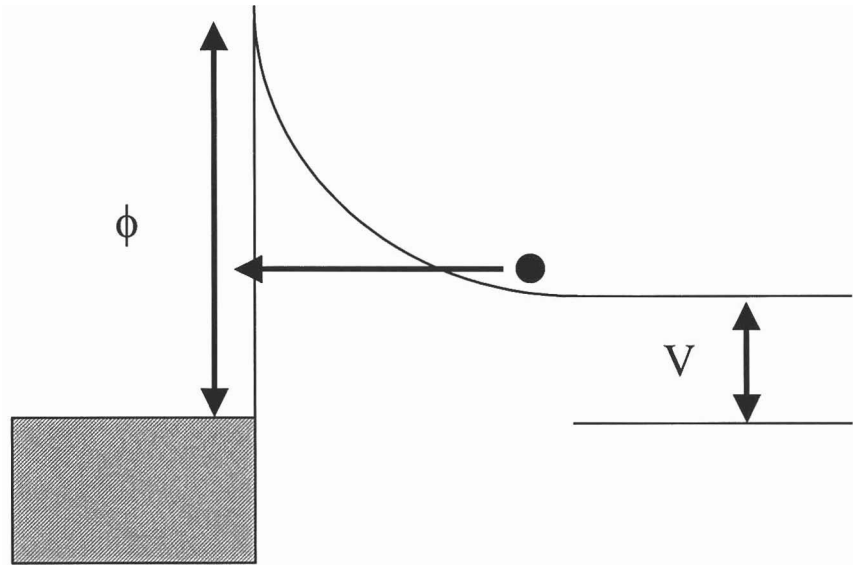

Fig. 3.13: Schematic representation of field emission conduction, where electrons tunnel through the barrier.

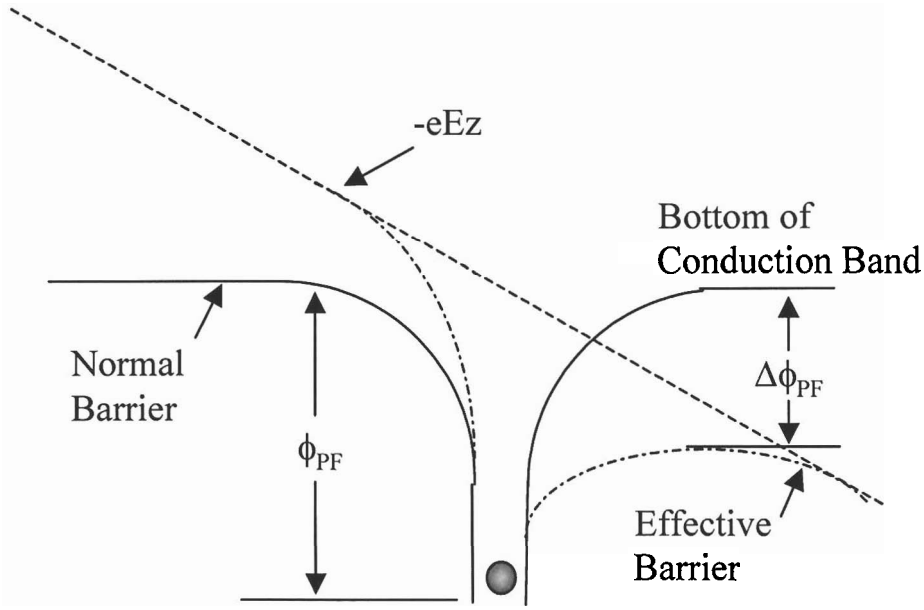

Fig. 3.14: Schematic representation of Frenkel-Poole conduction.

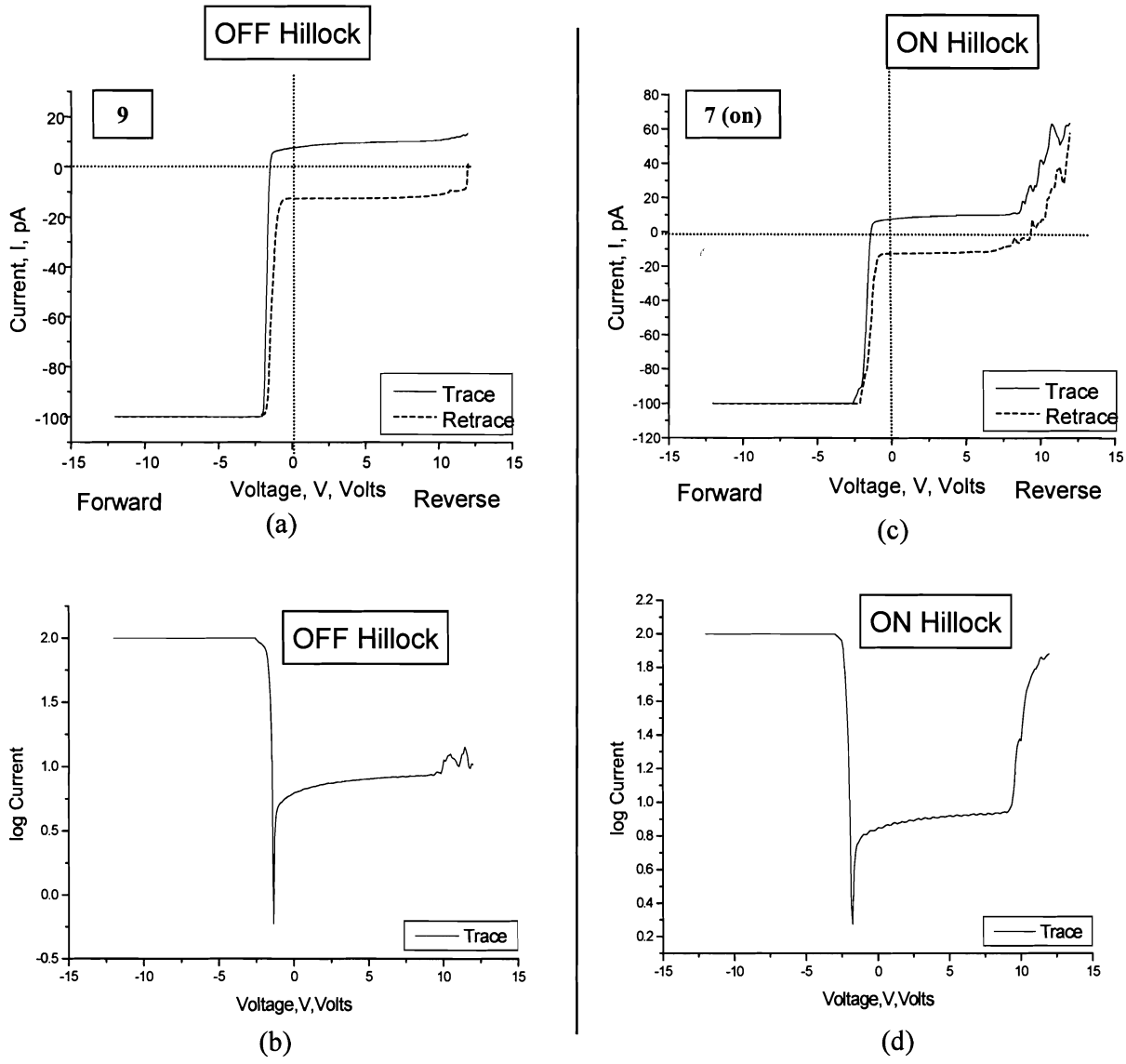

Fig. 3.15: Spectra for sample 1906 (a,b) off a hillock and (c,d) on a hillock. Used for curve-fitting in Figs. 3.17 and 3.19.

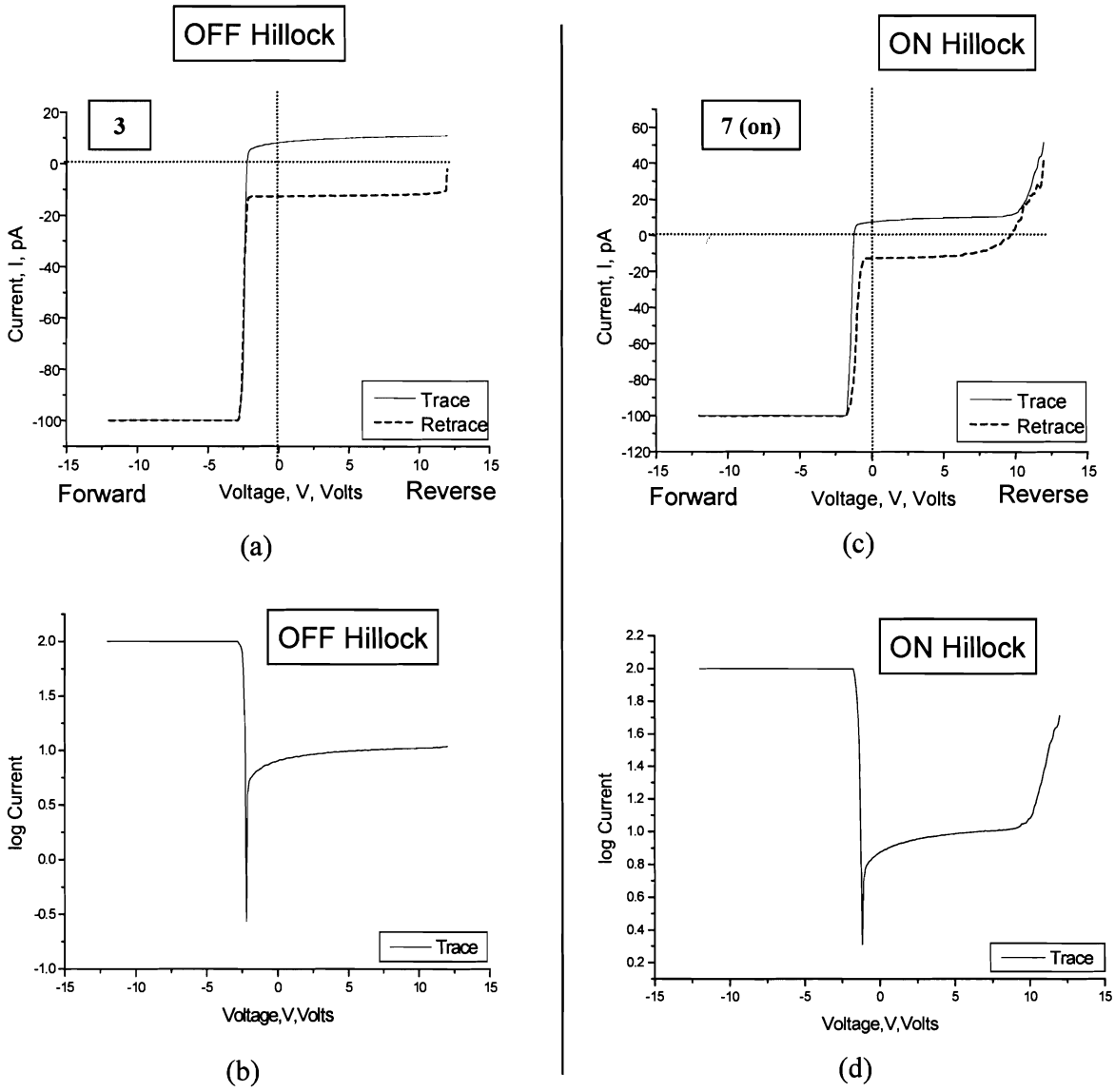

Fig. 3.16: Spectra for sample 1912 (a,b) off a hillock and (c,d) on a hillock. Used for curve-fitting in Fig. 3.18.

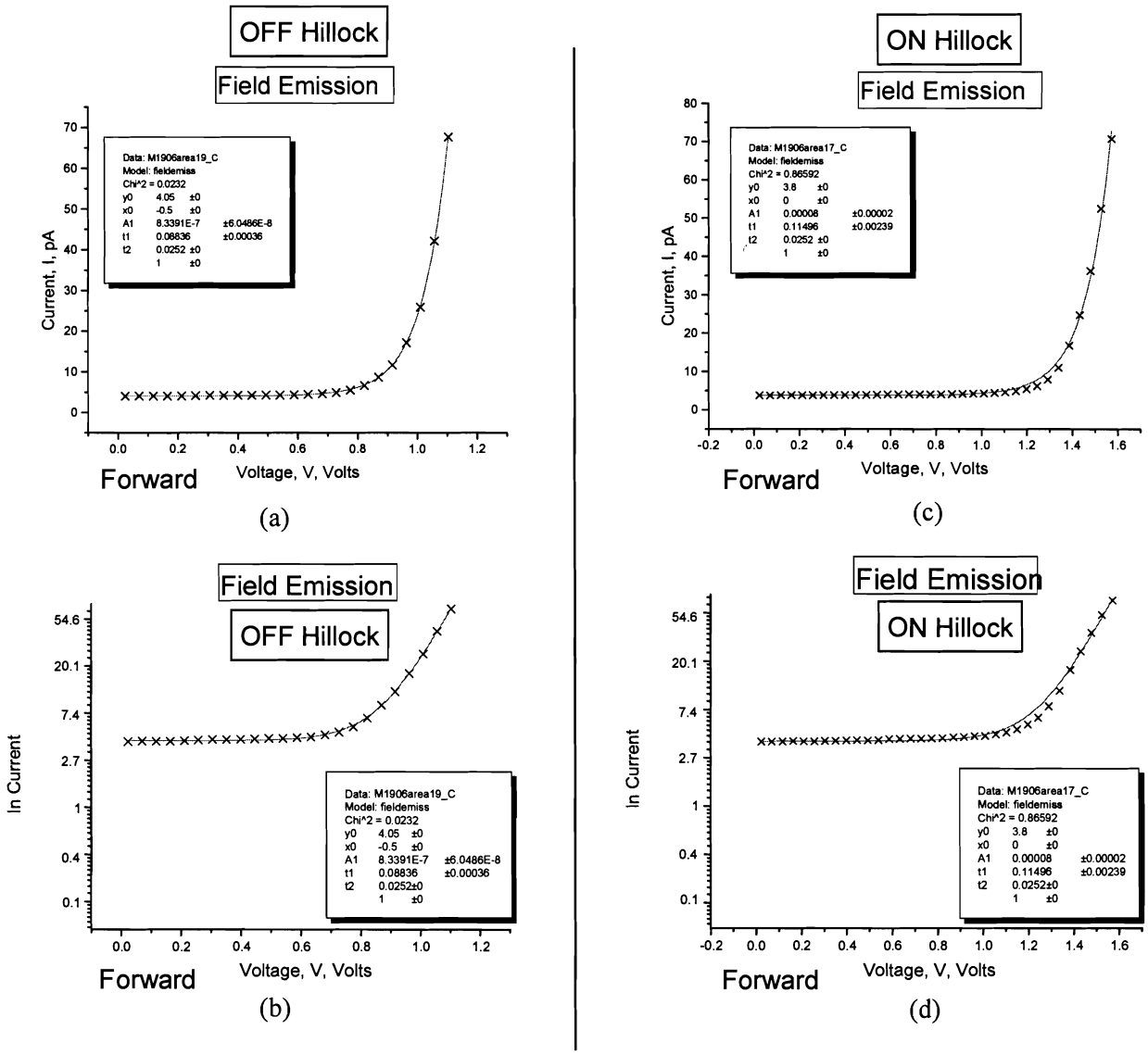

Fig. 3.17: Field emission fitting for forward-bias spectra of sample 1906 (a,b) off a hillock and (c,d) on a hillock.

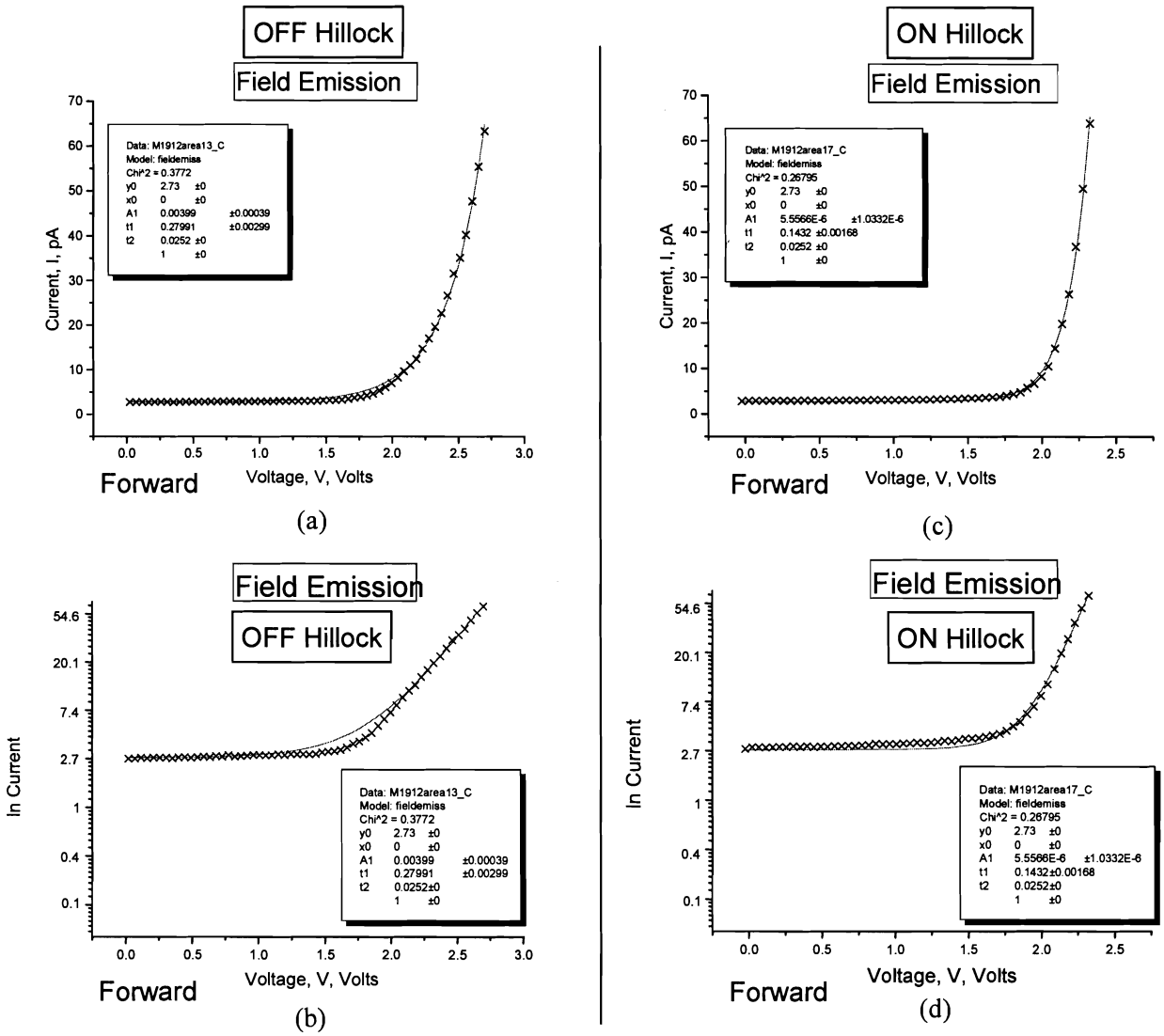

Fig. 3.18: Field emission fitting for forward-bias spectra of sample 1912 (a,b) off a hillock and (c,d) on a hillock.

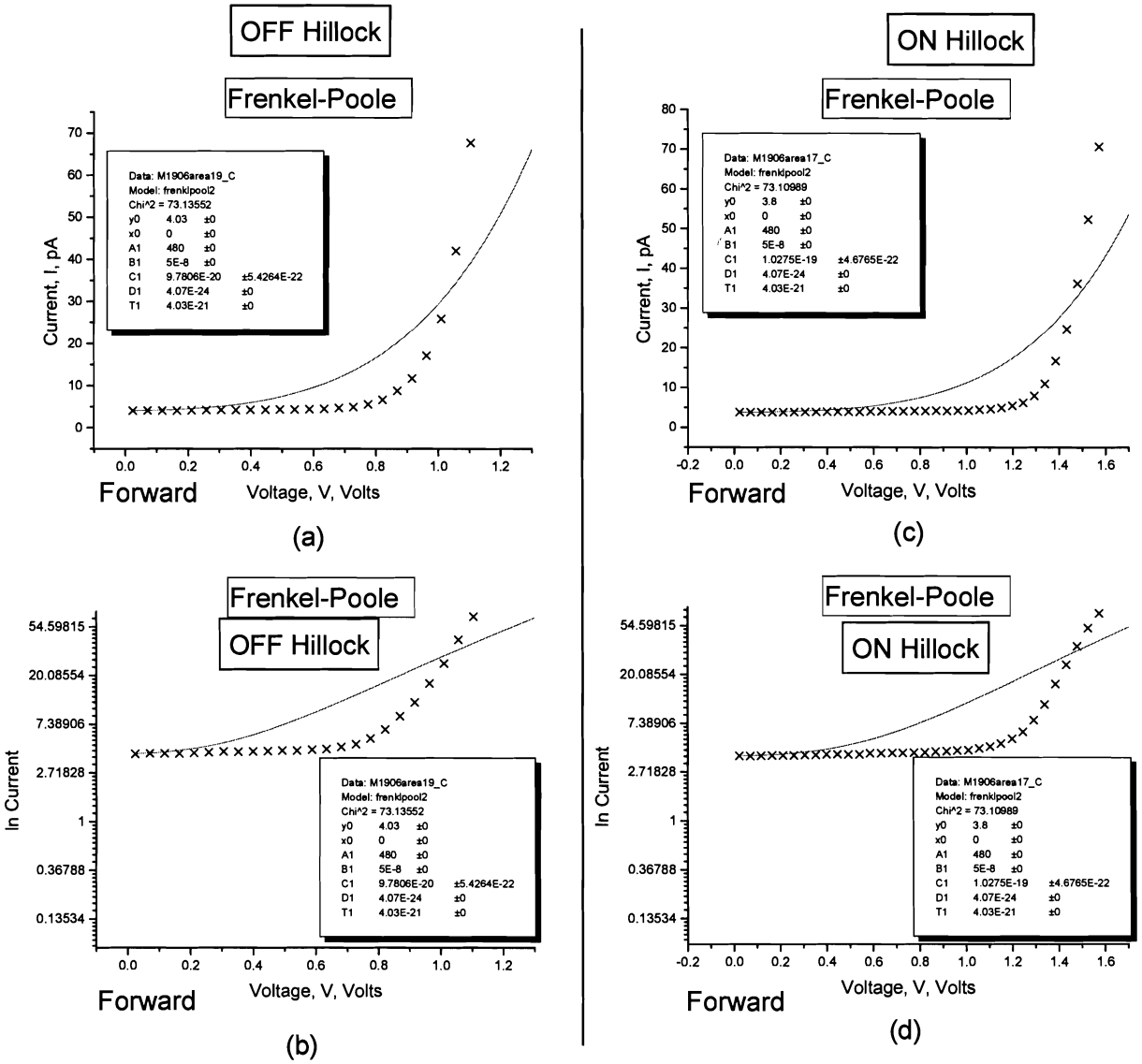

Fig. 3.19: Frenkel-Poole fitting for forward-bias spectra of sample 1906 (a,b) off a hillock and (c,d) on a hillock.

References

[1] J. C. Dickinson. *AFM, CAFM, and EFM Studies of the GaN System.* M.S. Thesis. Virginia Commonwealth University, 2000.

[2] H. Morkoç. *Nitride Semiconductors and Devices.* Springer-Verlag Berlin Heidelberg 1999.

[3] B. Heying, R. Averbeck, L. F. Chen, E. Haus, H. Riechert, and J. S. Speck. J. Appl. Phys. 88, 1855 (2000)

[4] L. He. *III-Nitride Semiconductors Grown by Plasma Assisted Molecular Beam Epitaxy.* Ph.D. Dissertation. Virginia Commonwealth University, 2004.

[5] B. Heying, E. J. Tarsa, C. R. Elsass, P. Fini, S. P. DenBaars, and J. S. Speck. J. Appl. Phys. 85, 6470. (1999)

[6] J. W. P. Hsu, M. J. Manfra, R. J. Molnar, B. Heying, and J. S. Speck. Appl. Phys. Lett. 81, 79. (2002)

[7] K. Shiojima, J. M. Woodall, C. J. Eiting, P. A. Grudowski, and R. D. Dupuis. J. Vac. Sci. Technol. B. 17, 2030. (1999)

[8] J. W. P. Hsu, M. J. Manfra, S. N. G. Chu, C. H. Chen, L. N. Pfeiffer, and R. J. Molnar. Appl. Phys. Lett. 78, 3980. (2001)

[9] J. W. P. Hsu, M. J. Manfra, D. V. Lang, S. Richter, S. N. G. Chu, A. M. Sergent, R. N. Kleiman, L. N. Pfeiffer, and R. J. Molnar. Appl. Phys. Lett. 78, 1685. (2001)

[10] B. S. Simpkins, D. M. Schaadt, E. T. Yu, and R. J. Molnar. J. Appl. Phys. 91, 9924. (2002)

[11] J. Spradlin, S. Dogan, J. Xie, R. Molnar, A. A. Baski, and H. Morkoç. Appl. Phys. Lett. 84, 4150. (2004)

[12] K. Shiojima and T. Suemitsu. J. Vac. Sci. Technol. B. 21, 698. (2003)

[13] K. Shiojima, R. Suemitsu, and M. Ogura. Appl. Phys. Lett. 78, 3636. (2001)

[14] E. J. Miller, E. T. Yu, P. Waltereit, and J. S. Speck. Appl. Phys. Lett. 84, 535. (2004)

[15] J. Elsner, R. Jones, M. I, Heggie, P. K. Stitch, M. Haugk, Th. Frauenheim, S. Öberg, and P. R. Briddon. Phys. Rev. B. 58, 12 571 (1998)

[16] G. Koley and M. G. Spencer. Appl. Phys. Lett. 78, 2873. (2001)

[17] B. S. Simpkins, E. T. Yu, P. Waltereit, and J. S. Speck. Mat. Res. Soc. Symp. Proc. Vol. 743. (2003)

[18] B. S. Simpkins, E. T. Yu, P. Waltereit, and J. S. Speck. 94, 1448. (2003)

[19] P. J. Hansen, Y. E. Strausser, A. N. Erickson, E. J. Tarsa, P. Kozodoy, E. G. Brazel, J. P. Ibbetson, U. Mishra, V. Narayanamurti, S. P. DenBaars, and J. S. Speck. Appl. Phys. Lett. 72, 2247. (1998)

[20] I. Arslan, S. Ogut, P. D. Nellist, and N. D. Browning. Proc. Of the 4th Sump. On Non Stoichiometric III-V Compounds, Vol. 27, p. 145. (2002)

[21] E. J. Miller, D. M. Schaadt, E. T. Yu, X. L. Sun, L. J. Brillson, P. Waltereit, and J. S. Speck. J. Appl. Phys. 94, 7611. (2003)

[22] D. Braun. J. Poly. Sci. B, 41, 2622 (2003)

[23] J. R. Yeargan and H. L. Taylor. J. Appl. Phys. 39, 5600. (1968)

APPENDIX A: AFM Topography Images

1840

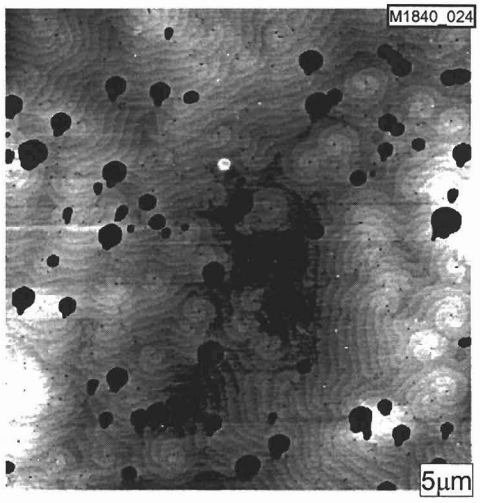

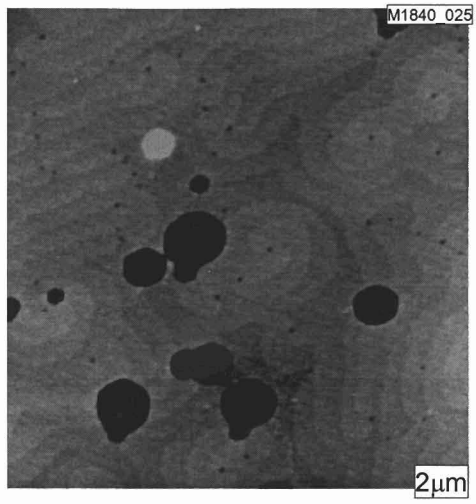

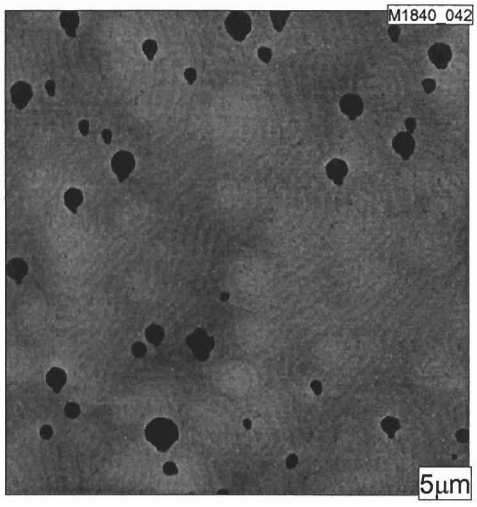

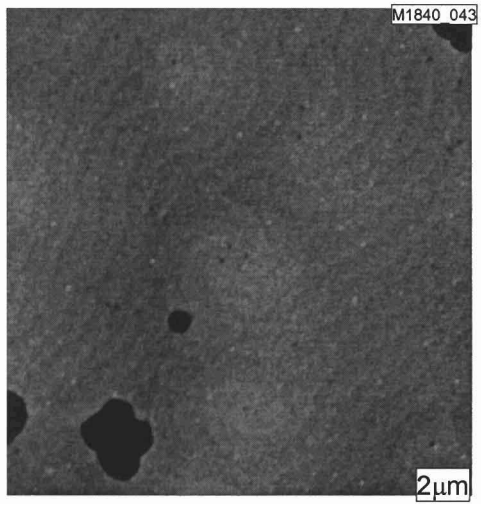

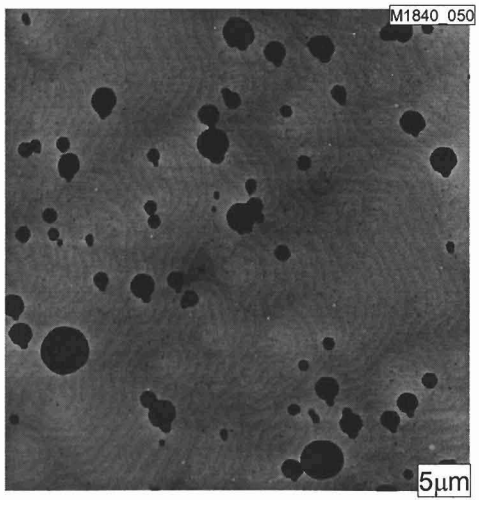

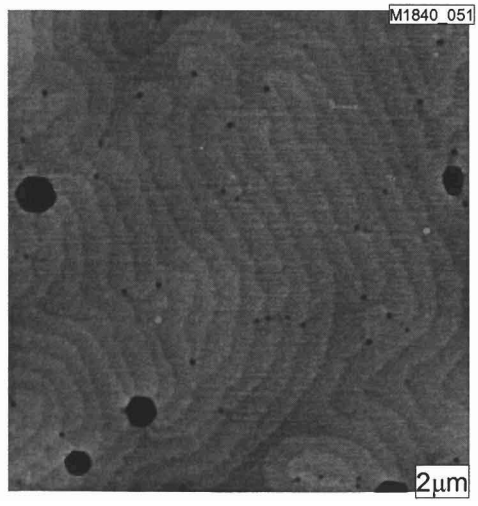

1899

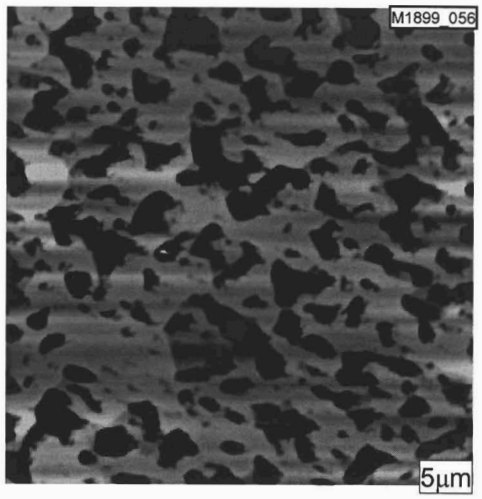
M1899_056
5µm

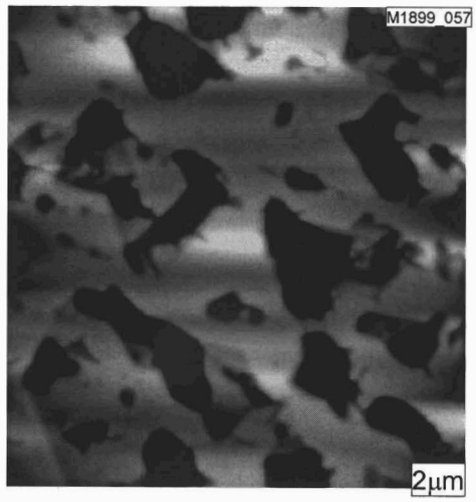
M1899_057
2µm

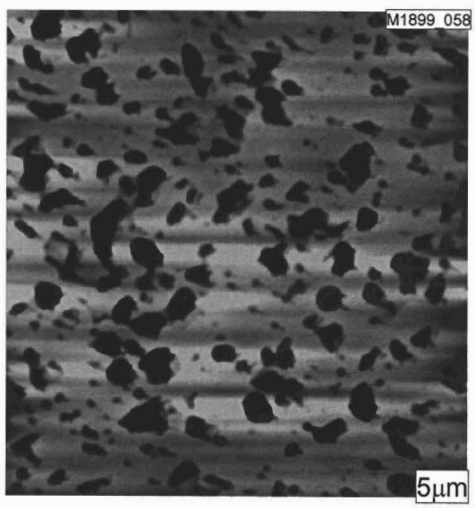
M1899_058
5µm

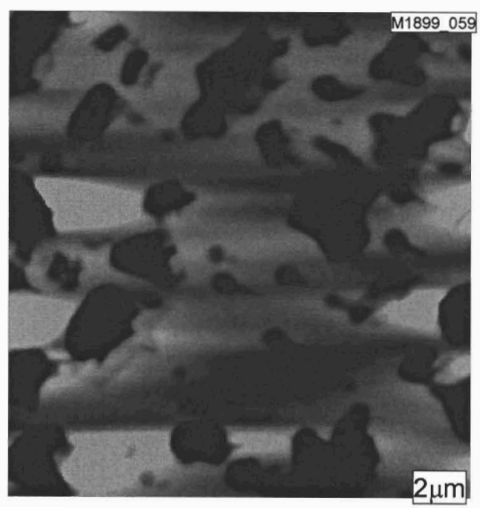
M1899_059
2µm

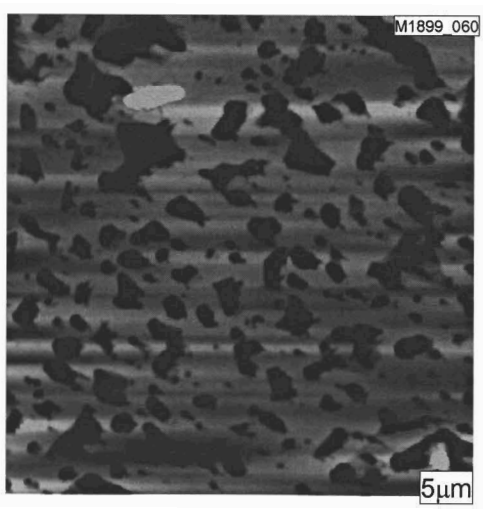
M1899_060
5µm

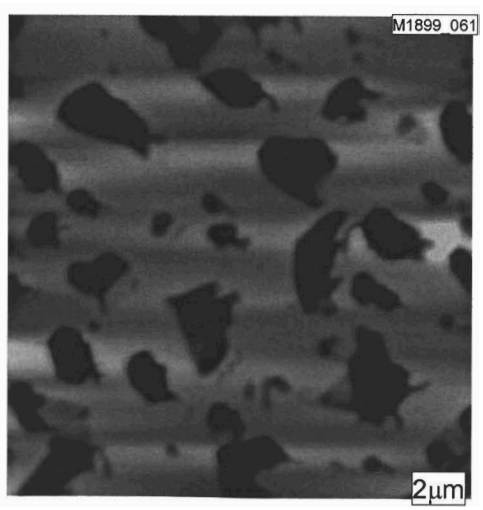
M1899_061
2µm

1903

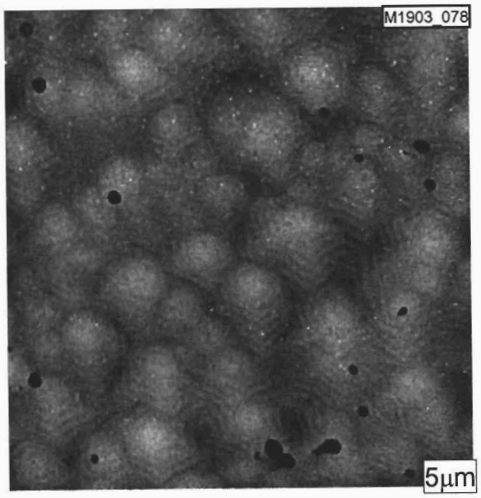
M1903_078
5µm

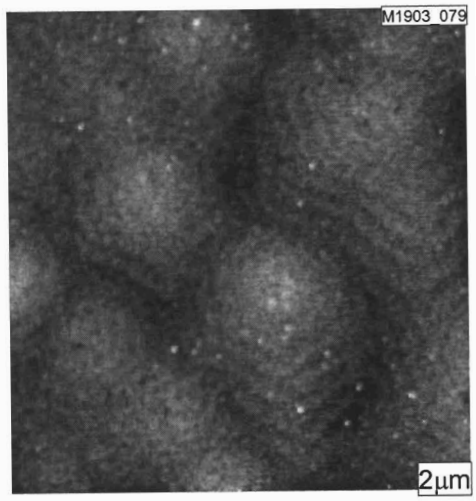
M1903_079
2µm

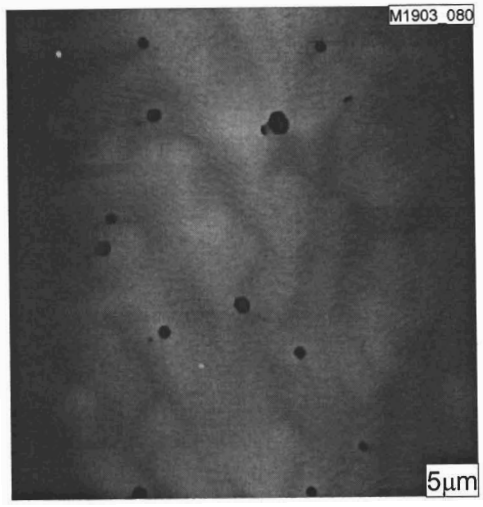
M1903_080
5µm

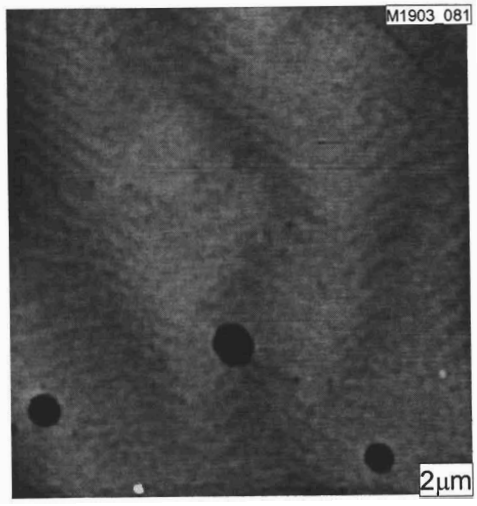
M1903_081
2µm

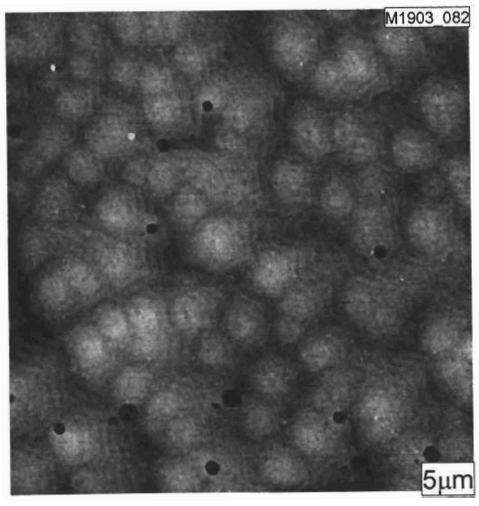
M1903_082
5µm

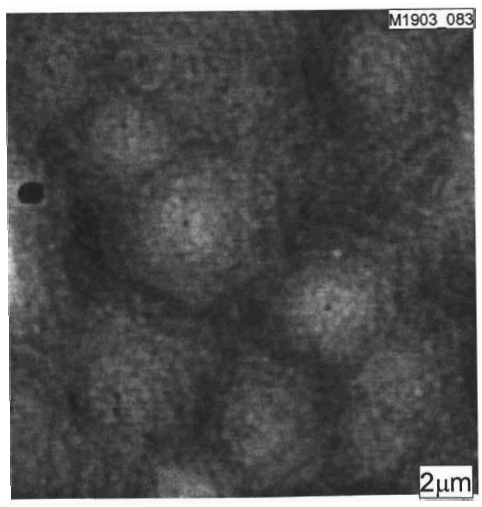
M1903_083
2µm

1906

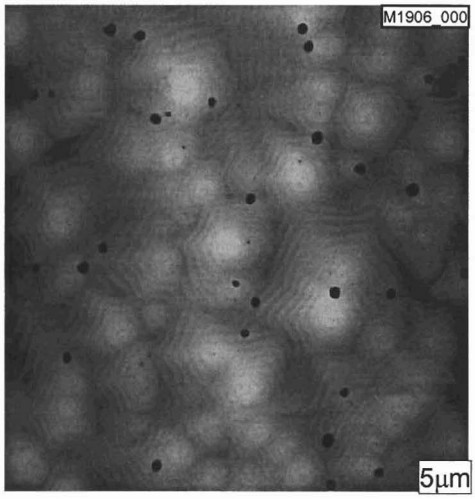
M1906_000
5µm

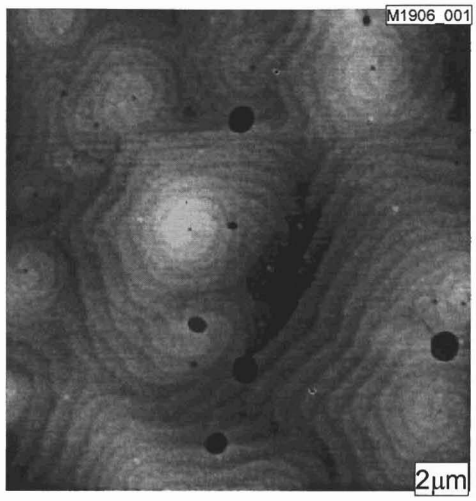
M1906_001
2µm

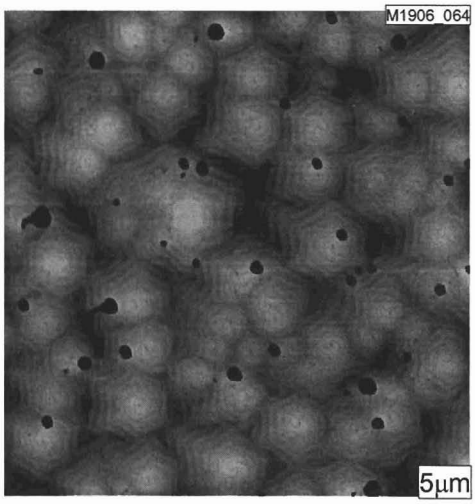
M1906_064
5µm

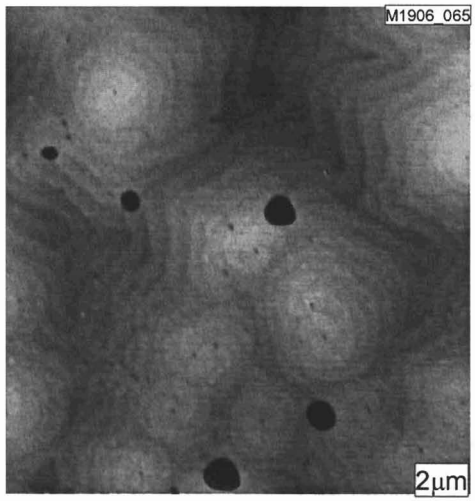
M1906_065
2µm

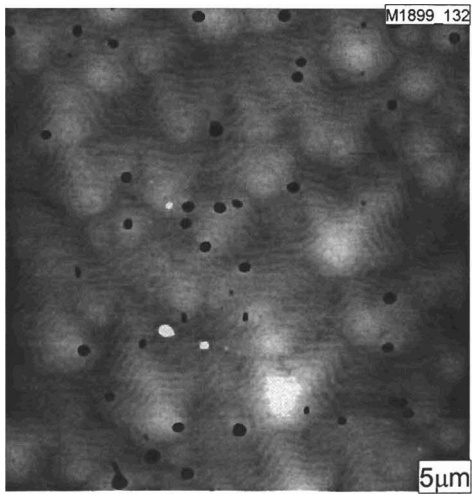
M1899_132
5µm

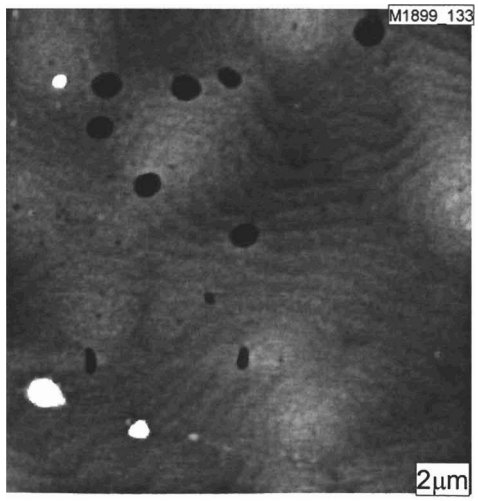
M1899_133
2µm

1912

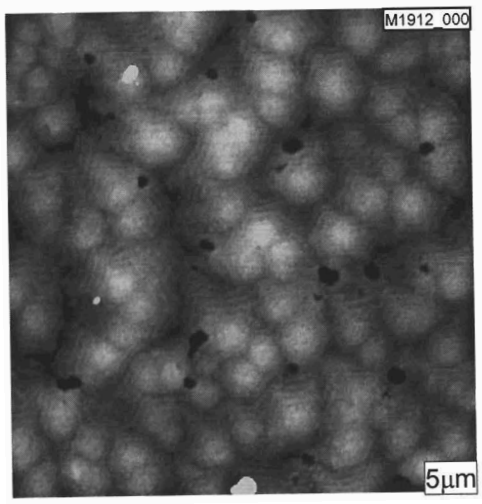

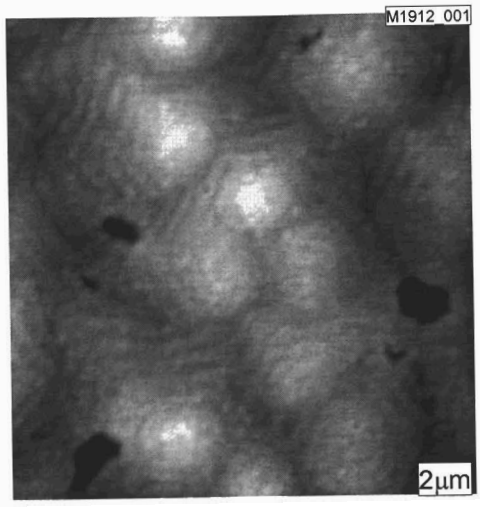

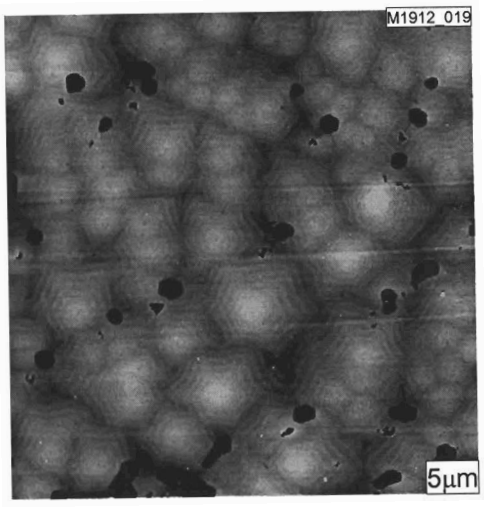

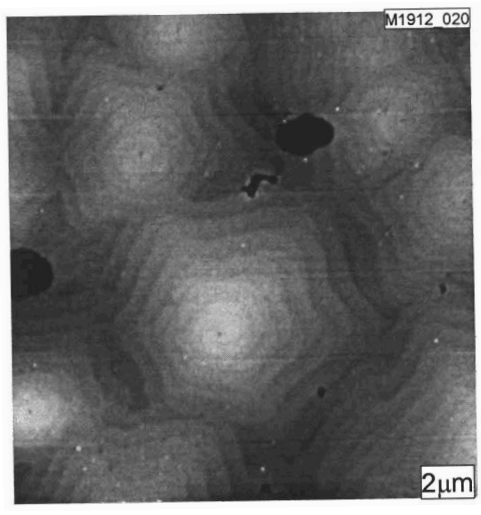

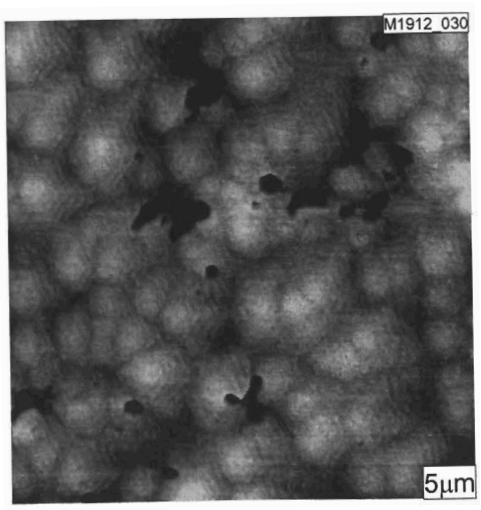

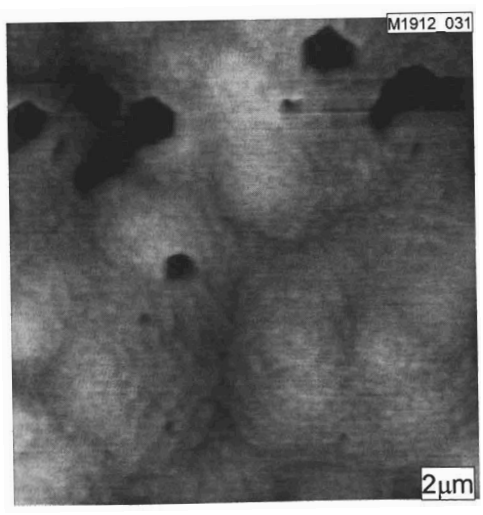

Appendix A.5

1916

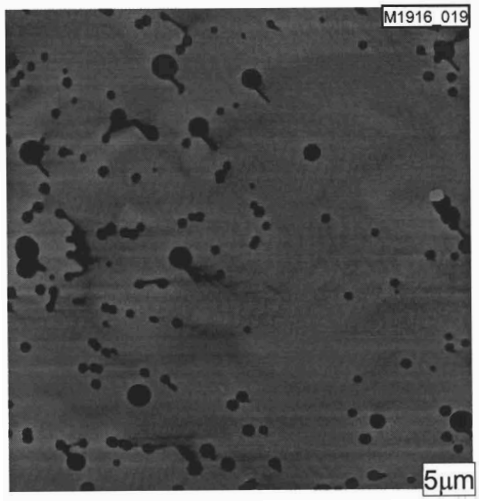
M1916_019
5µm

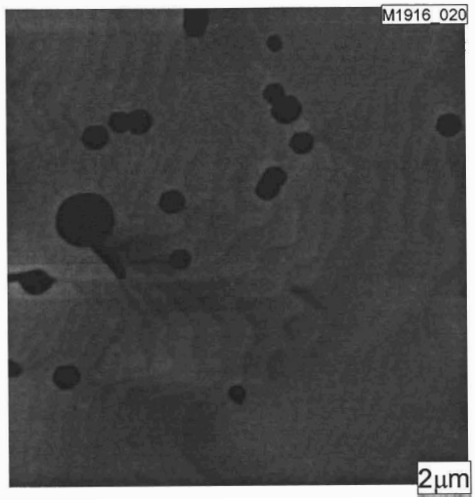
M1916_020
2µm

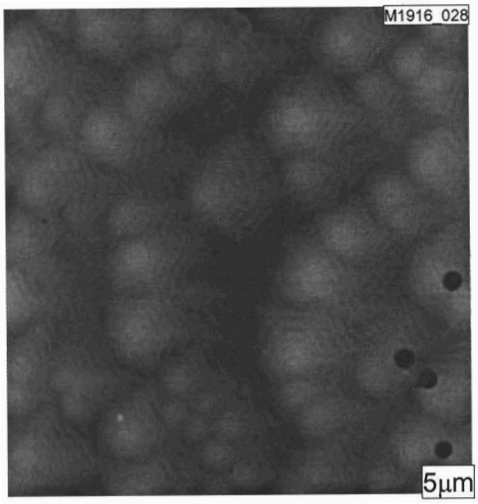
M1916_028
5µm

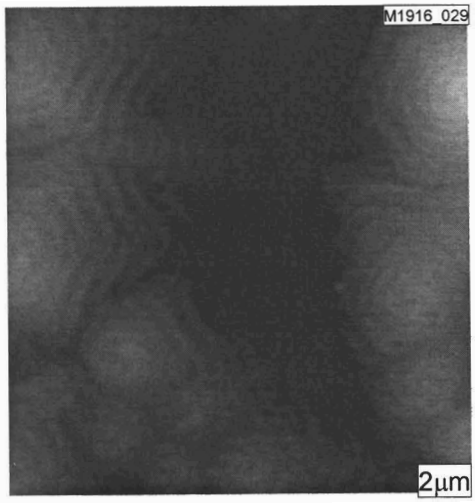
M1916_029
2µm

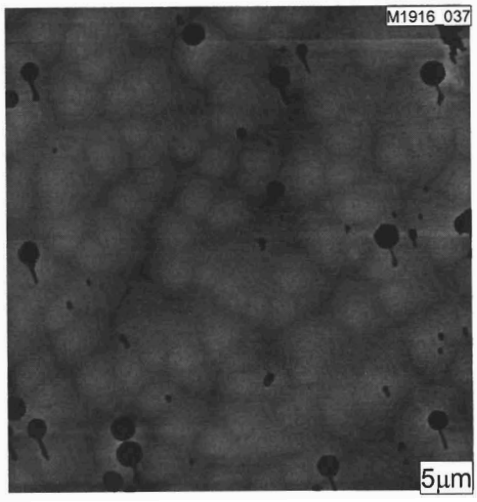
M1916_037
5µm

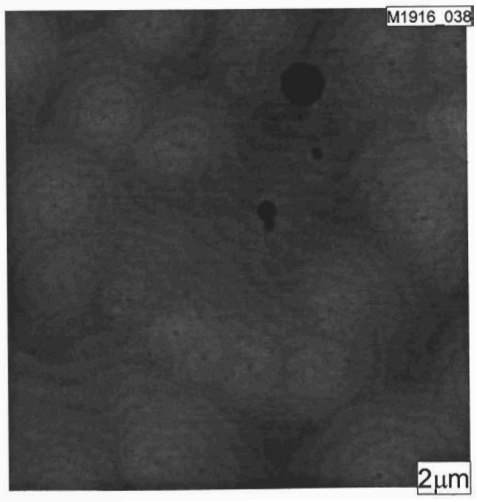
M1916_038
2µm

1921

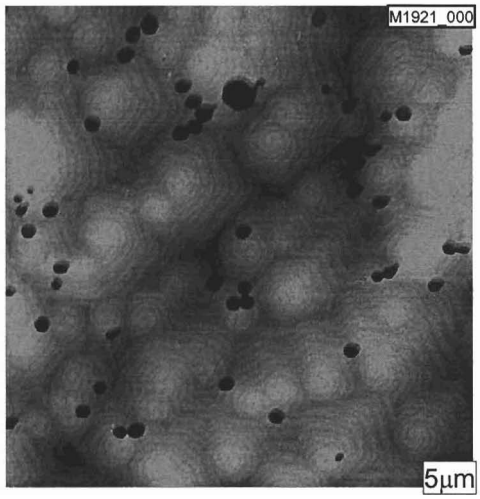

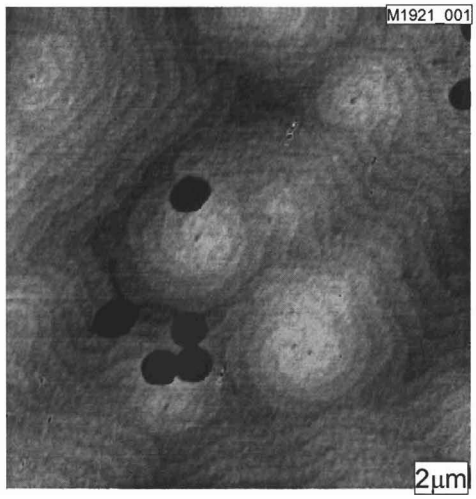

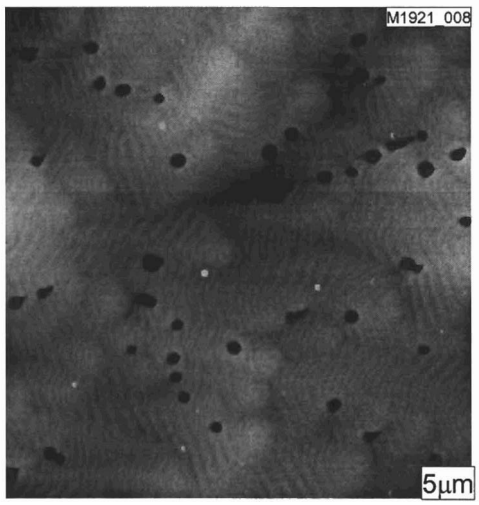

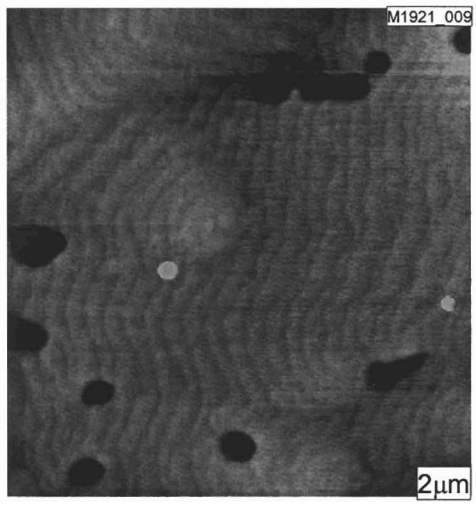

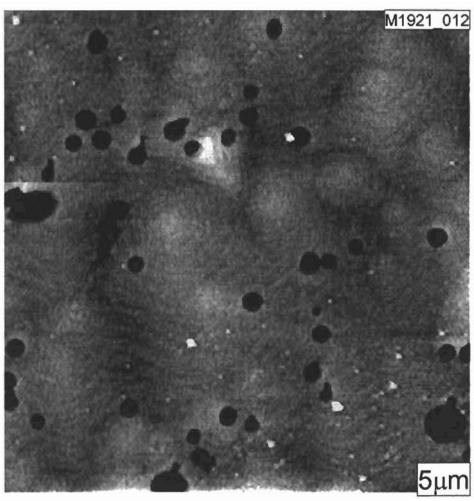

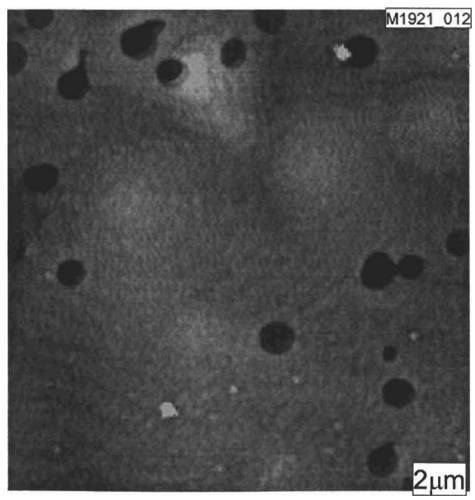

Appendix A.7

1966

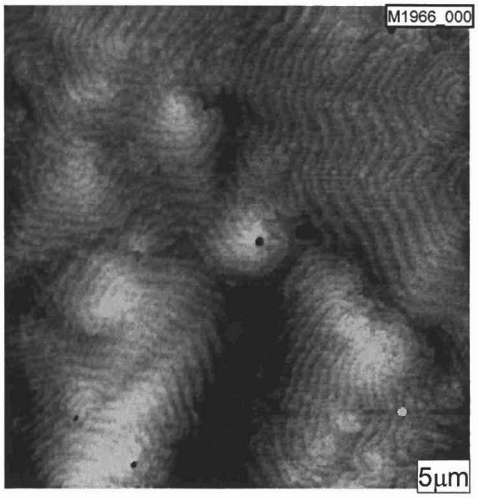

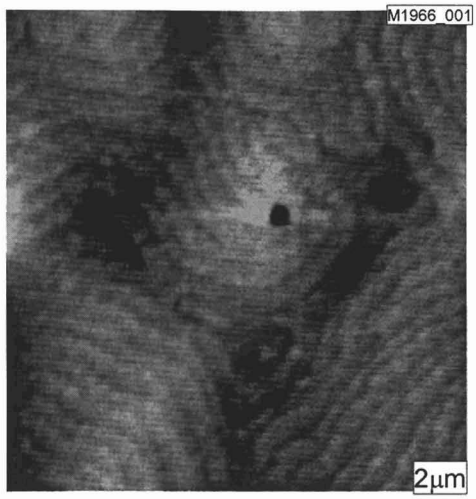

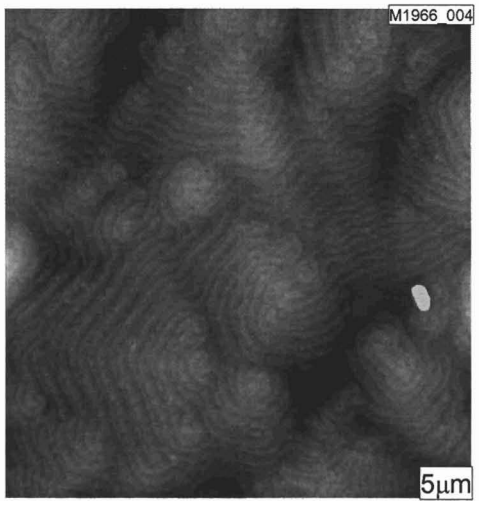

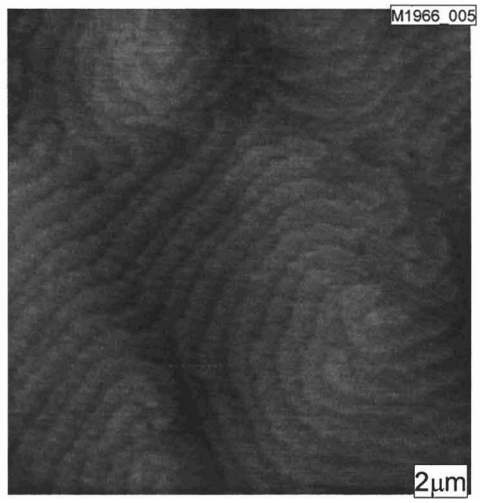

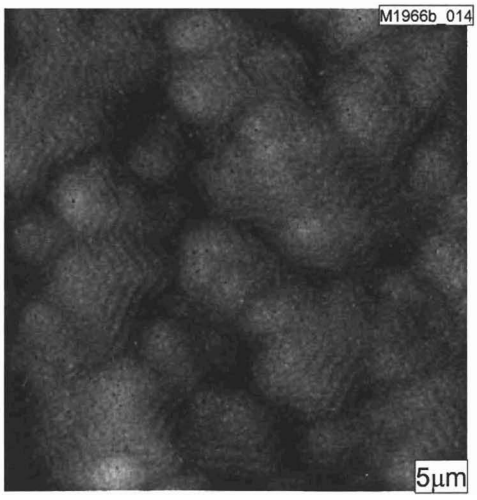

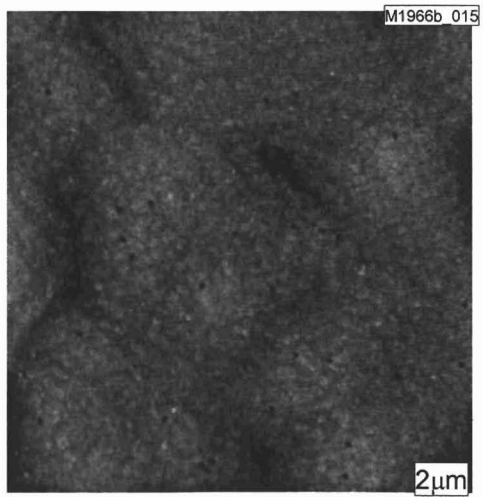

Appendix A.8

2004

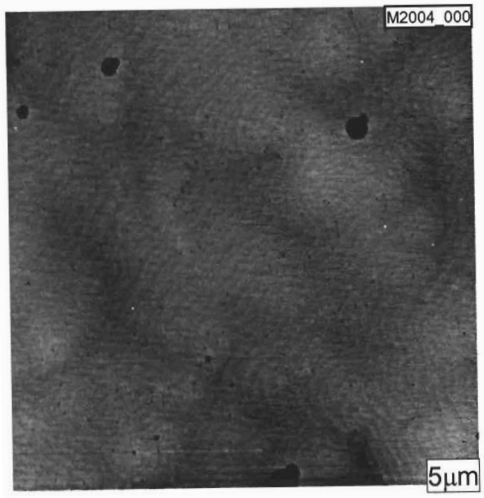
M2004_000
5µm

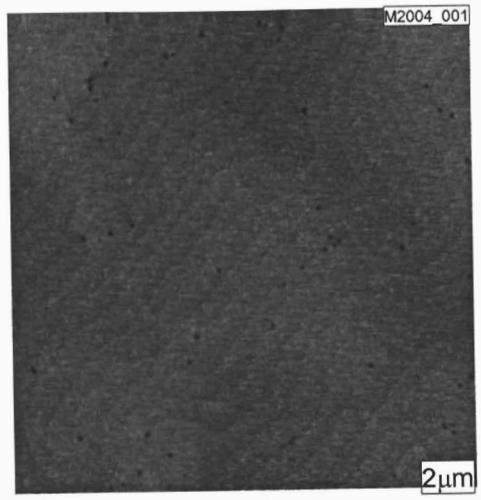
M2004_001
2µm

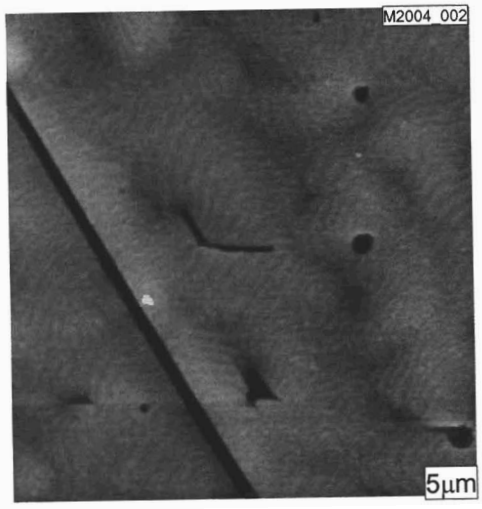
M2004_002
5µm

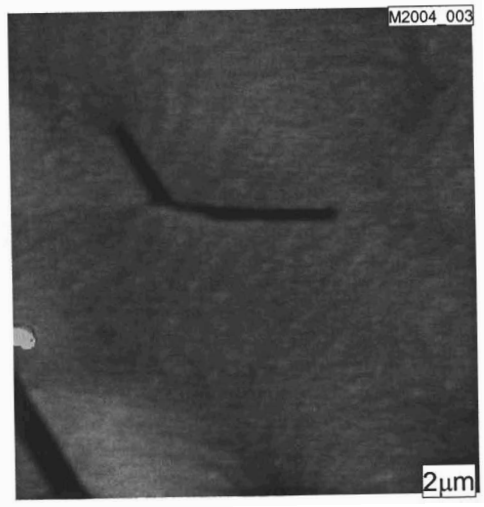
M2004_003
2µm

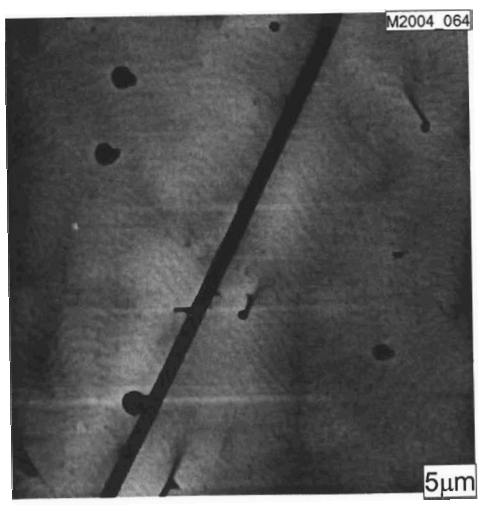
M2004_064
5µm

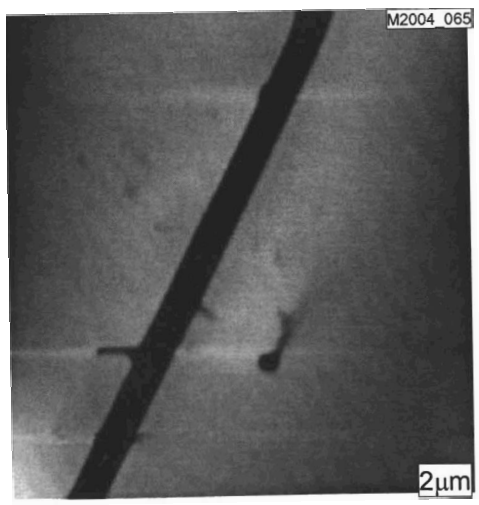
M2004_065
2µm

2009

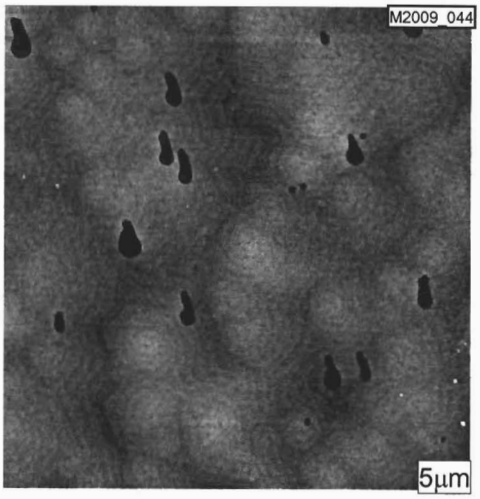

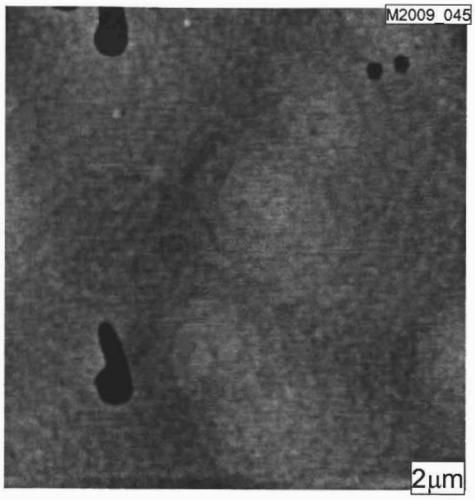

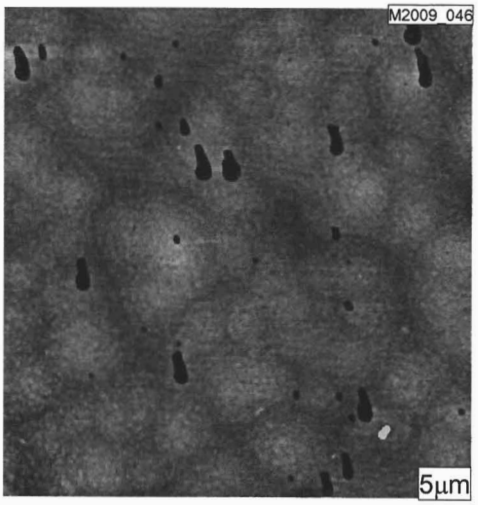

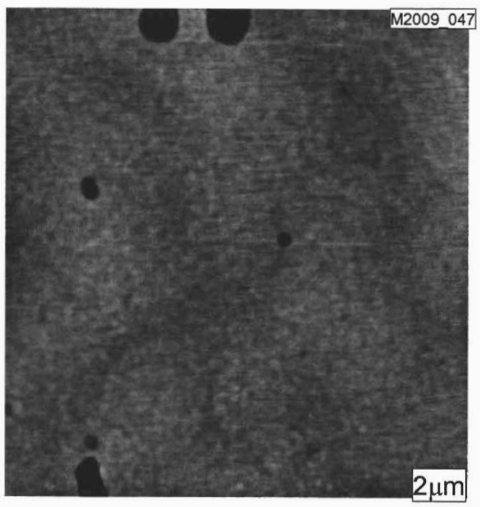

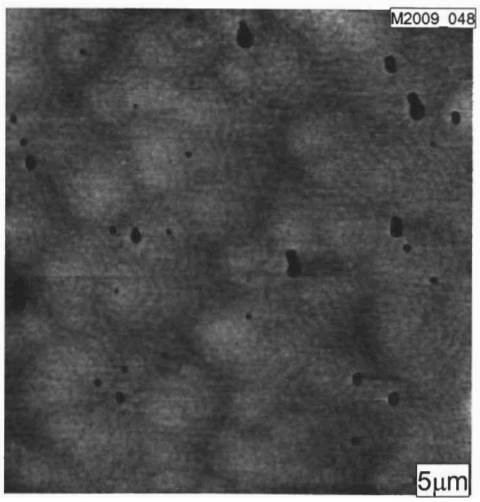

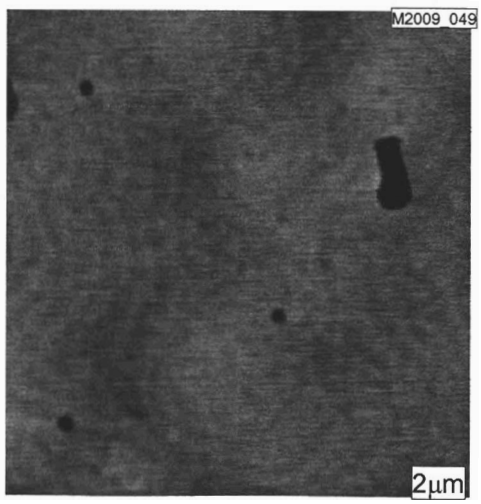

Appendix A.10

2024

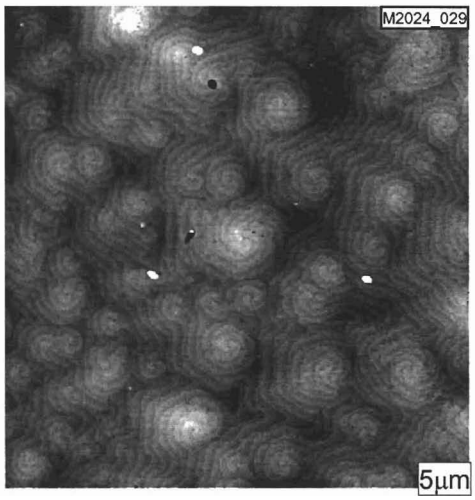
M2024_029
5µm

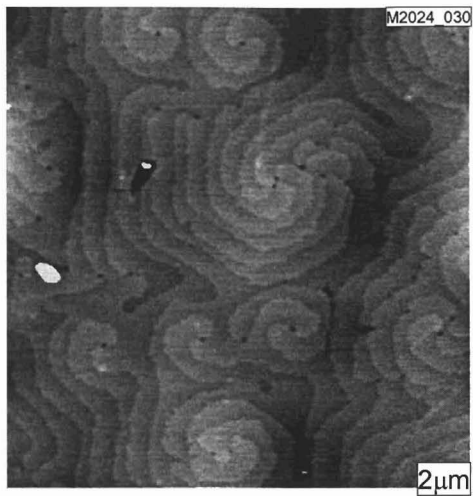
M2024_030
2µm

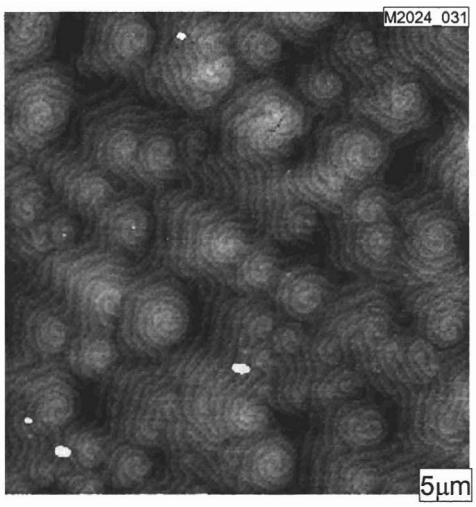
M2024_031
5µm

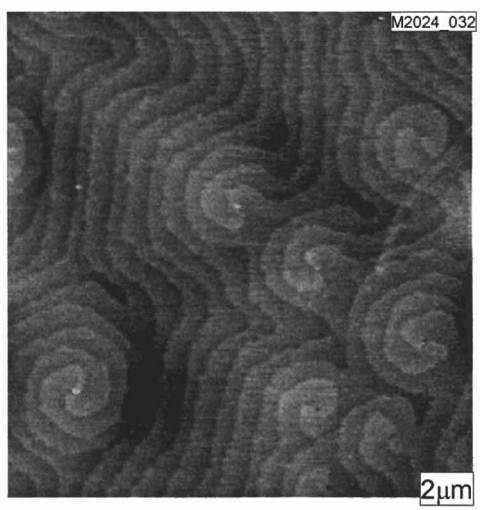
M2024_032
2µm

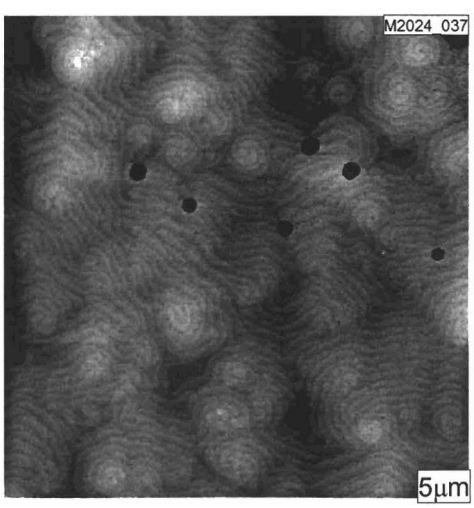
M2024_037
5µm

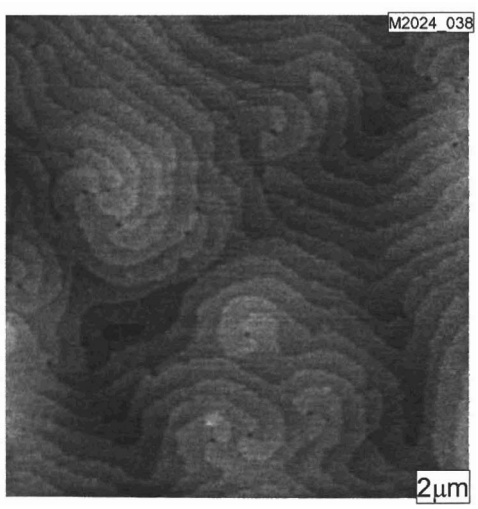
M2024_038
2µm

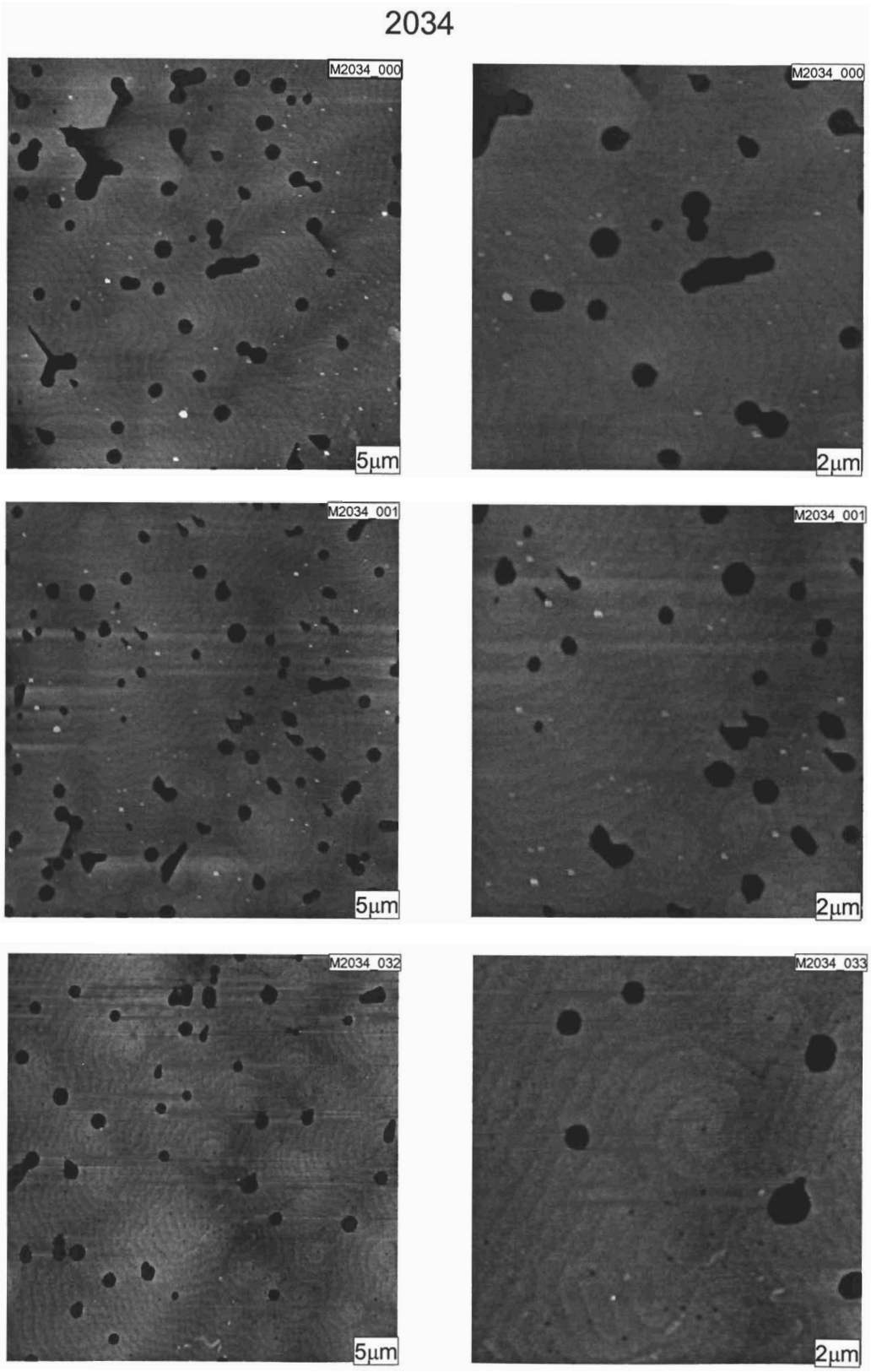
2034
M2034_000
5µm
M2034_000
2µm
M2034_001
5µm
M2034_001
2µm
M2034_032
5µm
M2034_033
2µm

2037

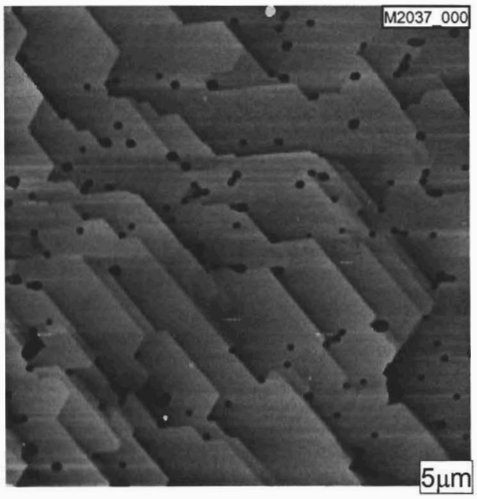
M2037_000
5µm

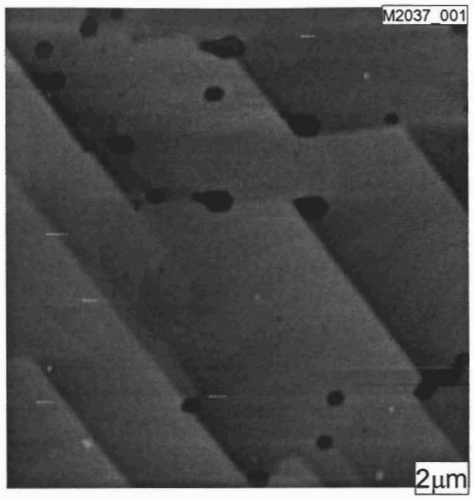
M2037_001
2µm

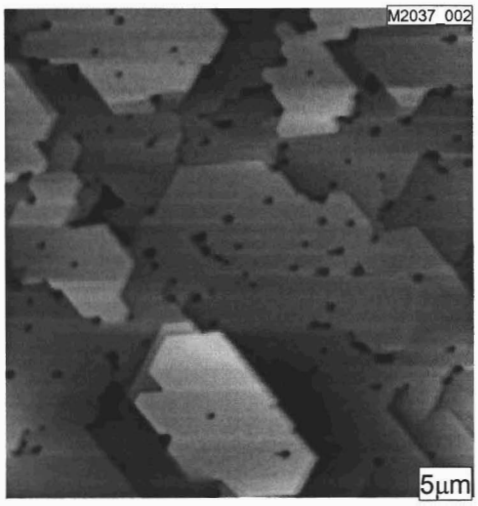
M2037_002
5µm

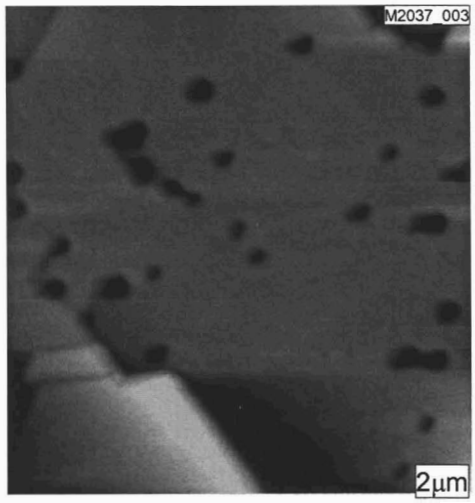
M2037_003
2µm

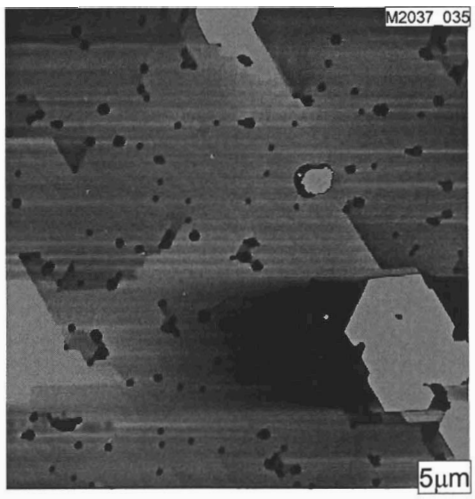
M2037_035
5µm

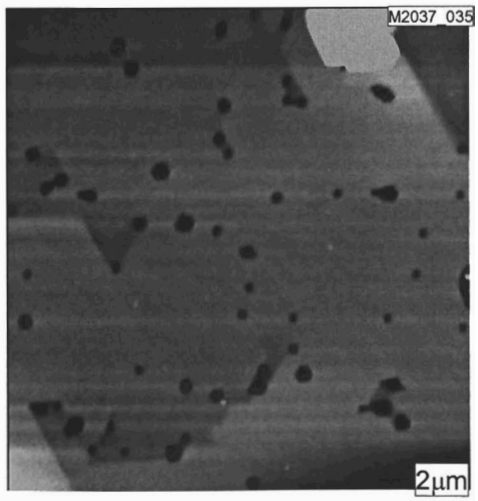
M2037_035
2µm

2042

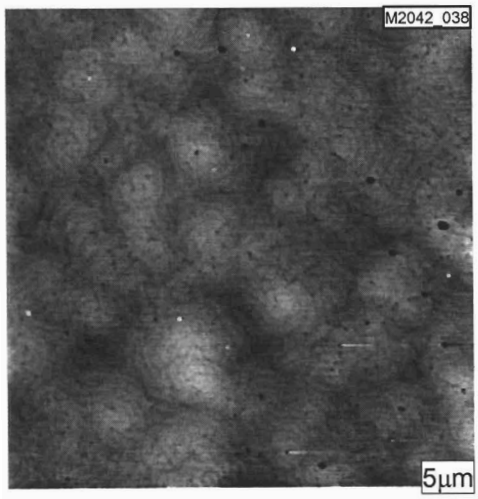

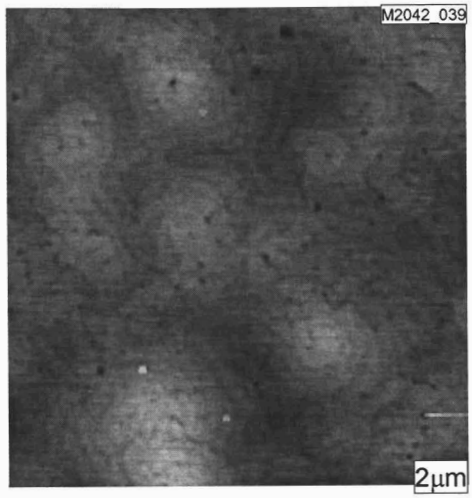

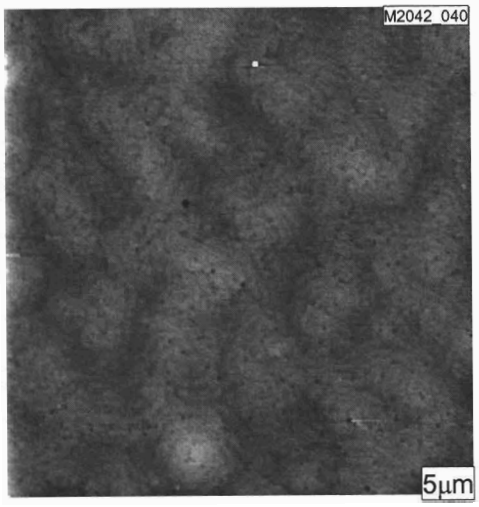

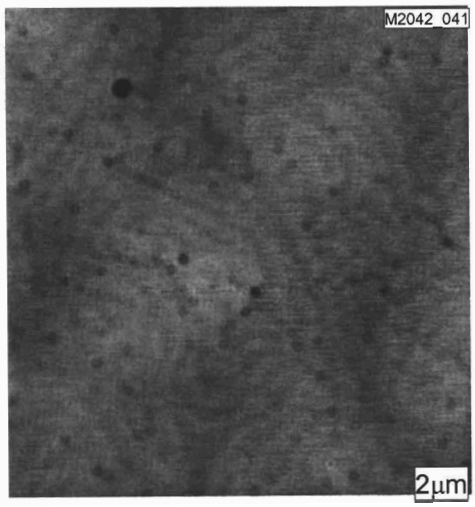

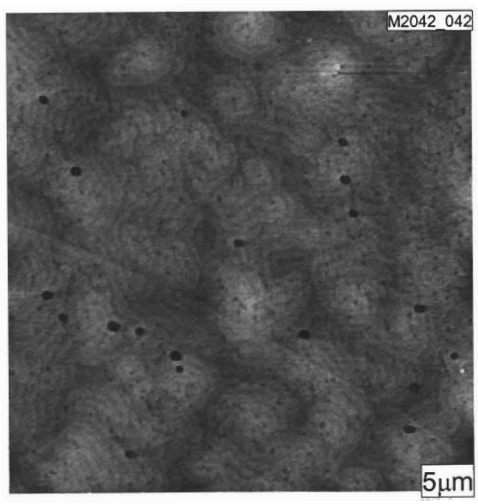

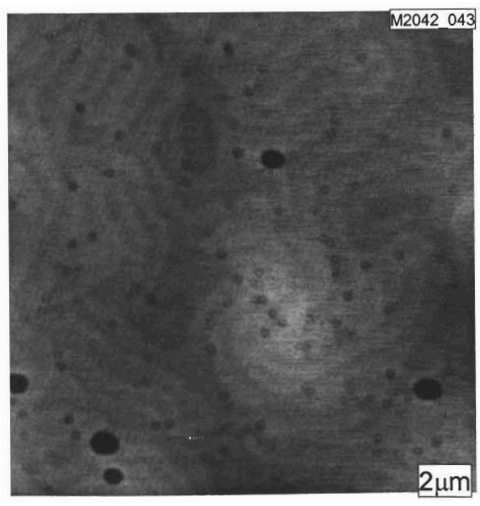

Appendix A.14

2043

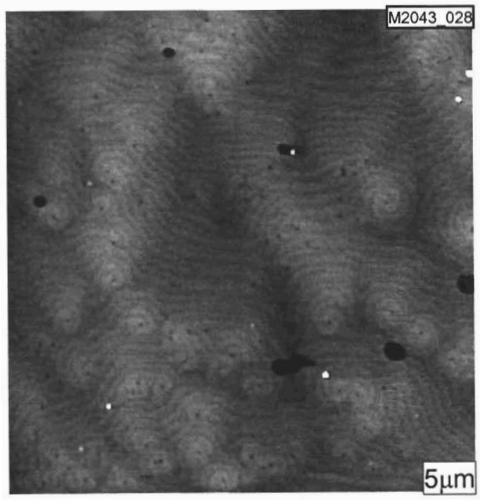
M2043_028
5µm

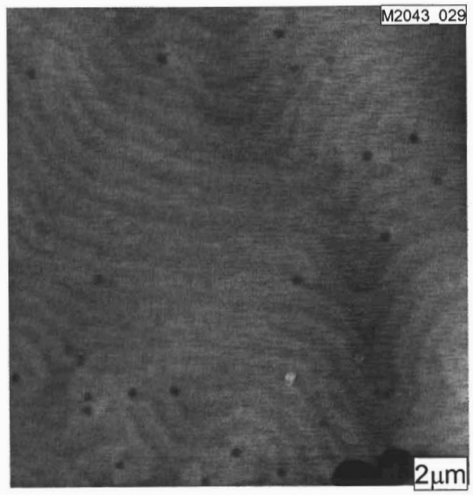
M2043_029
2µm

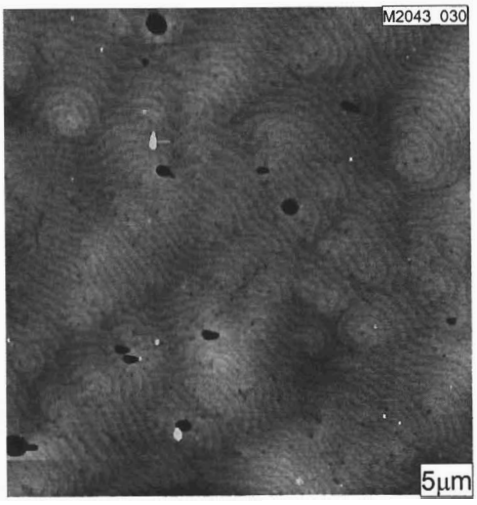
M2043_030
5µm

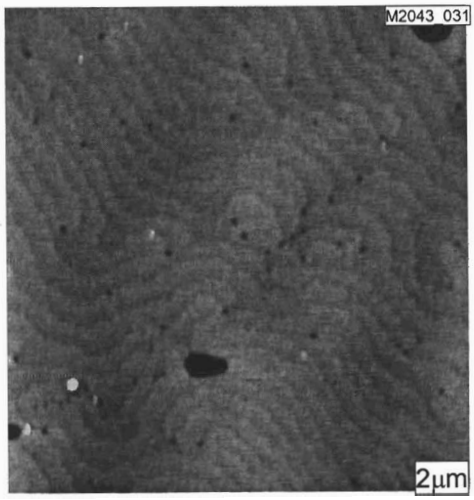
M2043_031
2µm

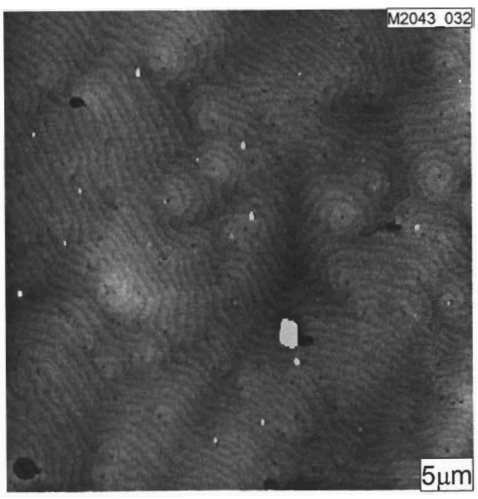
M2043_032
5µm

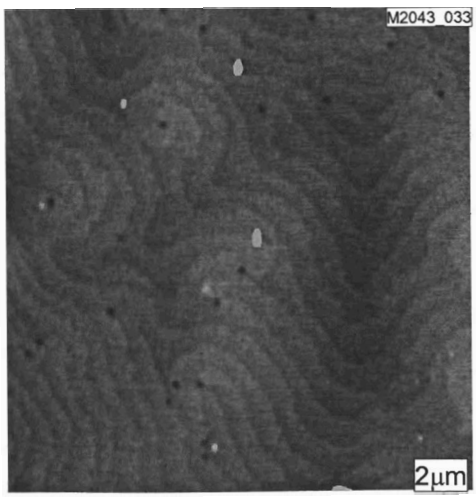
M2043_033
2µm

2161

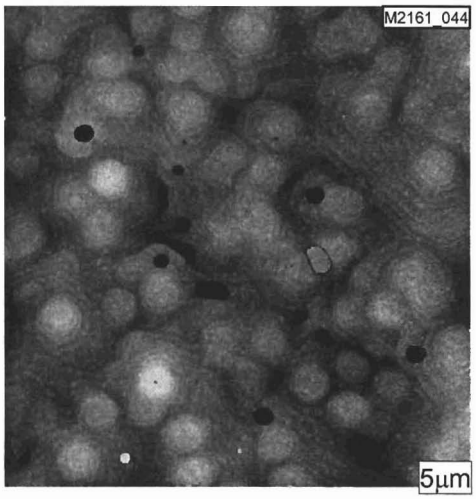

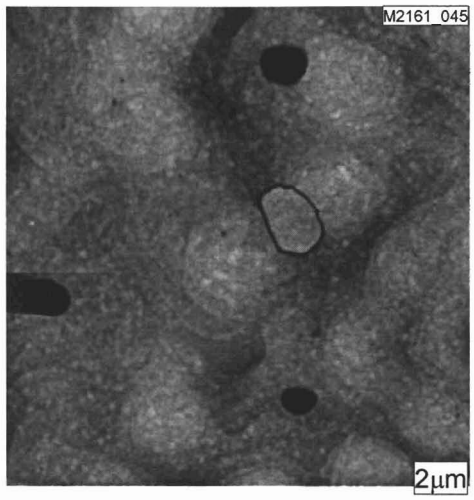

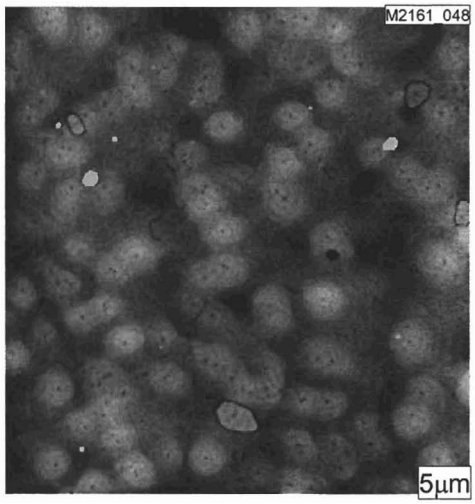

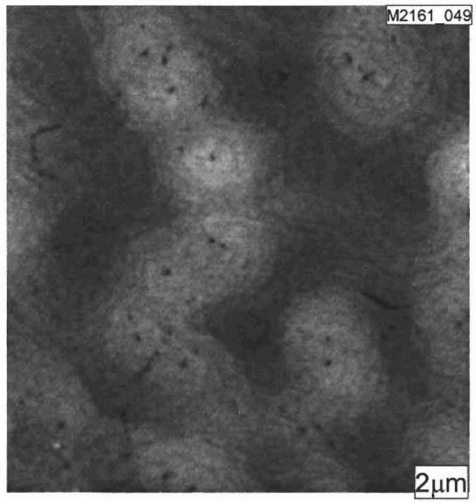

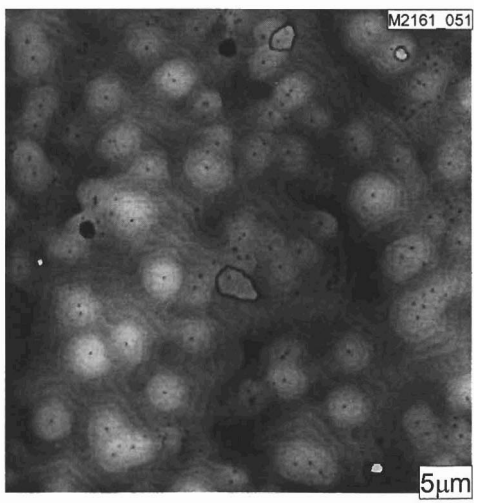

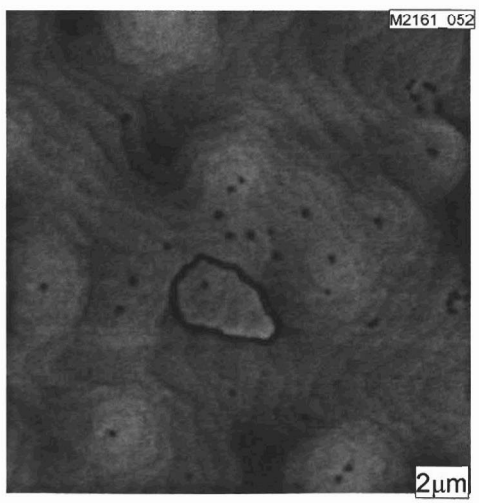

Appendix A.16

APPENDIX B: I-V Spectra (Linear Scale)

M1840 I-V Spectra (Top Left Corner): 0.5μm × 2μm, 12V

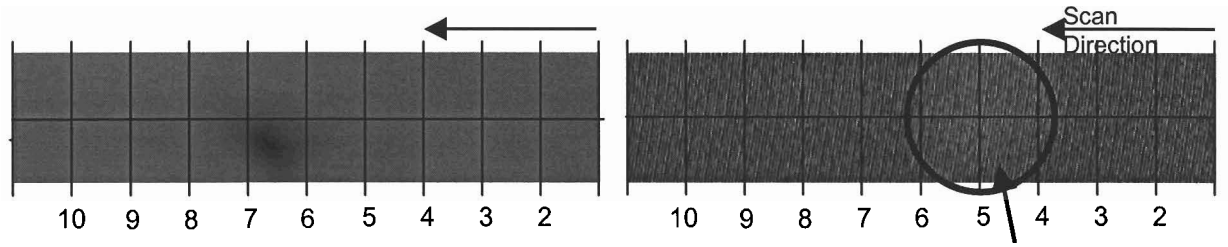

Note: All I-V spectra were taken at line intersections and are labeled according to the intersection number.

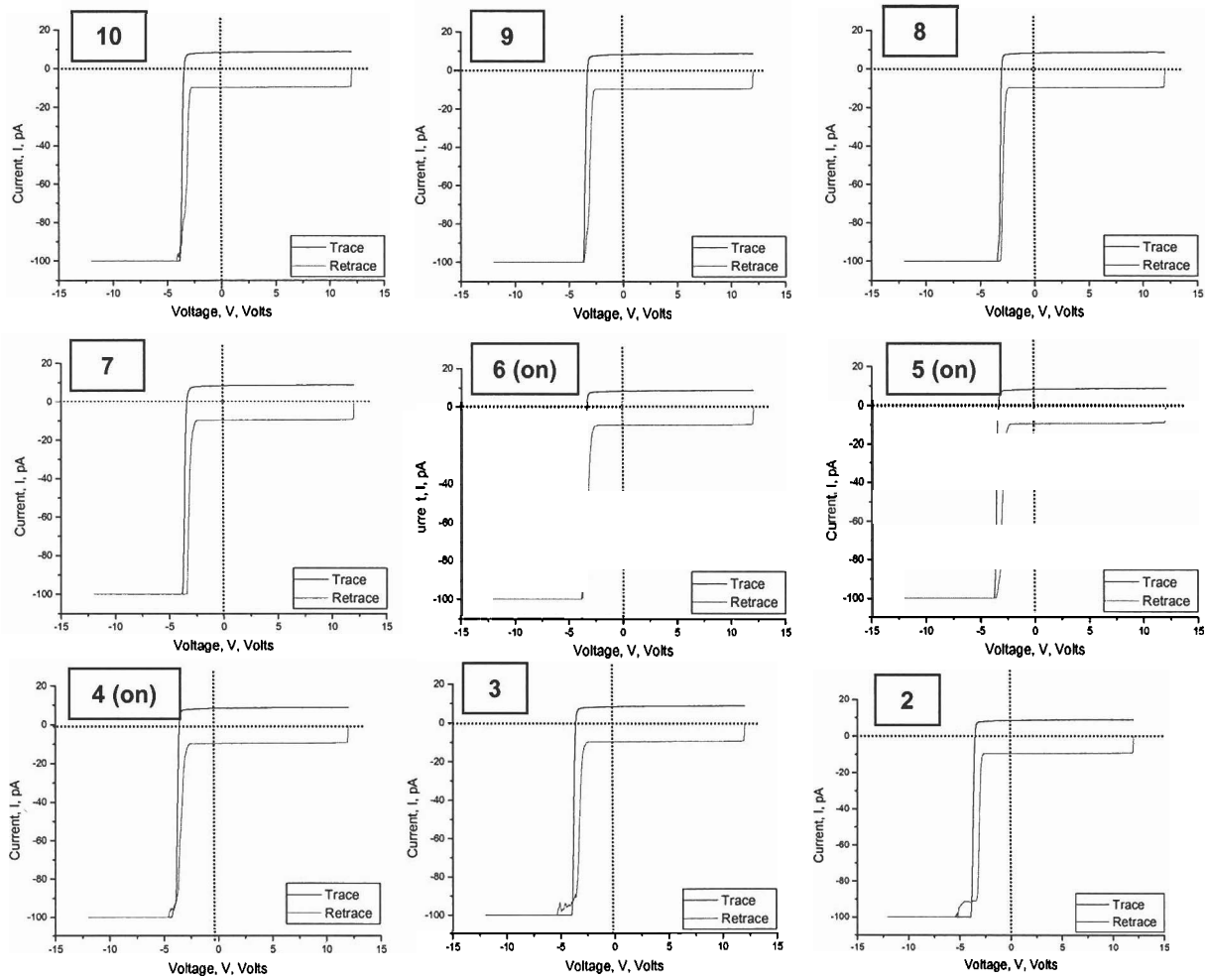

Note: All I-V spectra labeled (on) are taken on the conductive feature indicated.

M1840 I-V Spectra (Bottom Right Corner): 0.5μm × 2μm, 12V

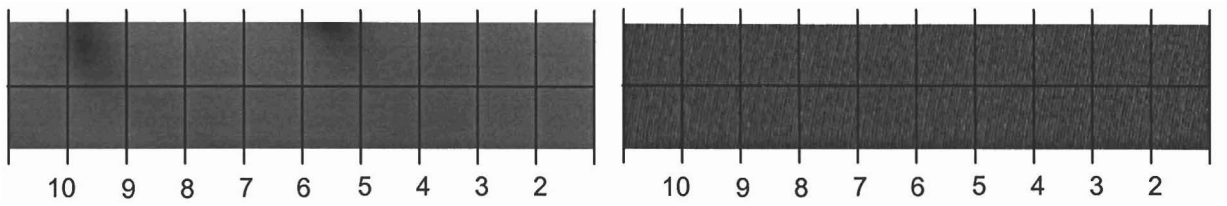

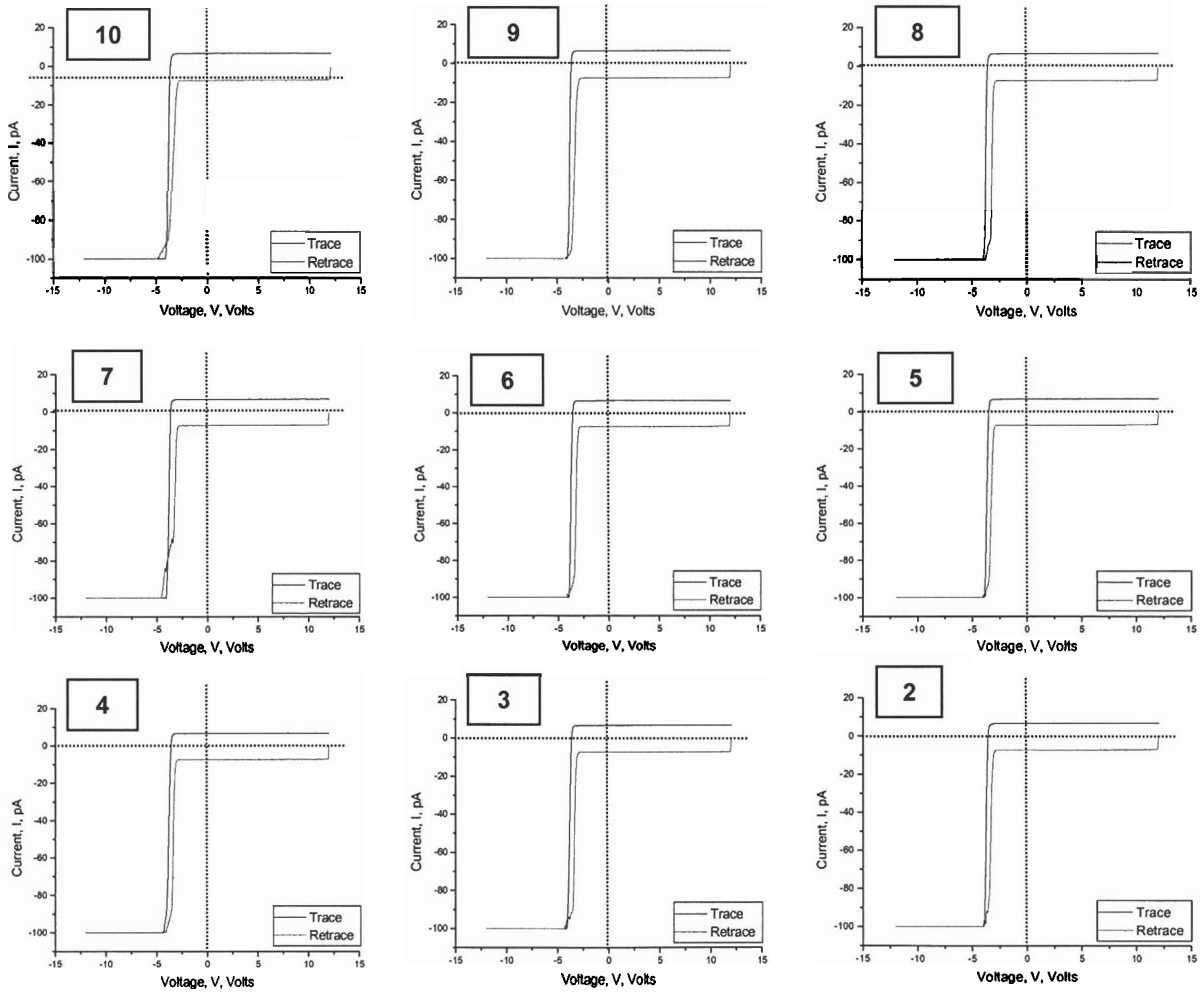

M1899 I-V Spectra (Upper Left Corner): 0.5μm × 2μm, 8V

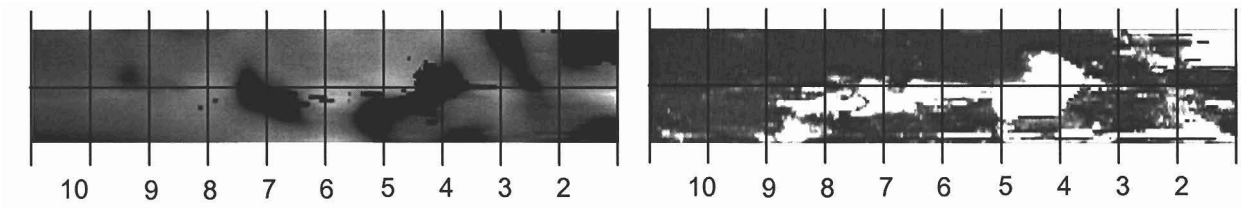

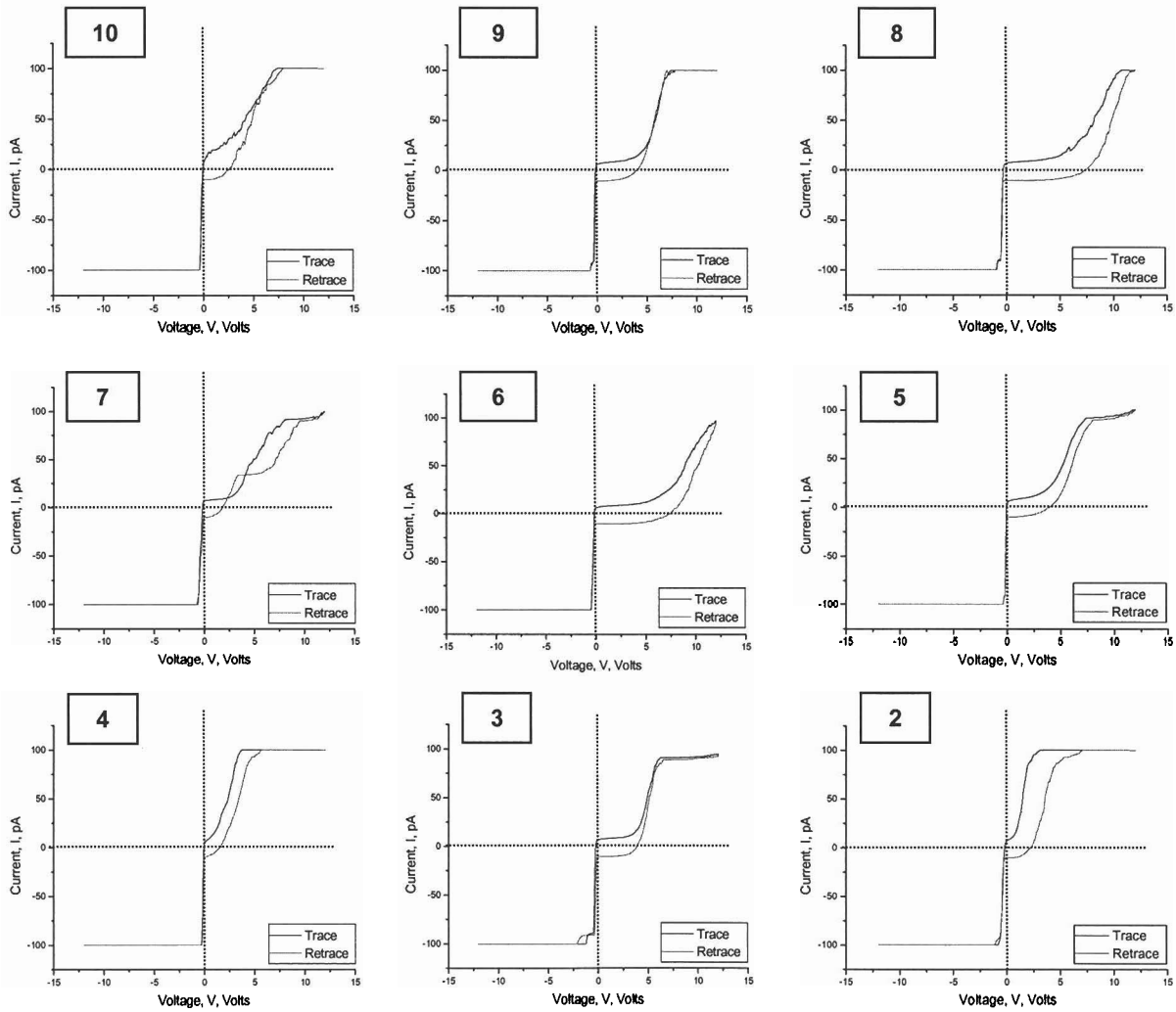

M1899 I-V Spectra (Lower Right Corner): 0.5μm × 2μm, 8V

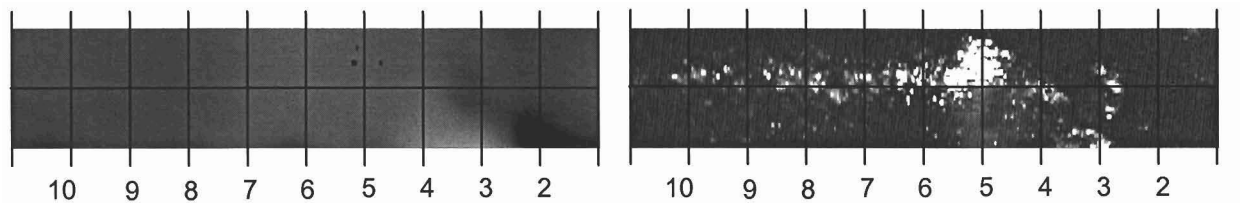

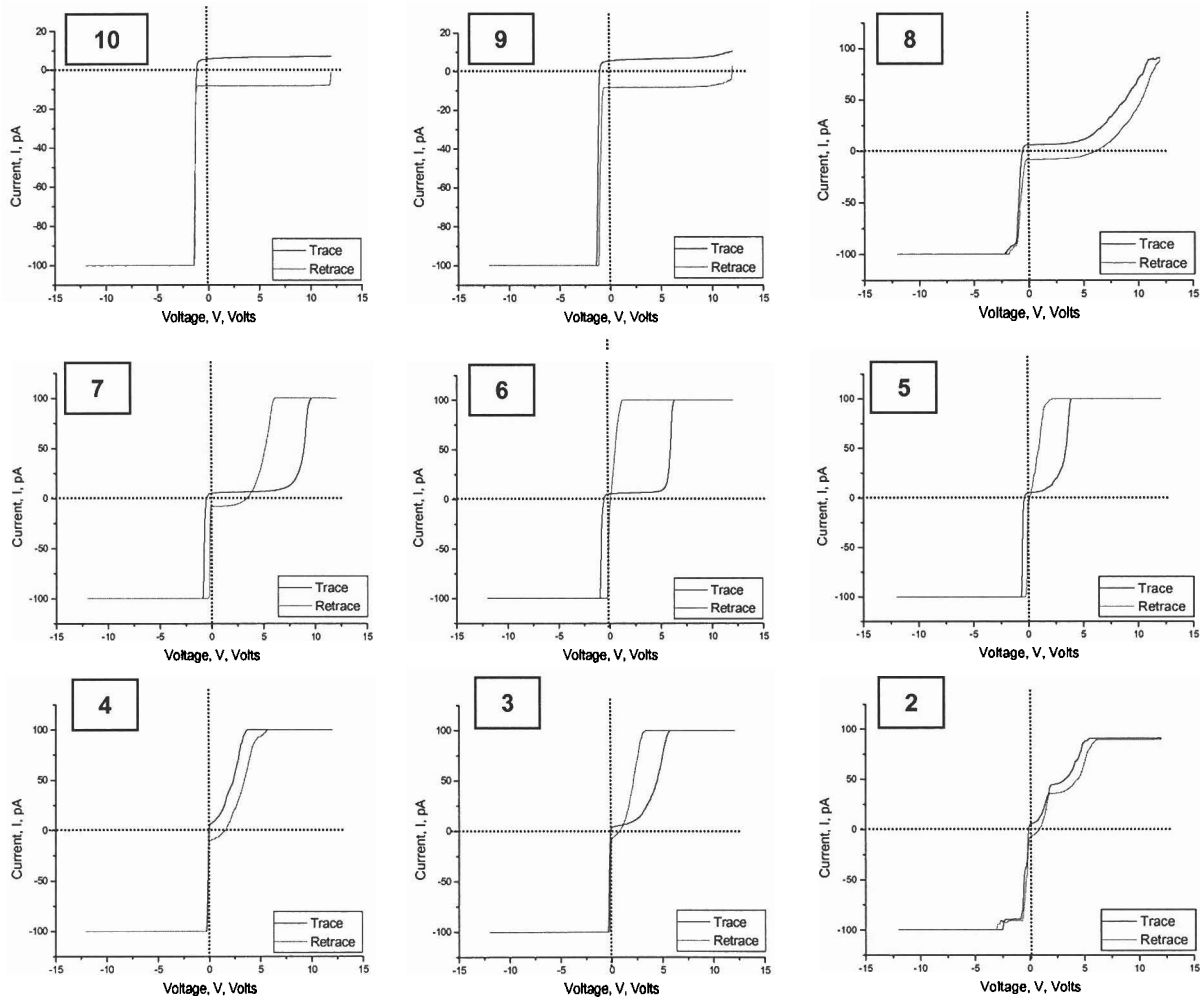

M1903 I-V Spectra (Upper Left Corner): 0.25μm × 1μm, 12V

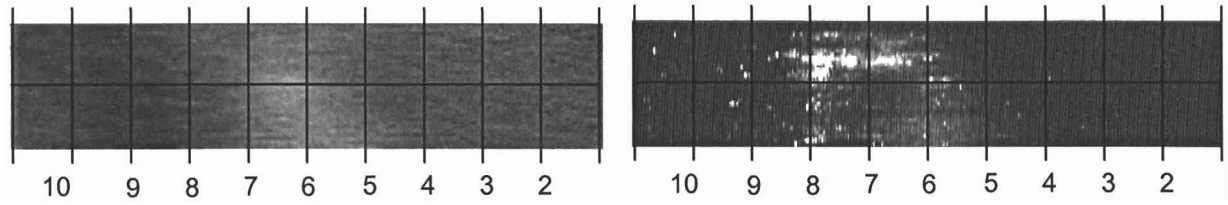

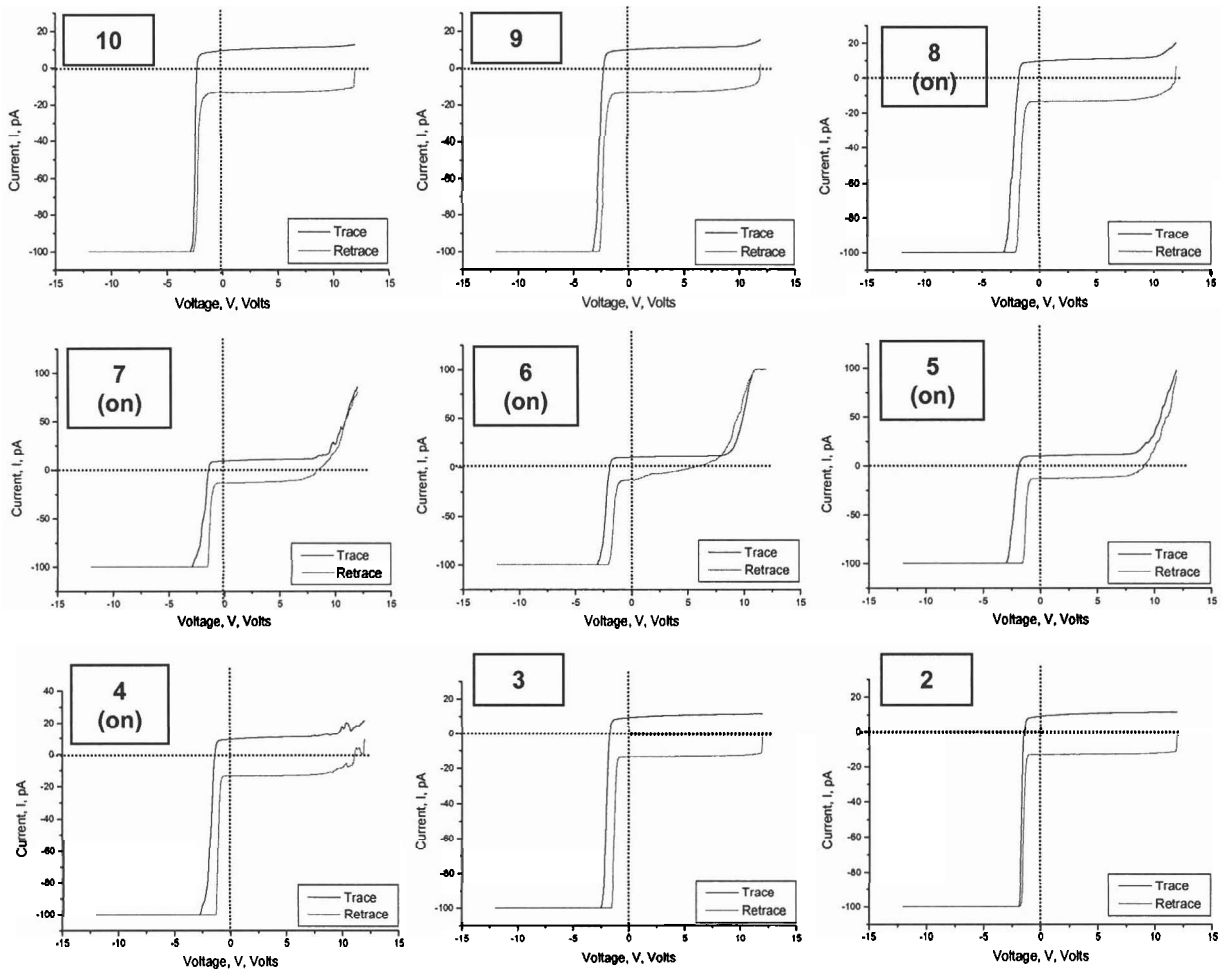

Appendix B.5

M1903 I-V Spectra (Lower Right Corner): 0.25μm × 1μm, 12V

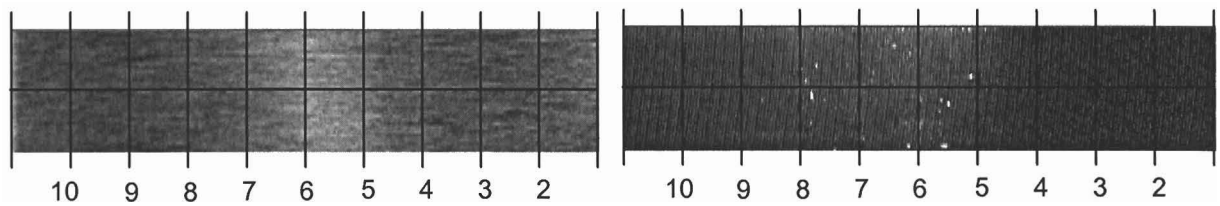

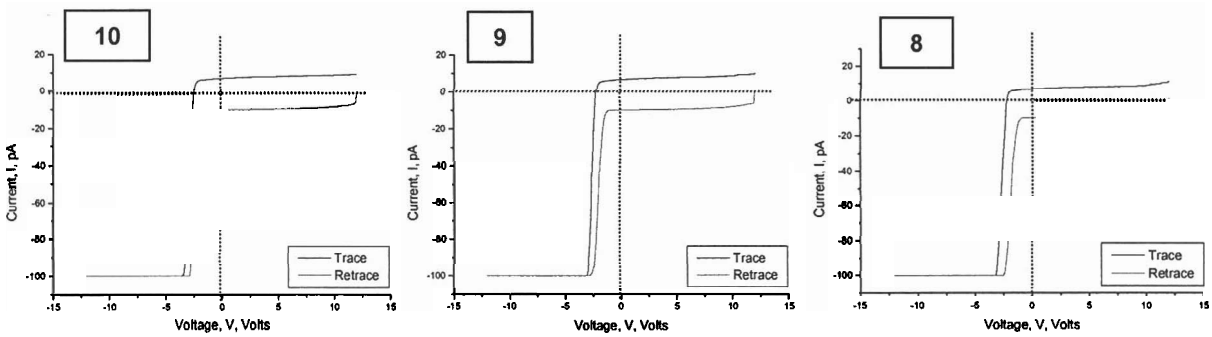

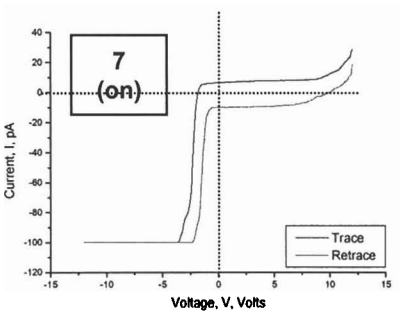

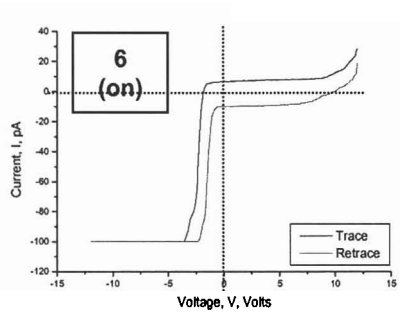

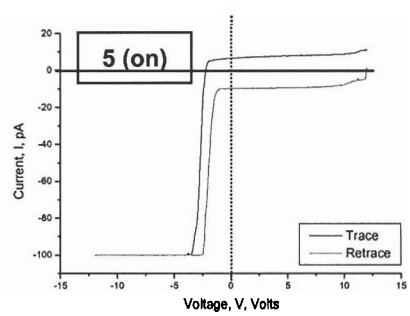

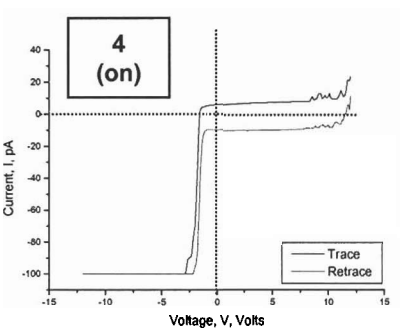

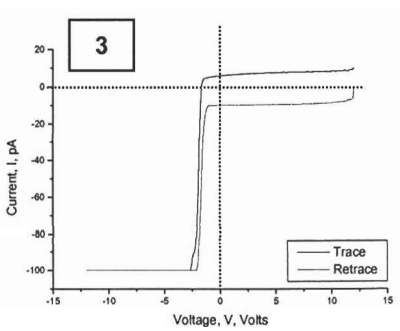

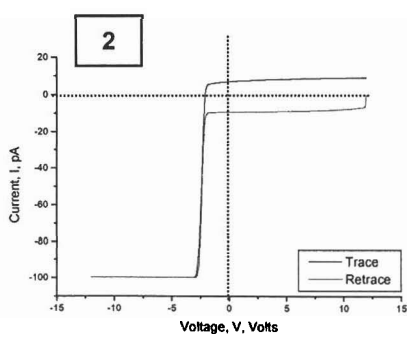

M1906 I-V Spectra (Upper Left Corner): 0.25μm × 1μm, 12V

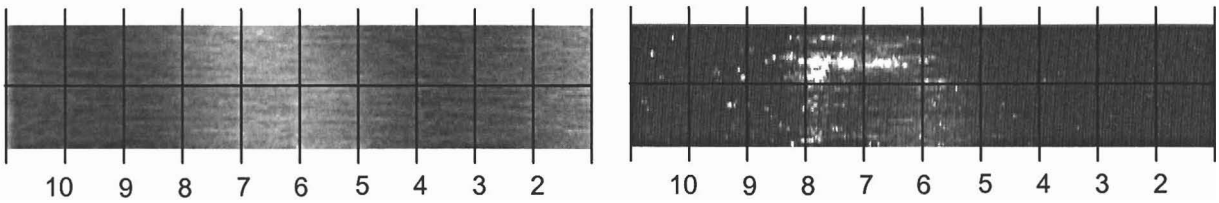

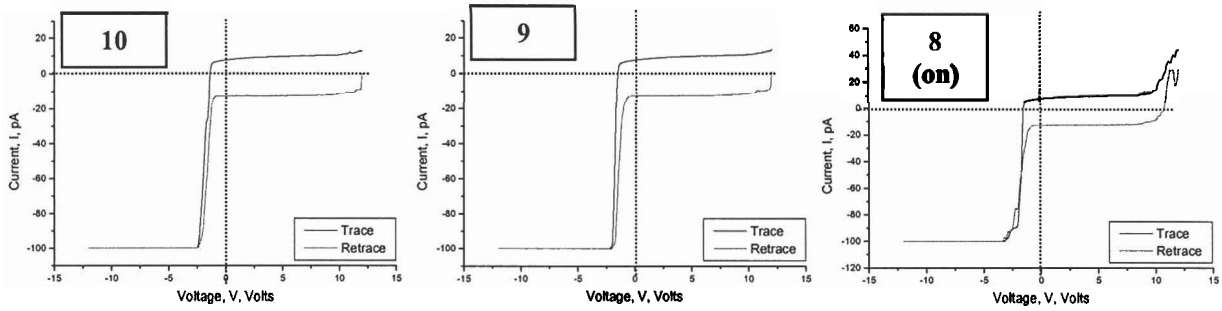

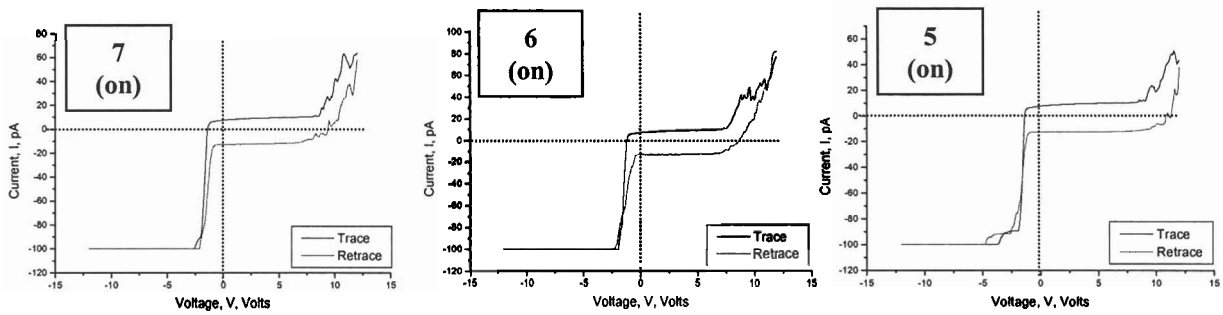

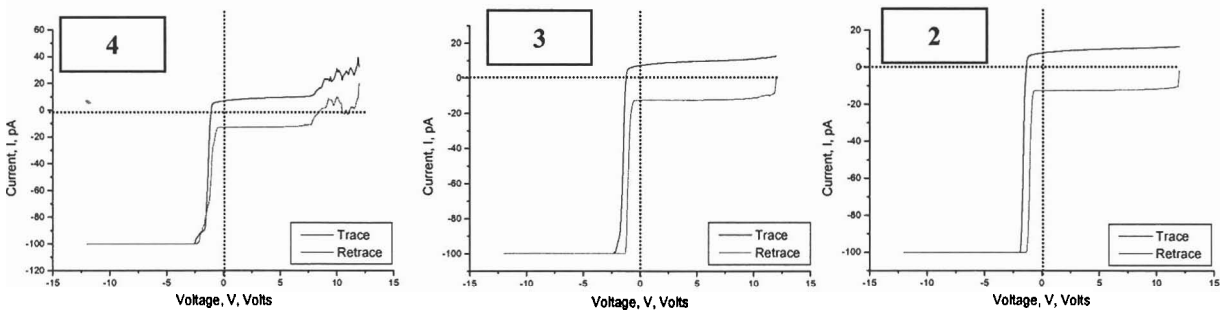

M1906 I-V Spectra (Lower Right Corner): 0.25μm × 1μm, 12V

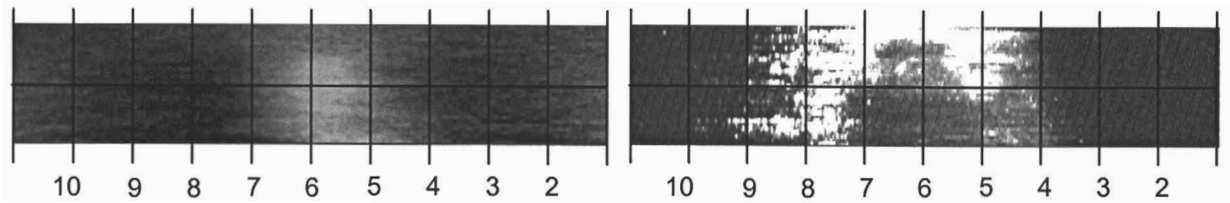

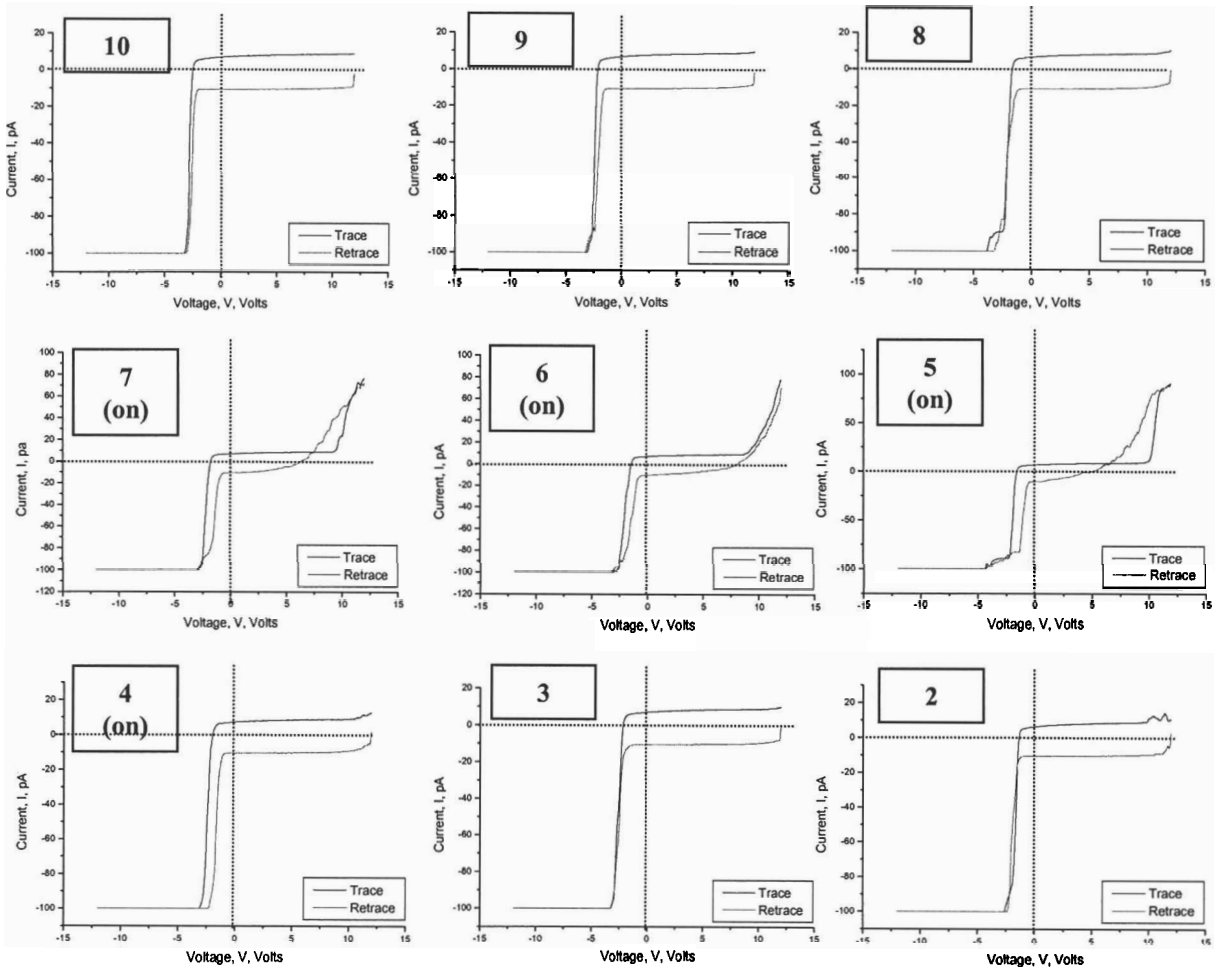

M1912 I-V Spectra (Upper Left Corner): 0.25μm × 1μm, 12V

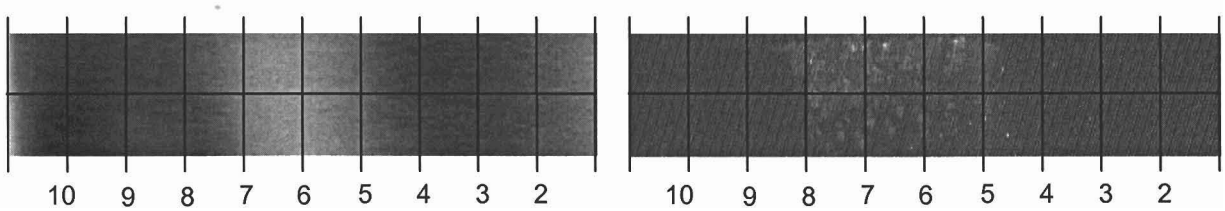

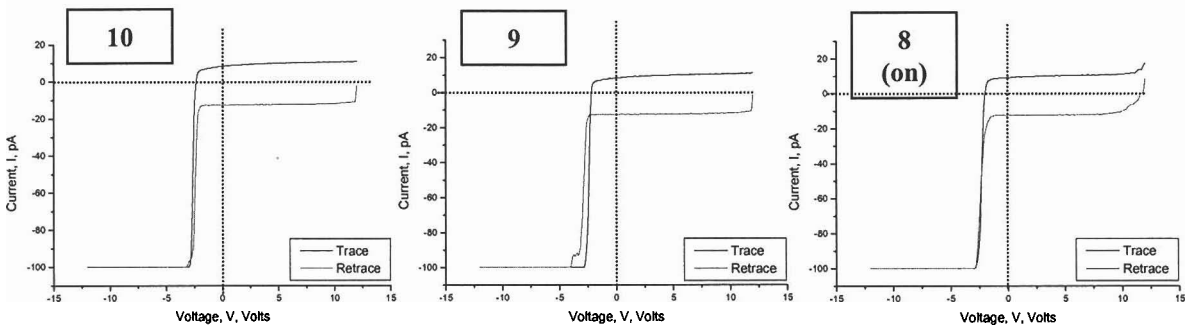

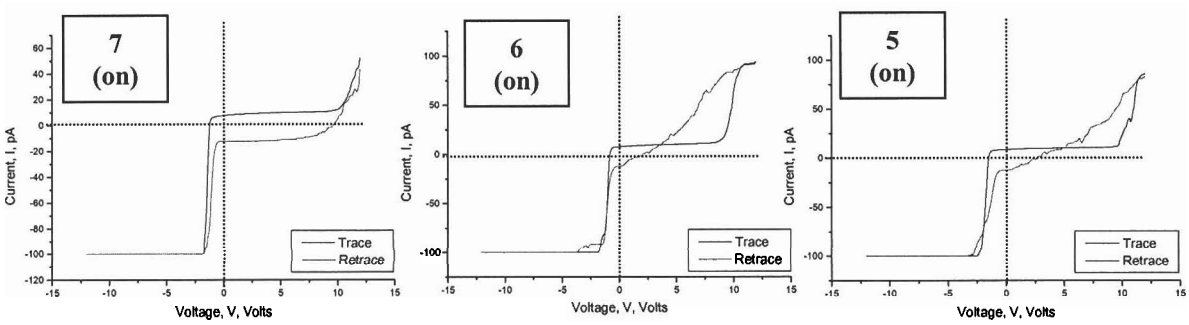

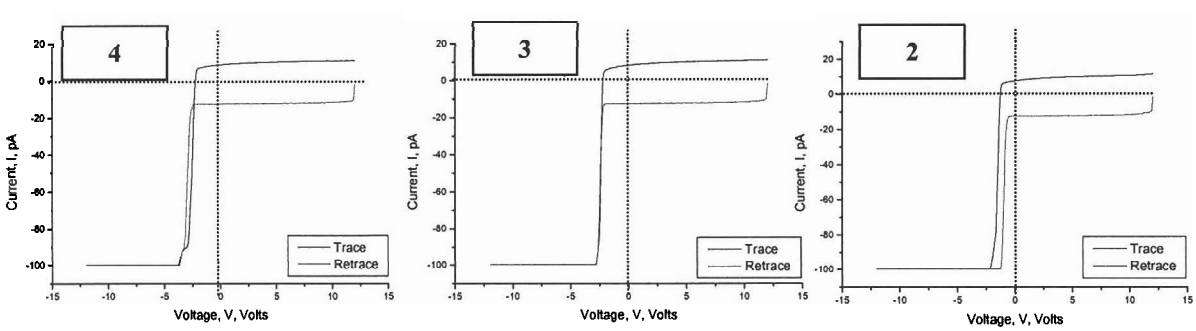

M1912 I-V Spectra (Lower Right Corner): 0.25μm × 1μm, 12V

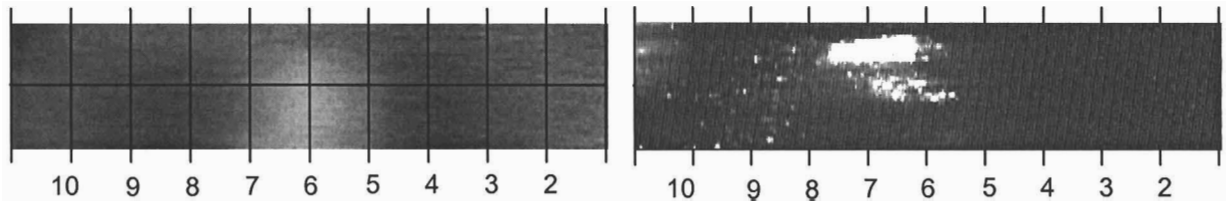

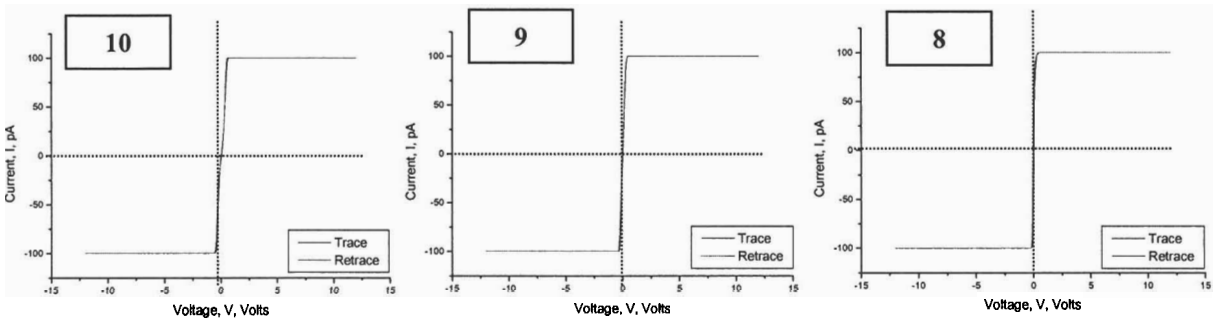

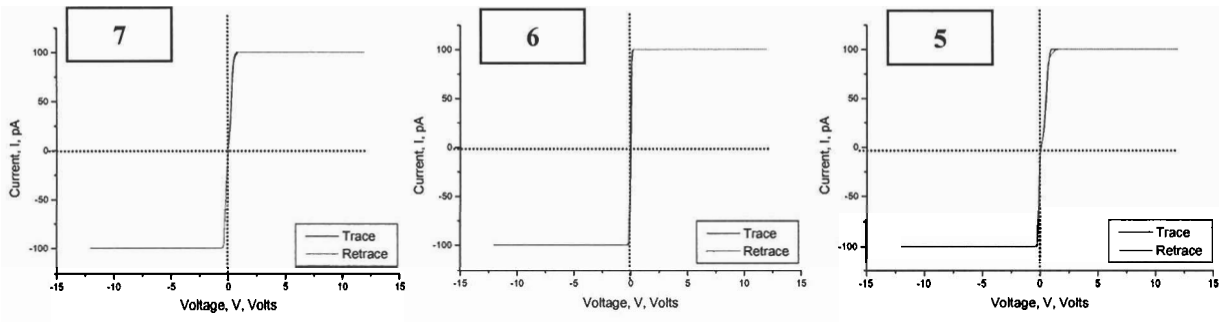

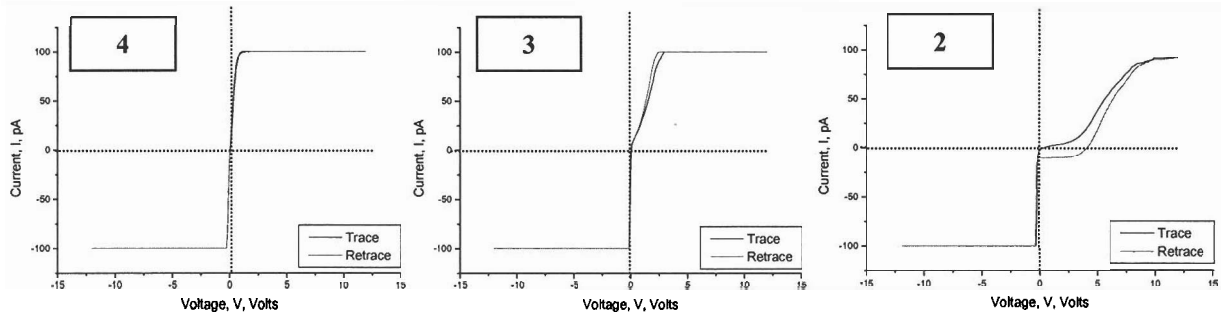

M1916 I-V Spectra (Upper Left Corner): 0.25μm × 1μm, 4V

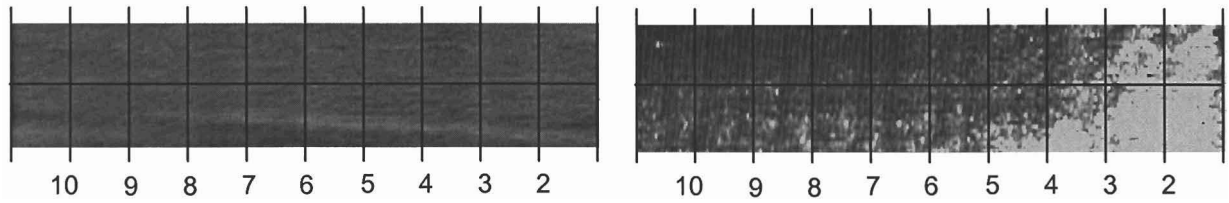

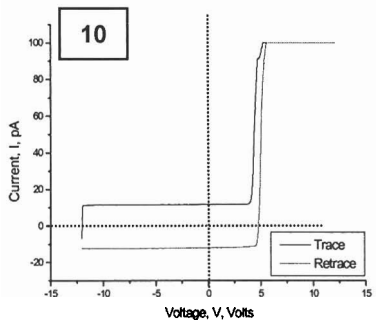

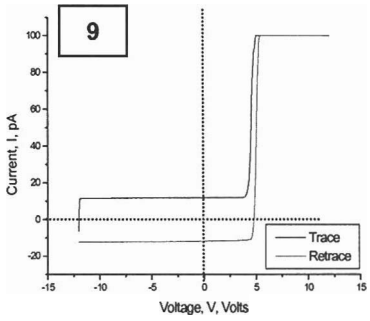

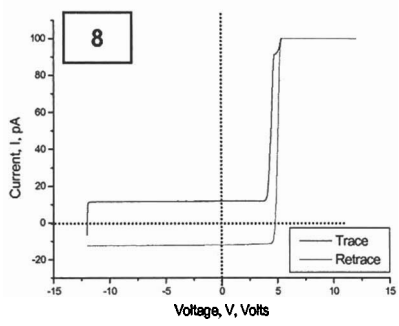

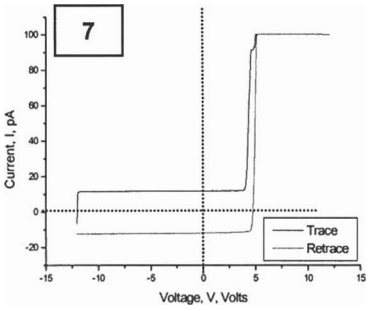

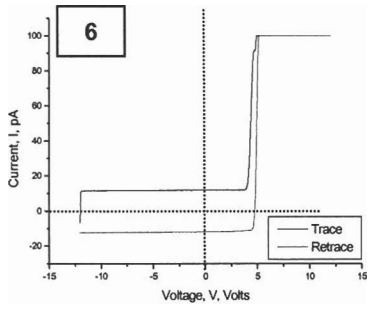

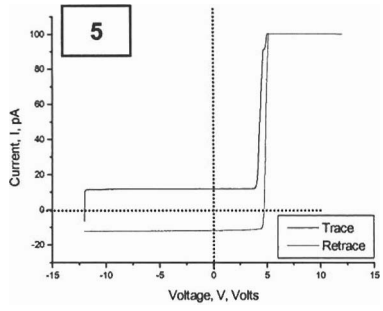

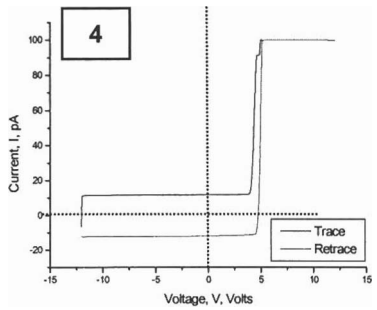

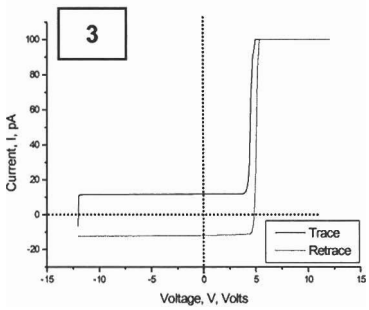

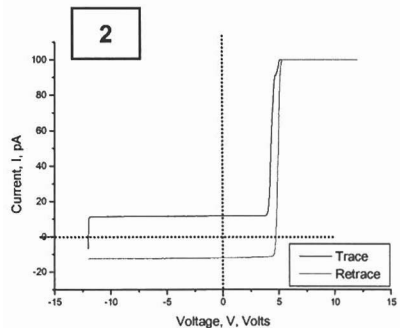

M1916 I-V Spectra (Lower Right Corner): 0.25μm × 1μm, 4V

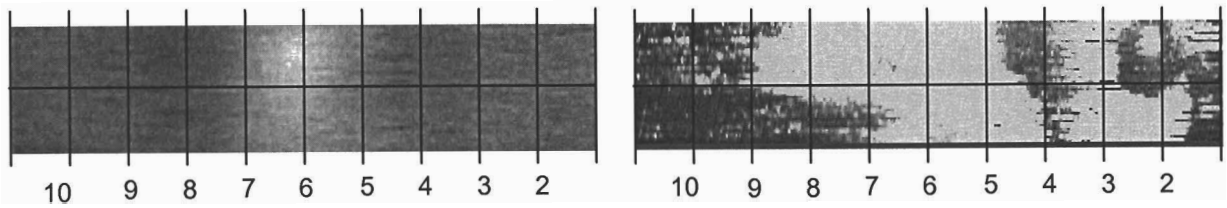

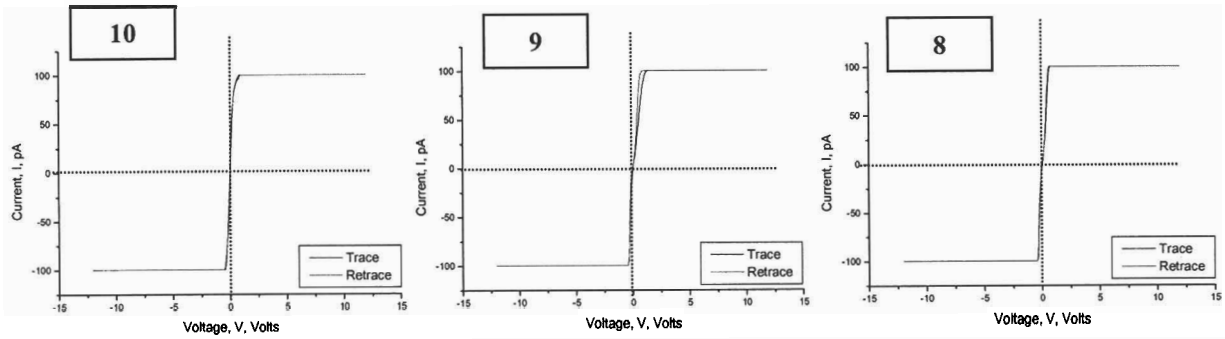

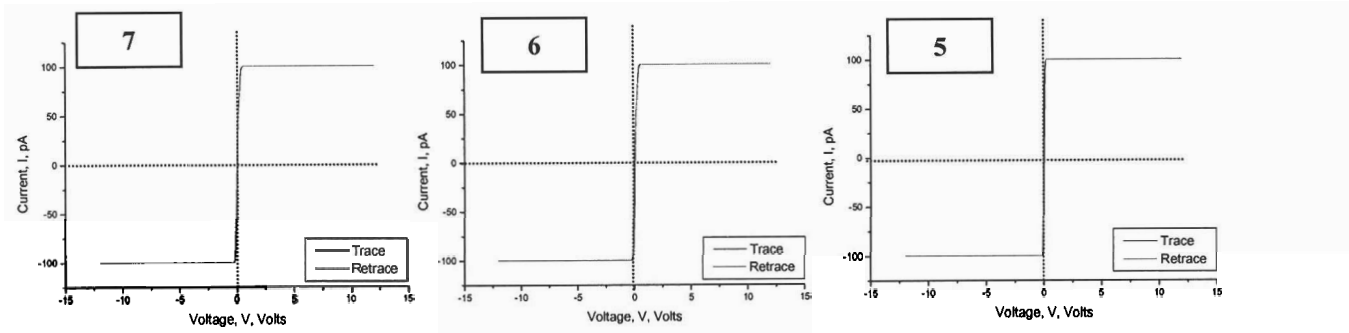

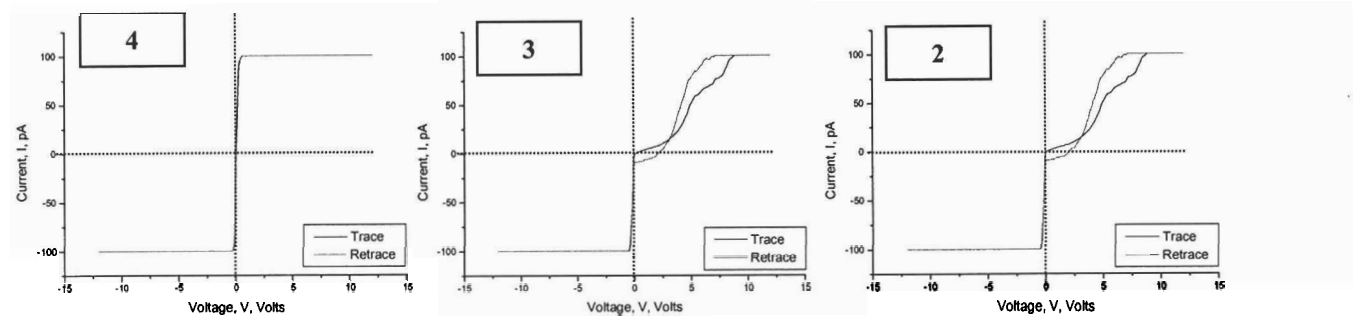

M1921 I-V Spectra (Upper Left Corner): 0.5μm × 2μm, 12V

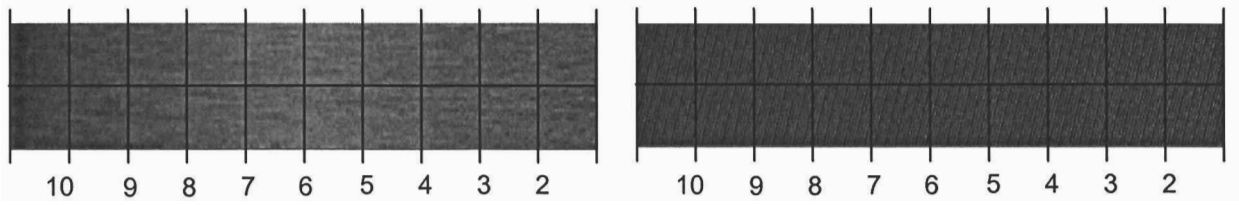

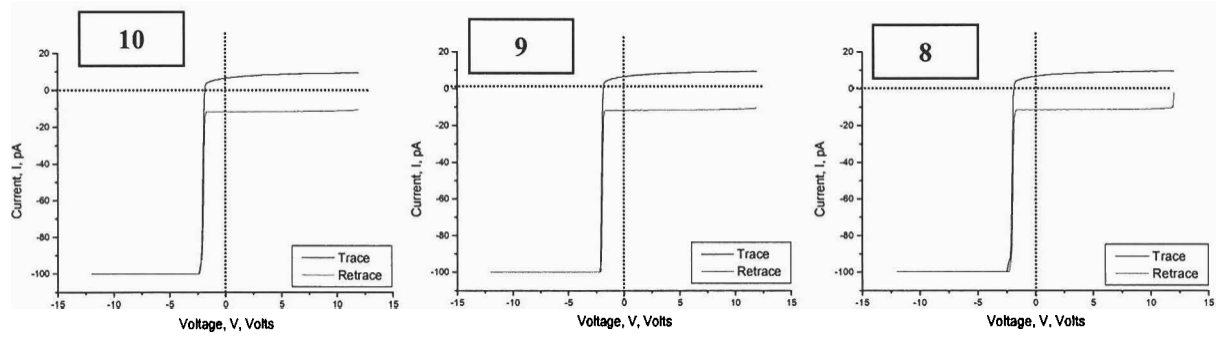

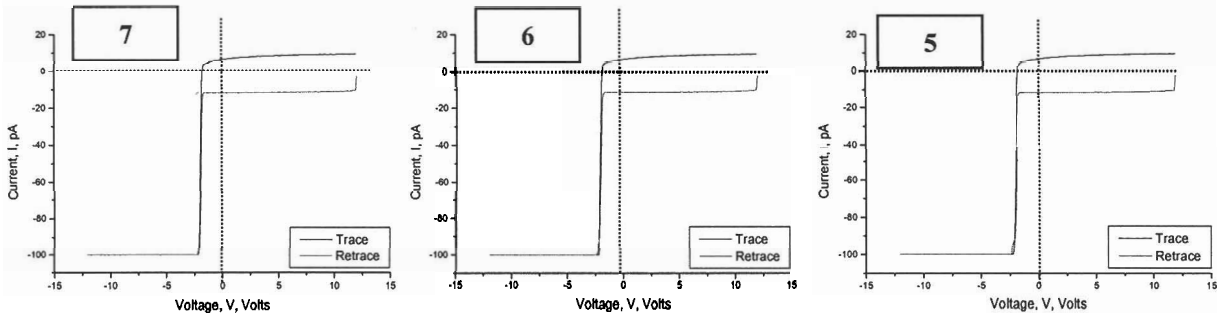

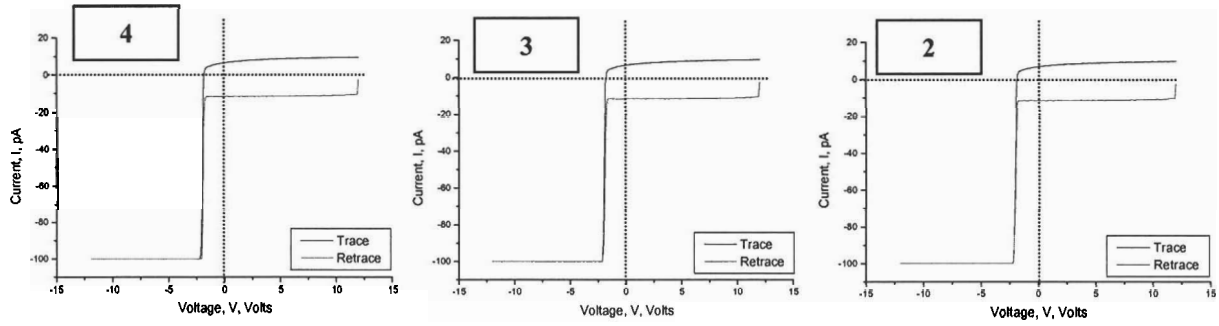

M1921 I-V Spectra (Lower Right Corner): 0.5μm × 2μm, 12V

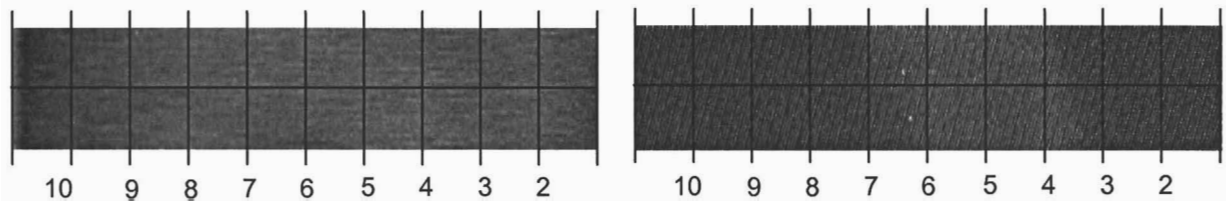

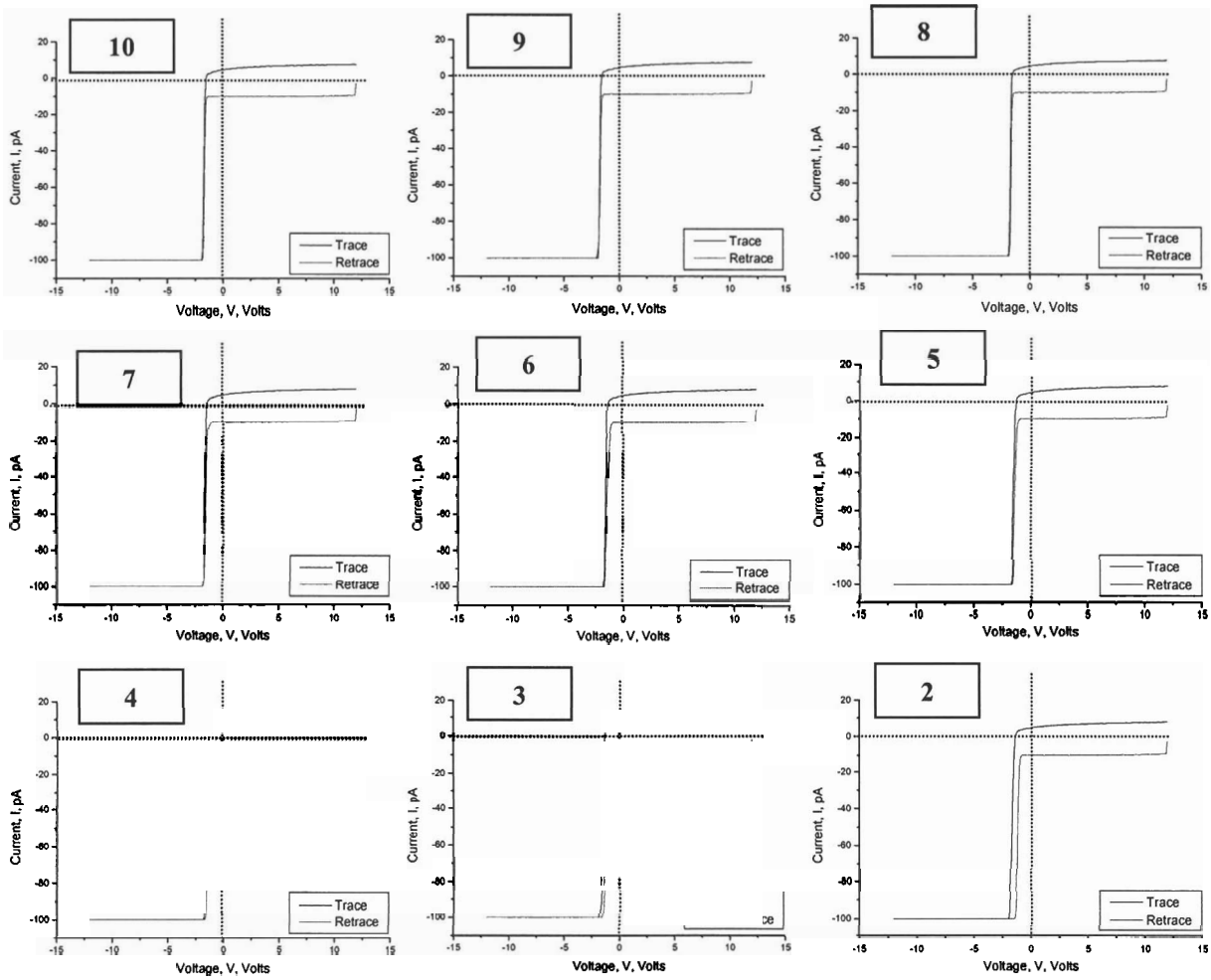

M1966 I-V Spectra (Upper Left Corner): 0.25μm × 1μm, 5V

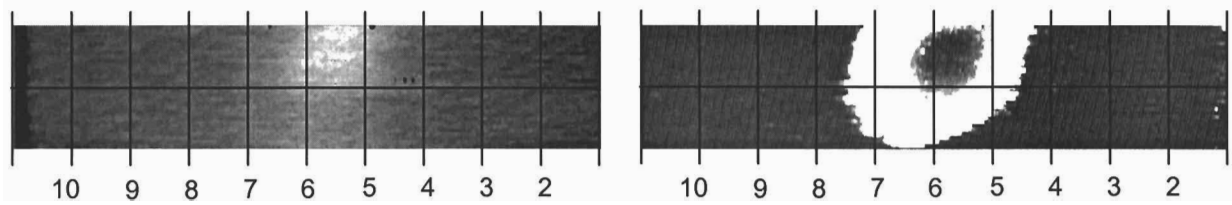

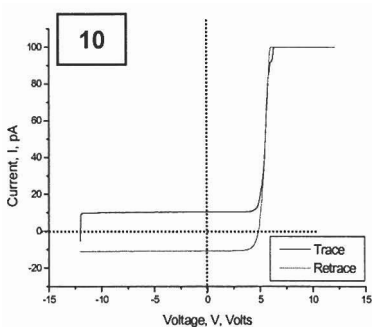

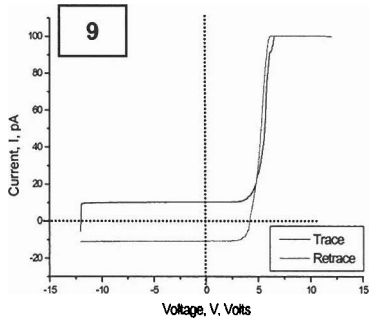

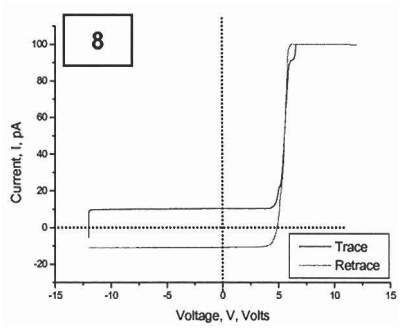

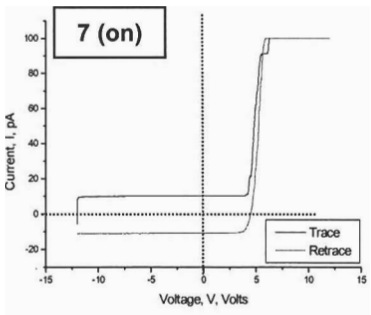

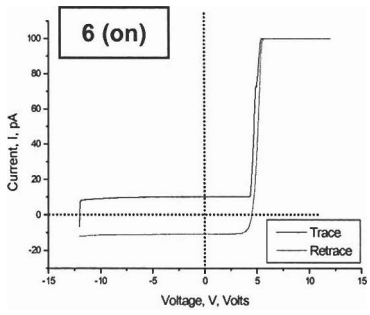

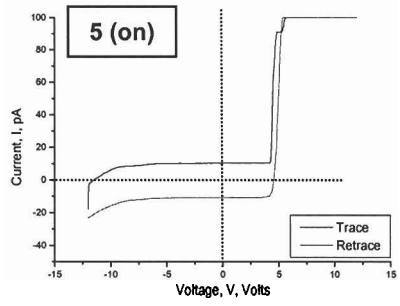

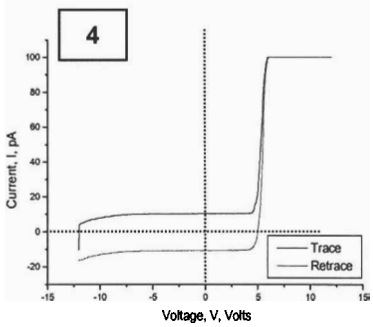

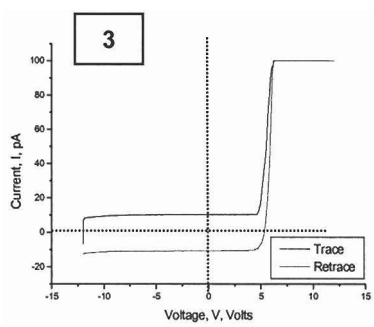

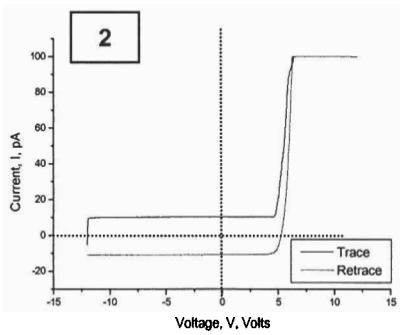

M1966 I-V Spectra (Lower Right Corner): 0.25μm × 1μm, 5V

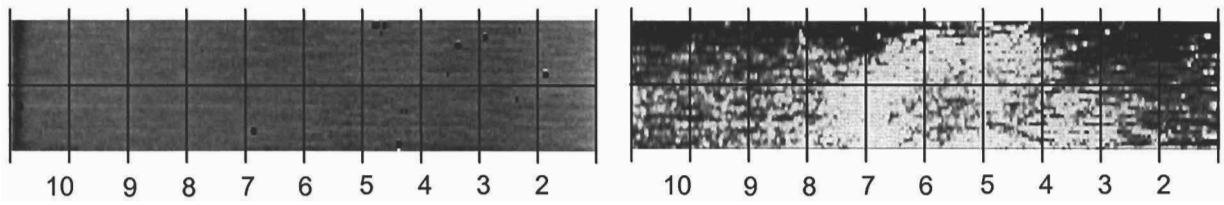

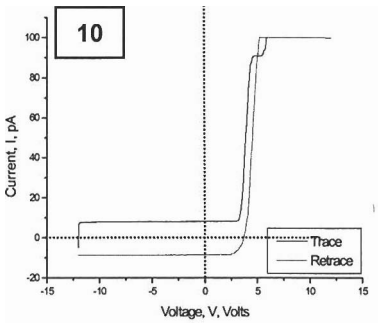

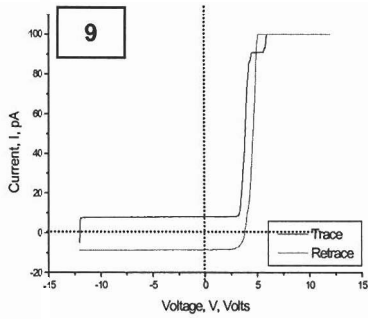

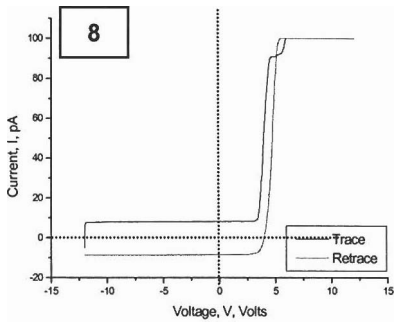

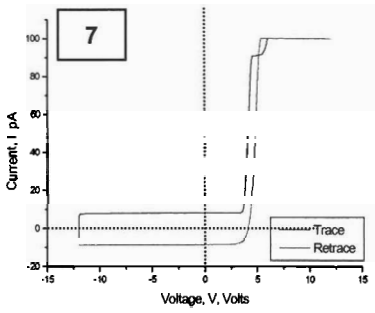

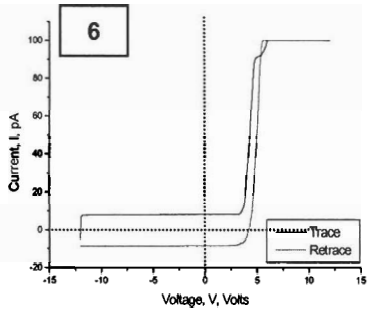

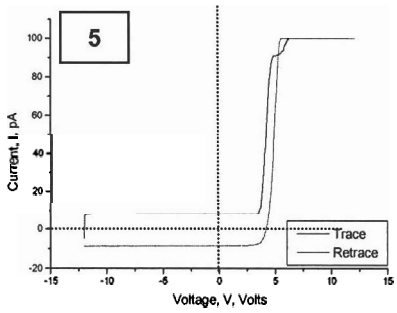

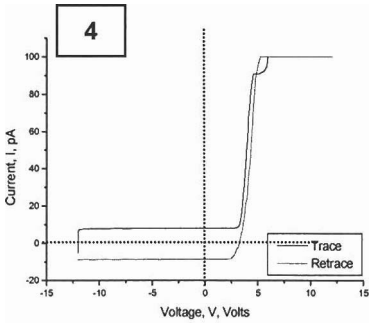

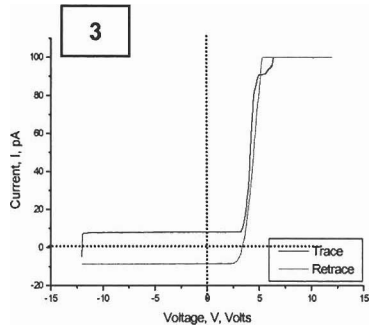

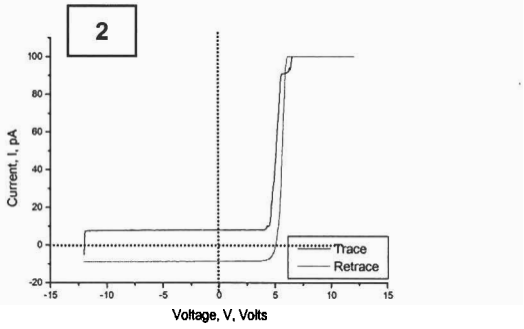

M1966b I-V Spectra (Upper Left Corner): 0.25μm × 1μm, 2V

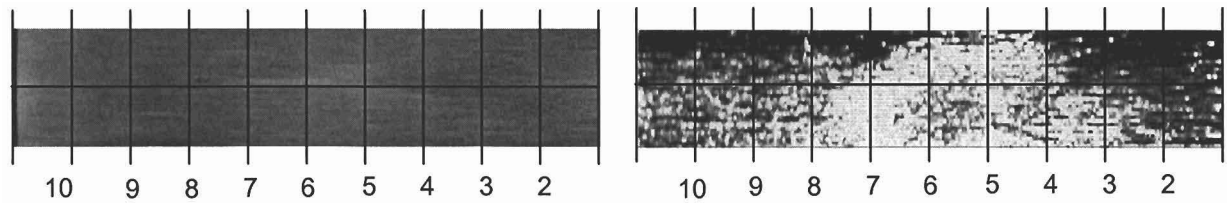

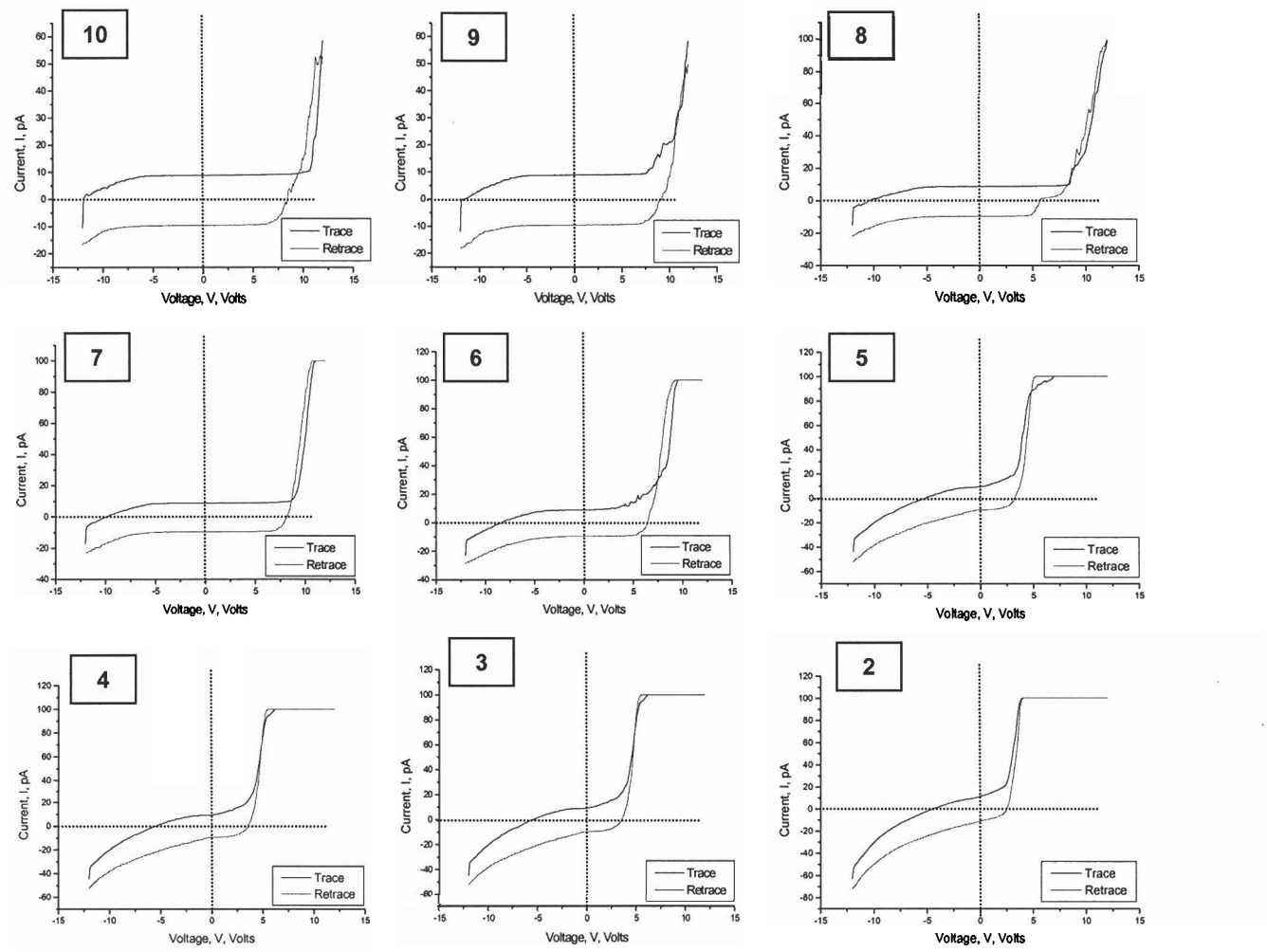

M1966b I-V Spectra (Lower Right Corner): 0.25μm × 1μm, 2V

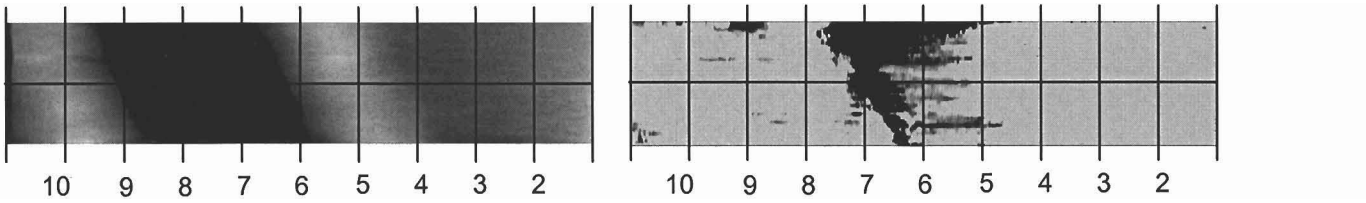

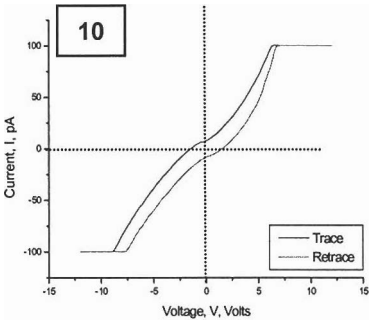

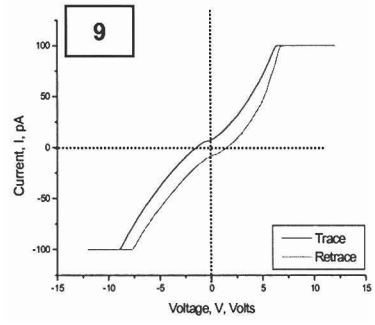

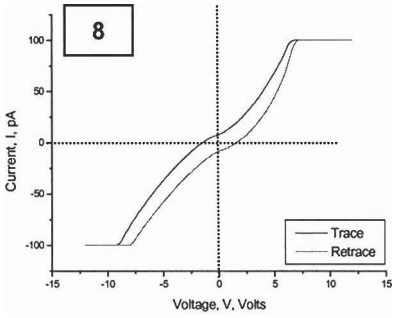

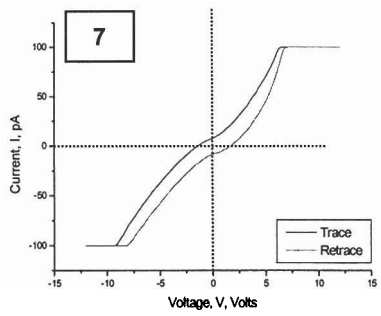

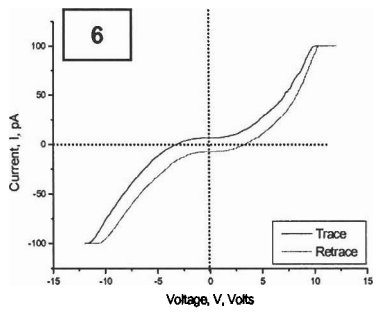

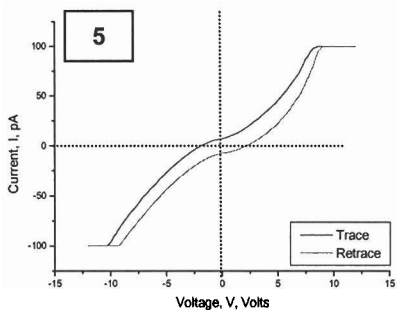

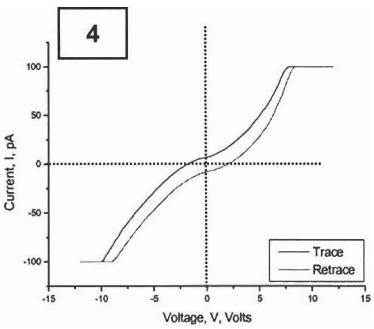

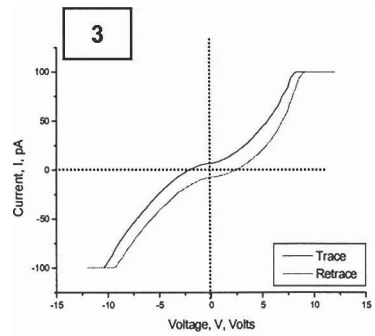

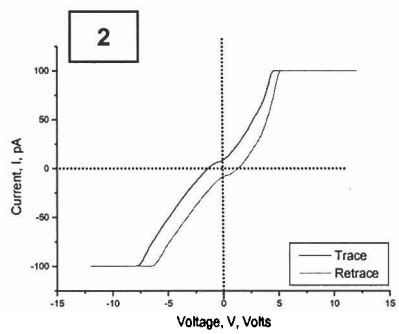

M2004 I-V Spectra (Upper Left Corner): 0.25μm × 1μm, 5V

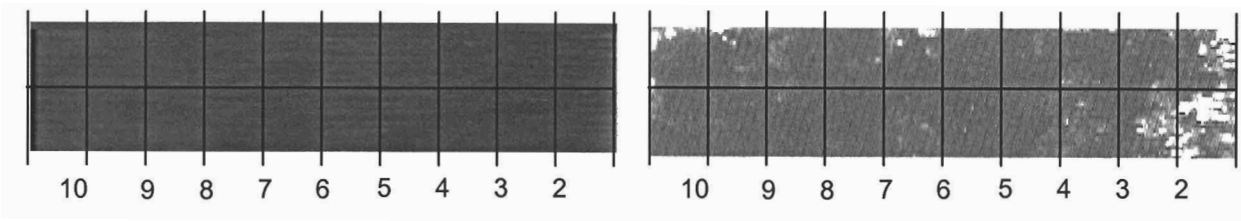

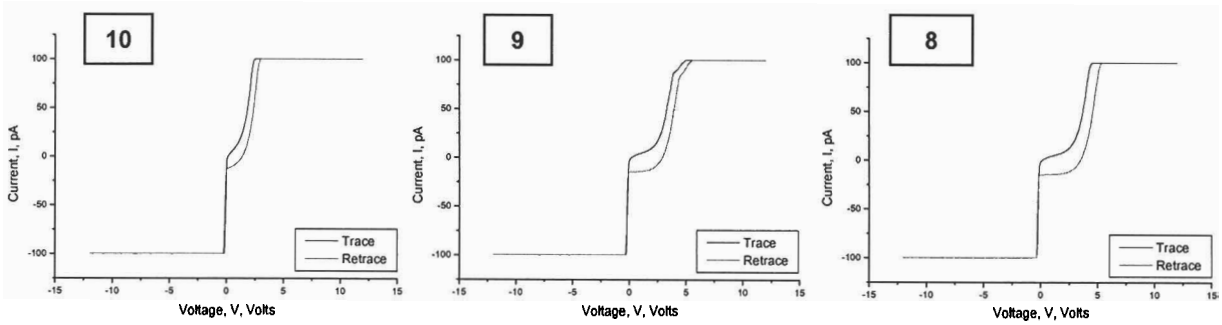

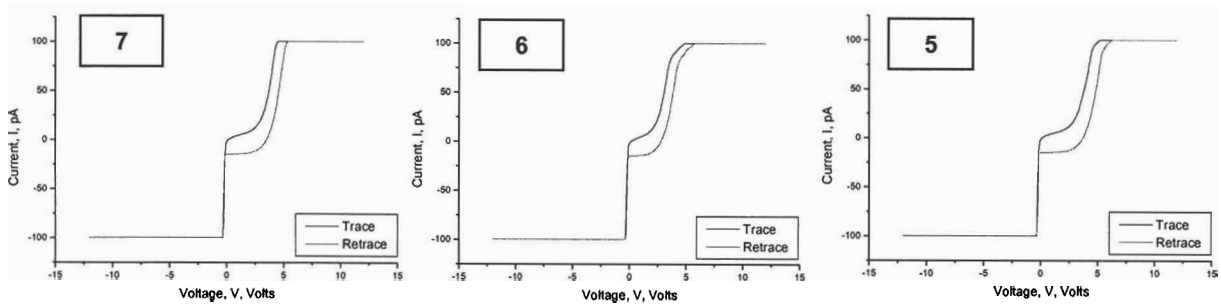

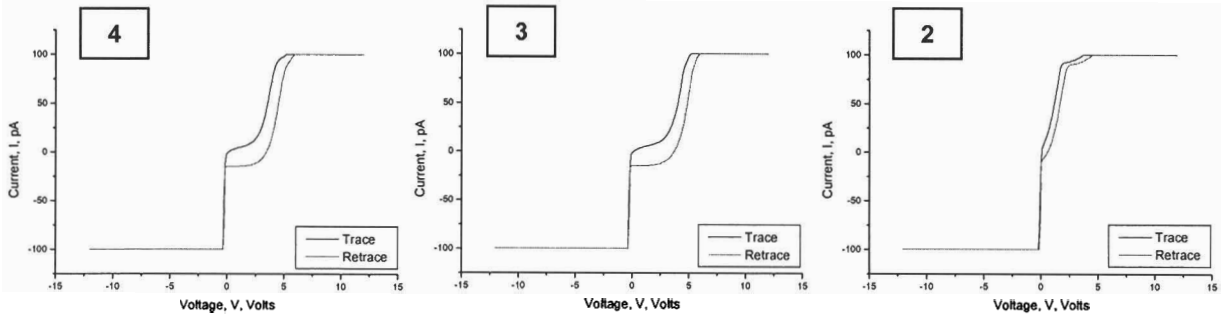

M2004 I-V Spectra (Lower Right Corner): 0.25μm × 1μm, 5V

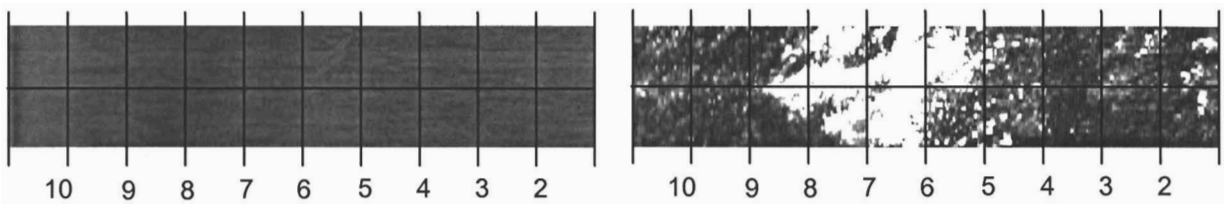

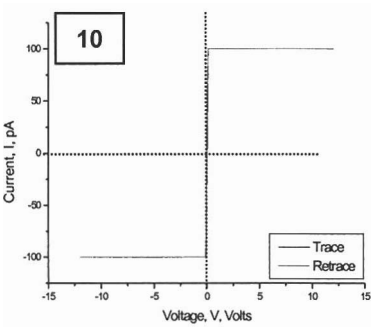

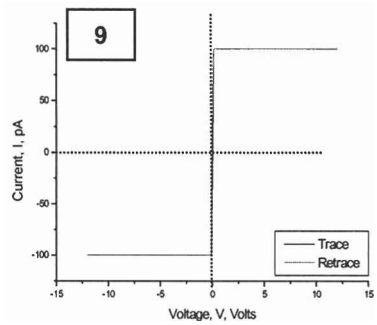

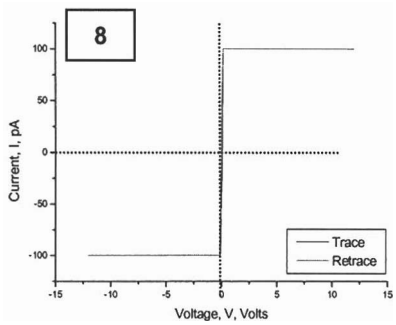

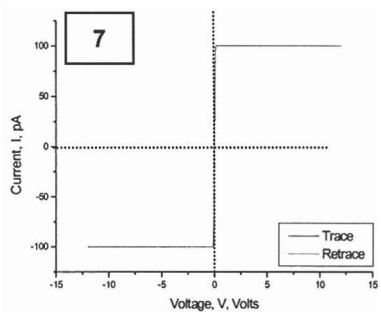

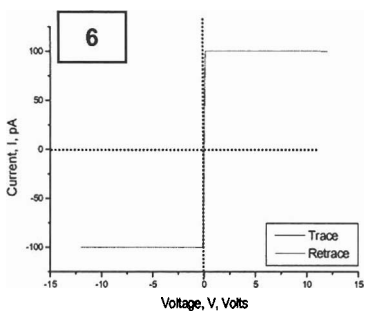

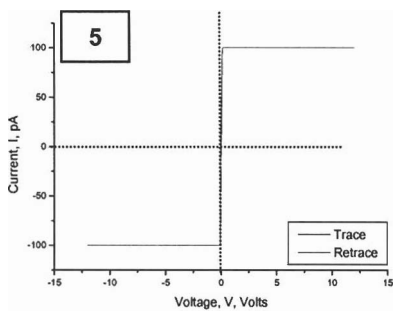

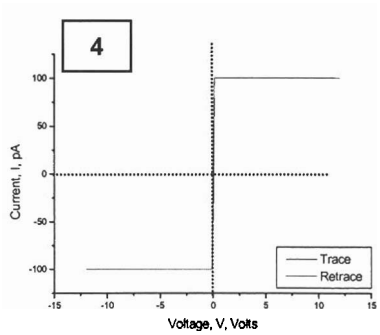

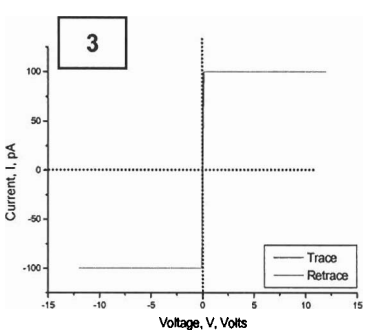

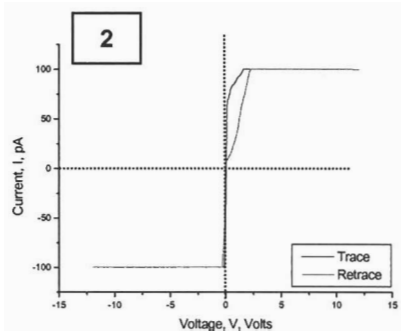

M2009 I-V Spectra (Upper Left Corner): 0.25μm × 1μm, 10V

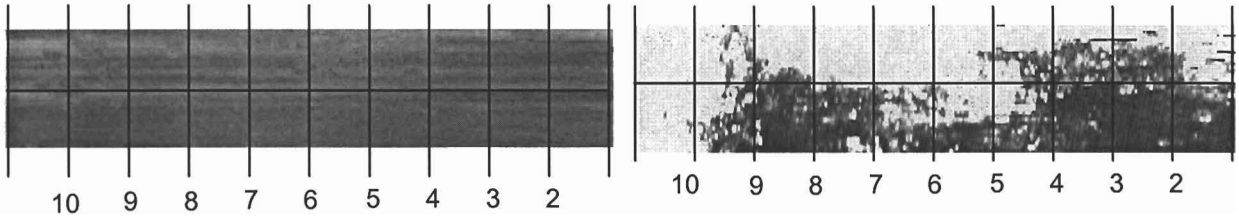

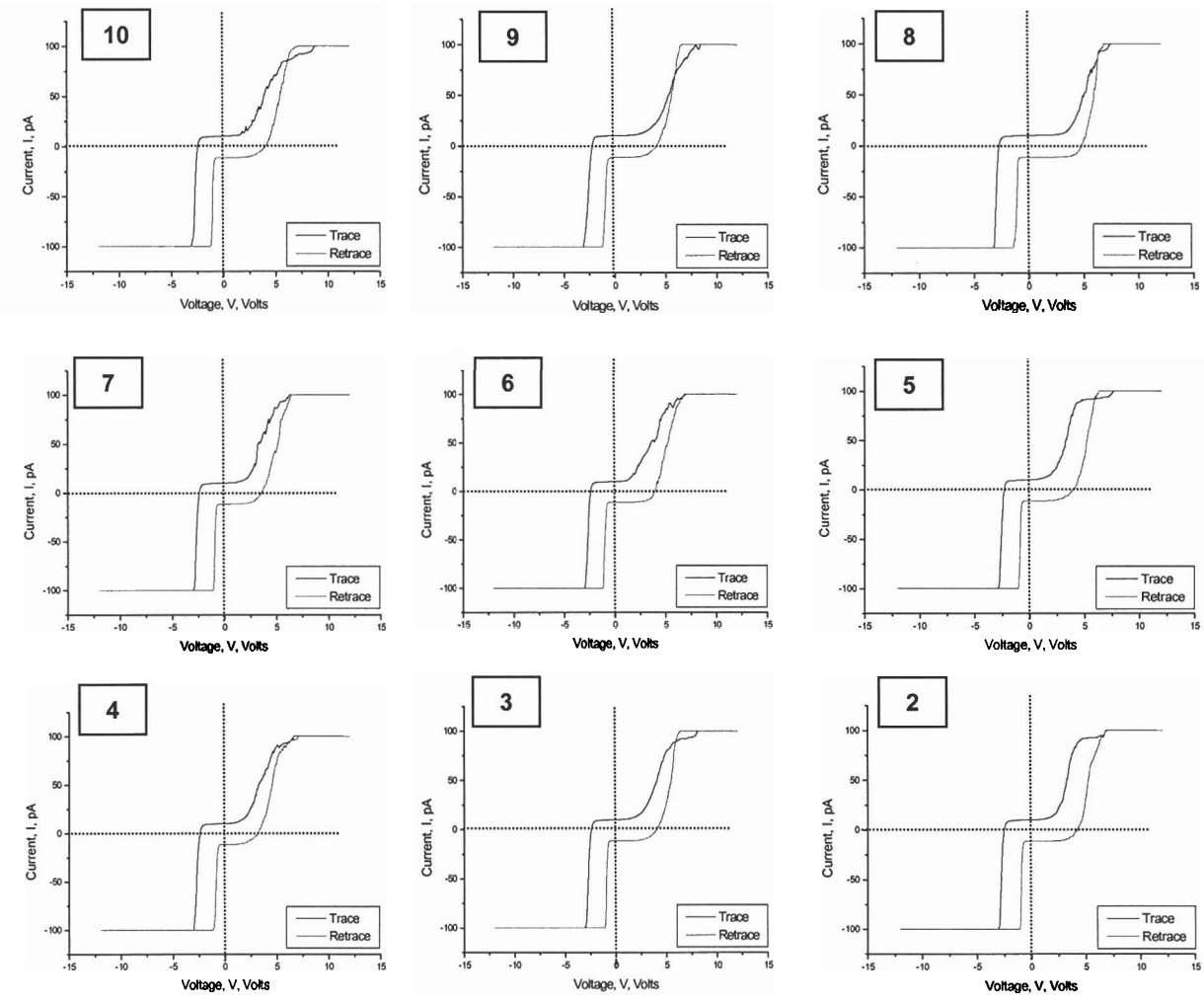

M2009 I-V Spectra (Lower Right Corner): 0.25μm × 1μm, 10V

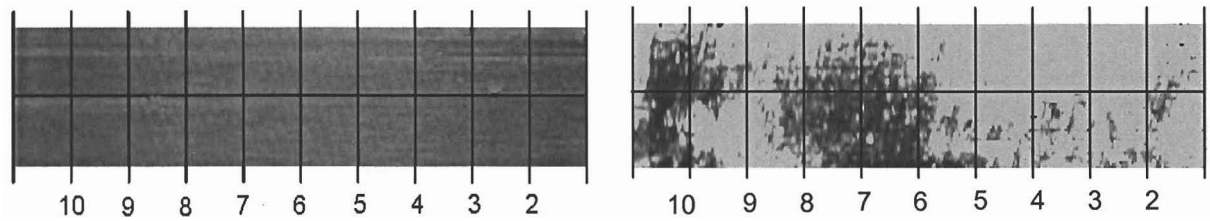

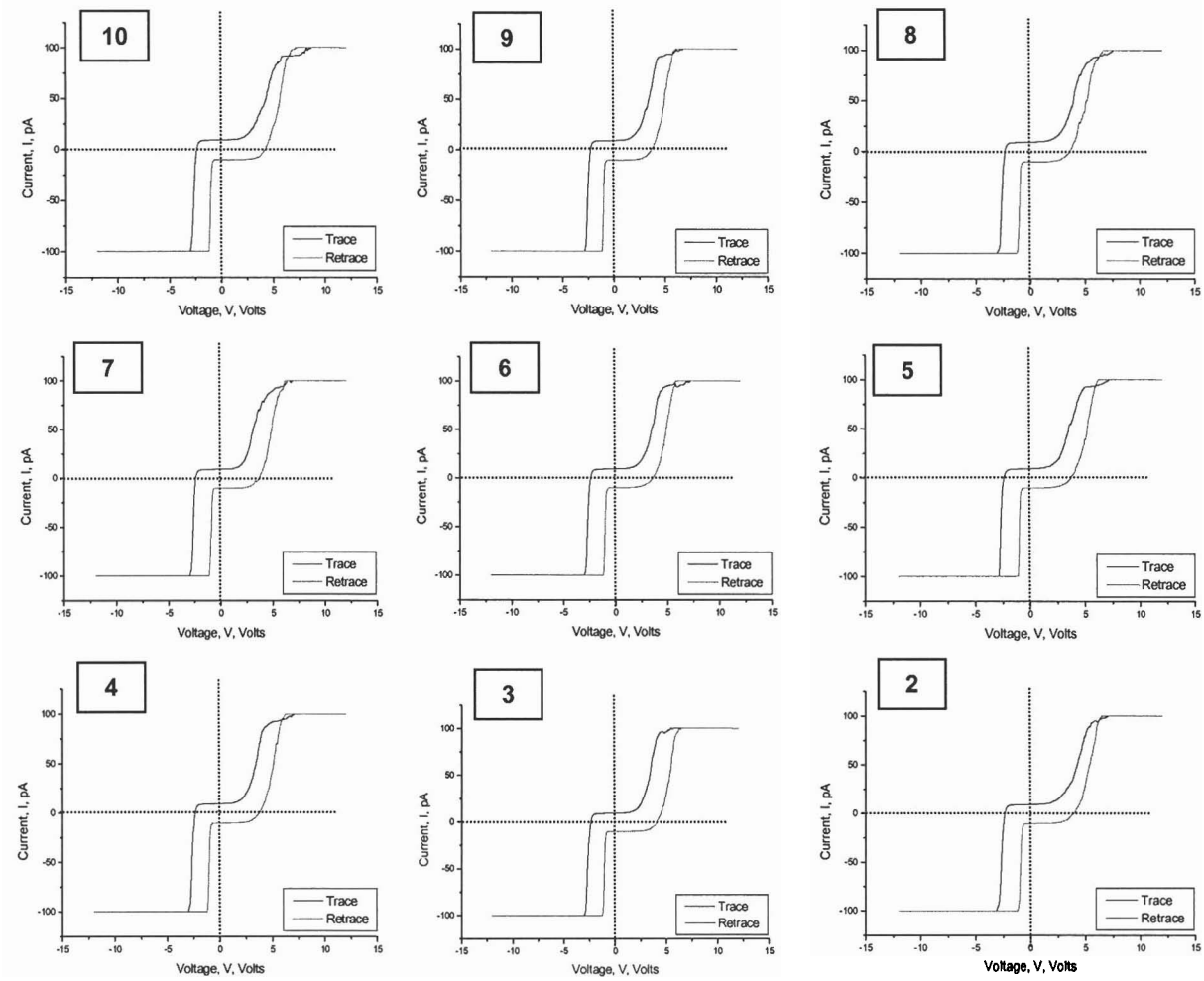

M2024 I-V Spectra (Upper Left Corner): 0.25μm × 1μm, 6V

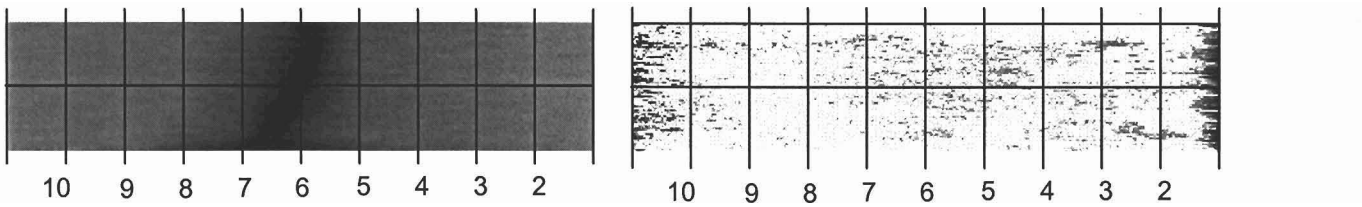

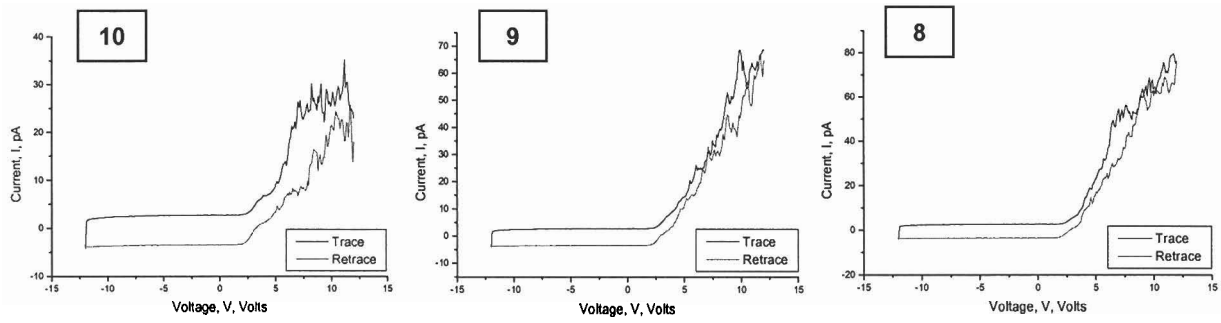

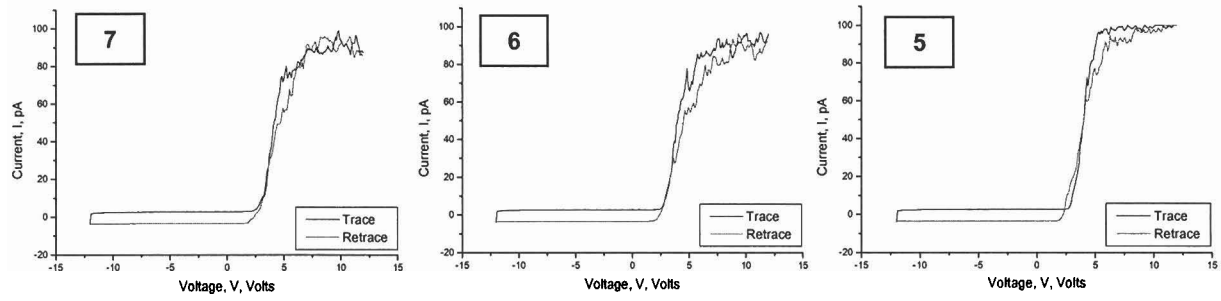

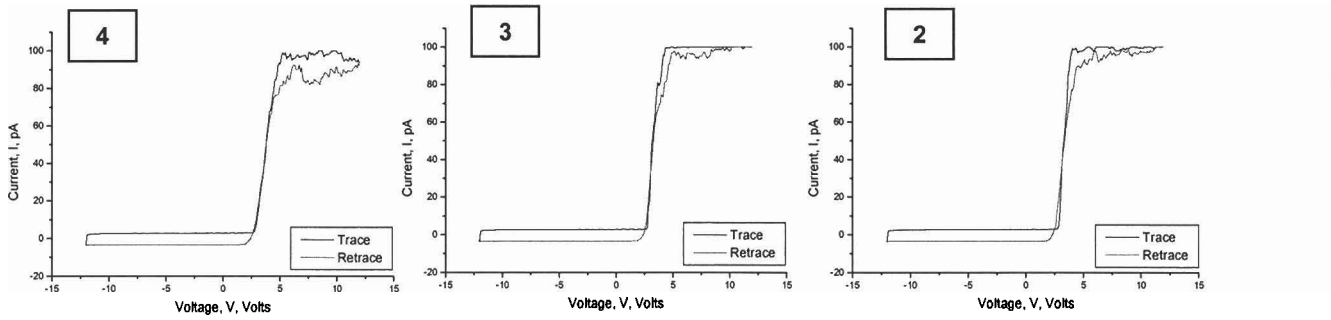

M2024 I-V Spectra (Lower Right Corner): 0.25μm × 1μm, 12V

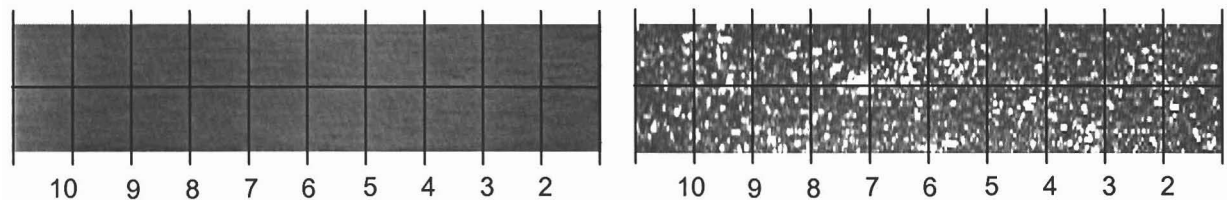

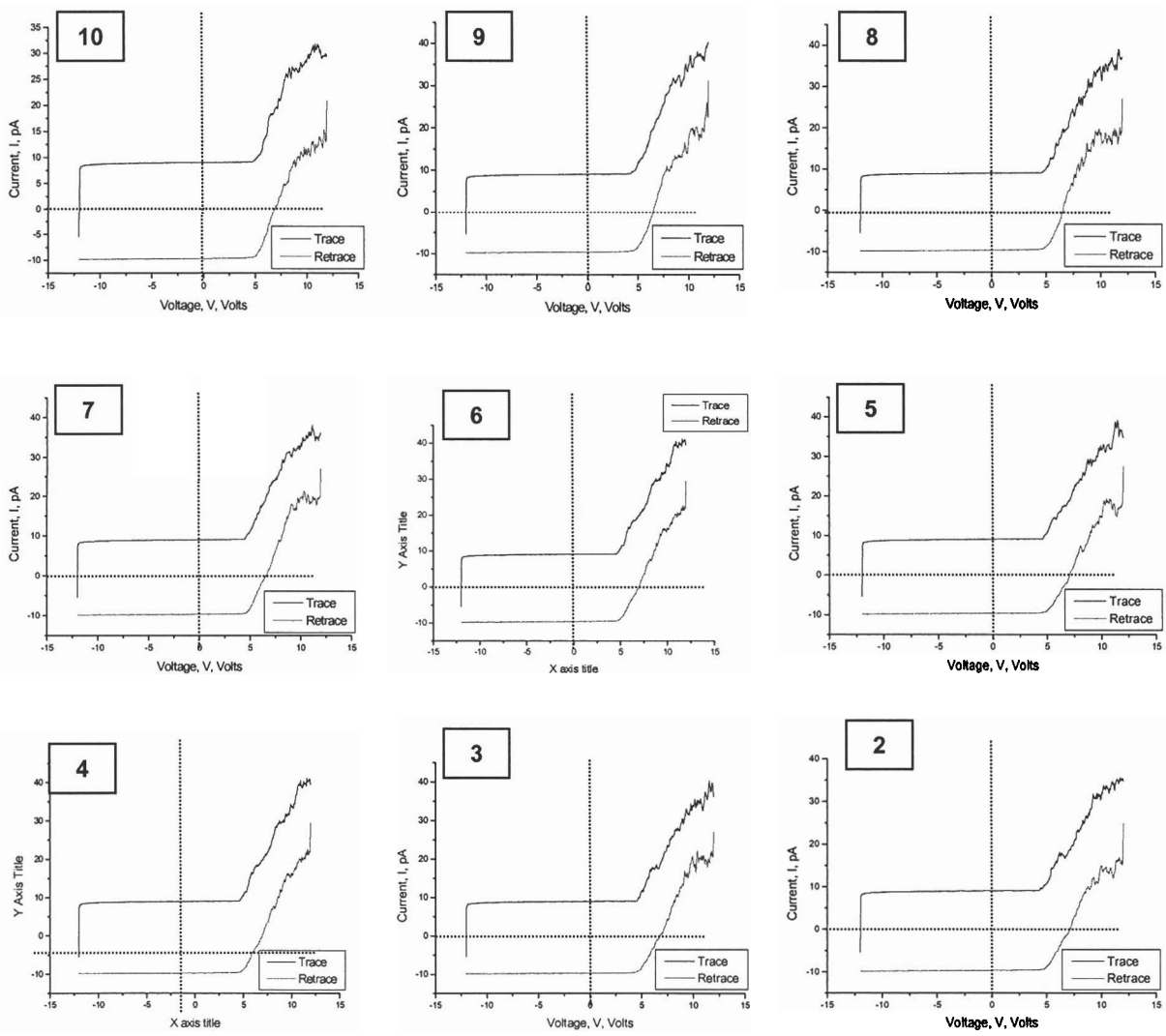

M2034 I-V Spectra (Upper Left Corner): 0.25μm × 1μm, 7V

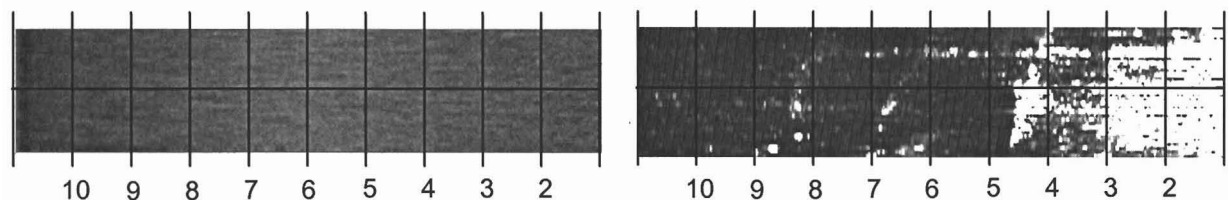

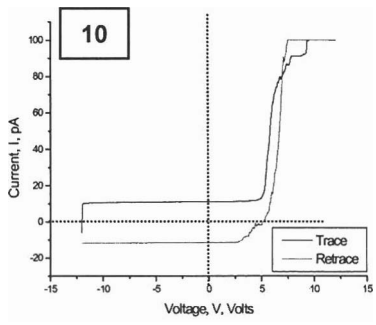

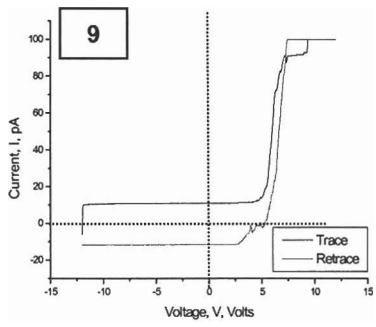

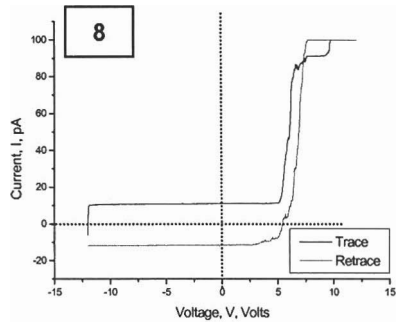

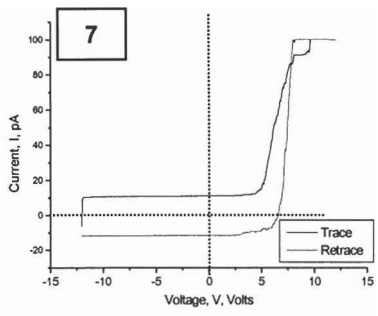

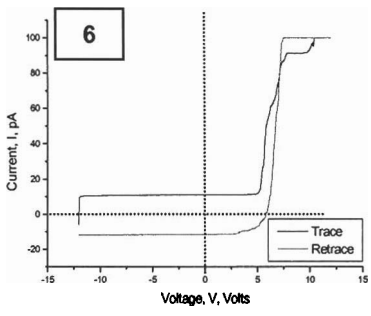

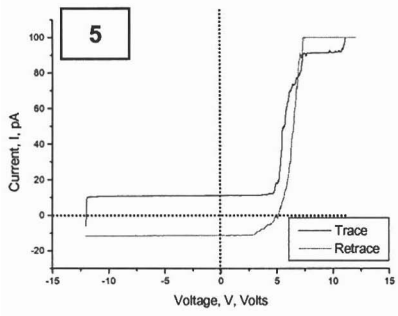

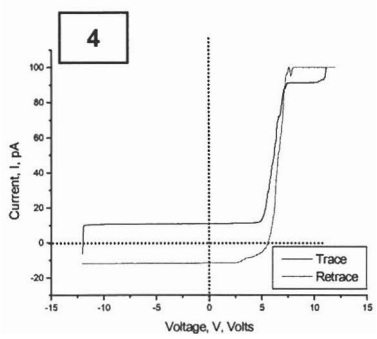

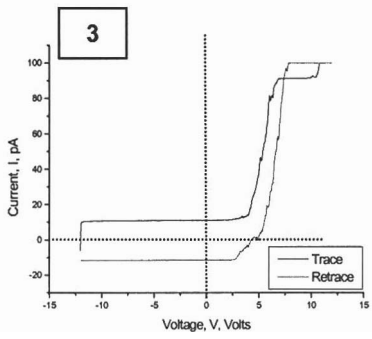

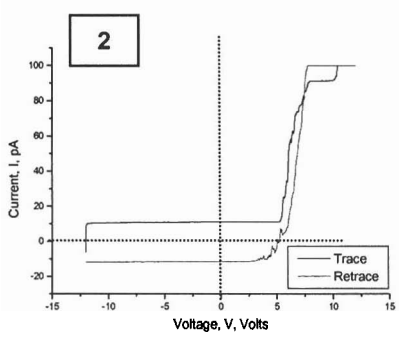

M2034 I-V Spectra (Lower Right Corner): 0.25μm × 1μm, 4V

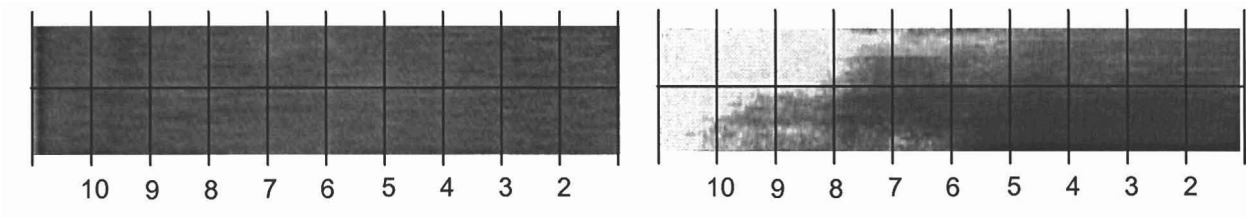

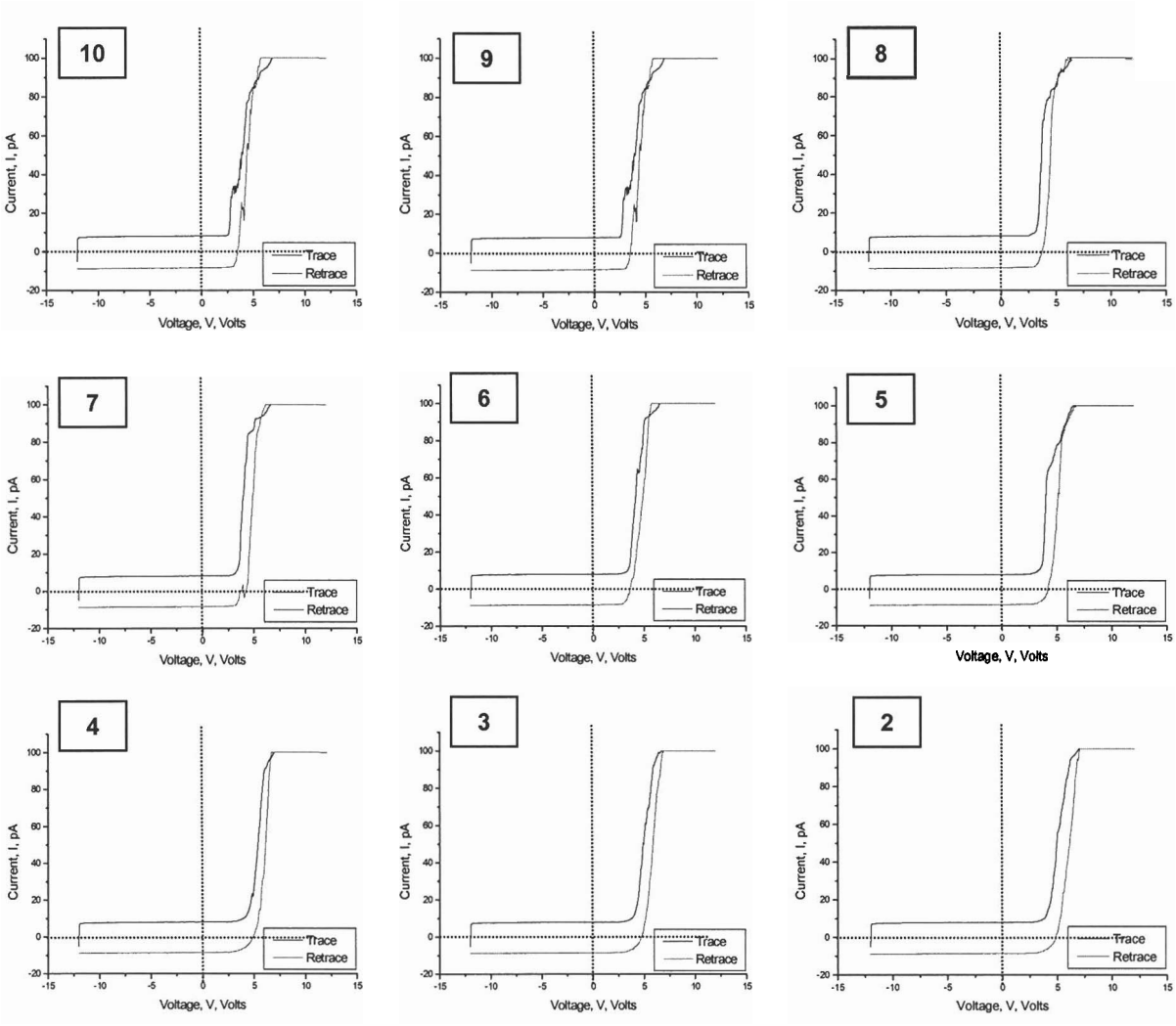

Appendix B.26

M2037 I-V Spectra (Upper Left Corner): 0.25μm × 1μm, 4V

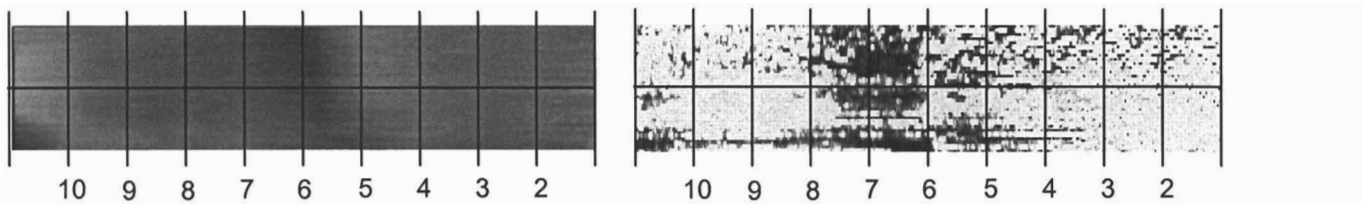

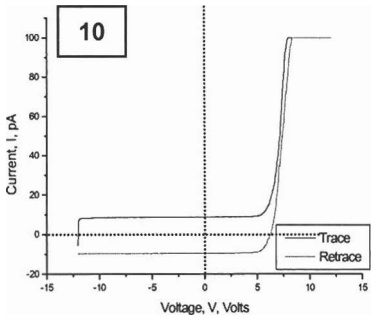

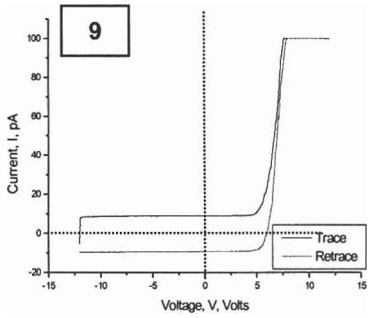

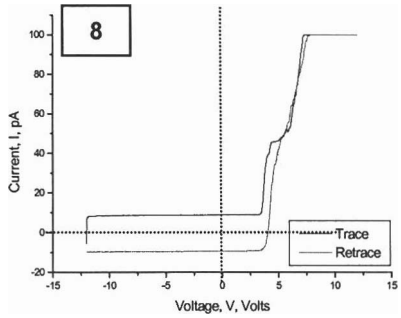

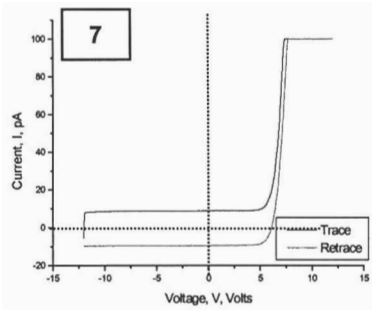

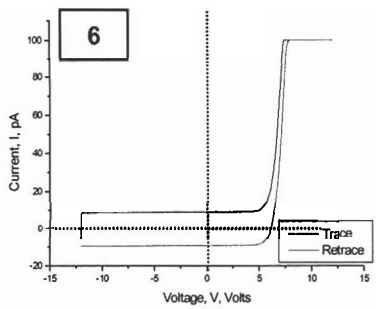

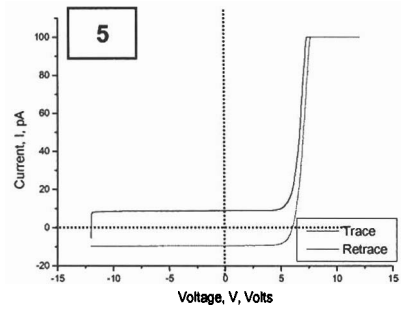

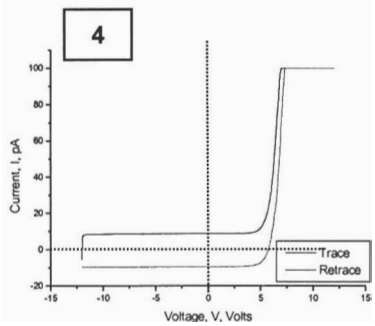

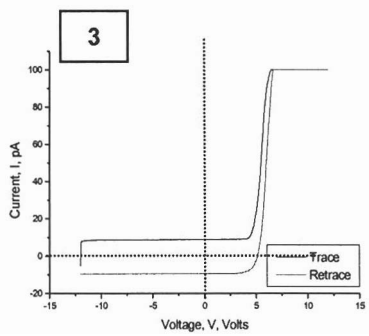

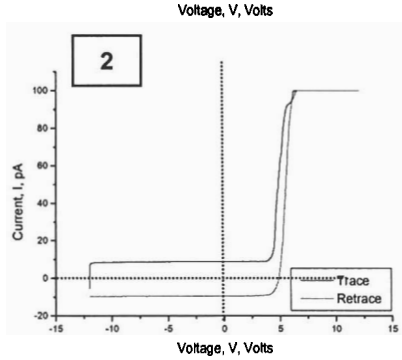

M2037 I-V Spectra (Lower Right Corner): 0.25μm × 1μm, 4V

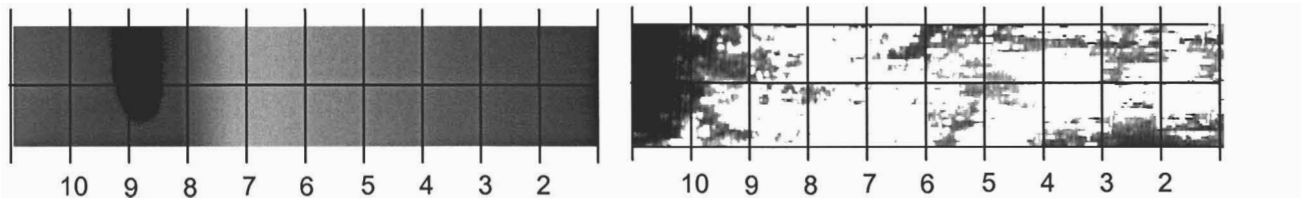

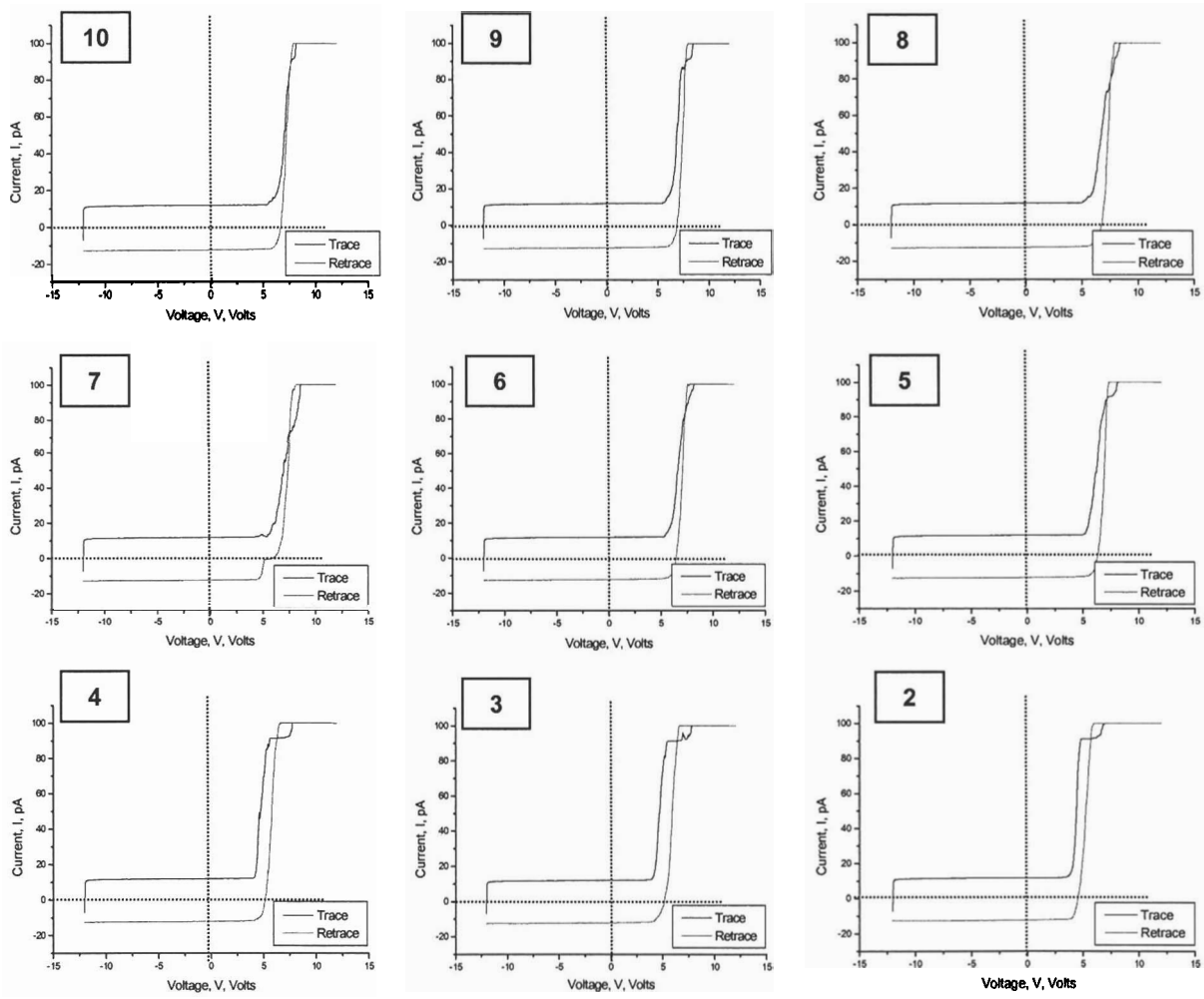

M2042 I-V Spectra (Upper Left Corner): 0.25μm × 1μm, 12V

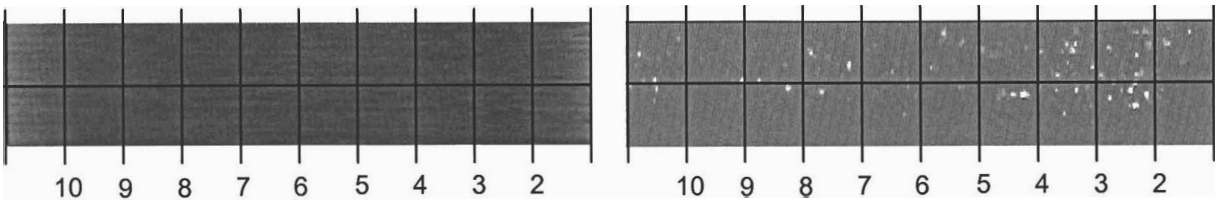

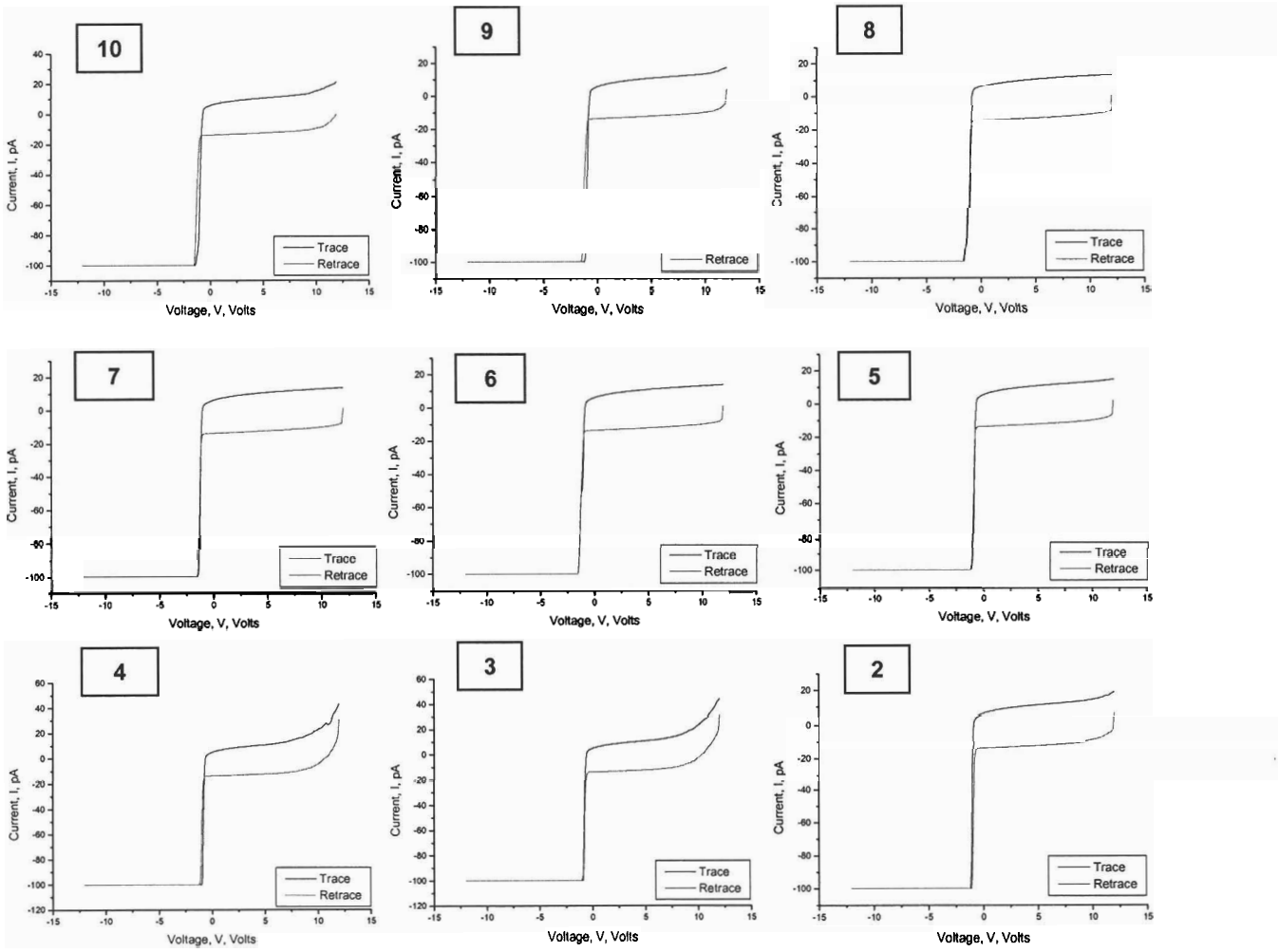

M2042 I-V Spectra (Lower Right Corner): 0.25μm × 1μm, 12V

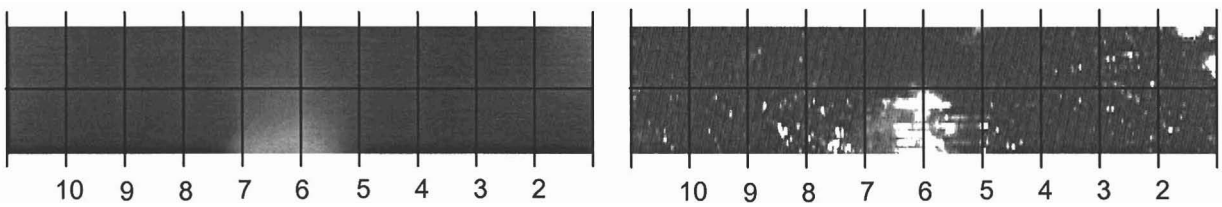

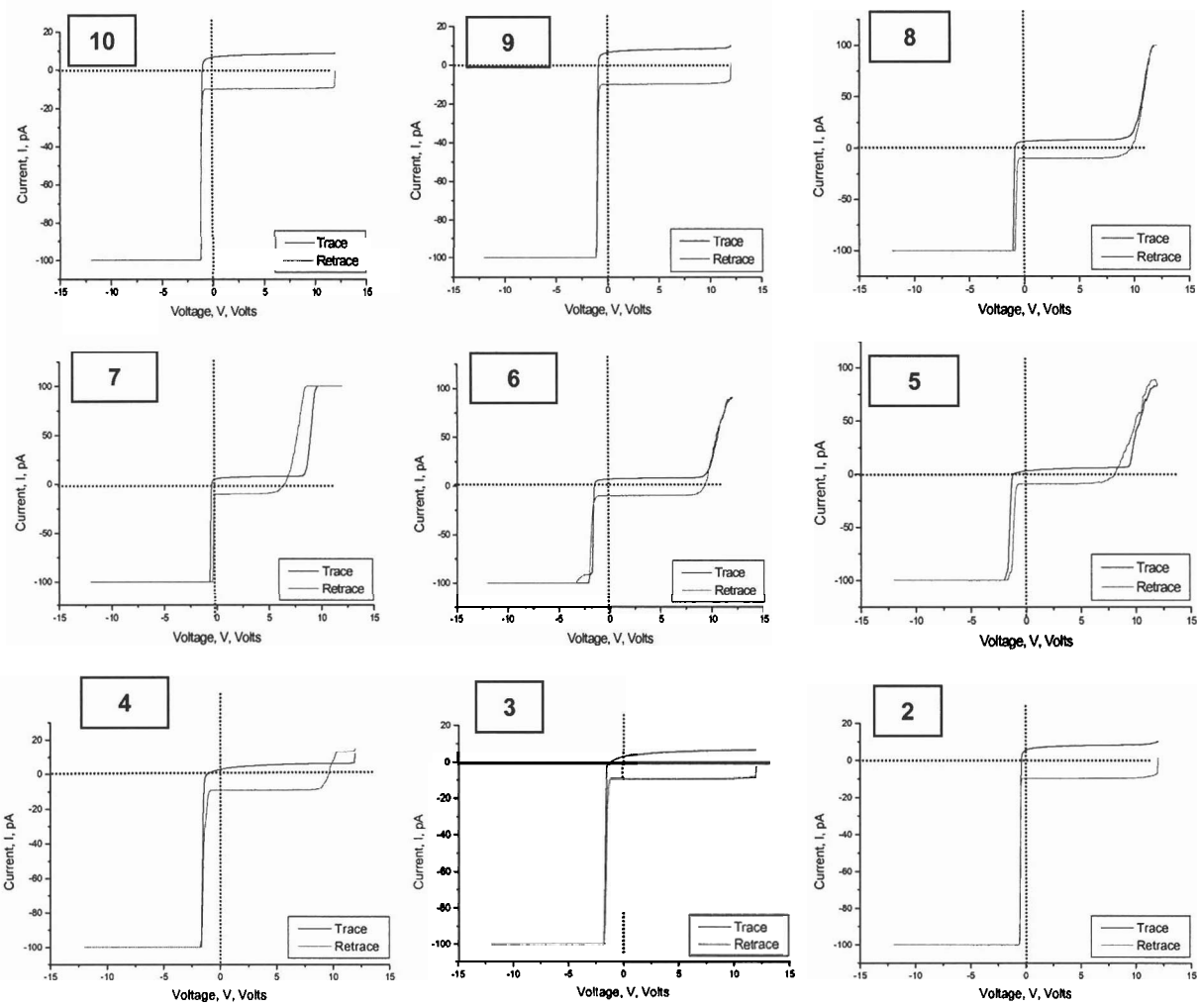

M2042b I-V Spectra (Upper Left Corner): 0.25μm × 1μm, 1V

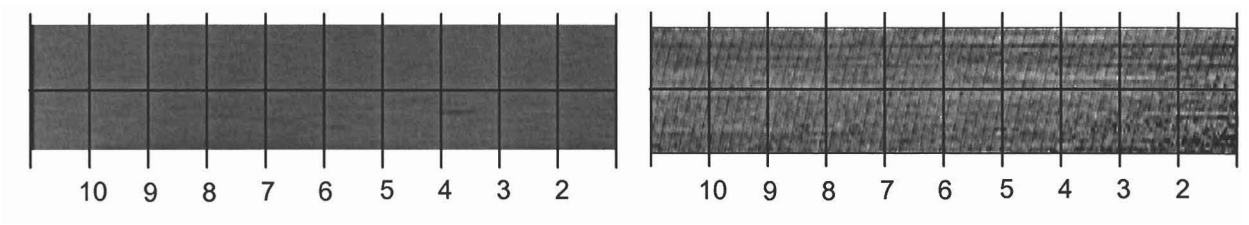

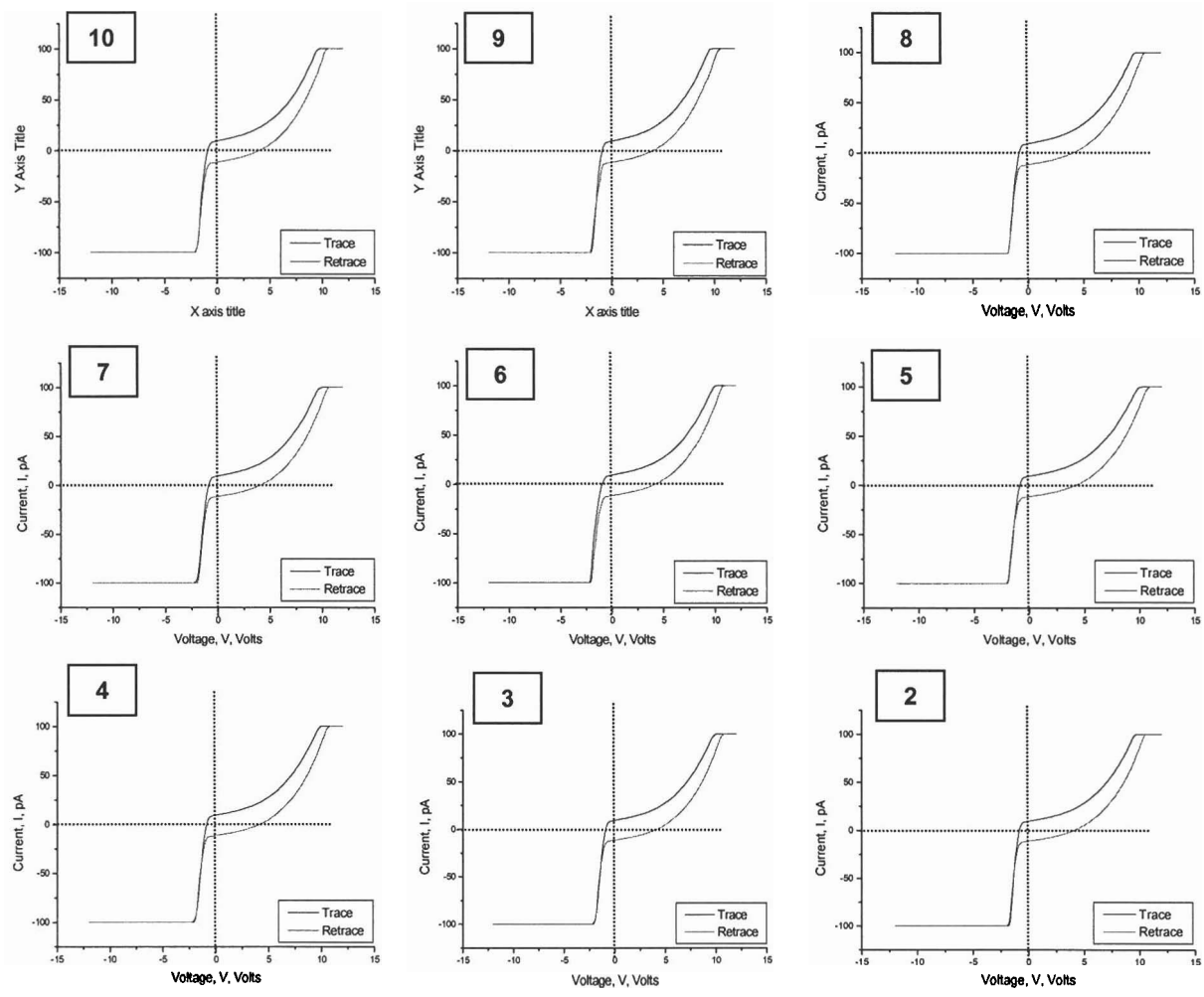

M2042b I-V Spectra (Lower Right Corner): 0.25μm × 1μm, 3V

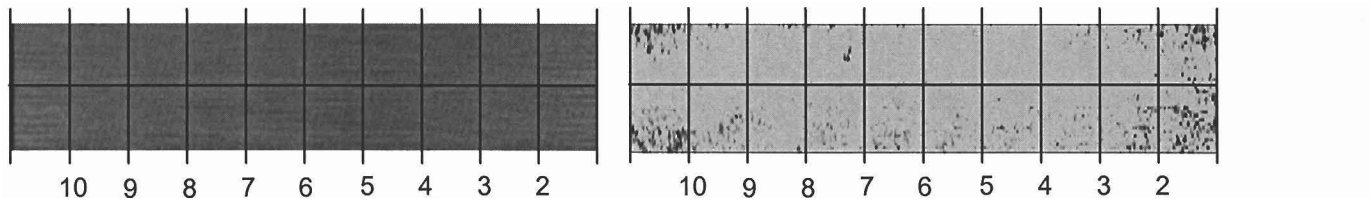

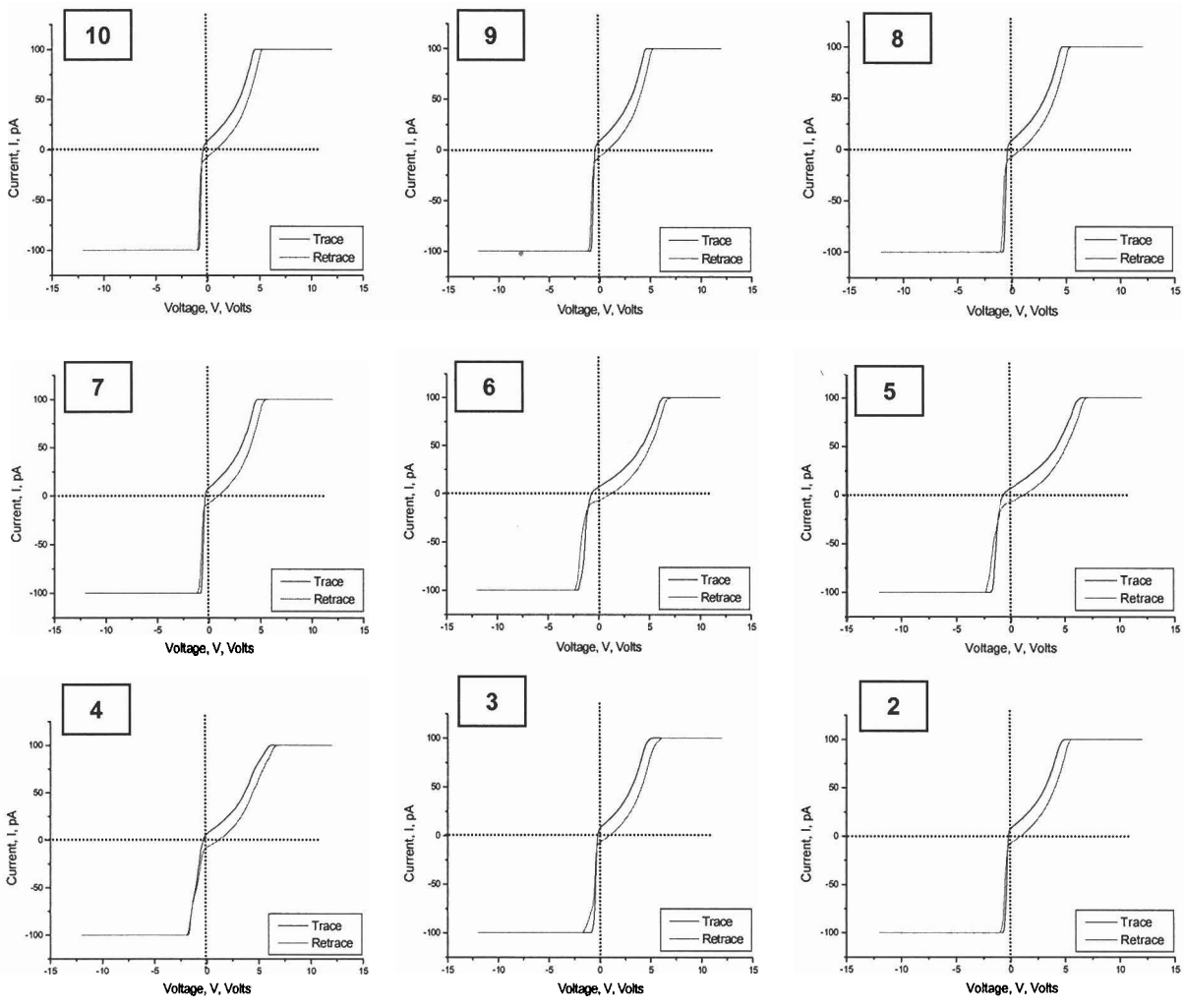

M2043 I-V (Upper Left Corner): 0.25μm × 1μm, 4V

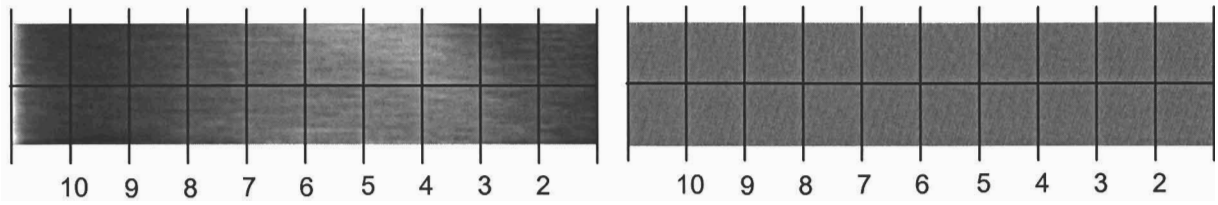

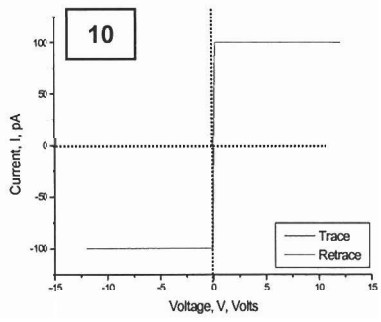

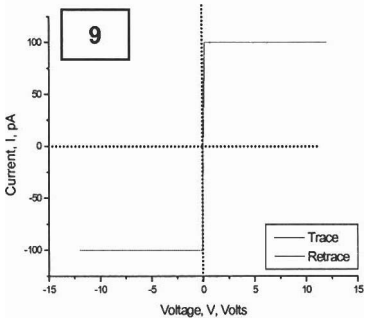

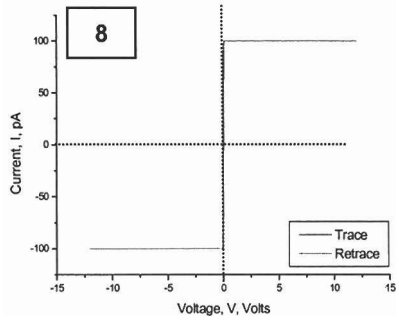

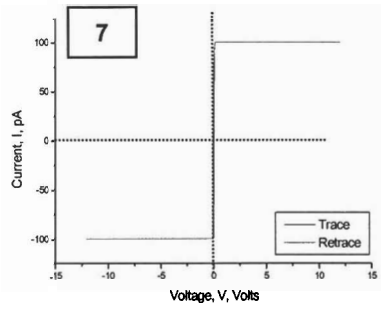

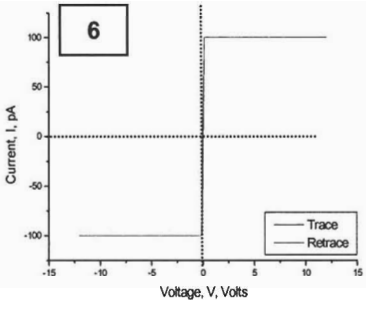

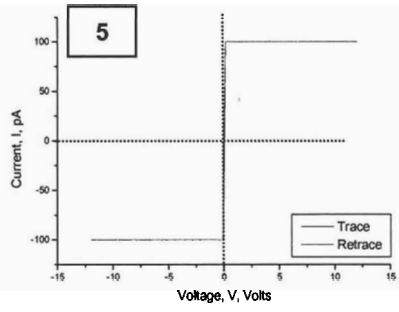

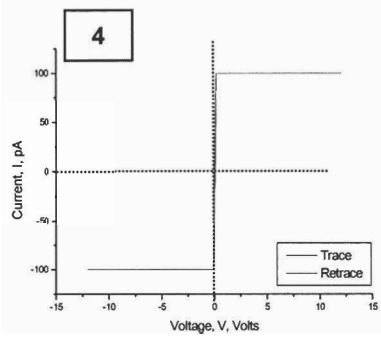

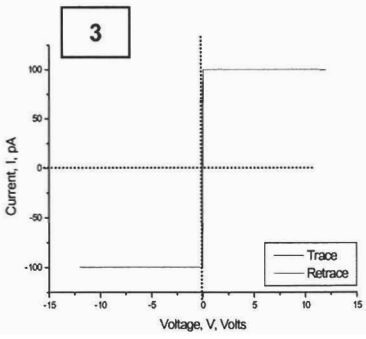

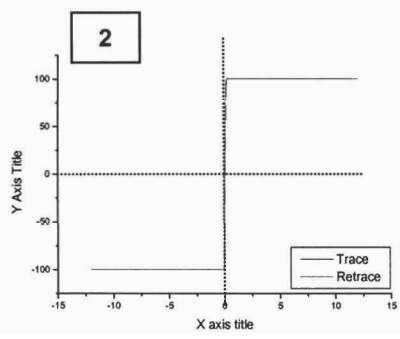

M2043 I-V Spectra (Lower Right Corner): 0.25μm × 1μm, 11V

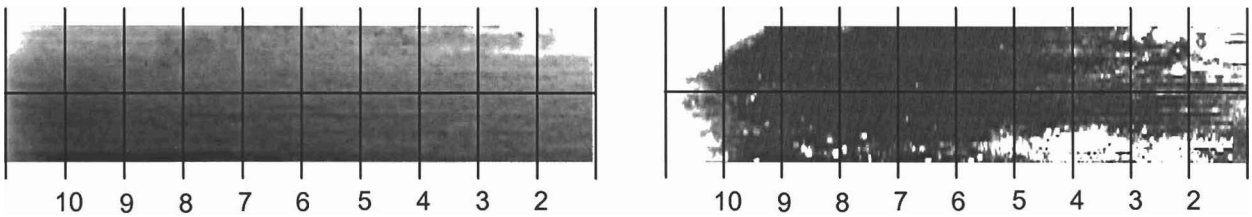

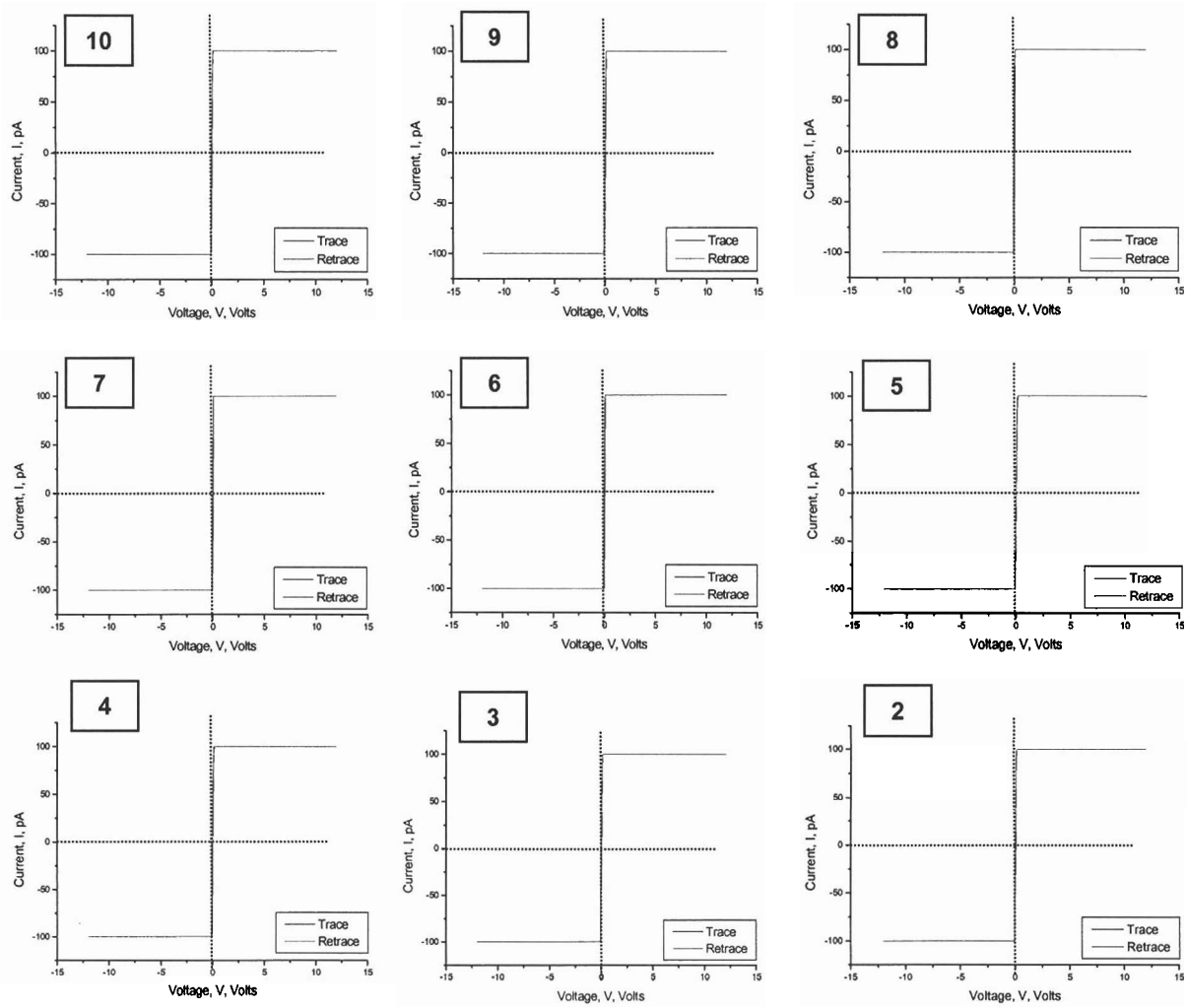

M2161 I-V Spectra (Upper Left Corner): 0.25μm × 1μm, 0.5V

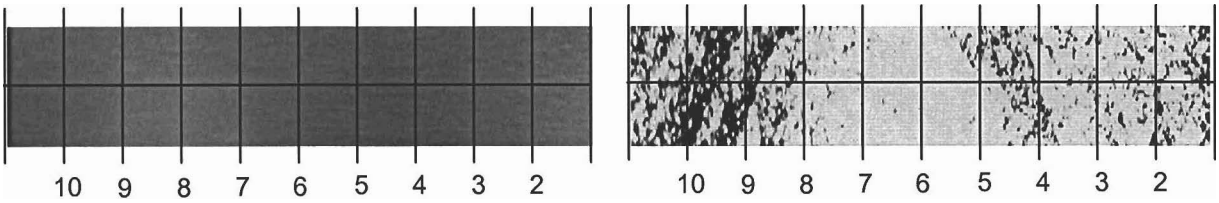

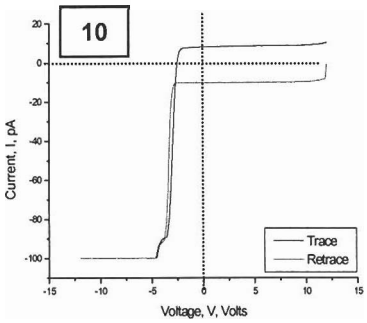

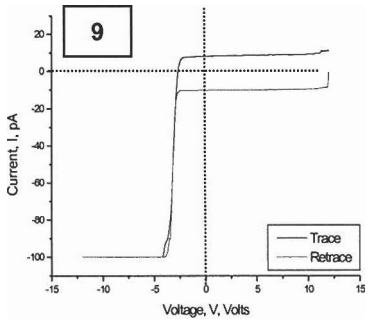

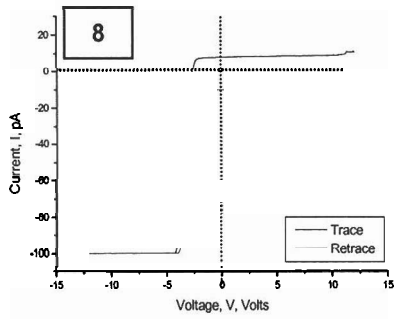

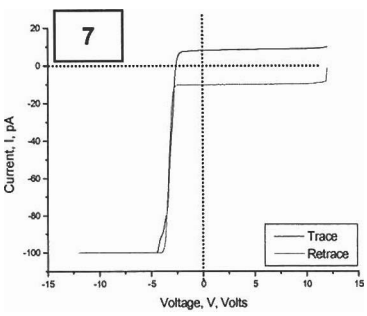

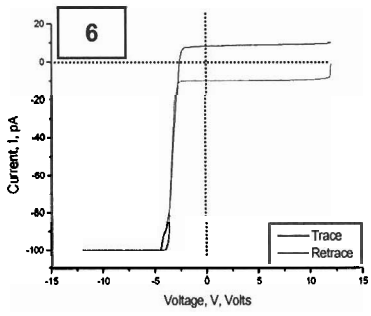

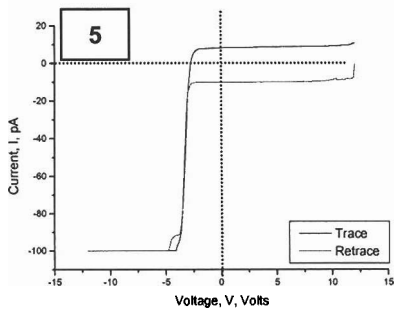

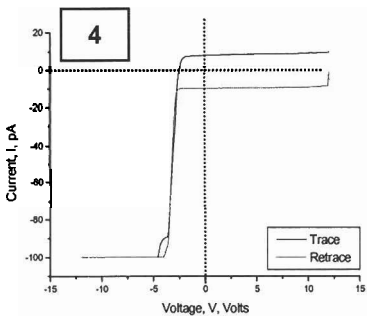

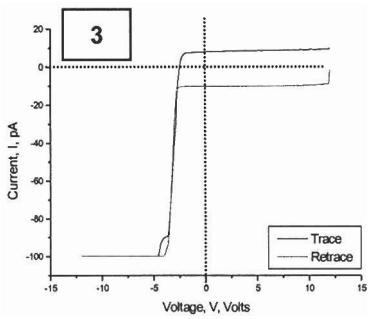

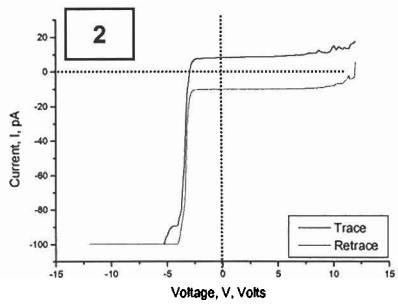

M2161 I-V Spectra (Lower Right Corner): 0.25μm × 1μm, 4V

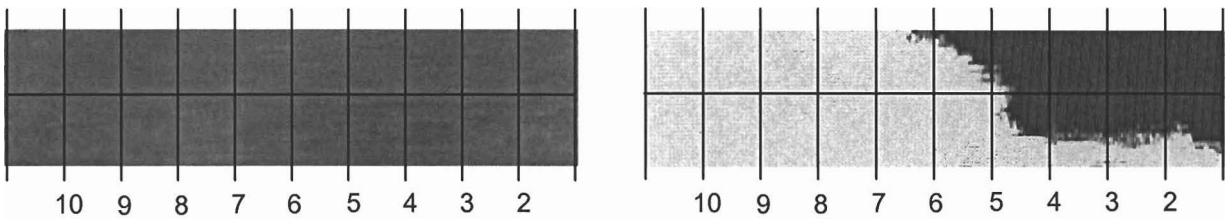

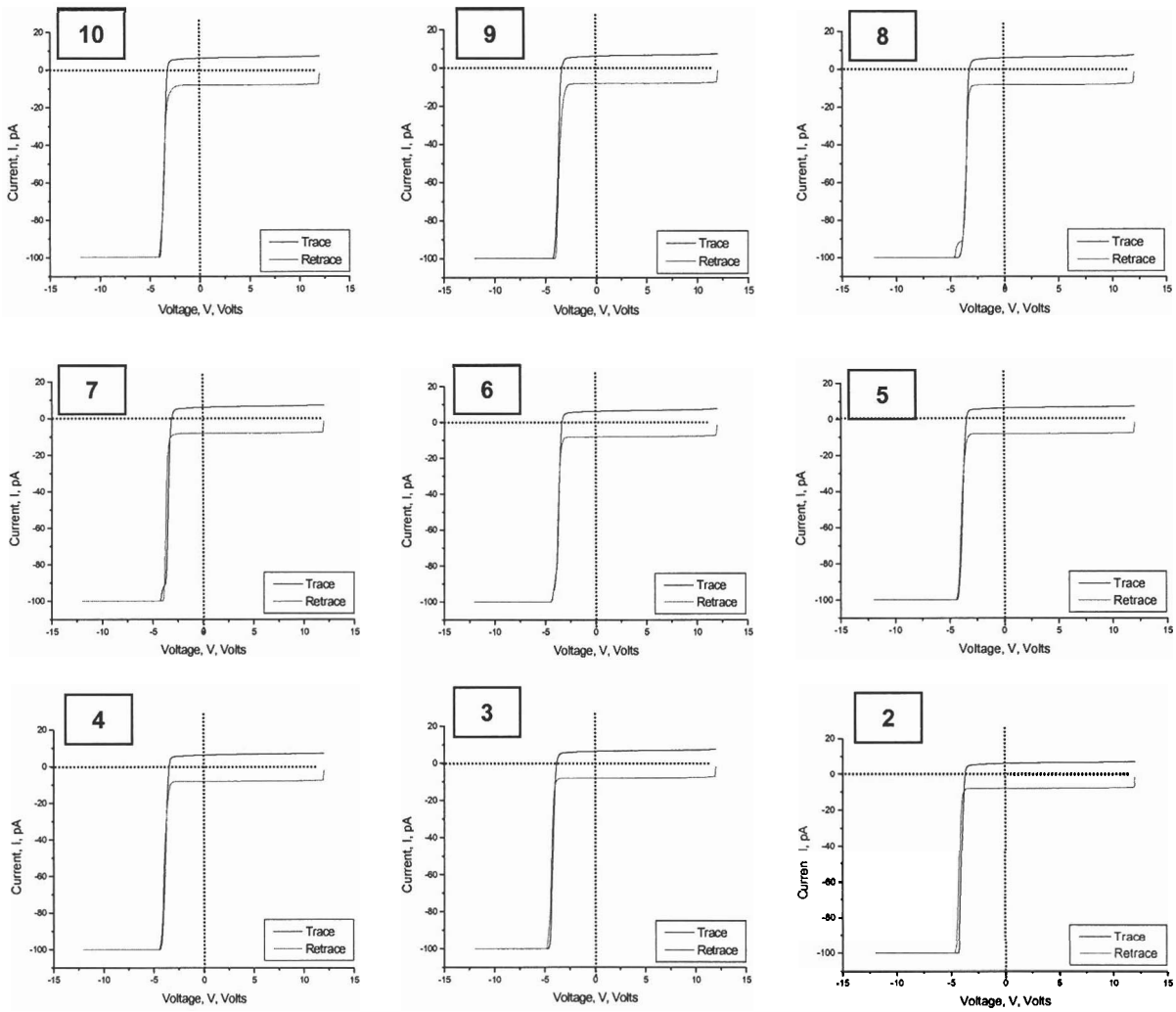

APPENDIX C: I-V Spectra (Log Scale)

M1840 I-V Spectra (Top Left Corner): 0.5μm × 2μm, 12V

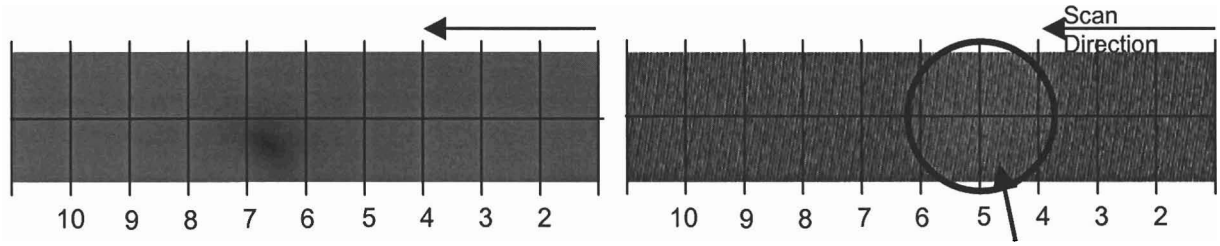

Note: All I-V spectra were taken at line intersections and are labeled according to the intersection number.

Feature of interest

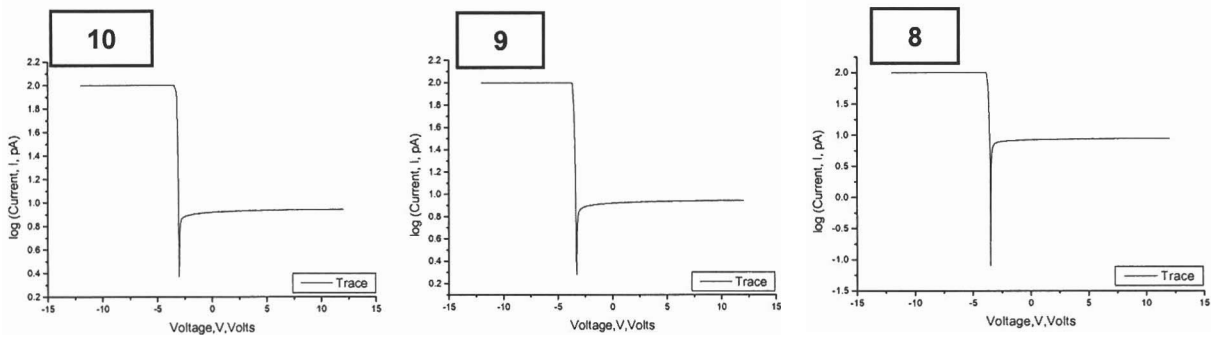

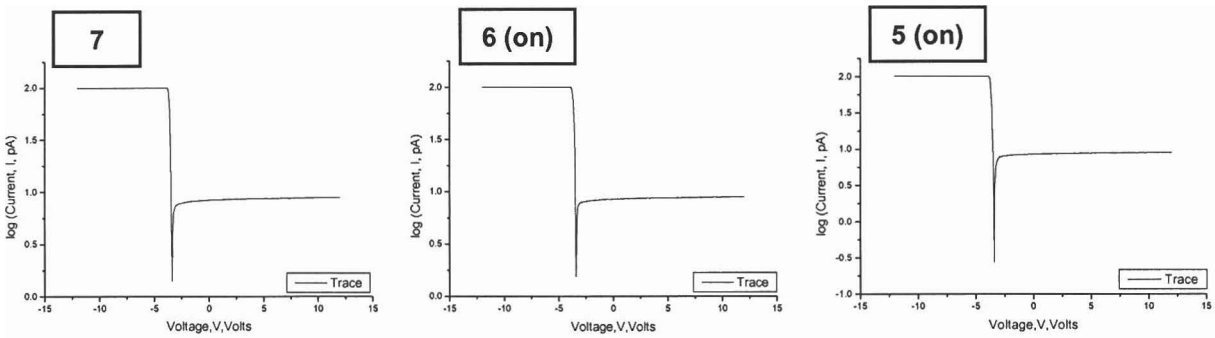

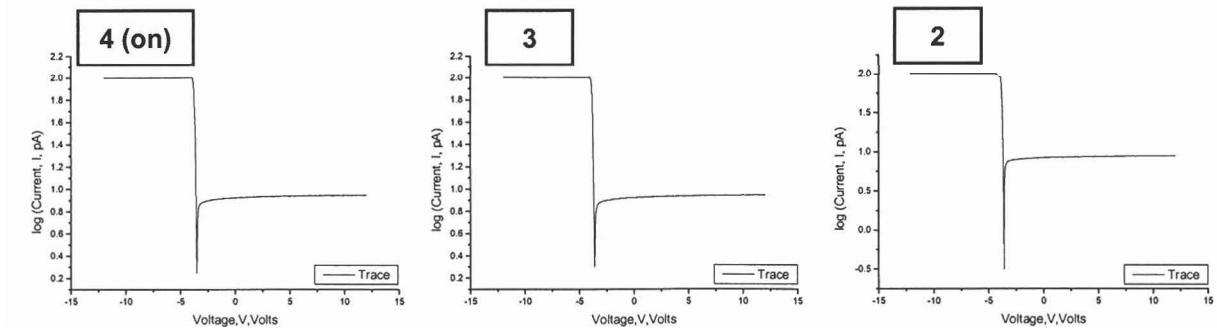

M1840 I-V Spectra (Bottom Right Corner): 0.5μm × 2μm, 12V

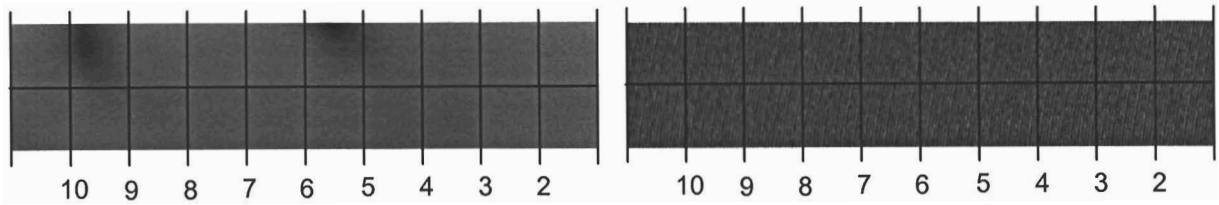

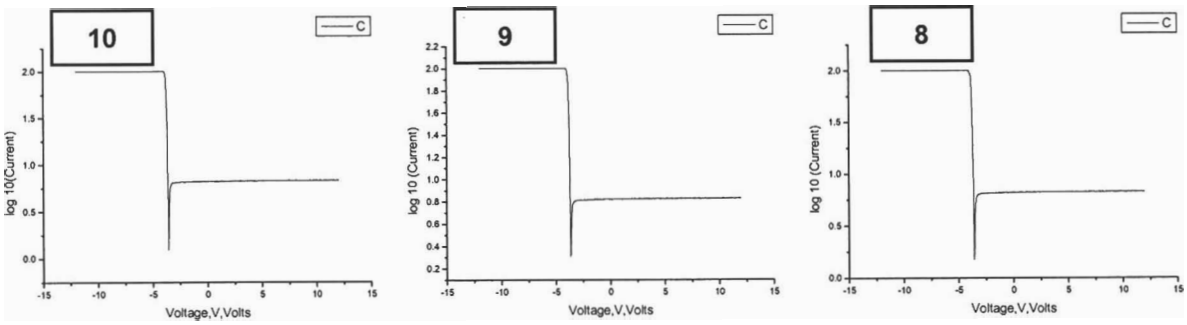

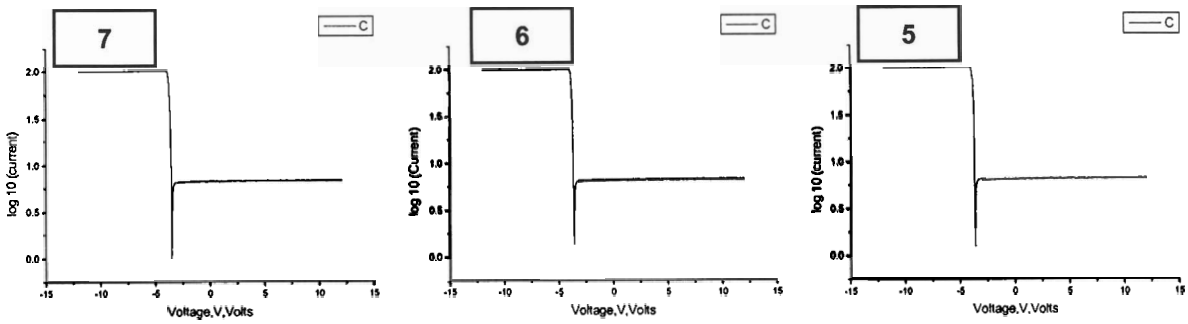

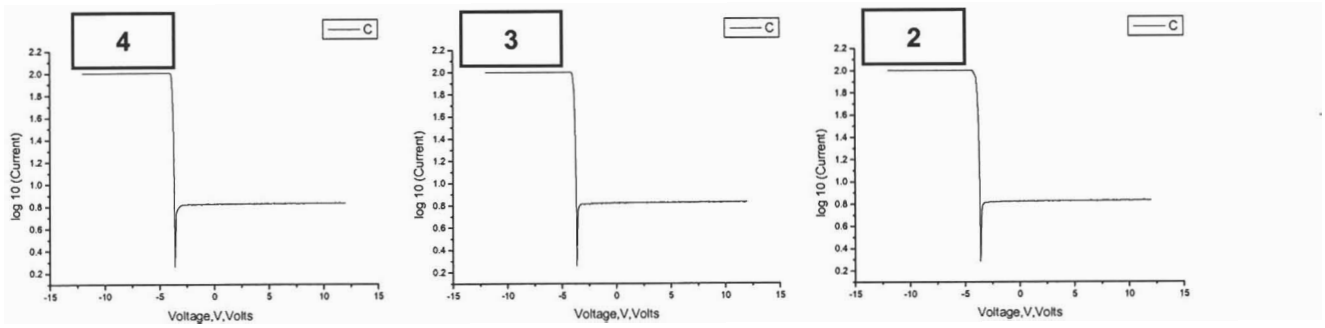

M1899 I-V Spectra (Upper Left Corner): 0.5μm × 2μm, 8V

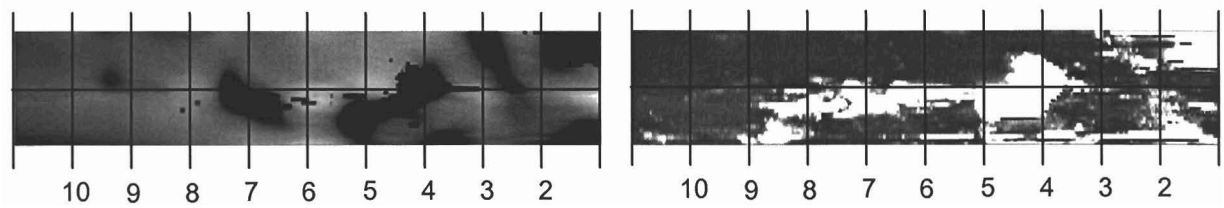

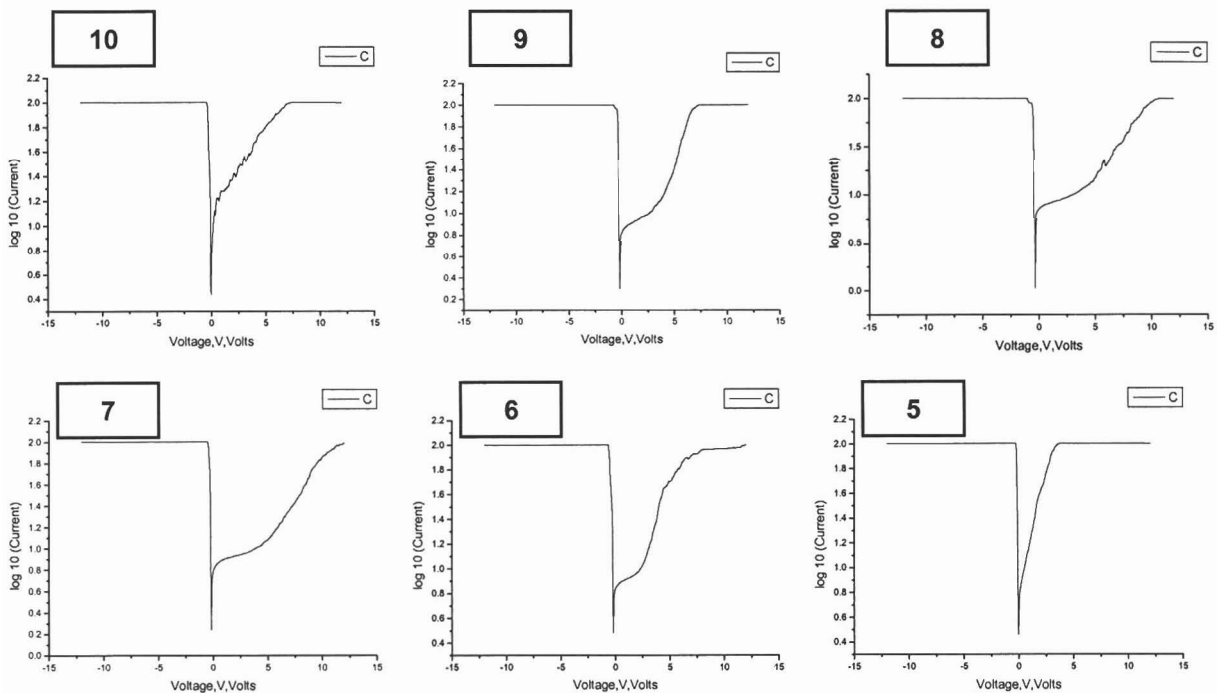

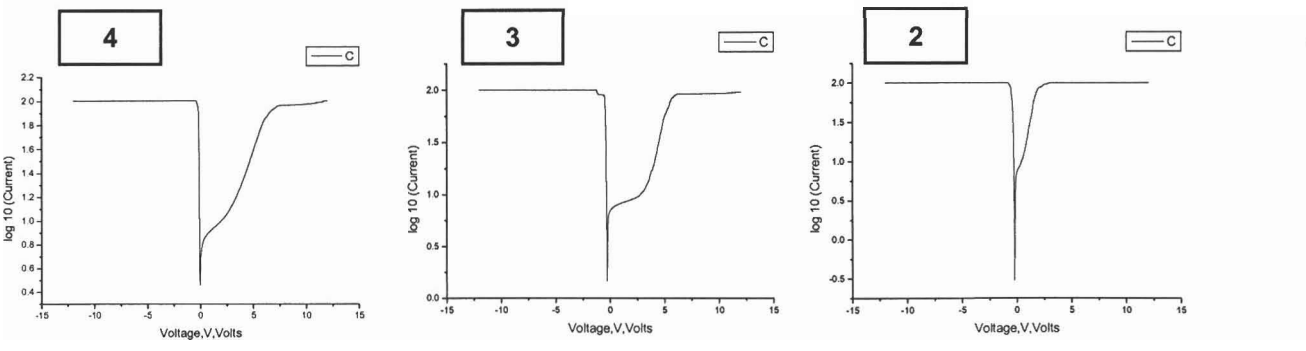

M1899 I-V Spectra (Lower Right Corner): 0.5μm × 2μm, 8V

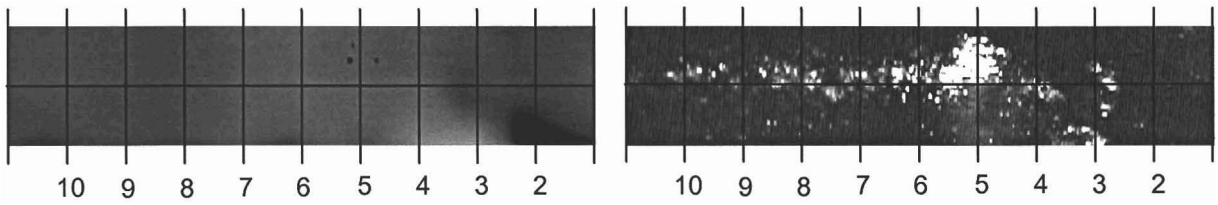

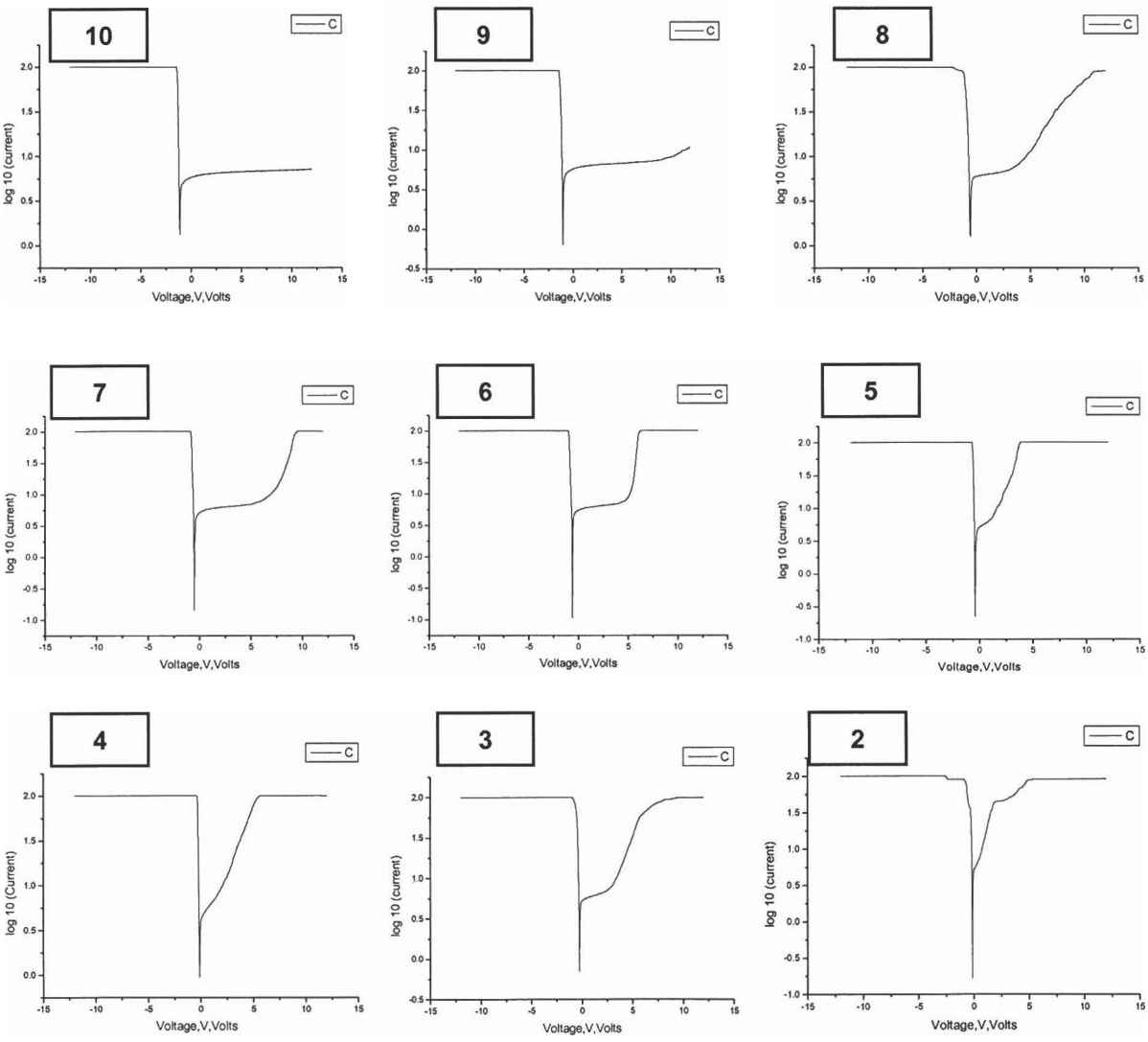

M1903 I-V Spectra (Upper Left Corner): 0.25μm × 1μm, 12V

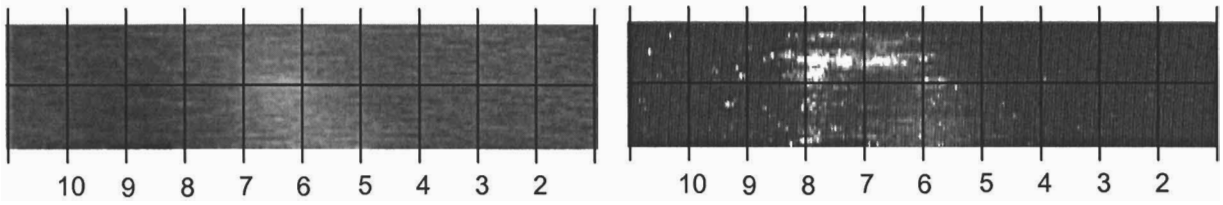

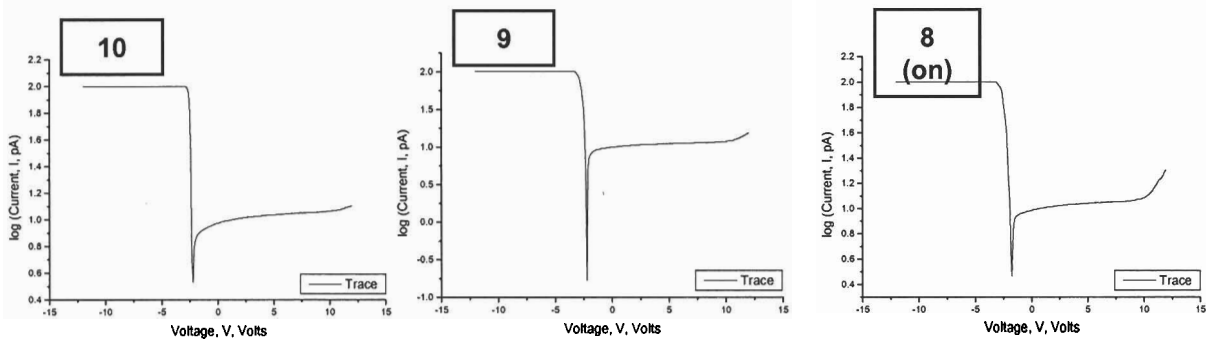

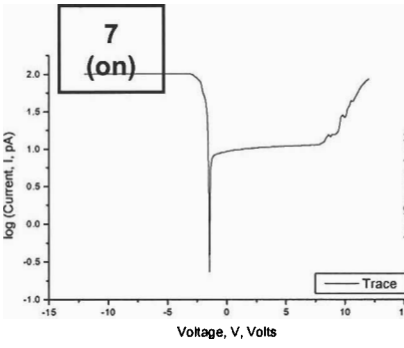

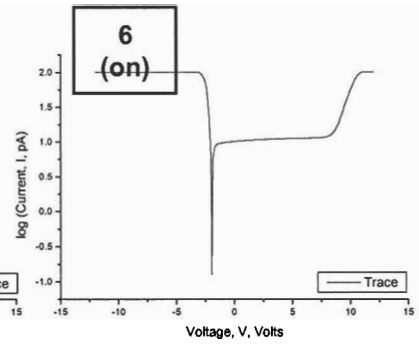

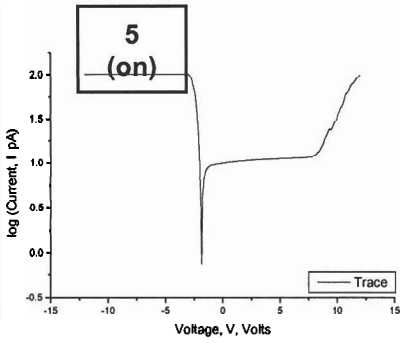

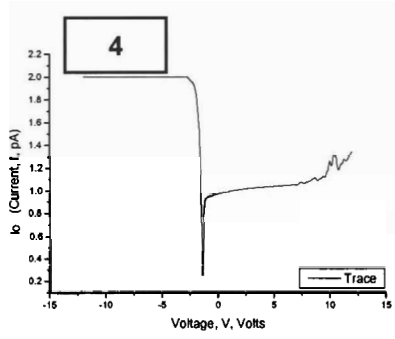

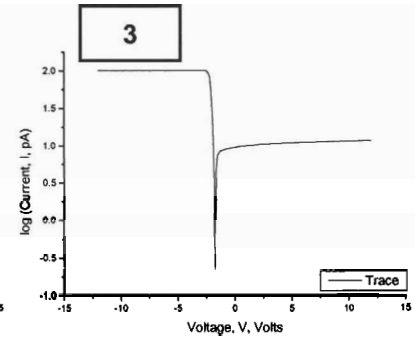

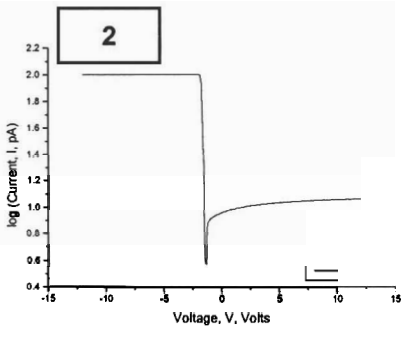

M1903 I-V Spectra (Lower Right Corner): 0.25μm × 1μm, 12V

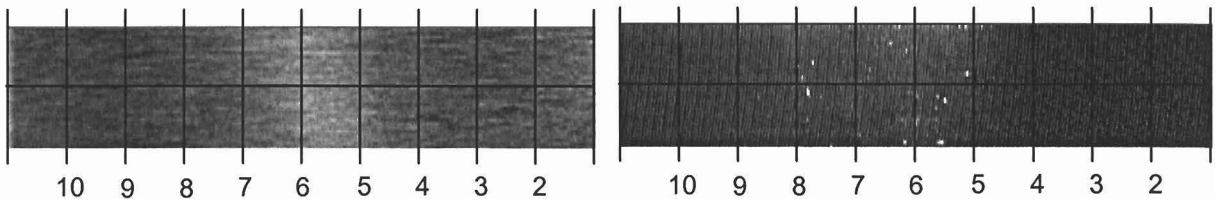

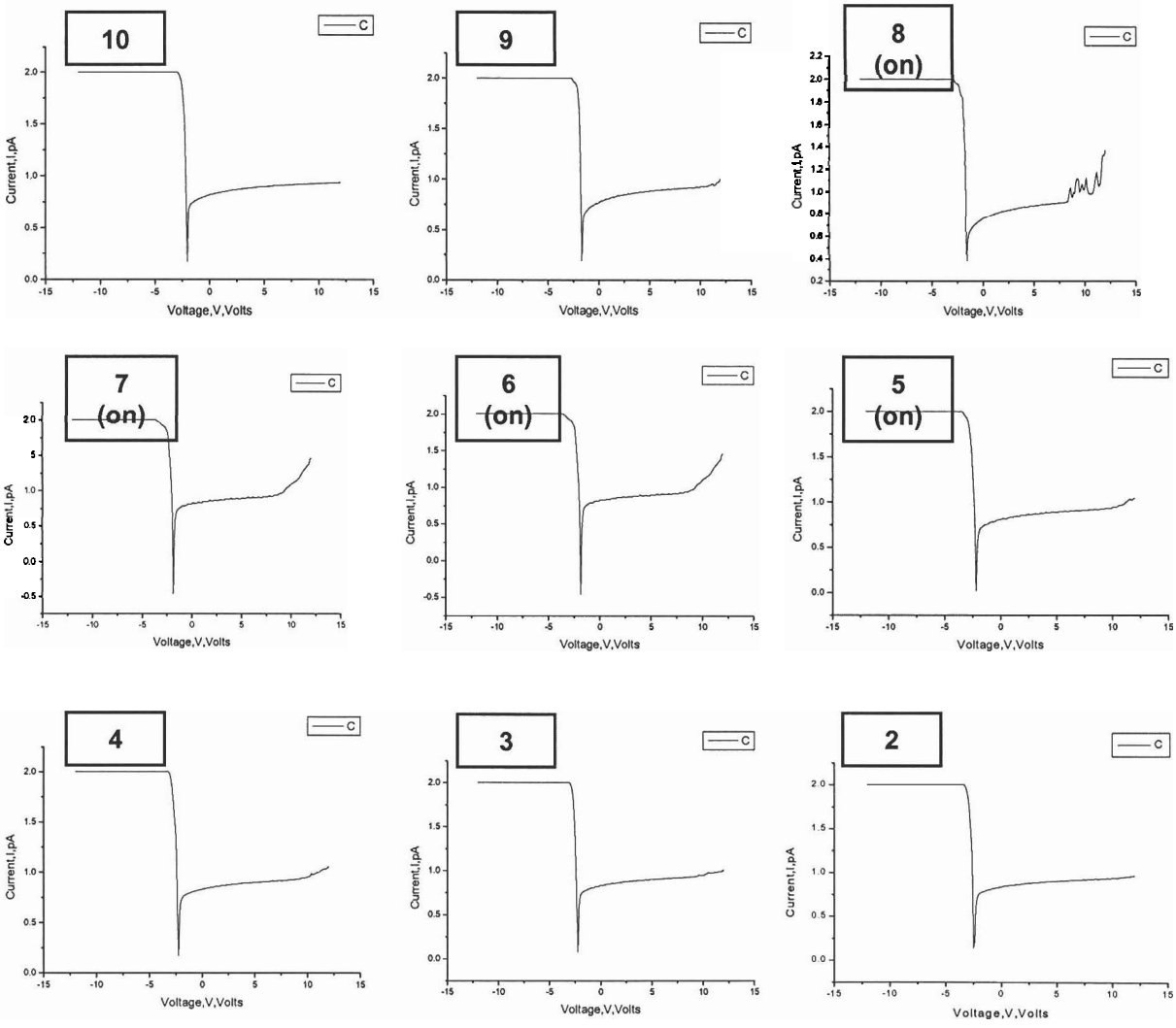

M1906 I-V Spectra (Upper Left Corner): 0.25μm × 1μm, 12V

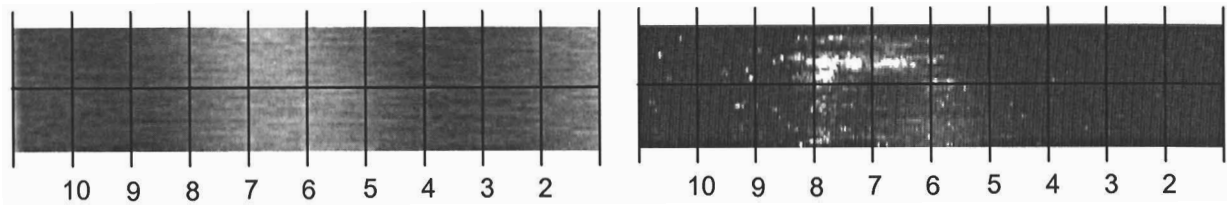

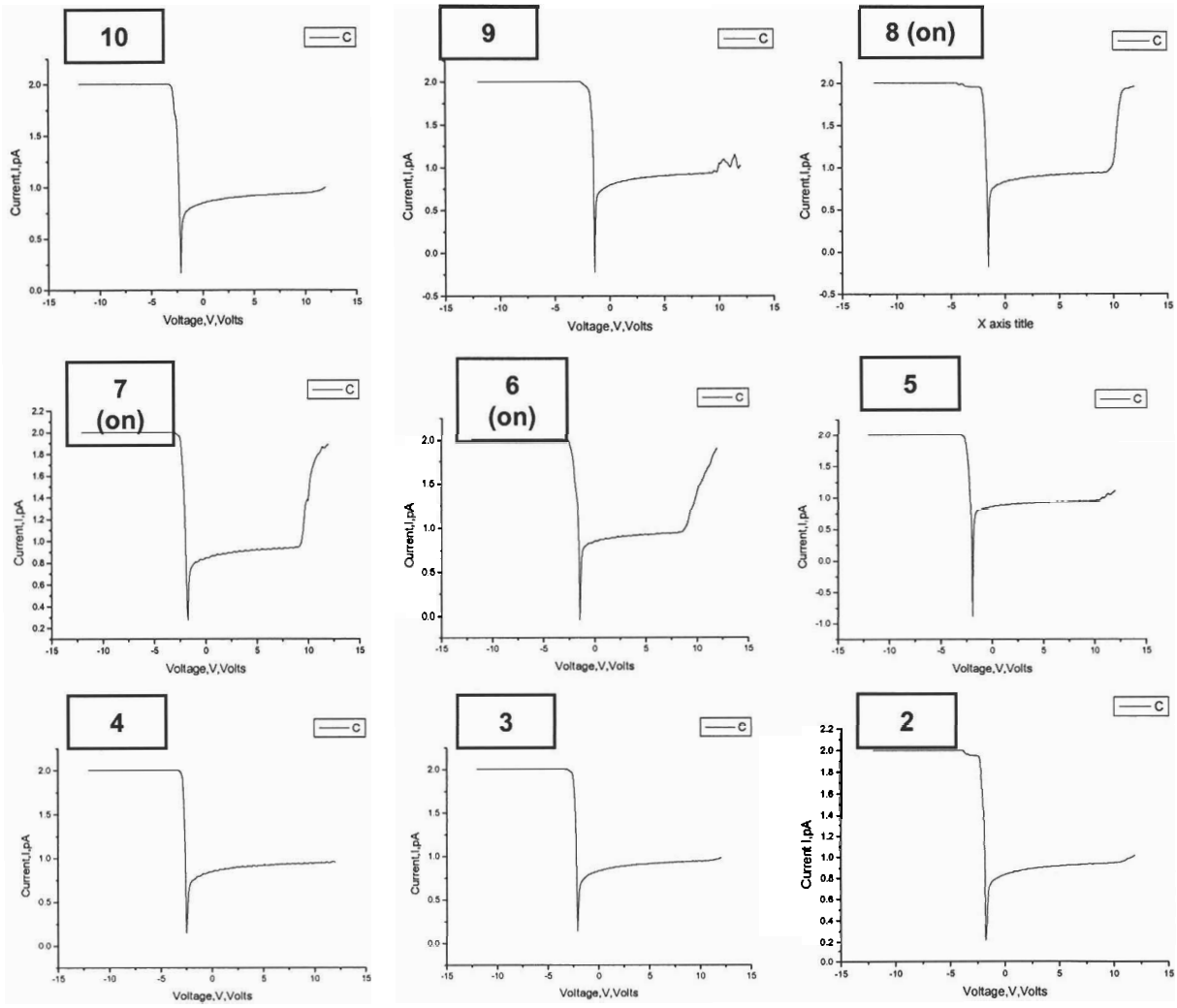

M1906 I-V Spectra (Lower Right Corner): 0.25μm × 1μm, 12V

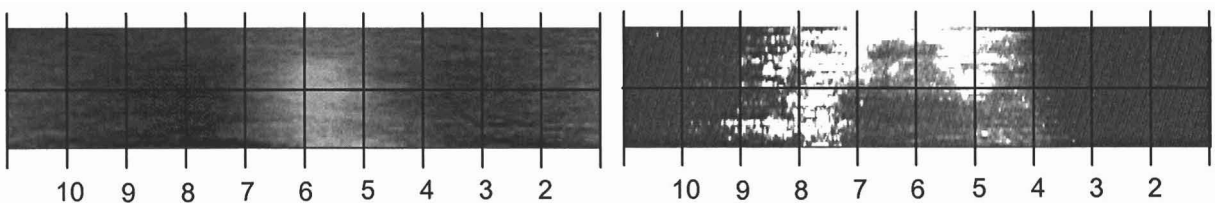

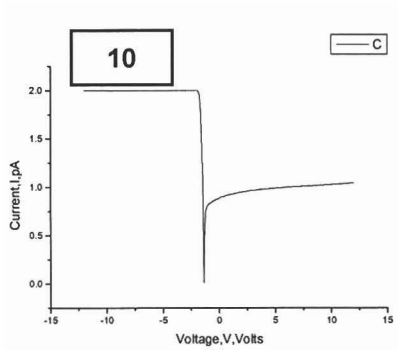

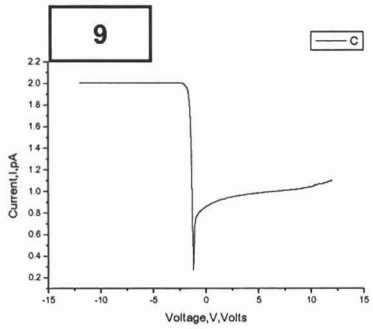

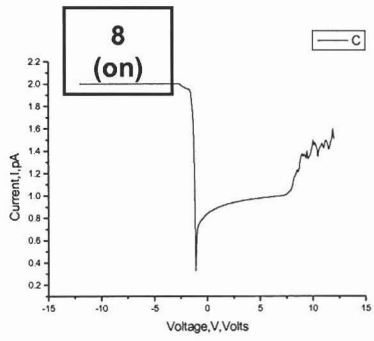

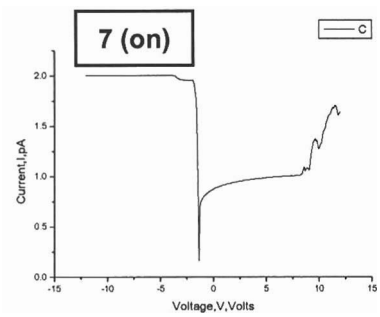

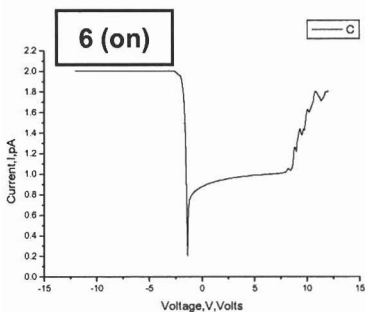

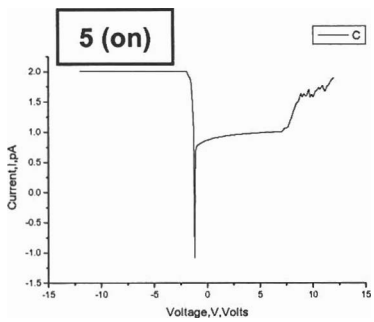

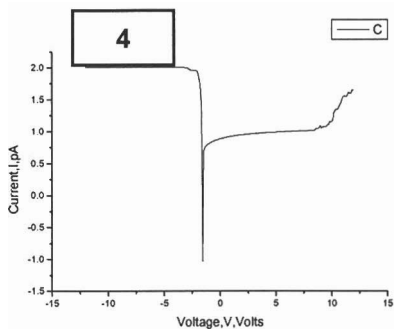

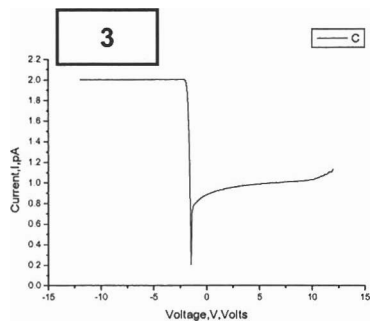

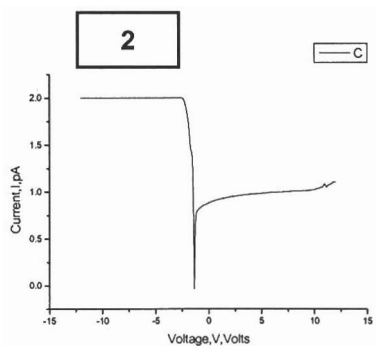

M1912 I-V Spectra (Upper Left Corner): 0.25μm × 1μm, 12V

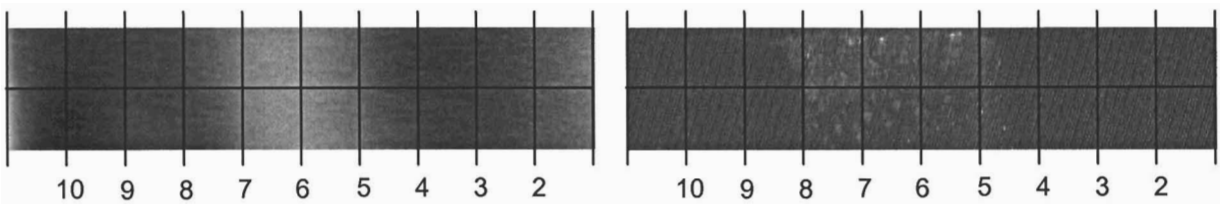

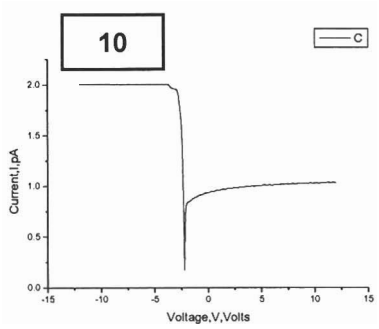

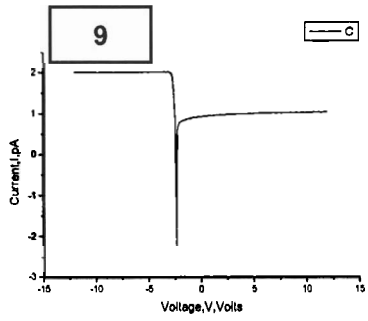

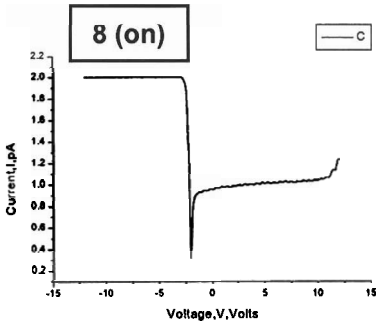

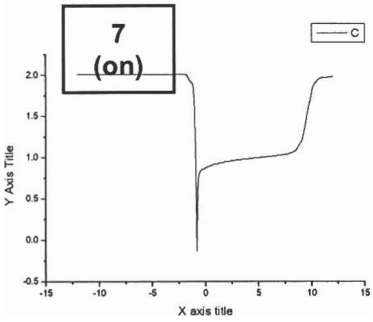

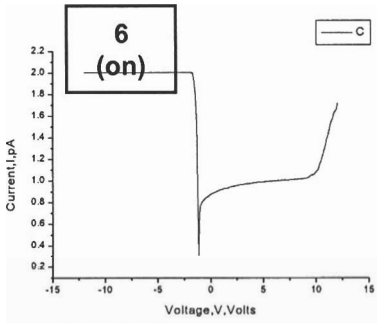

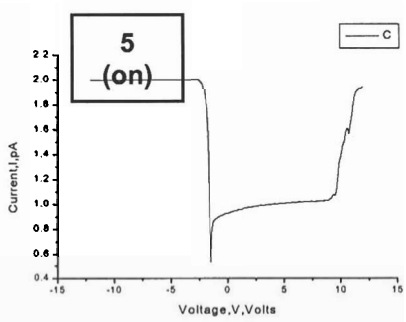

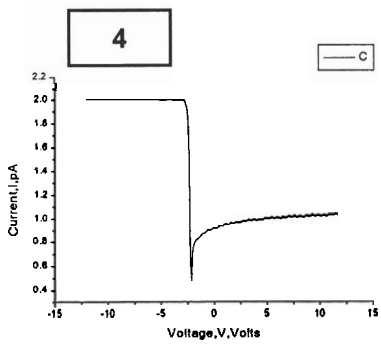

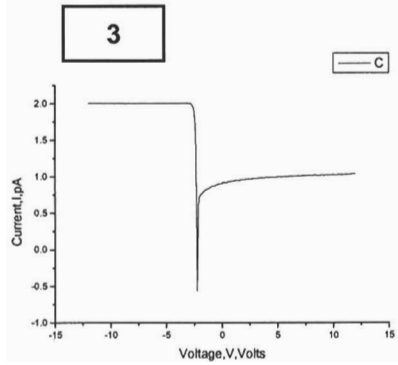

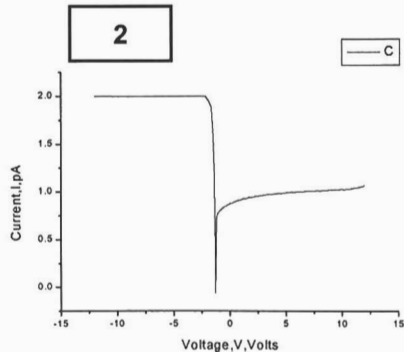

M1912 I-V Spectra (Lower Right Corner): 0.25μm × 1μm, 12V

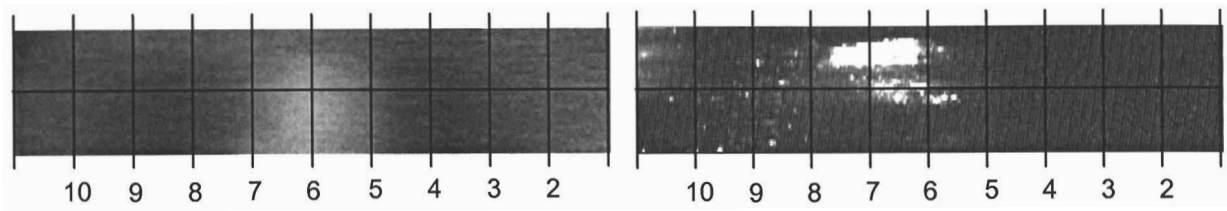

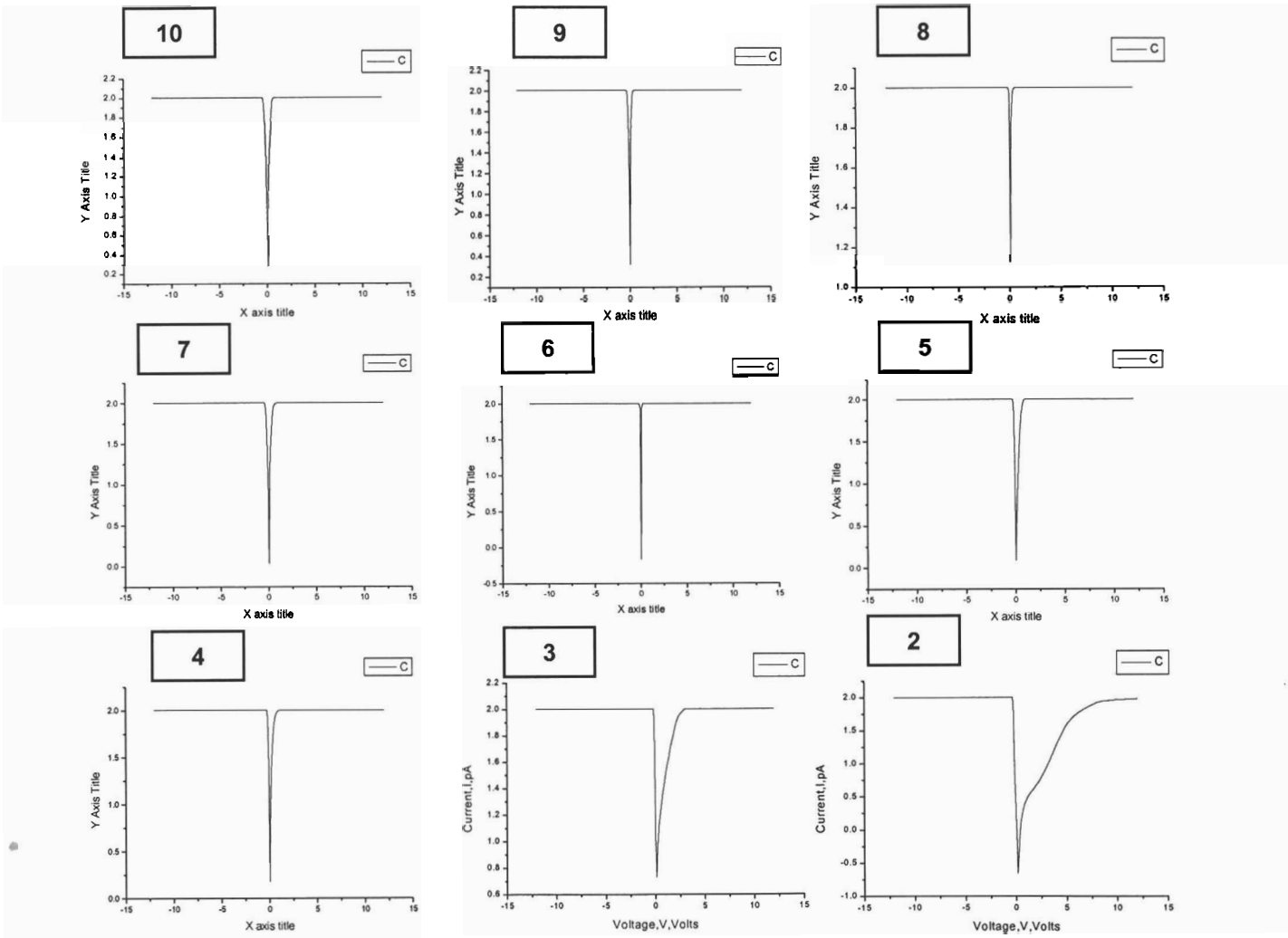

M1916 I-V Spectra (Upper Left Corner): 0.25μm × 1μm, 4V

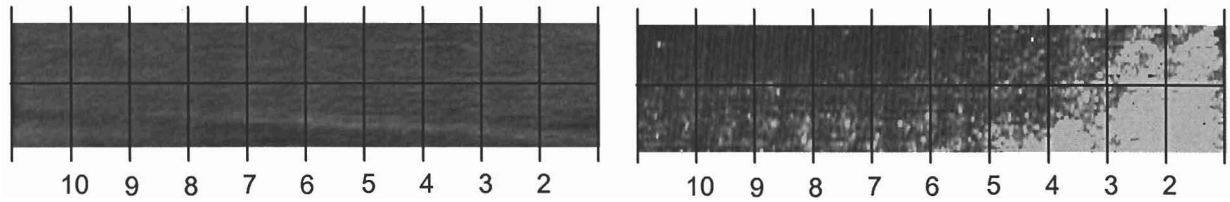

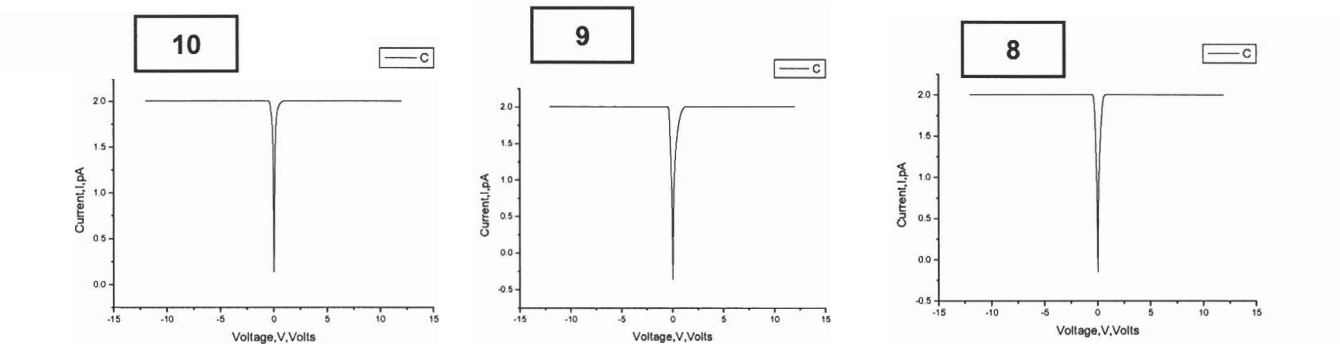

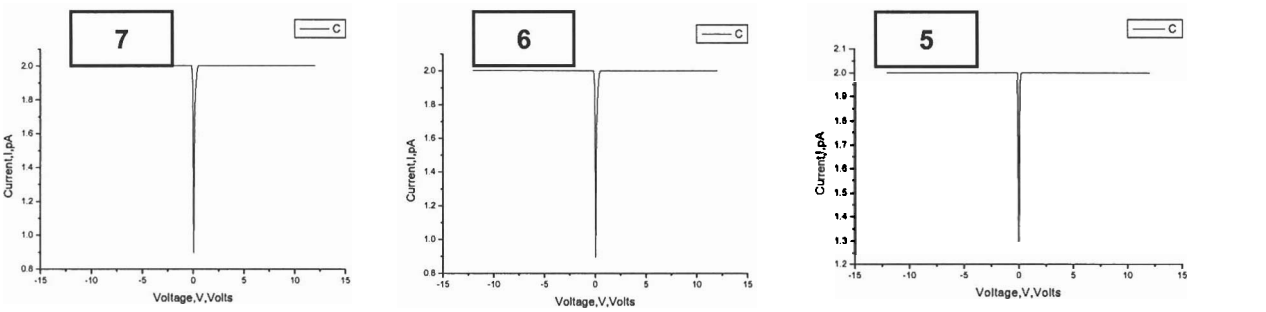

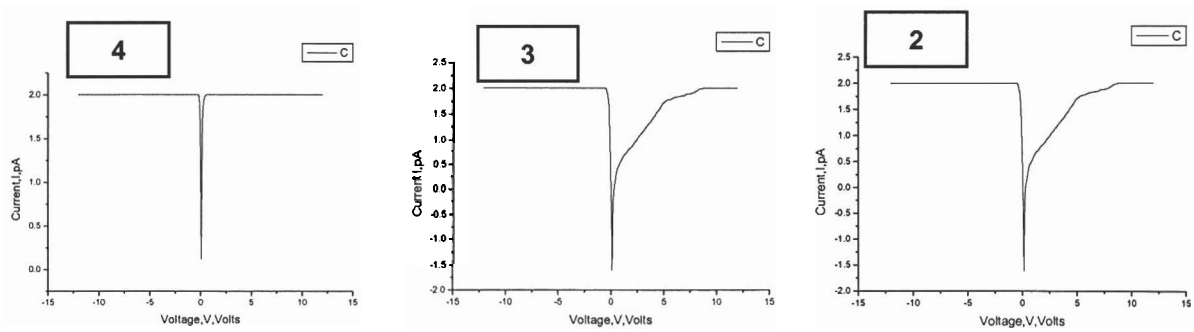

M1916 I-V Spectra (Lower Right Corner): 0.25μm × 1μm, 4V

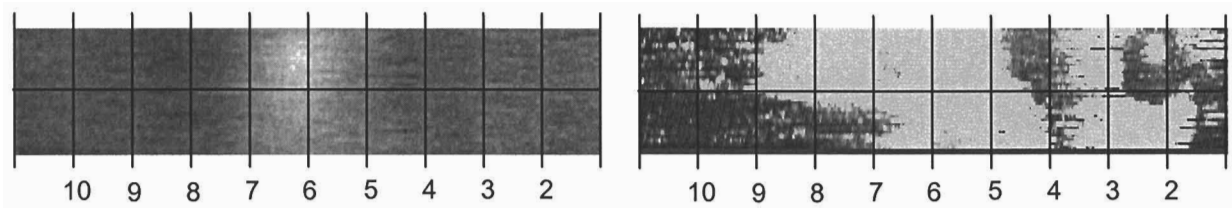

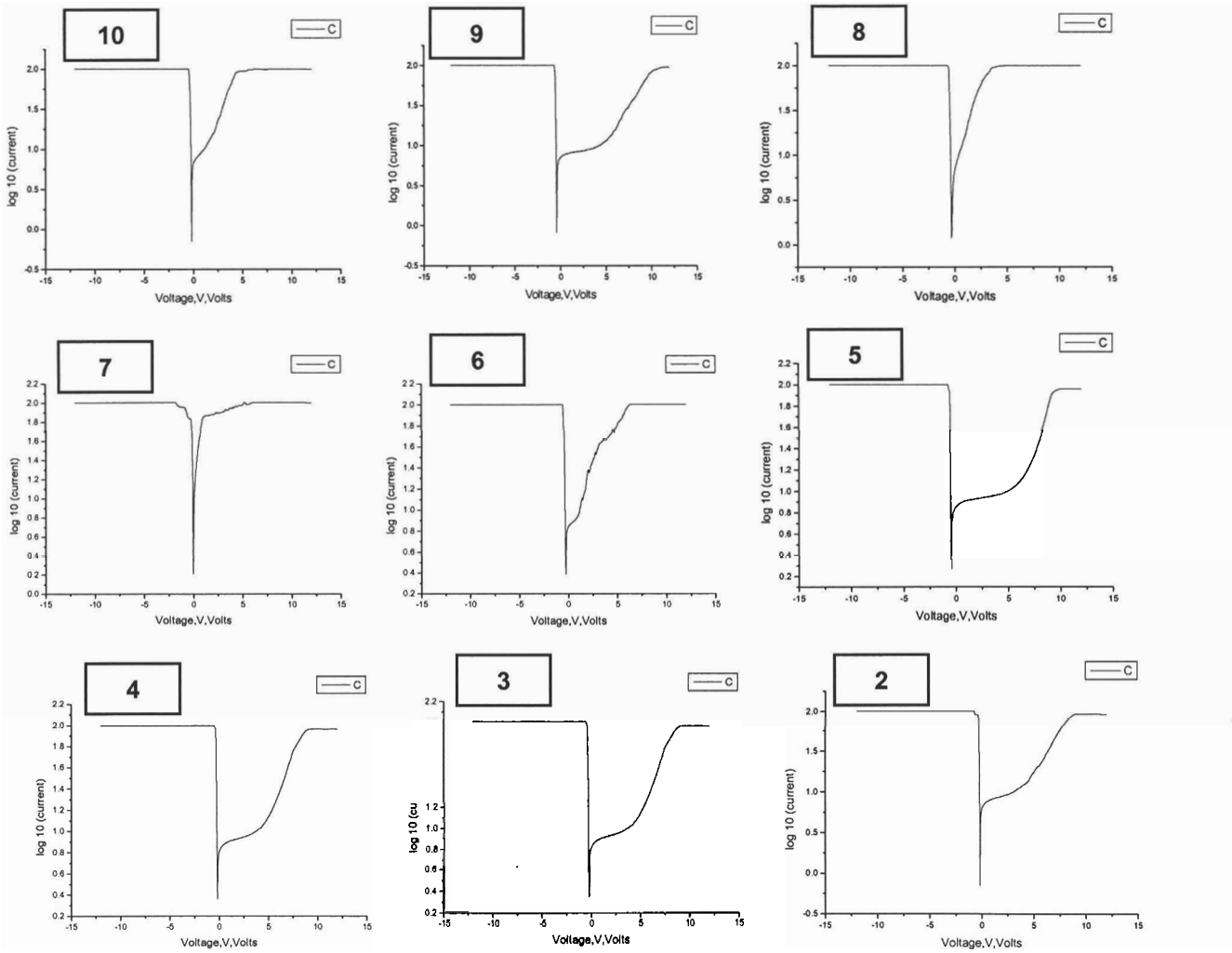

M1921 I-V Spectra (Upper Left Corner): 0.5μm × 2μm, 12V

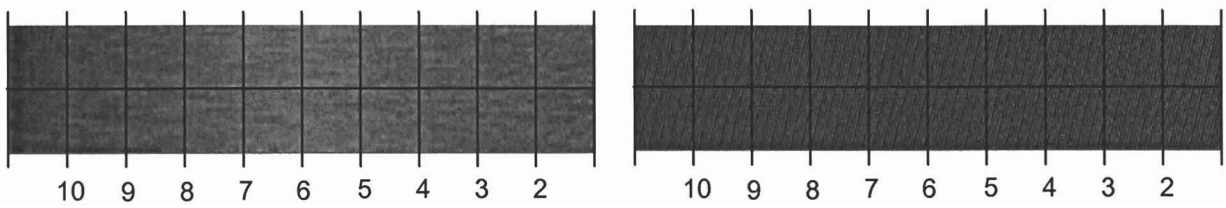

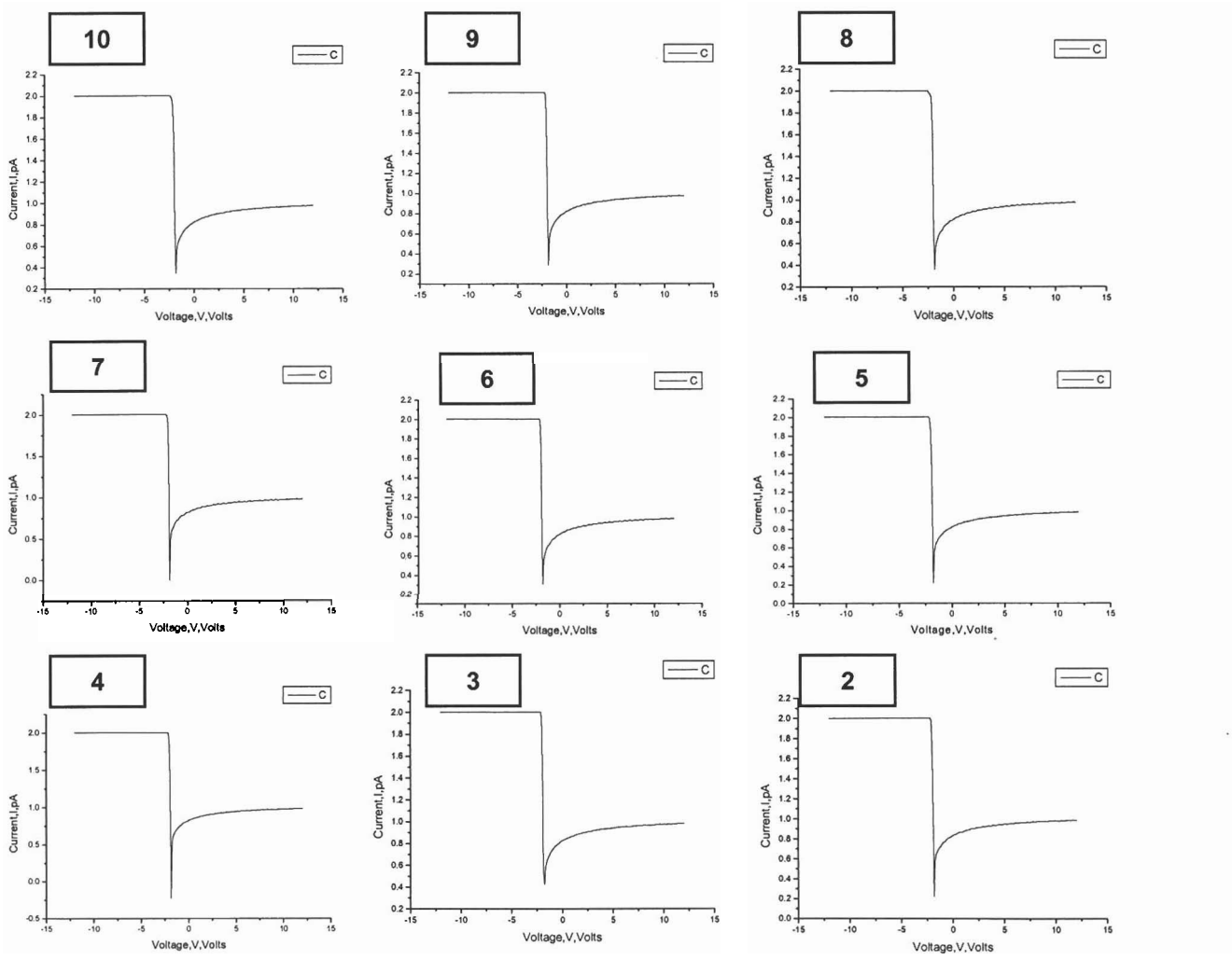

M1921 I-V Spectra (Lower Right Corner): 0.5μm × 2μm, 12V

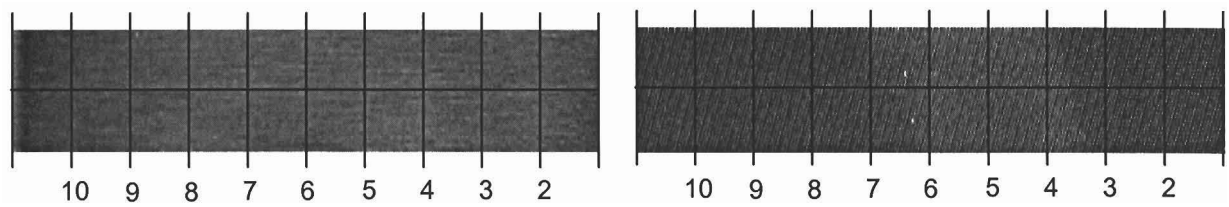

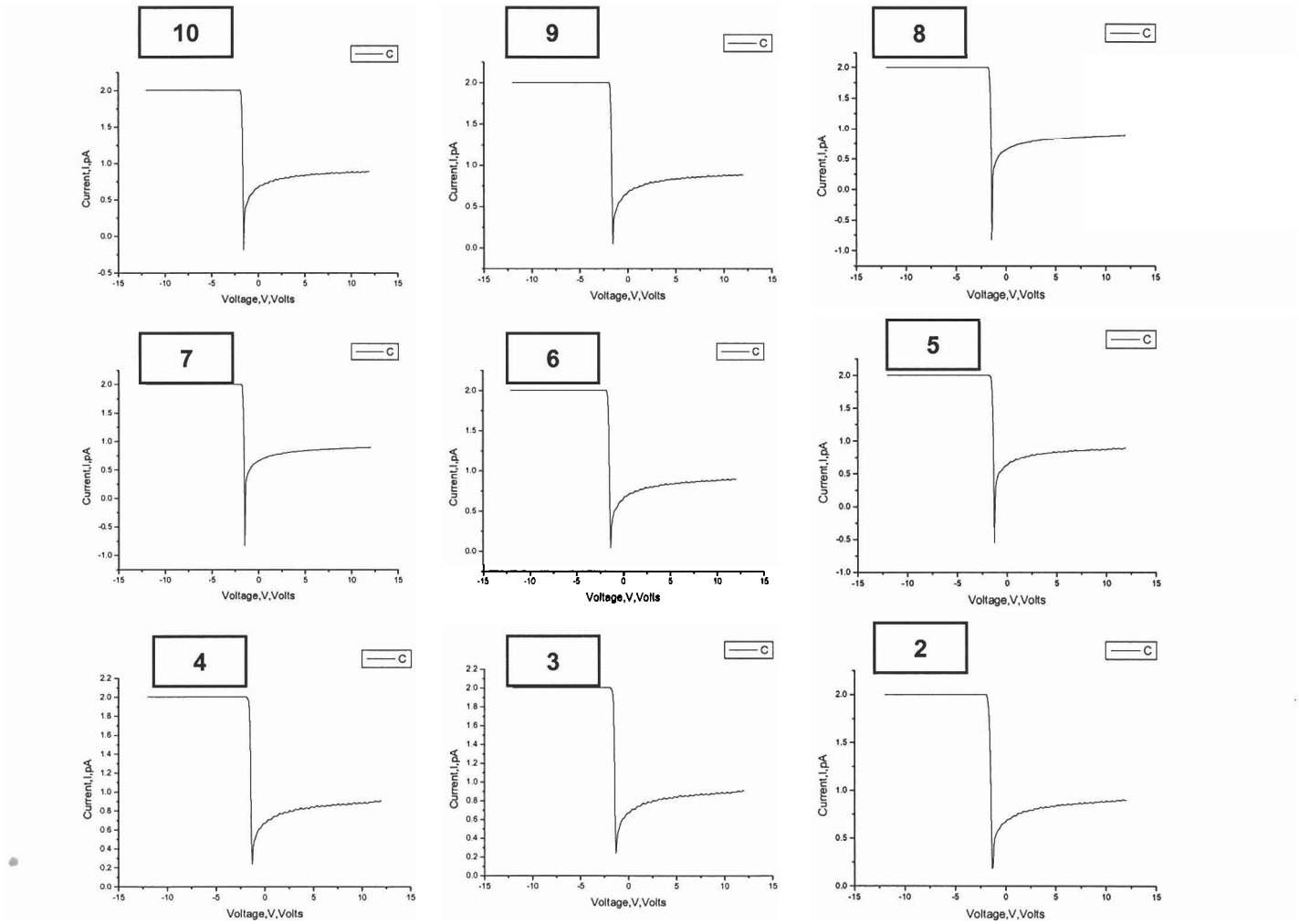

M1966 I-V Spectra (Upper Left Corner): 0.25μm × 1μm, 5V

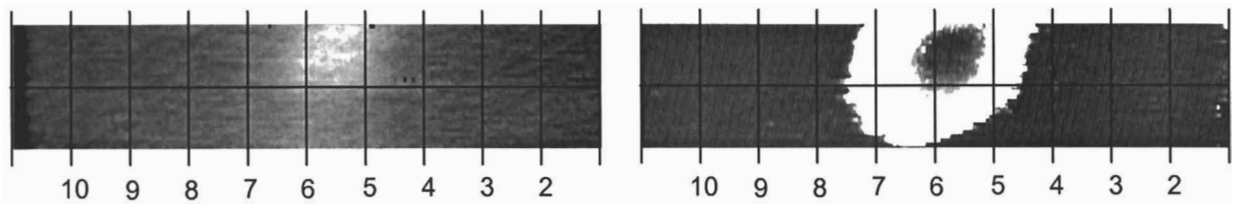

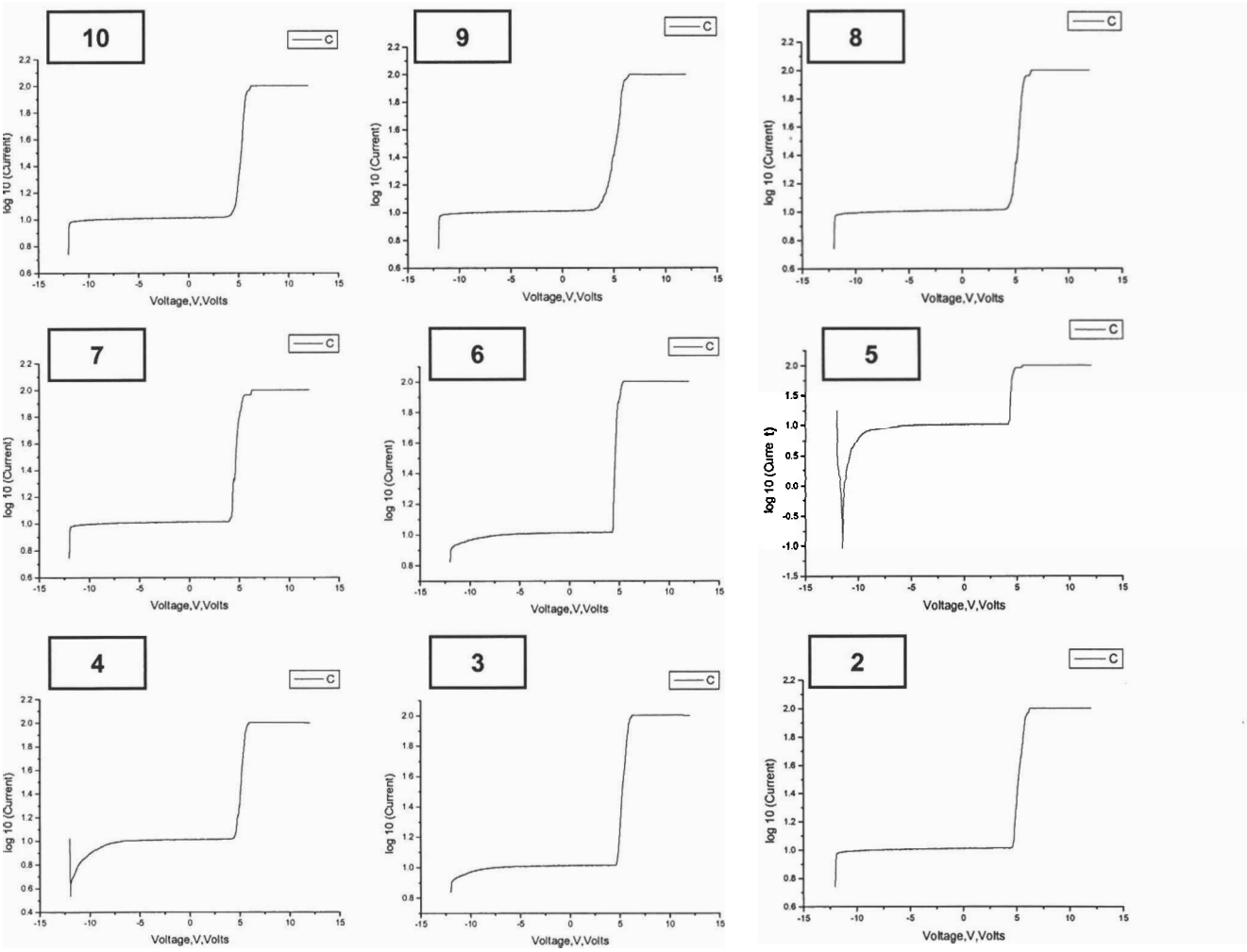

M1966 I-V Spectra (Lower Right Corner): 0.25μm × 1μm, 5V

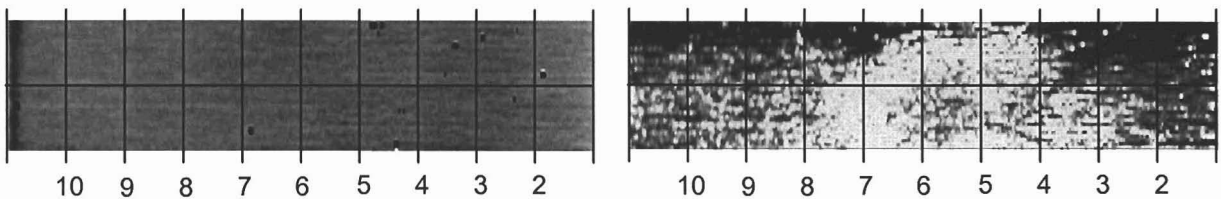

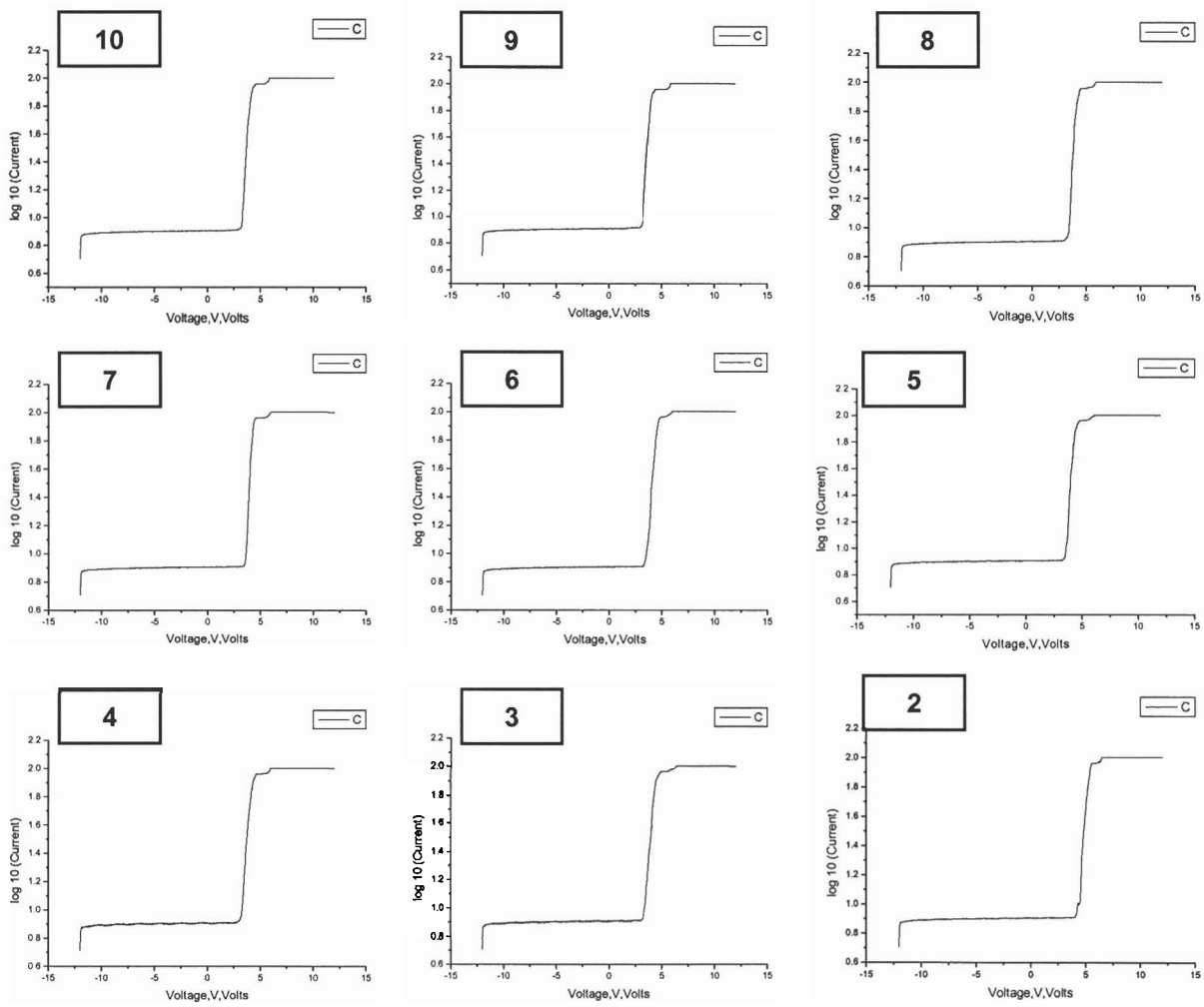

M1966b I-V Spectra (Upper Left Corner): 0.25μm × 1μm, 2V

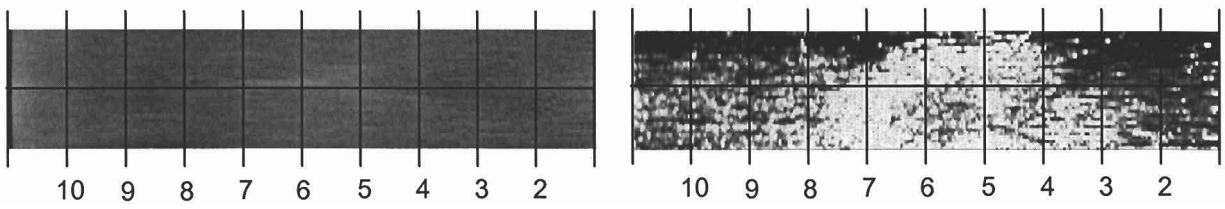

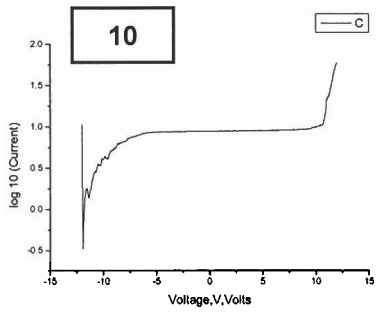

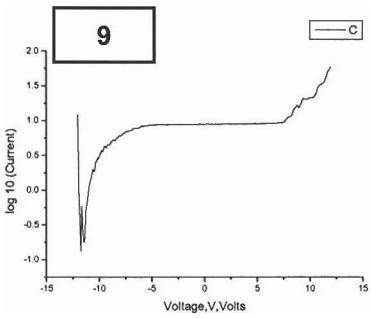

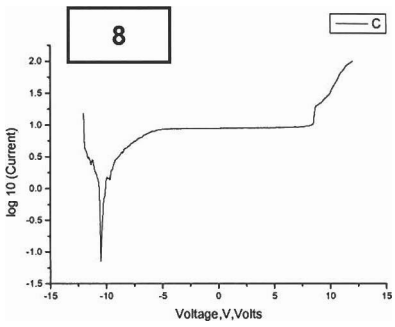

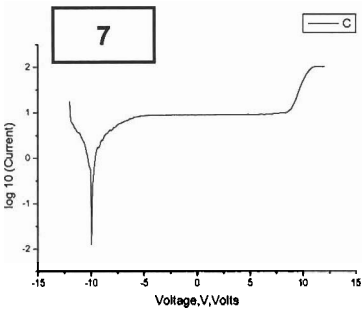

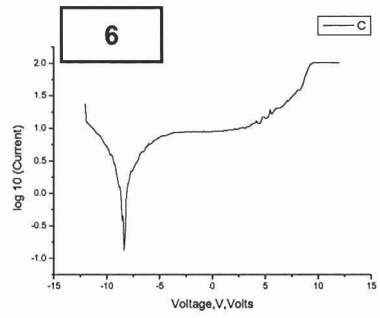

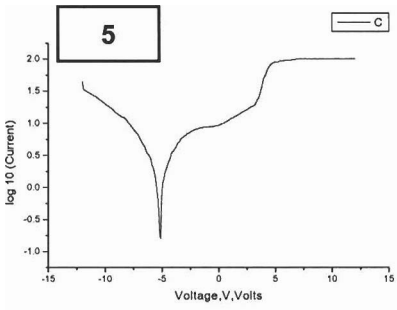

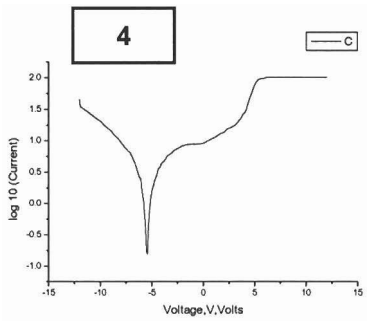

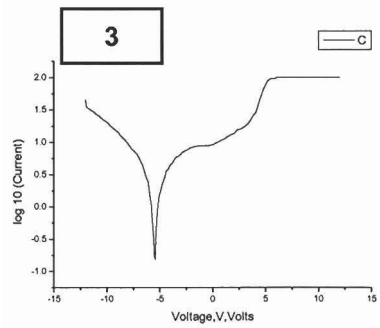

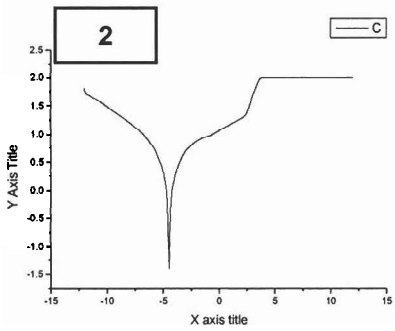

M1966b I-V Spectra (Lower Right Corner): 0.25μm × 1μm, 2V

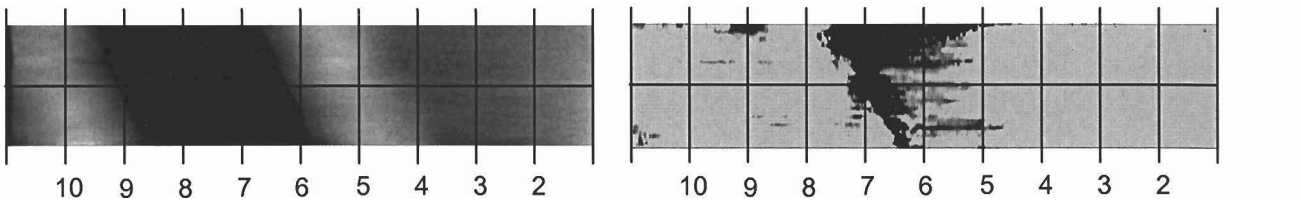

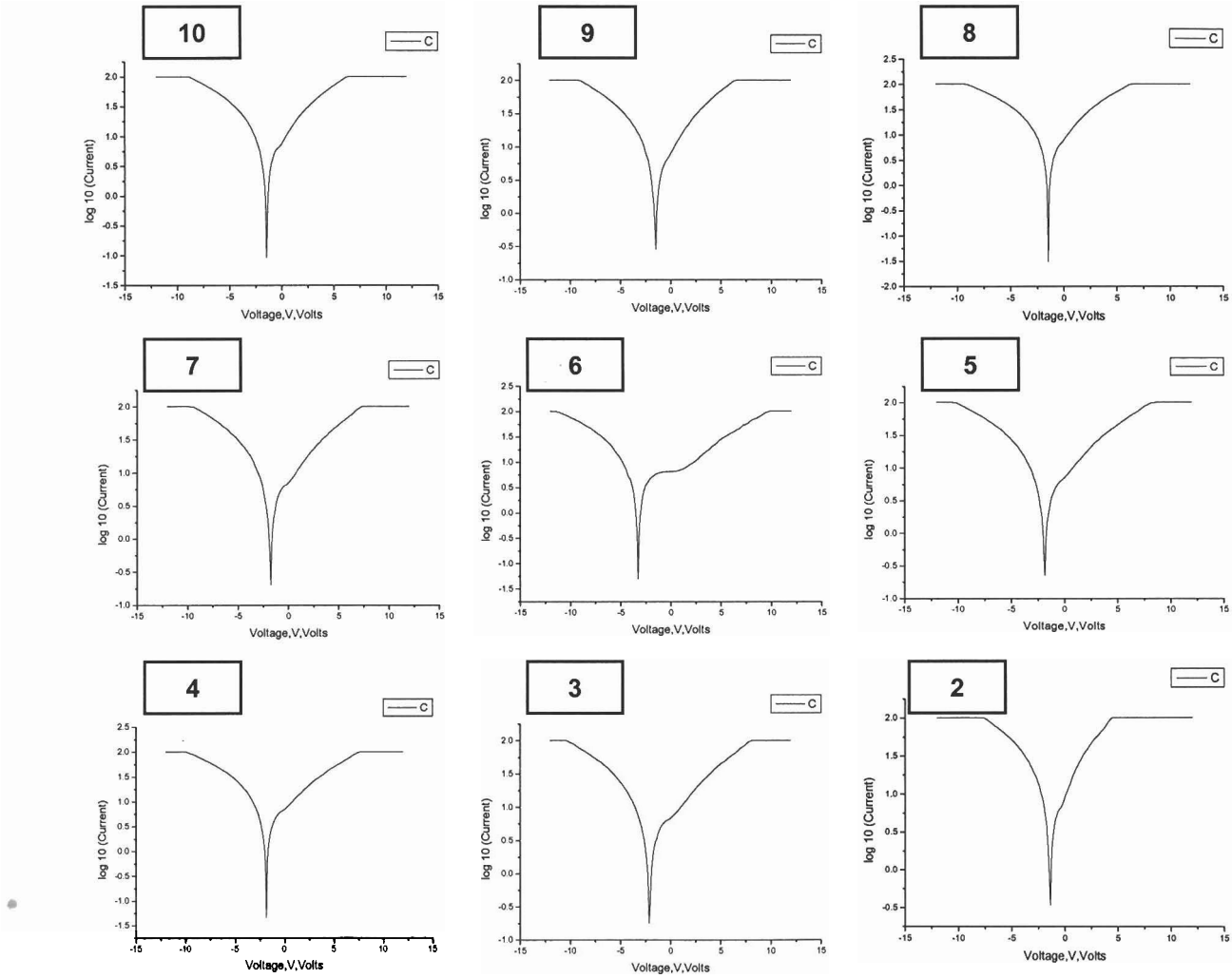

M2004 I-V Spectra (Upper Left Corner): 0.25μm × 1μm, 5V

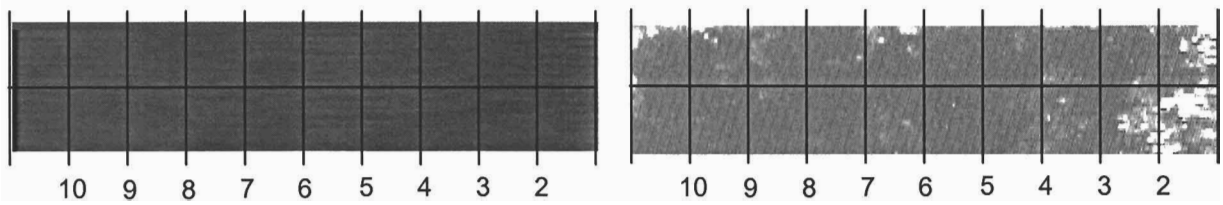

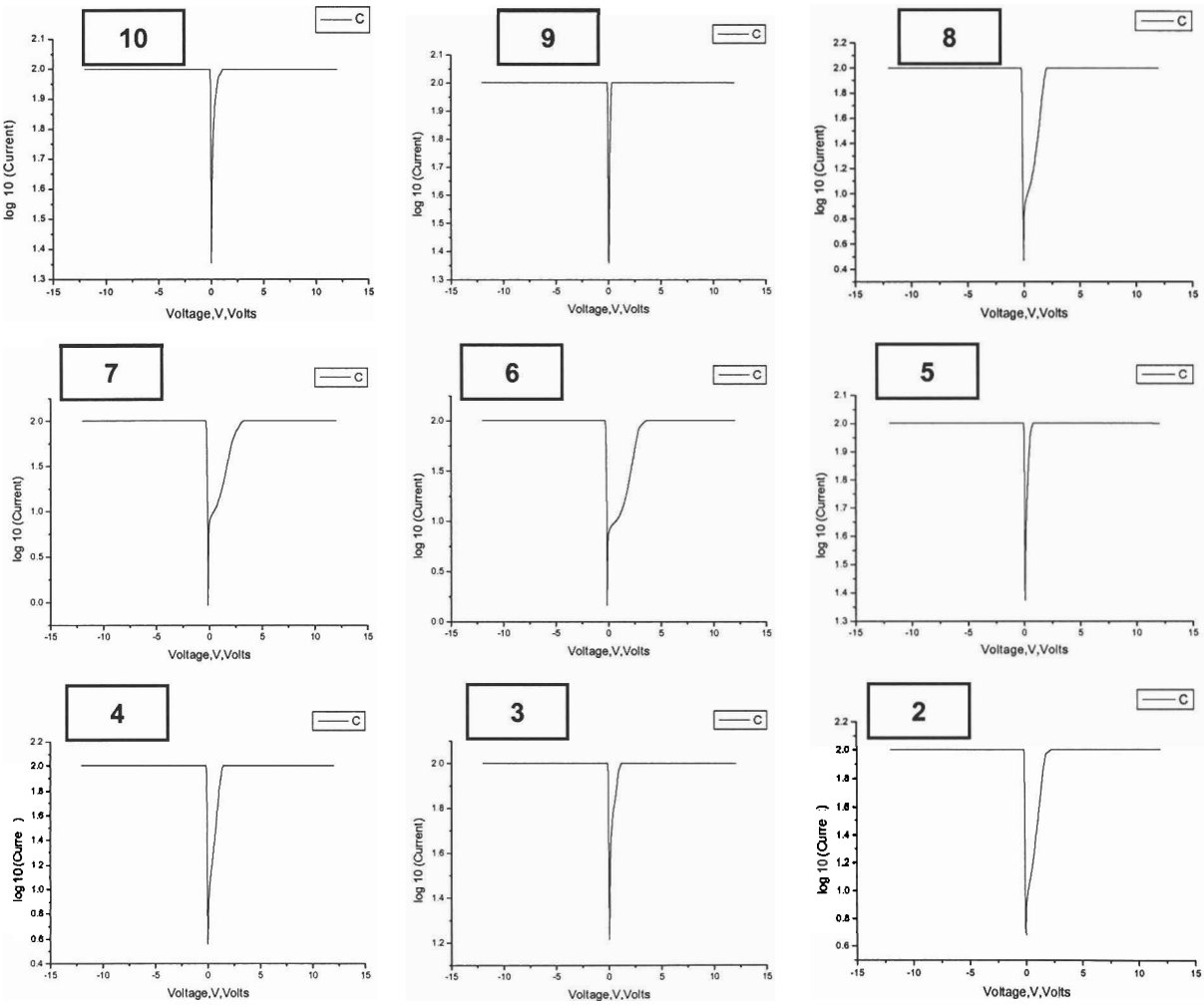

M2004 I-V Spectra (Lower Right Corner): 0.25μm × 1μm, 5V

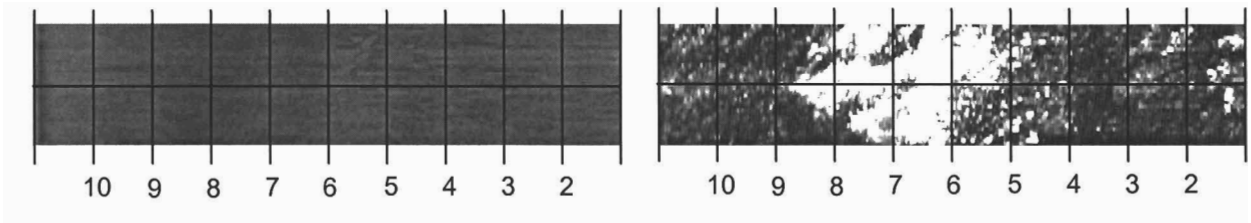

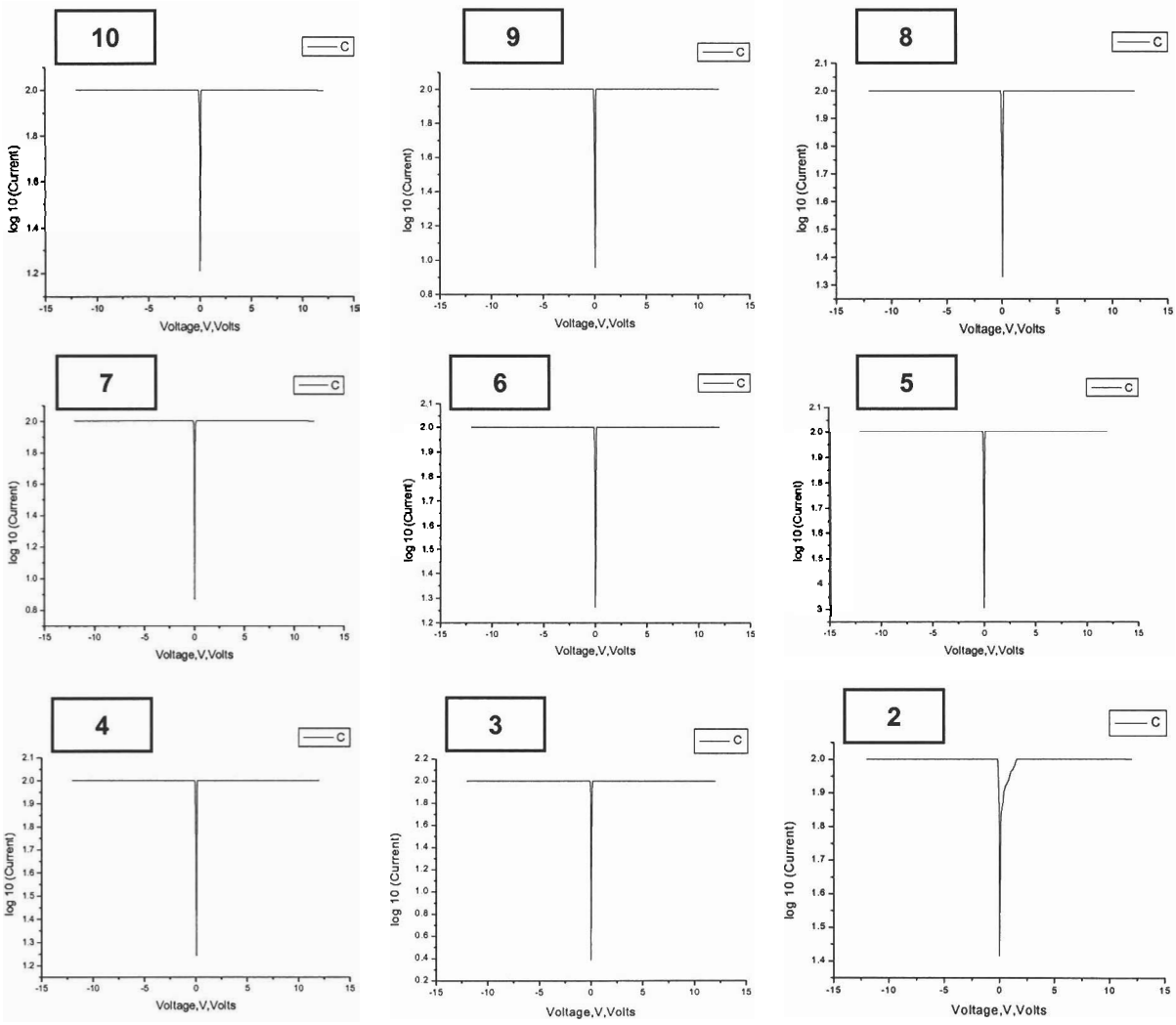

M2009 I-V Spectra (Upper Left Corner): 0.25μm × 1μm, 10V

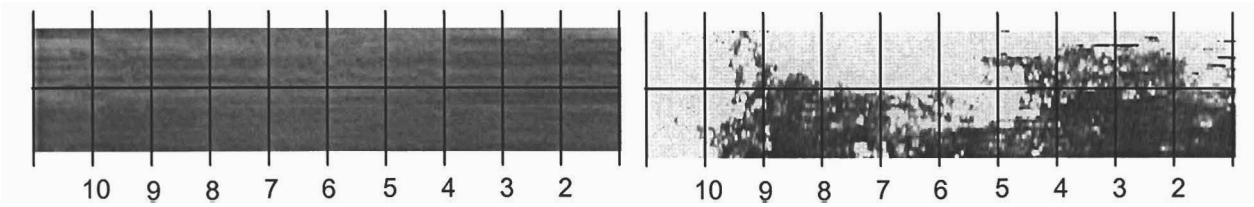

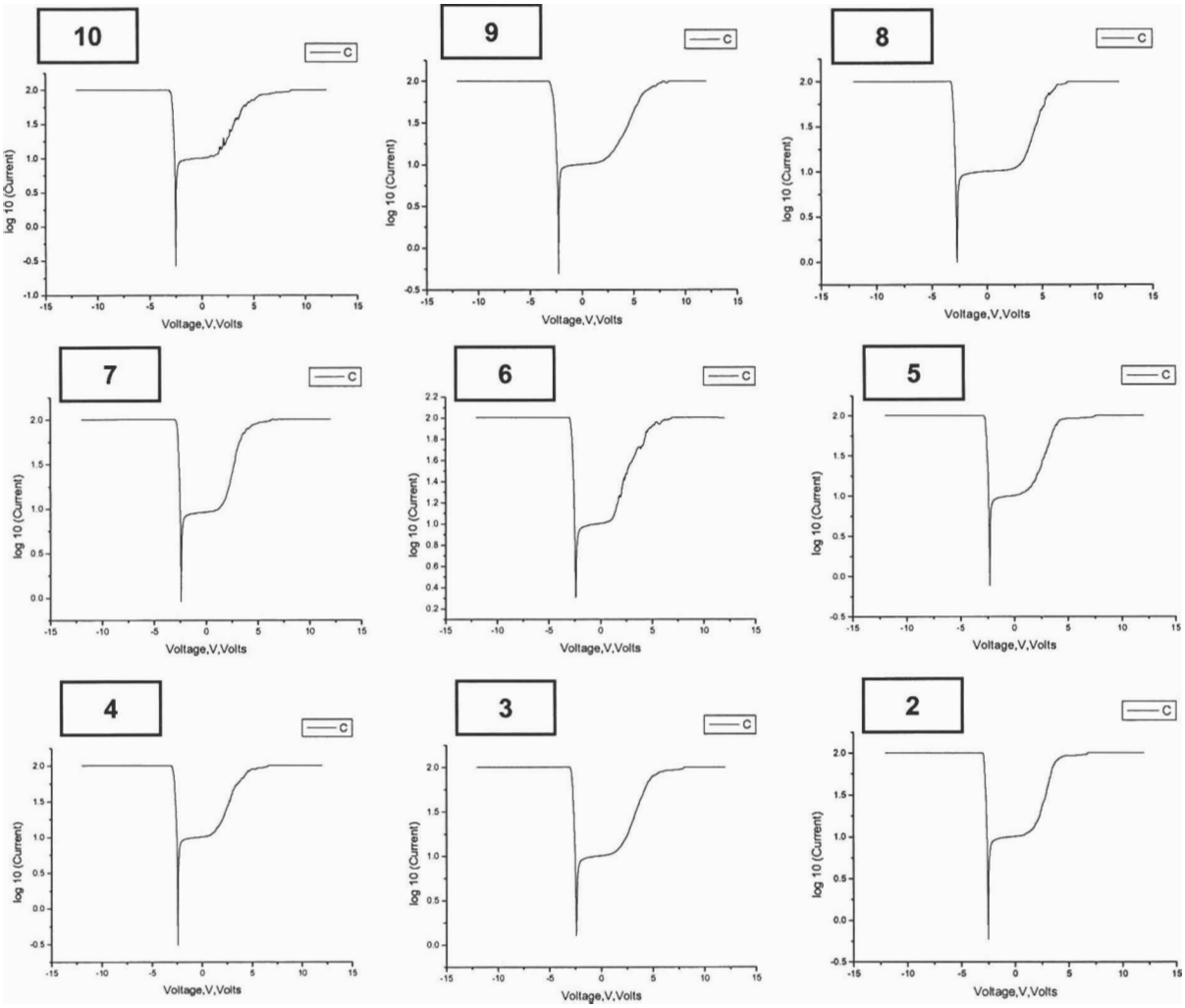

M2009 I-V Spectra (Lower Right Corner): 0.25μm × 1μm, 10V

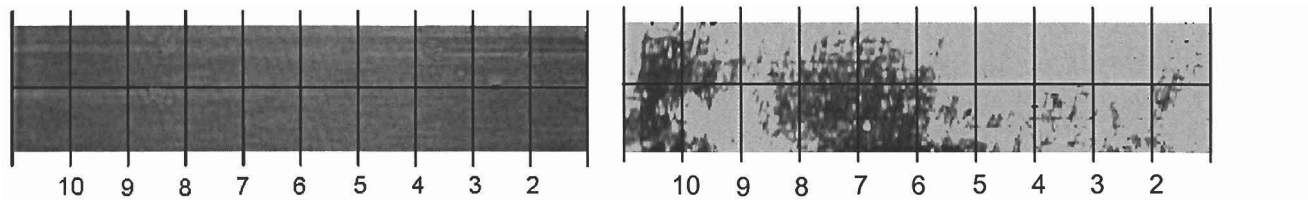

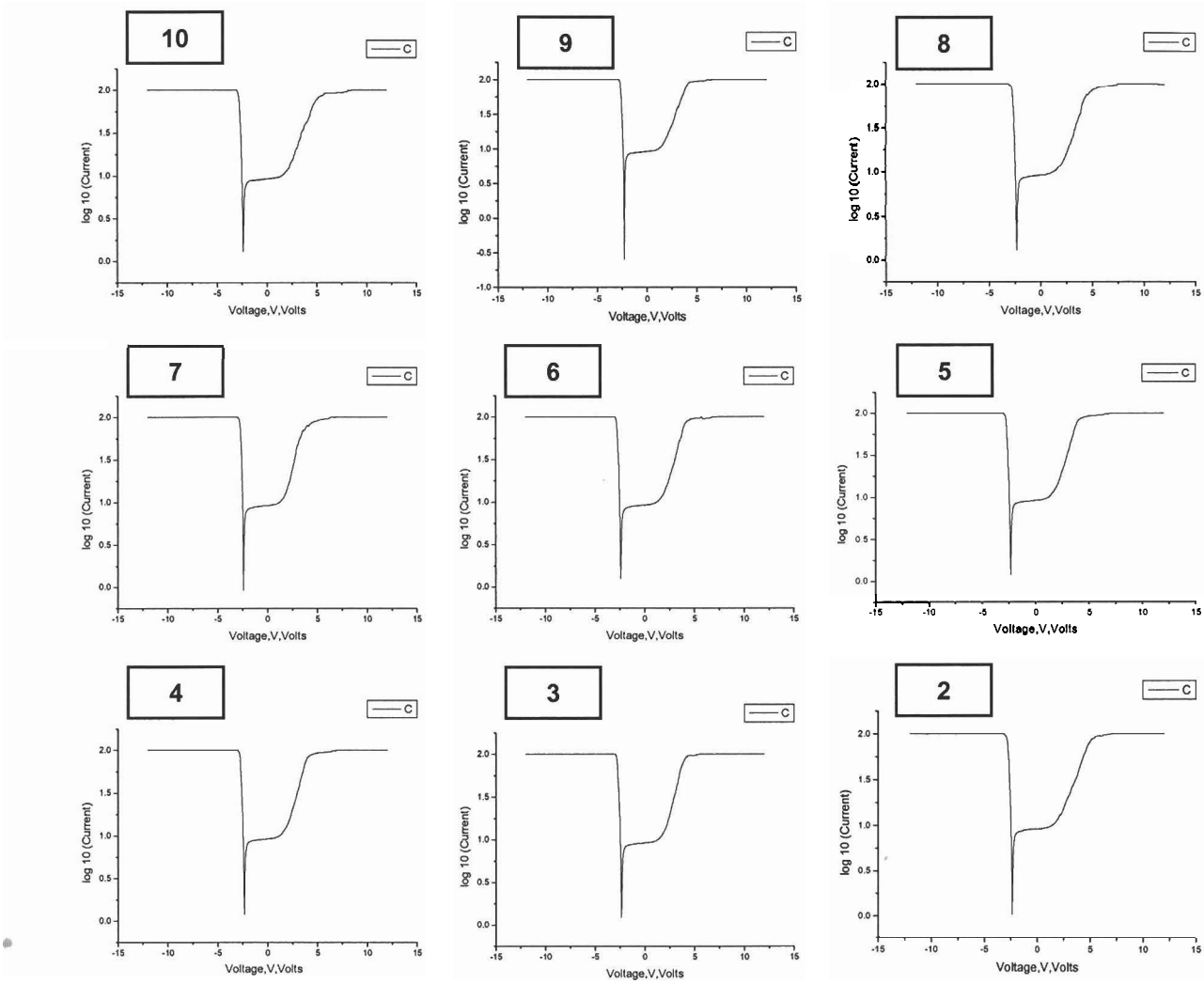

M2024 I-V Spectra (Upper Left Corner): 0.25μm × 1μm, 6V

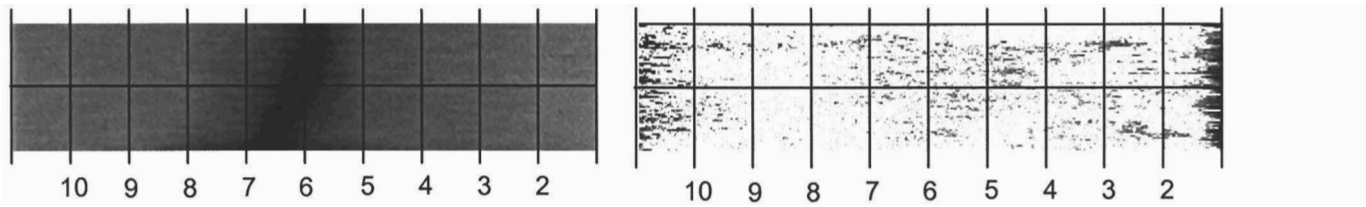

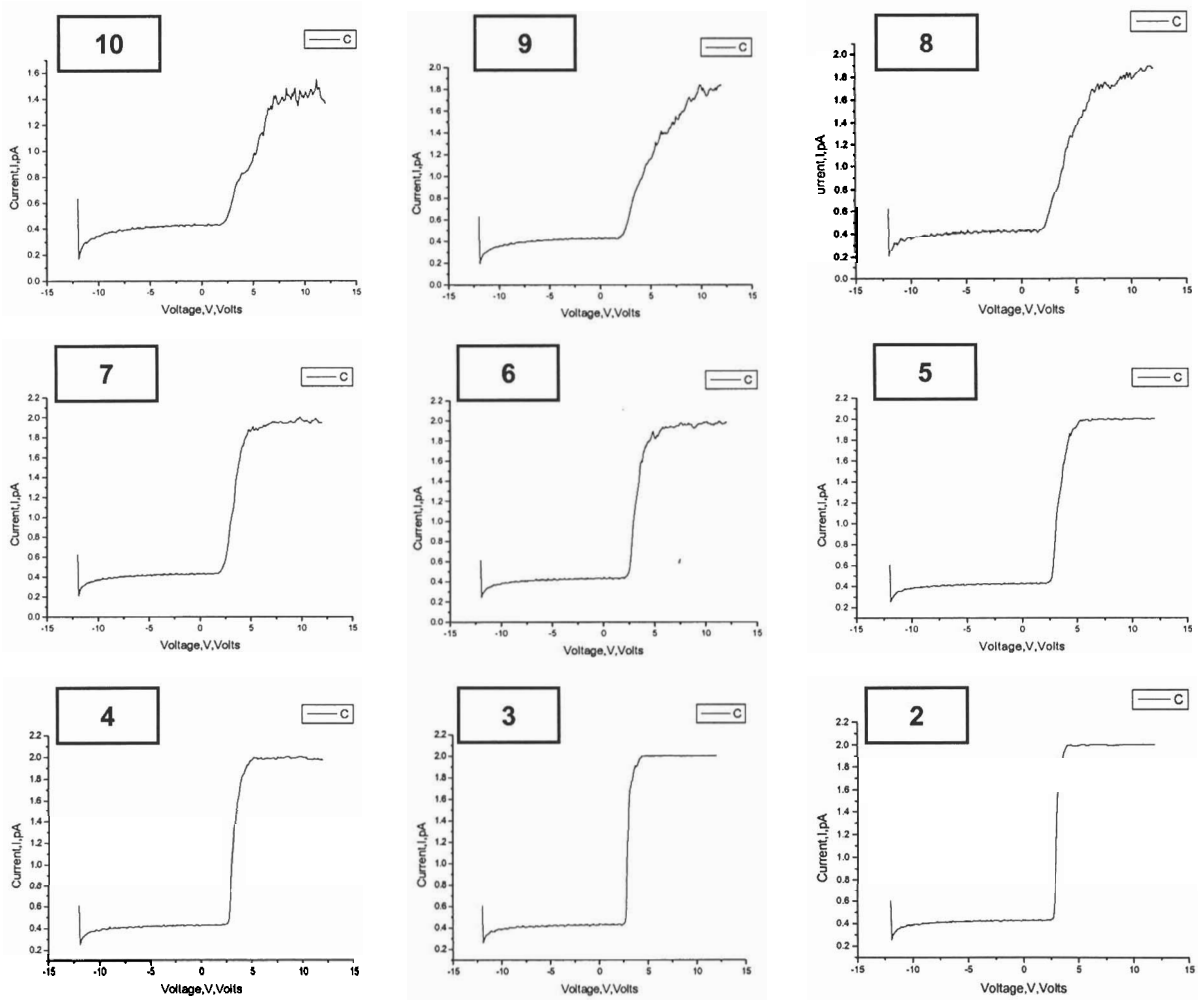

M2024 I-V Spectra (Lower Right Corner): 0.25μm × 1μm, 12V

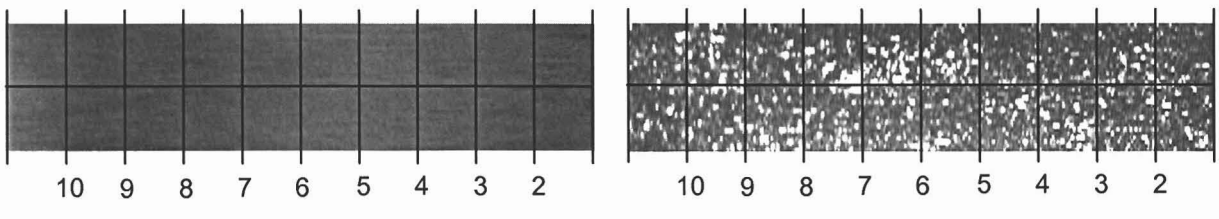

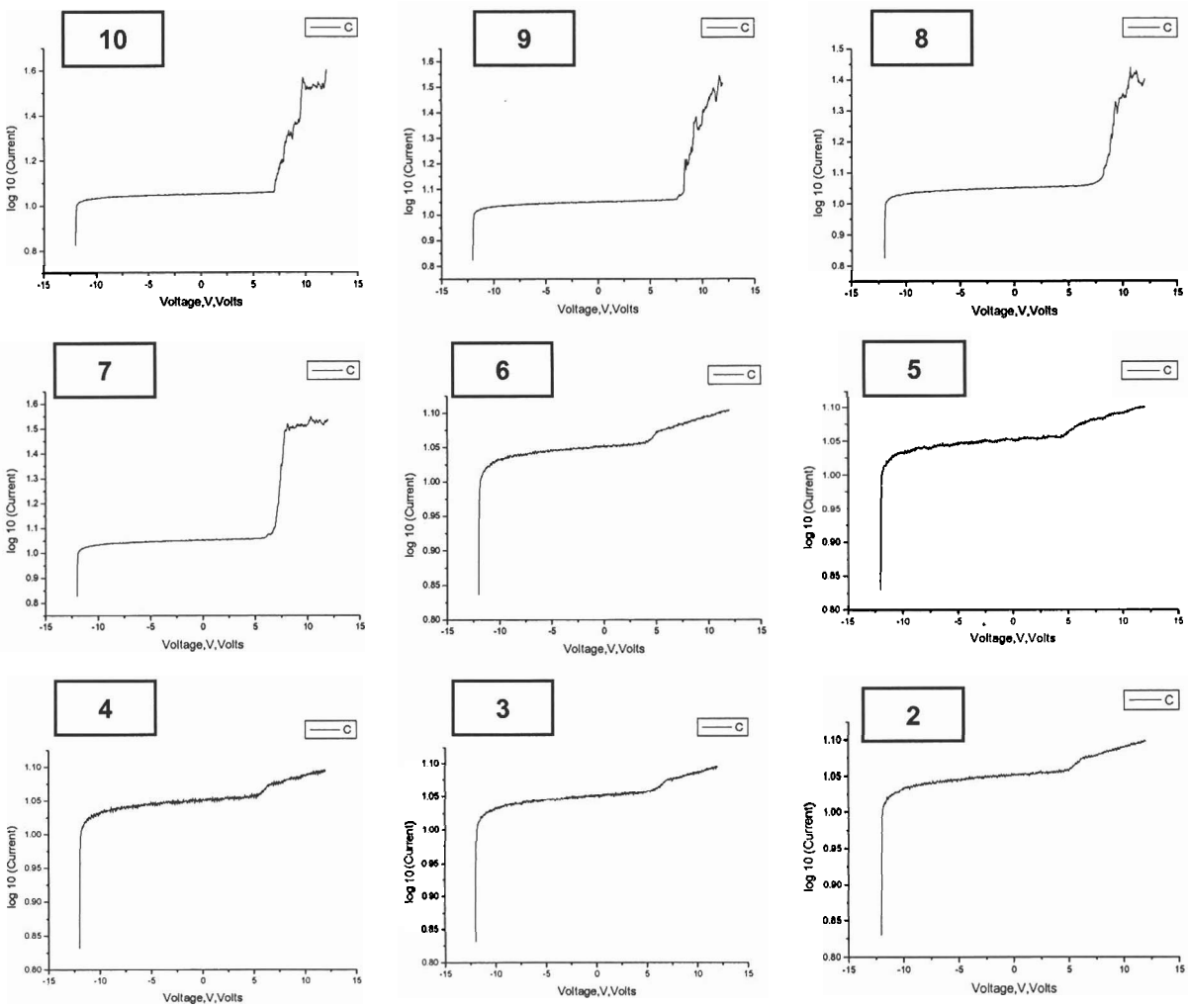

M2034 I-V Spectra (Upper Left Corner): 0.25μm × 1μm, 7V

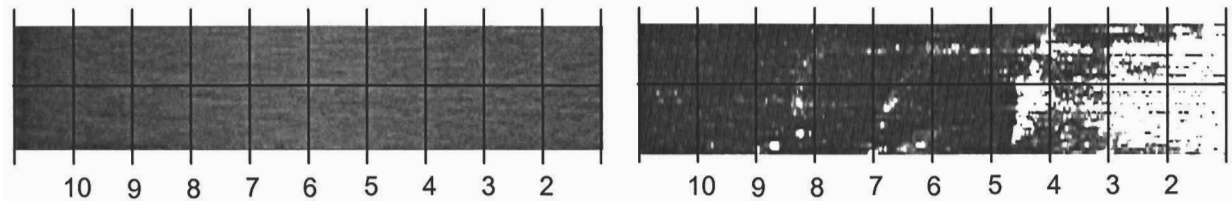

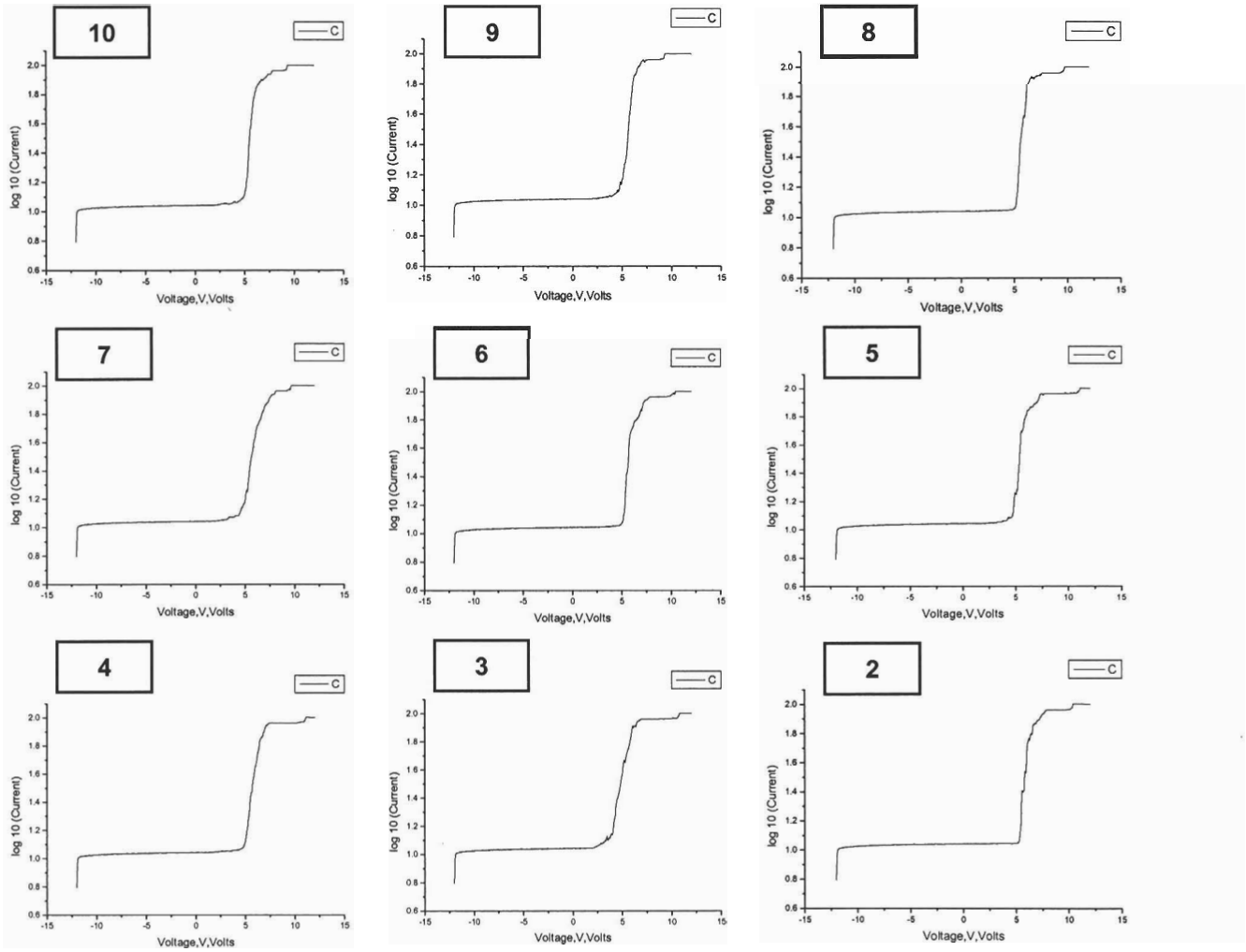

M2034 I-V Spectra (Lower Right Corner): 0.25μm × 1μm, 4V

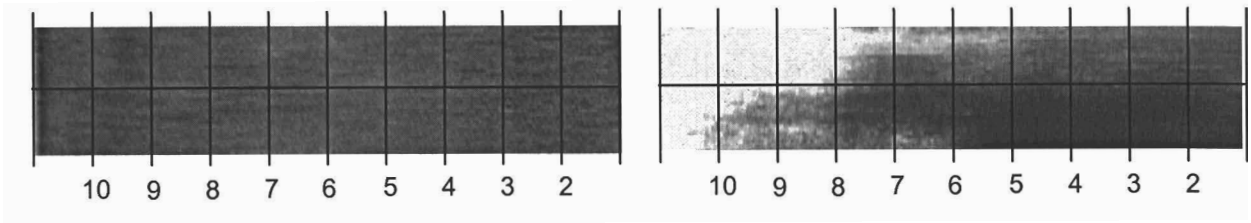

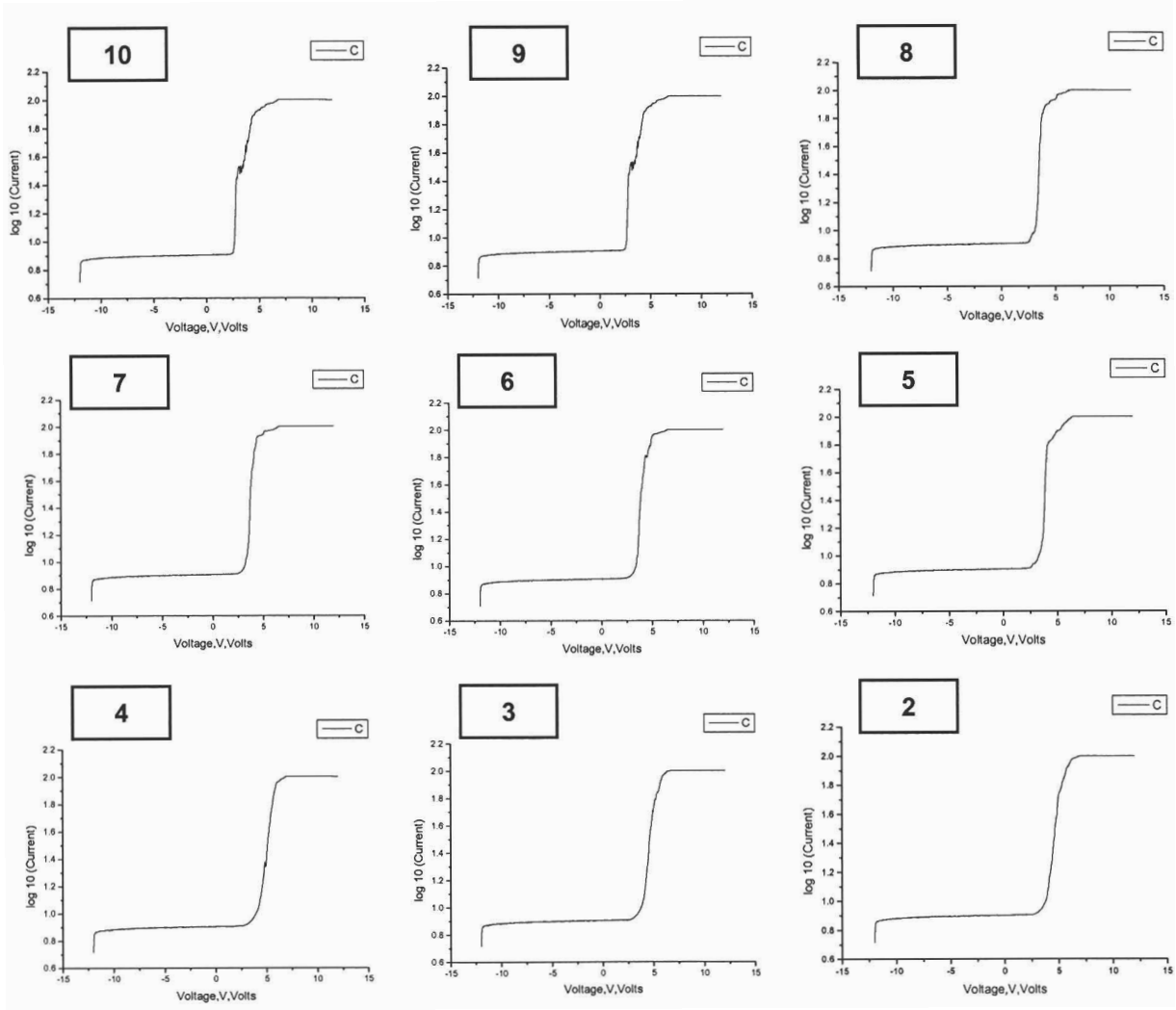

M2037 I-V Spectra (Upper Left Corner): 0.25μm × 1μm, 4V

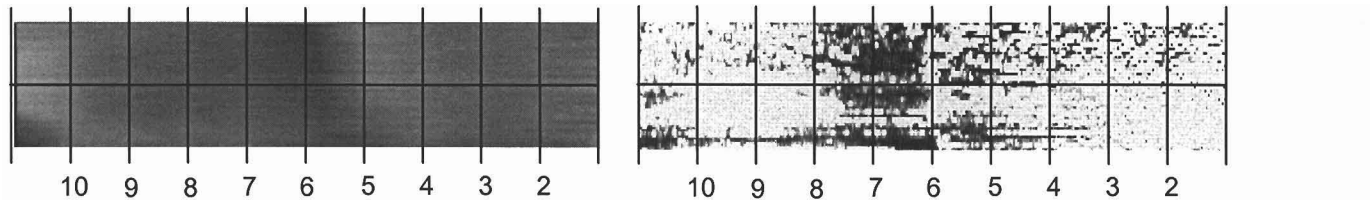

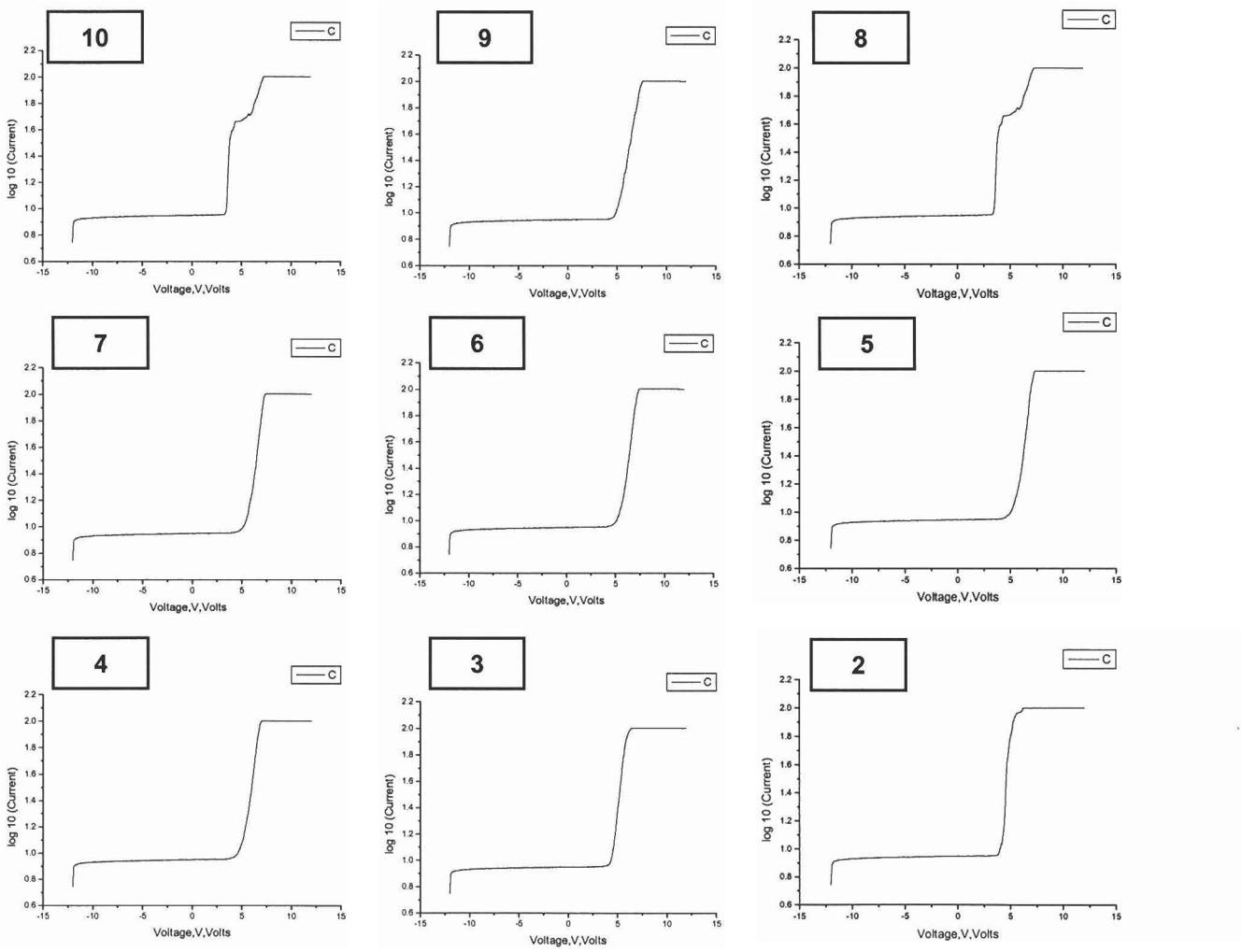

M2037 I-V Spectra (Lower Right Corner): 0.25μm × 1μm, 4V

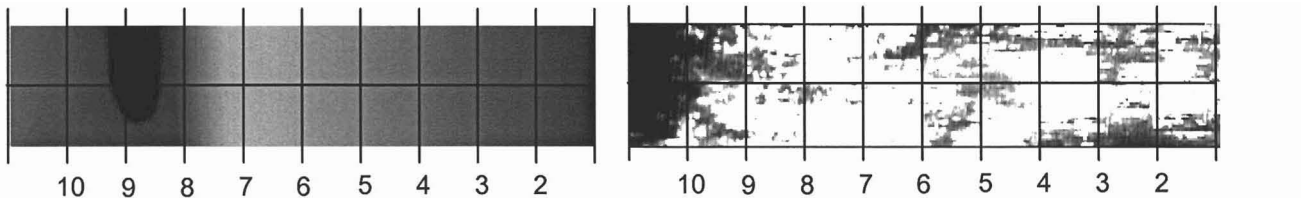

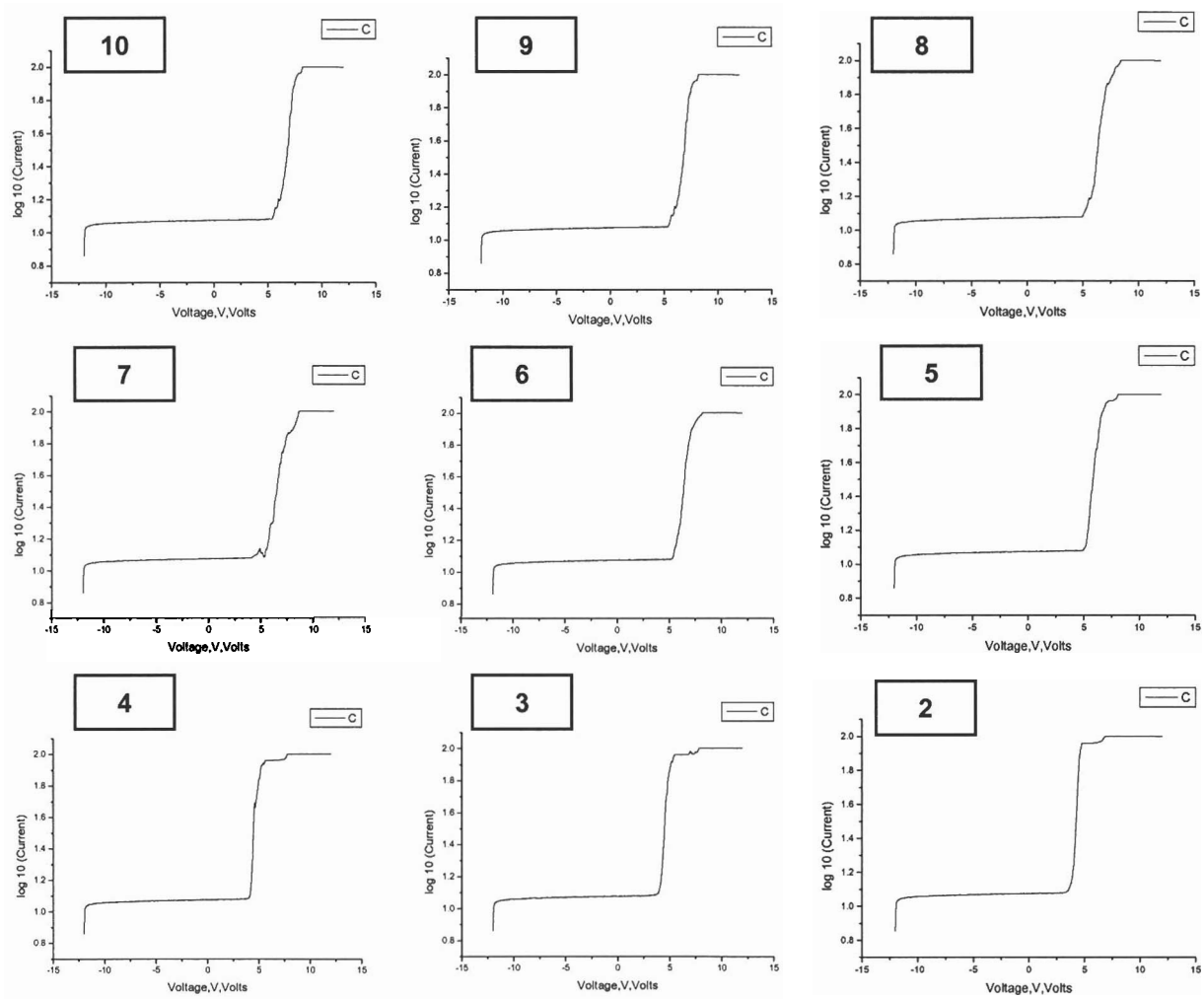

M2042 I-V Spectra (Upper Left Corner): 0.25μm × 1μm, 12V

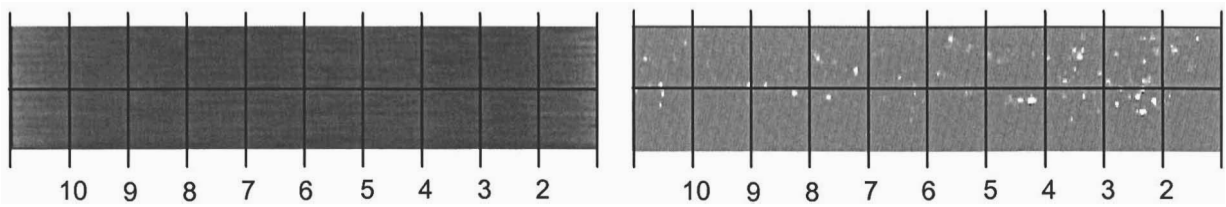

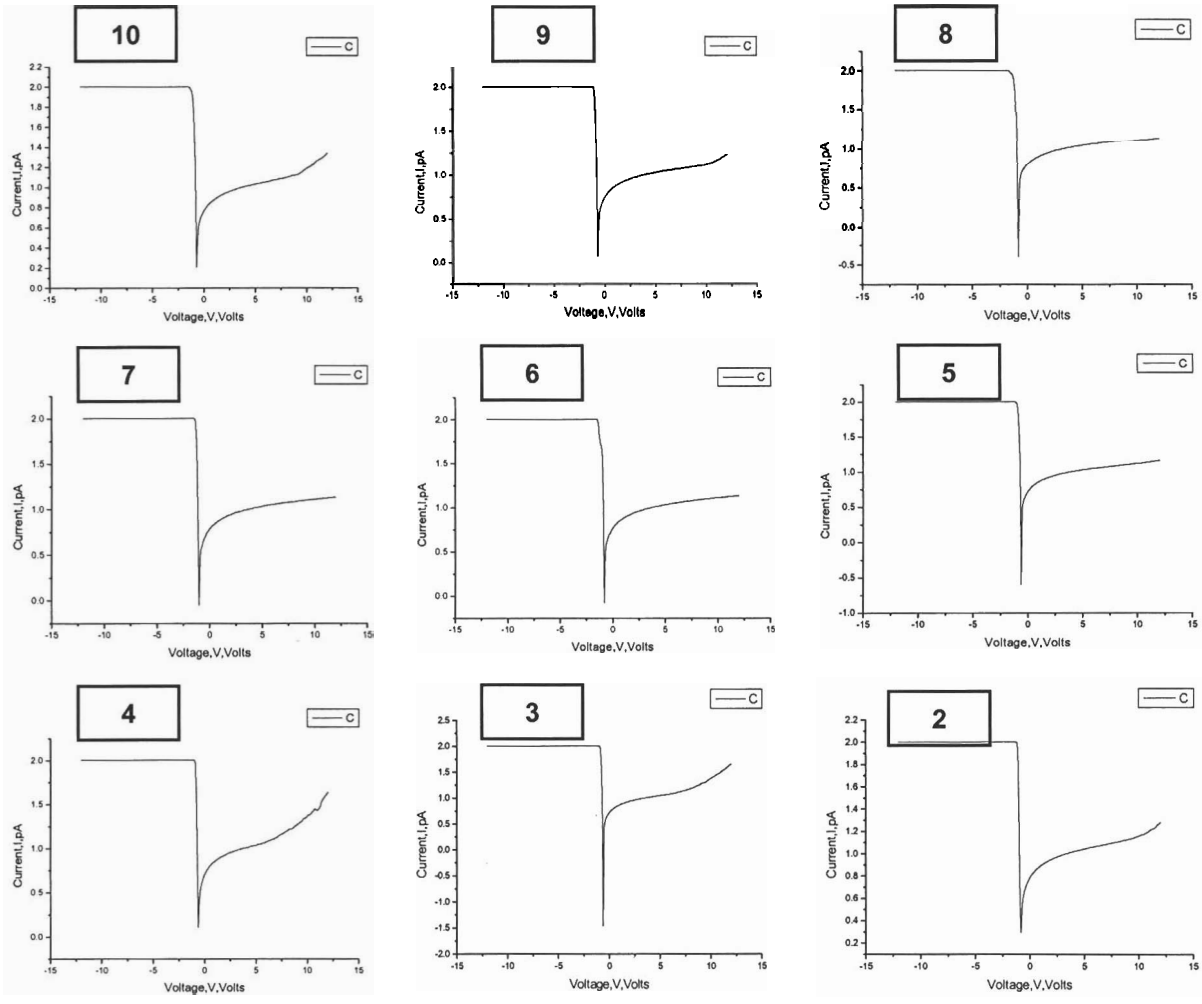

M2042 I-V Spectra (Lower Right Corner): 0.25μm × 1μm, 12V

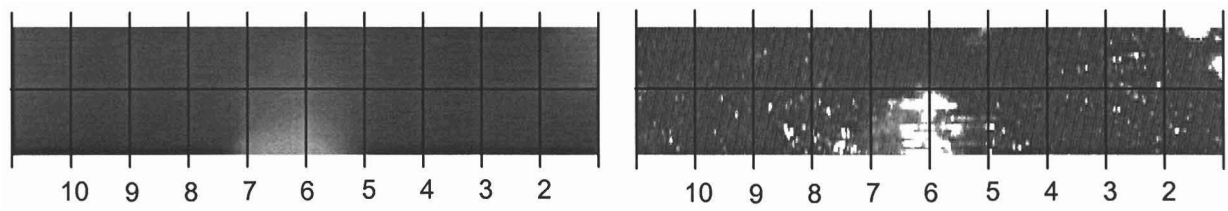

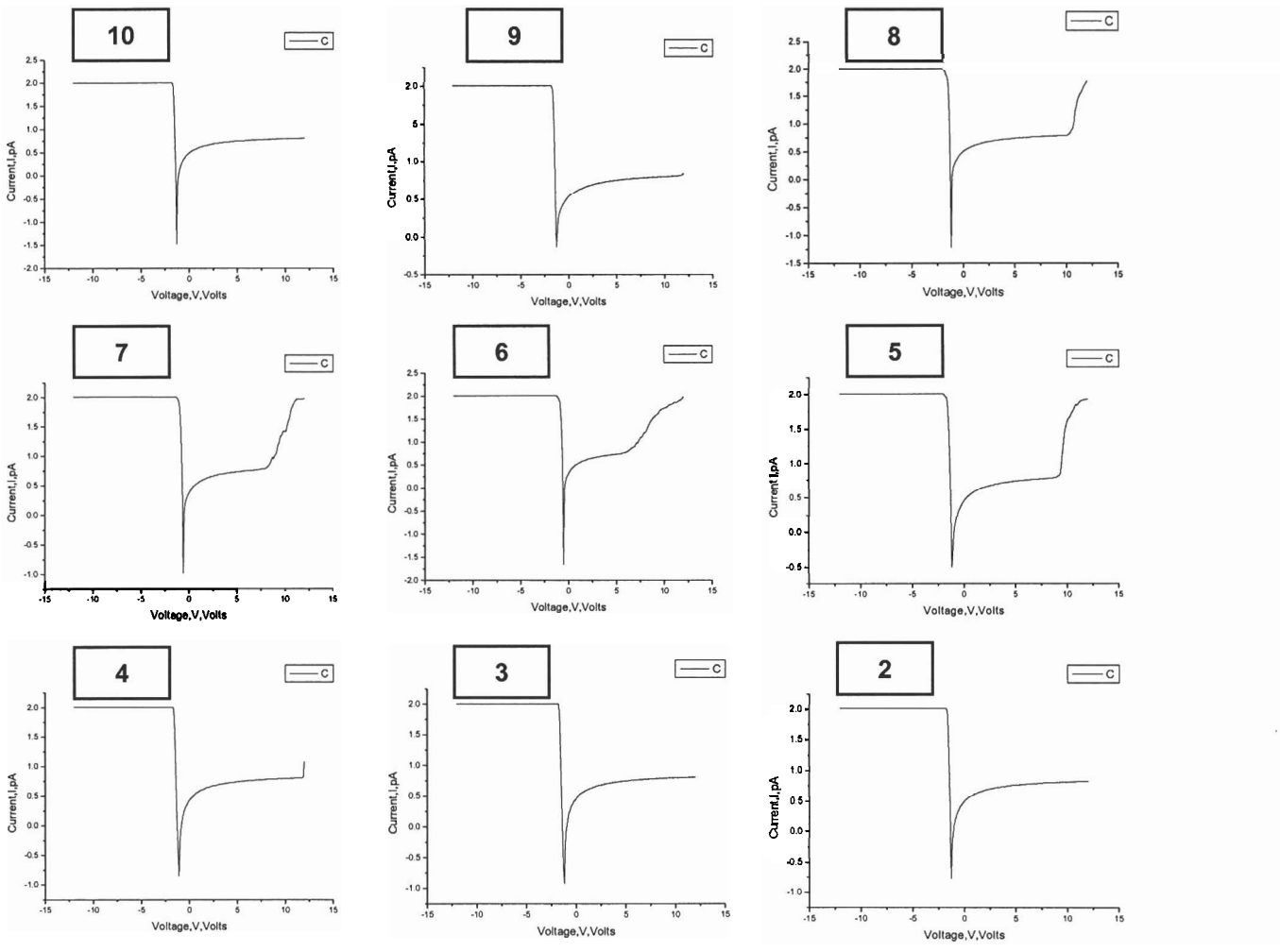

M2042b I-V Spectra (Upper Left Corner): 0.25μm × 1μm, 1V

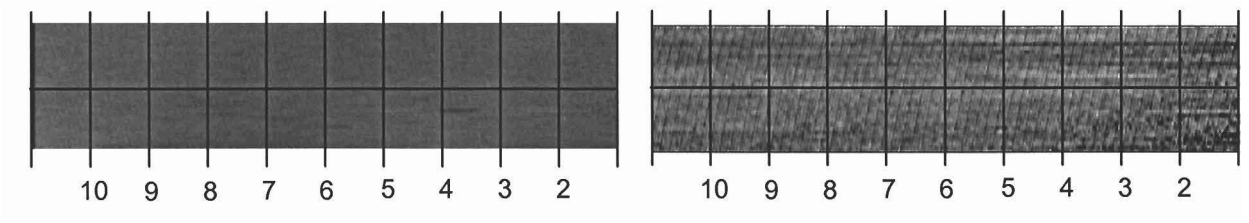

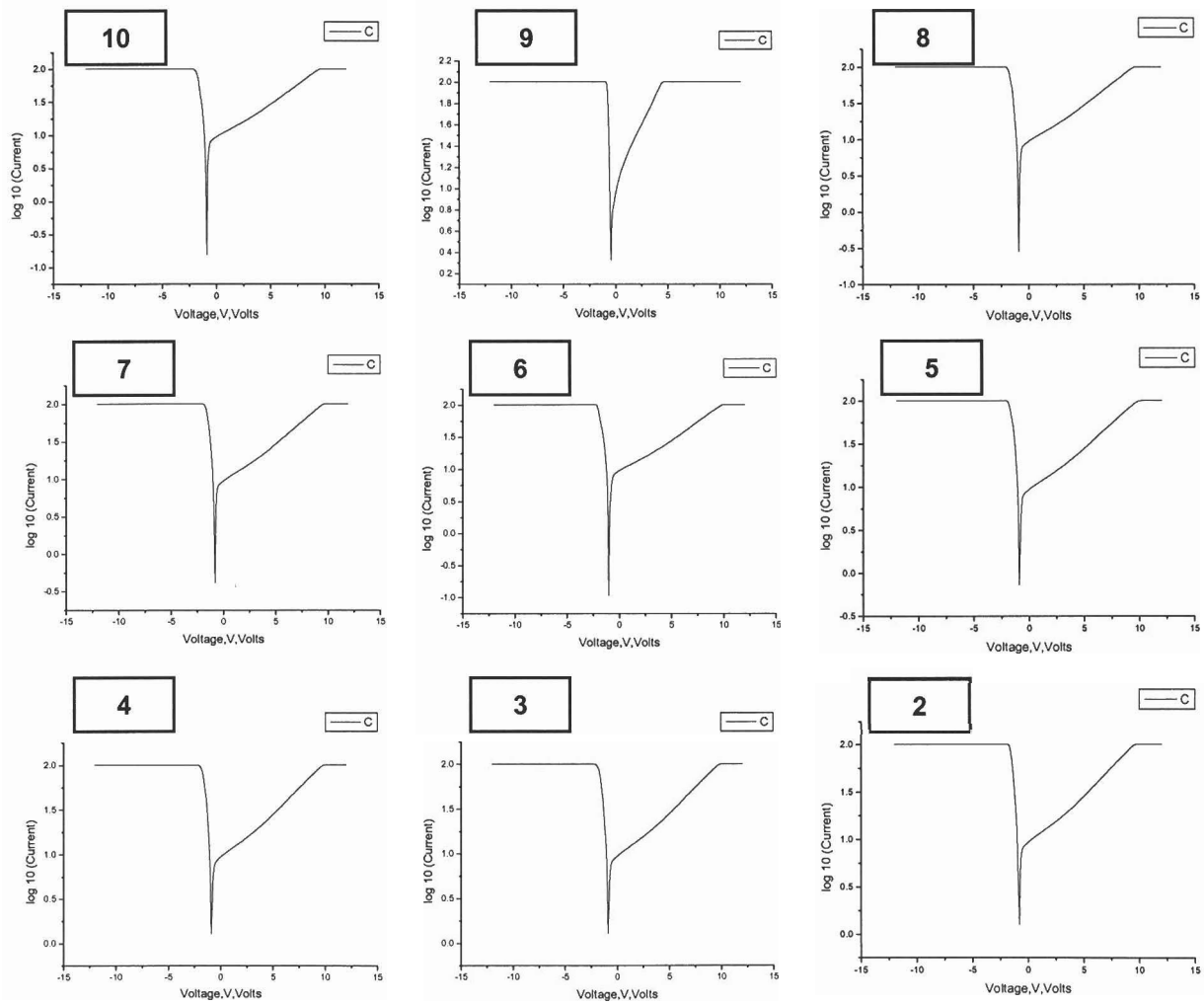

M2042b I-V Spectra (Lower Right Corner): 0.25μm × 1μm, 3V

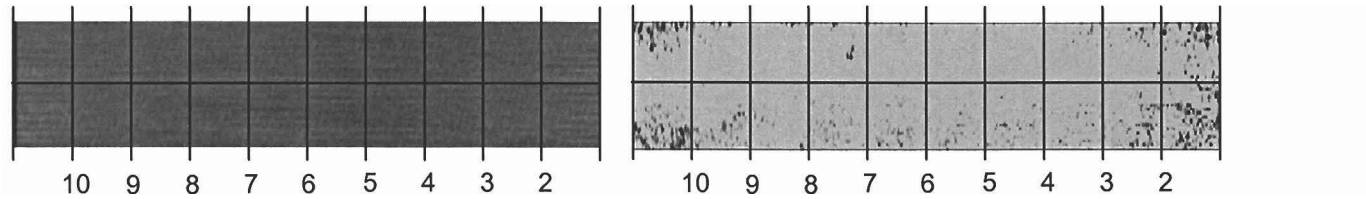

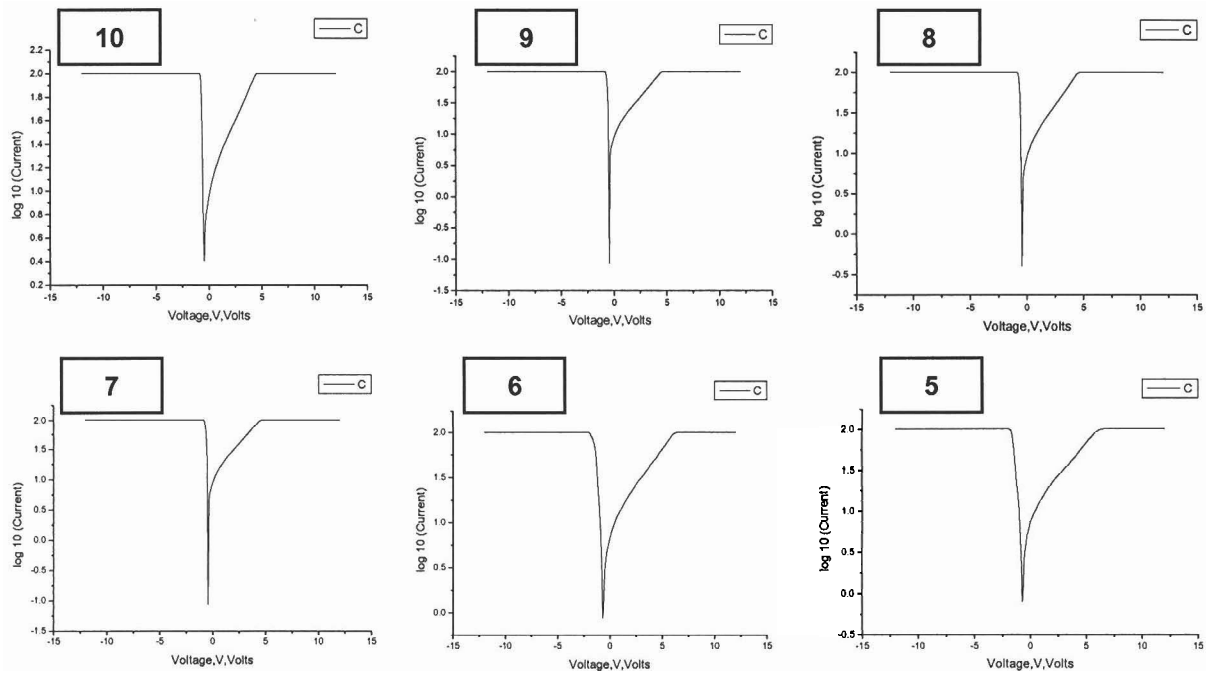

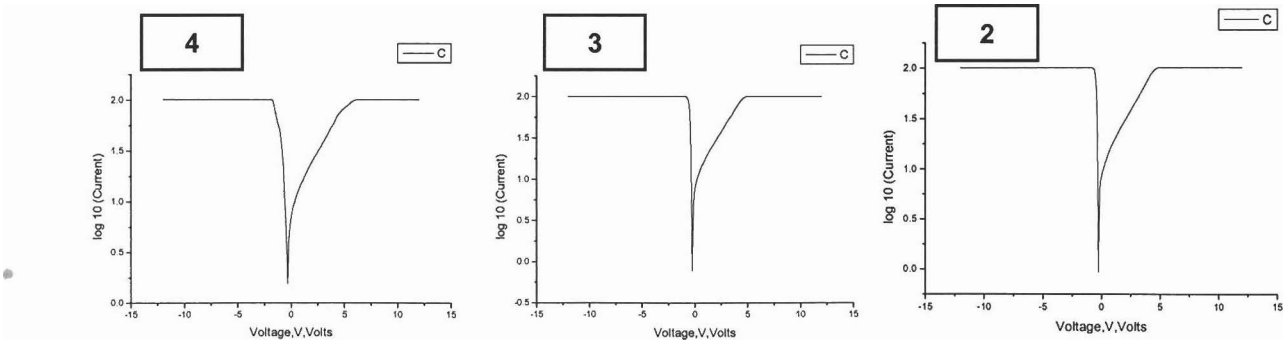

M2043 I-V (Upper Left Corner): 0.25μm × 1μm, 4V

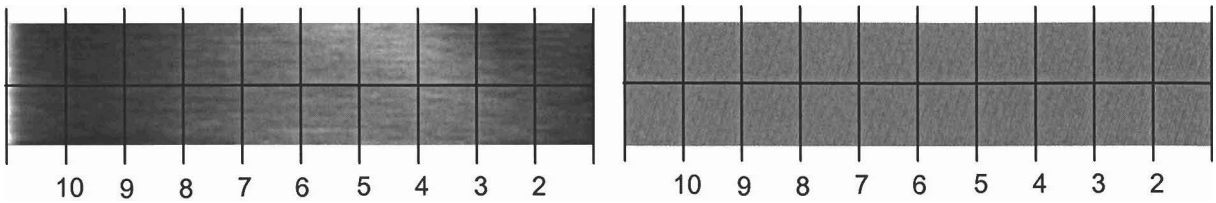

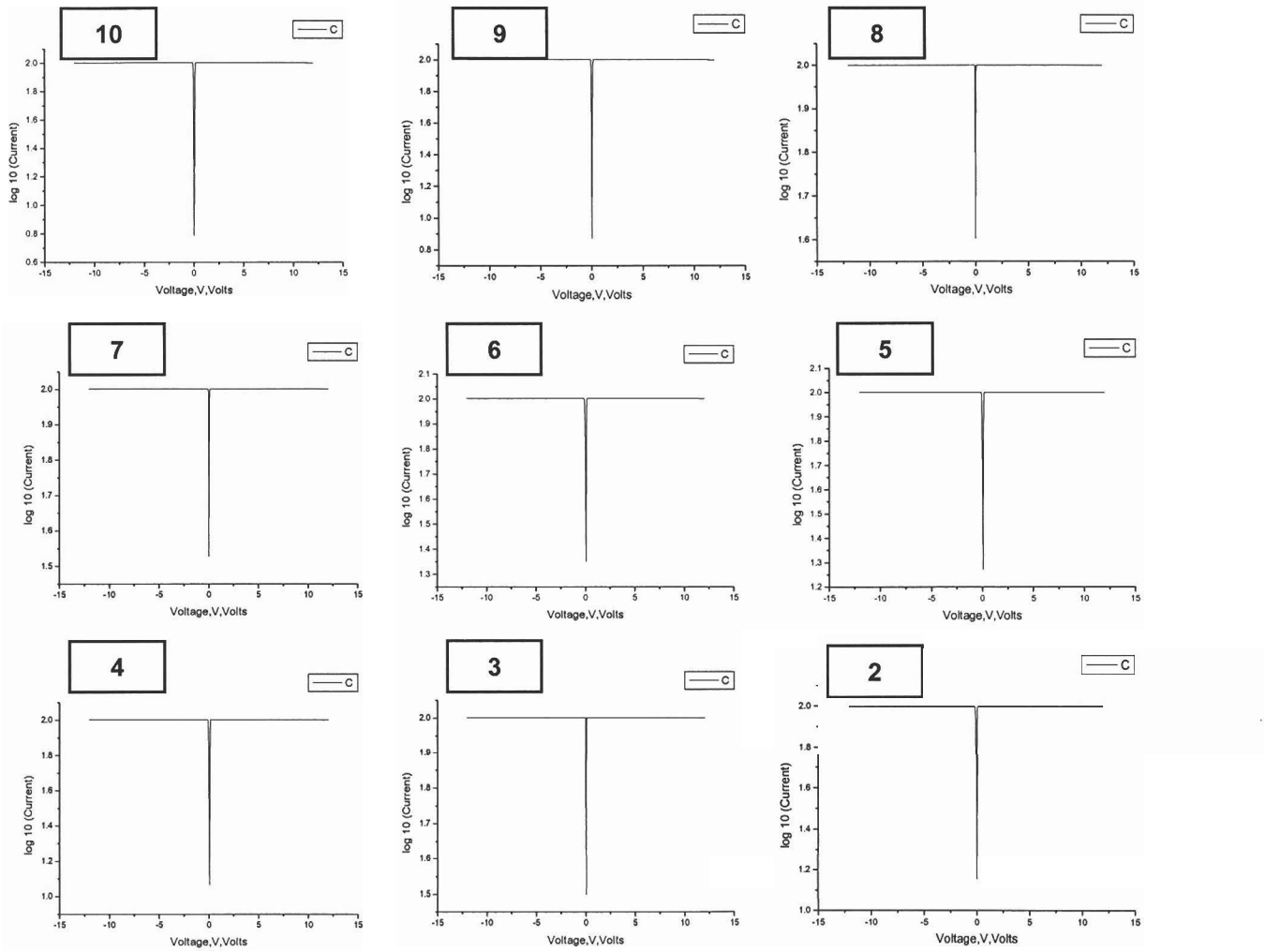

M2043 I-V Spectra (Lower Right Corner): 0.25μm × 1μm, 11V

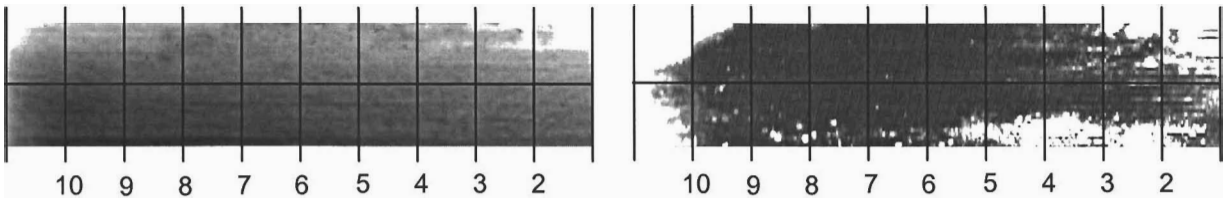

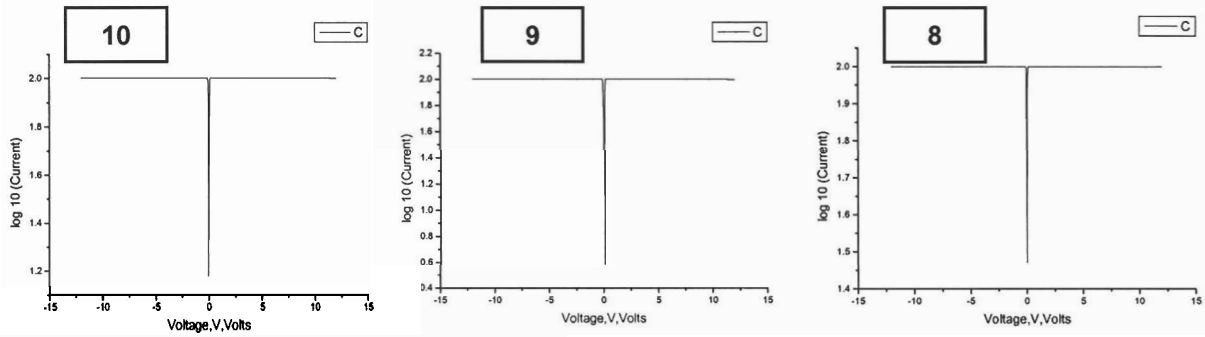

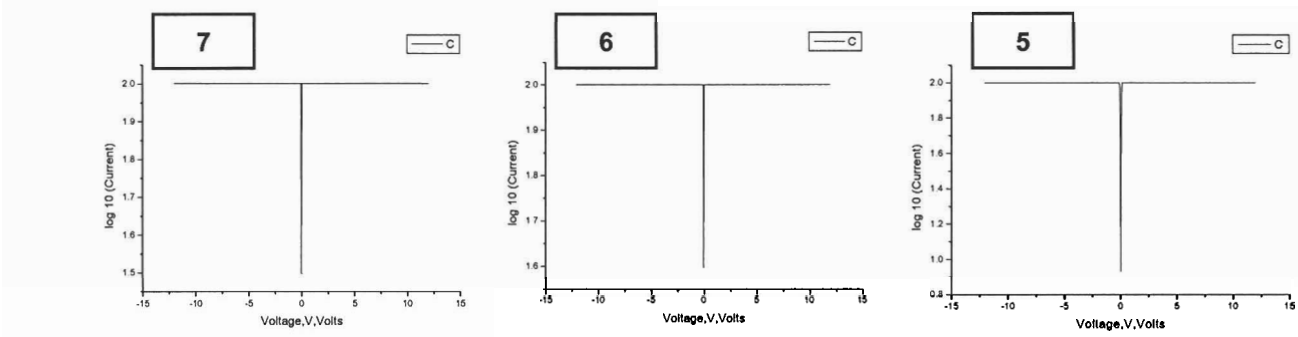

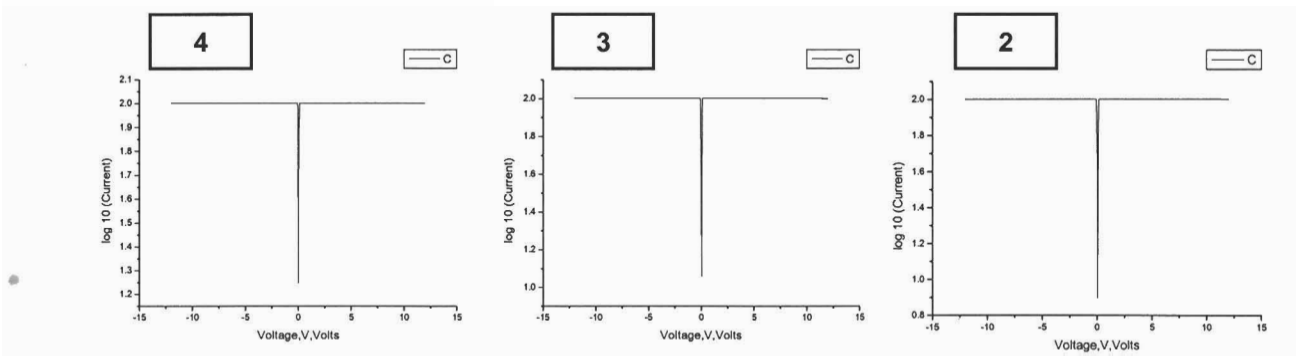

M2161 I-V Spectra (Upper Left Corner): 0.25μm × 1μm, 0.5V

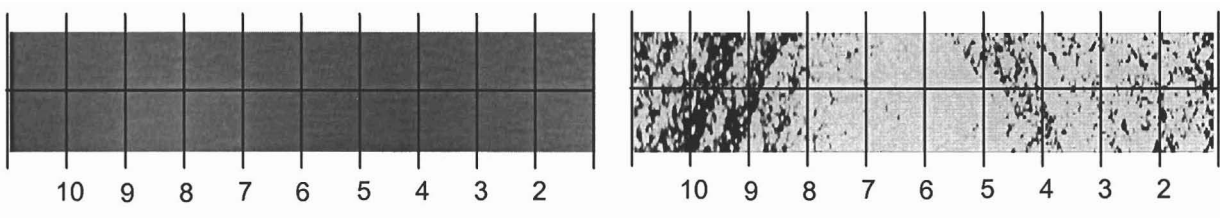

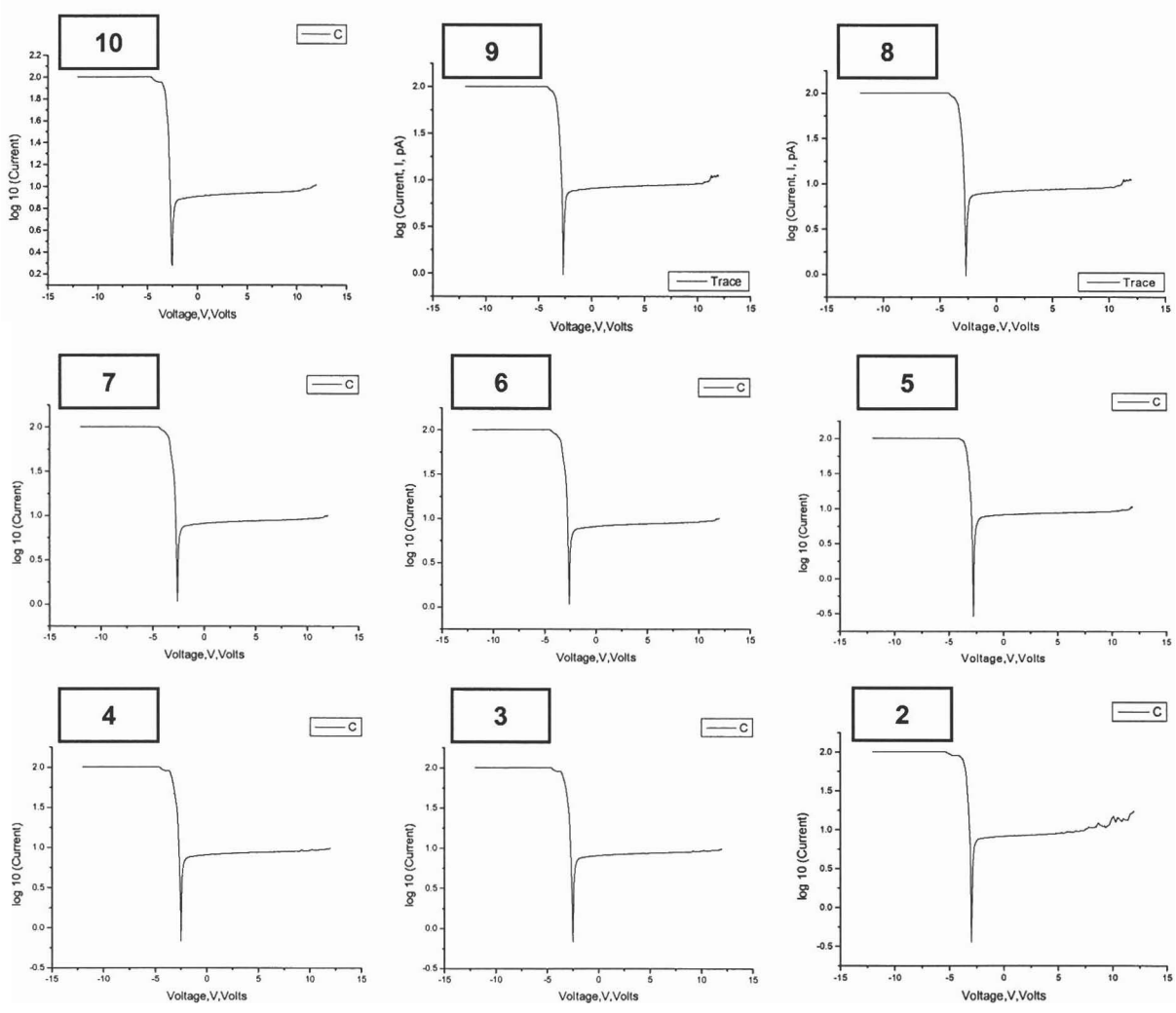

M2161 I-V Spectra (Lower Right Corner): 0.25μm × 1μm, 4V